182

Polymer Analysis
Polymer Theory

182
Advances in Polymer Science

Advances in Polymer Science

Recently Published and Forthcoming Volumes

Polymer Analysis
Polymer Theory

With contributions by

S. Anantawaraskul · H. Aoki · A. Blumen · A. A. Gurtovenko
H. Hillborg · S. Ito · H. Schönherr · J. B. P. Soares · G. J. Vansco
P. M. Wood-Adams

Springer

Advances in Polymer Science
Also Available Electronically

For all customers who have a standing order to Advances in Polymer Science, we offer the electronic version via SpringerLink free of charge. Please contact your librarian who can receive a password or free access to the full articles by registering at:

springerlink.com

If you do not have a subscription, you can still view the tables of contents of the volumes and the abstract of each article by going to the SpringerLink Homepage, clicking on "Browse by Online Libraries", then "Chemical Sciences", and finally choose Advances in Polymer Science.

You will find information about the

– Editorial Board
– Aims and Scope
– Instructions for Authors
– Sample Contribution

at springeronline.com using the search function.

Contents

Fractionation of Semicrystalline Polymers by Crystallization Analysis Fractionation and Temperature Rising Elution Fractionation

Siripon Anantawaraskul[1,3] · João B. P. Soares[2] (✉) · Paula M. Wood-Adams[4]

[1]Department of Chemical Engineering, McGill University, 3610 University Street, Montreal, H3A 2B2, Canada

[2]Department of Chemical Engineering, University of Waterloo, Waterloo, ON, N2L 3G1, Canada
jsoares@cape.uwaterloo.ca

[3]Department of Chemical Engineering, Kasetsart University, 50 Phaholyothin Road, 10900 Bangkok, Thailand

[4]Department of Mechanical and Industrial Engineering, Concordia University, 1455 de Maisonneuve Blvd. West, Montreal, H3G 1M8, Canada

Abstract Crystallization analysis fractionation (Crystaf) and temperature rising elution fractionation (Tref) are analytical techniques for determining the distribution of chain crystallizabilities of semicrystalline polymers. These techniques fractionate polymer chains on the basis of the differences in their chain microstructures that affect their crystallizabilities in dilute solutions. Both techniques can be used to estimate the chemical composition distribution of copolymers and the tacticity distribution of homopolymers. This information is crucial for understanding polymerization mechanisms and constructing structure–property relationships. This review covers the theoretical aspects of both techniques, describes their basic operation procedures and applications, and discusses the mathematical models proposed for Crystaf and Tref.

Abbreviations

A-Tref	Analytical temperature rising elution fractionation
CC	Average comonomer content
CCD	Chemical composition distribution
CR	Cooling rate
Crystaf	Crystallization analysis fractionation
DSC	Differential scanning calorimetry
FTIR	Fourier transform IR
HDPE	High-density polyethylene
LDPE	Low-density polyethylene
LLDPE	Linear low-density polyethylene
MWD	Molecular weight distribution
P-Tref	Preparative temperature rising elution fractionation
SEC	Size-exclusion chromatography
SNA	Successive nucleation/annealing
SSF	Successive solution fractionation
Tref	Temperature rising elution fractionation
ΔT_C	Temperature difference between Crystaf peak temperatures

1
Introduction

Polymer microstructural characterization provides information that is essential to understand polymerization mechanisms and to construct structure–property relationships required for the production of polymers with a set of well-defined molecular and macroscopic properties.

Crystallization analysis fractionation (Crystaf) is a recently developed characterization technique that fractionates polymer chains according to their crystallizabilities in a dilute solution [1, 2]. This technique is based on the continuous nonisothermal crystallization of polymer chains from a dilute solution. During crystallization, the concentration of polymer in solution is measured as a function of crystallization temperature, generating a cumulative concentration profile such as the one shown in Fig. 1. The derivative of this cumulative concentration profile is proportional to the fraction of polymer crystallized at each temperature interval and represents the distribution of chain crystallizabilities in the sample.

For ethylene/1-olefin copolymers, chain crystallizability is mainly controlled by the fraction of noncrystallizable comonomer units in the chain. Consequently, the differential Crystaf profile shown in Fig. 1, together with an appropriate calibration curve, can be used to estimate the copolymer chemical composition distribution (CCD), also called the short-chain branch distribution. The CCD of a copolymer describes the distribution of the
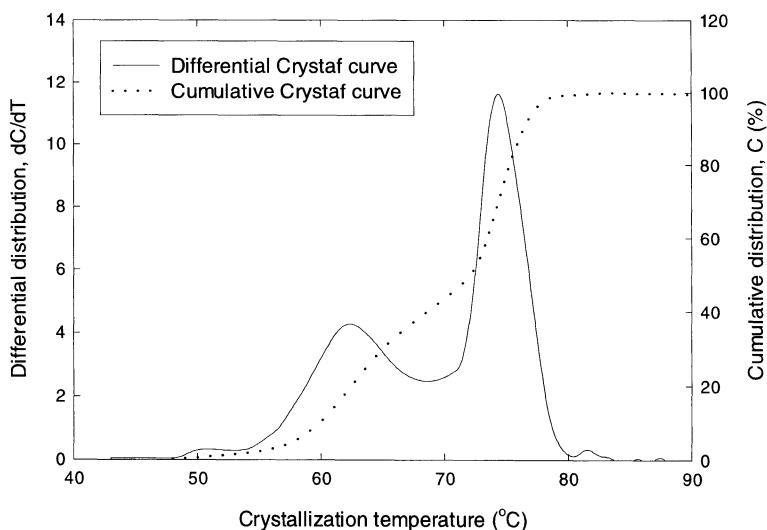
Fig. 1 Cumulative and differential crystallization analysis fractionation (*Crystaf*) profiles of a blend of two polyolefins
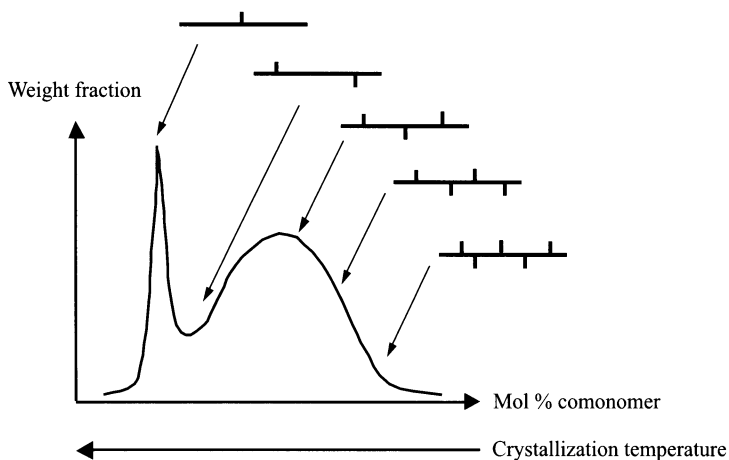
Fig. 2 Chemical composition distribution (*CCD*) of a typical Ziegler–Natta linear low-density polyethylene, reflecting the composition heterogeneity of these copolymers

comonomer fraction in its chains, reflecting its composition heterogeneity (Fig. 2). Composition heterogeneity in copolymers can significantly influence their physical properties. For example, linear low-density polyethylene (LLDPE) with a narrow CCD has much better film properties than LLDPE with a broad CCD [3, 4].

Several factors may contribute to CCD heterogeneity [5]. The more pervasive one is the statistical nature of polymerization which forces the composition of any synthetic copolymer chain to be always distributed around a certain average value. For multi-site-type catalysts, e.g. heterogeneous Ziegler–Natta catalysts, each active site type has a distinct set of polymerization kinetics constants and produces polymer chains with different average microstructures. Therefore, the polymers synthesized with these catalysts are mixtures of chains with different average chain lengths and average comonomer compositions (Fig. 3). Nonuniform polymerization conditions, i.e. temporal and spatial variations in monomer concentration and temperature during polymerization, may also be responsible for CCD heterogeneity. Comonomer compositional drift, a commonly encountered phenomenon in batch and semibatch polymerizations, can significantly broaden the CCD of copolymers.

In the case of stereoregular polymers, such as isotactic and syndiotactic polypropylene, chain tacticity is the main factor affecting crystallizability. Crystaf can also be used to measure the distribution of tacticity. Since the distribution of tacticity is often modeled with pseudo binary copolymerization models (i.e. the meso and racemic insertions stand for the comonomer type in the case of a copolymer), the following discussion for copolymers can be easily modified to describe the tacticity distribution of stereoregular polymers.

Sites with low comonomer incorporation produce longer chains

Sites with high comonomer incorporation produce shorter chains

Weight fraction

Mol % comonomer
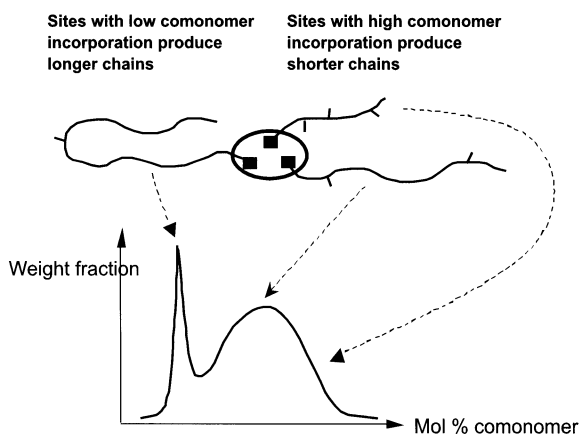
Fig. 3 Copolymers produced by Ziegler–Natta catalysts exhibiting a broad CCD. Chains made by different active sites have different microstructural distributions

Crystaf was developed as an alternative to temperature rising elution fractionation (Tref). Although both techniques are based on similar fractionation mechanisms and provide comparable results, Tref operation tends to be more time-consuming because it involves two fractionation steps, crystallization and elution, while Crystaf requires only the crystallization step. Similarly to Crystaf, the most important fractionation step in Tref occurs during the crystallization step, but data collection in Tref is done only during the elu-

solvent + polymer   IR

Detector response

Atactic PP

LLDPE

Isotactic PP

Elution temperature

solvent
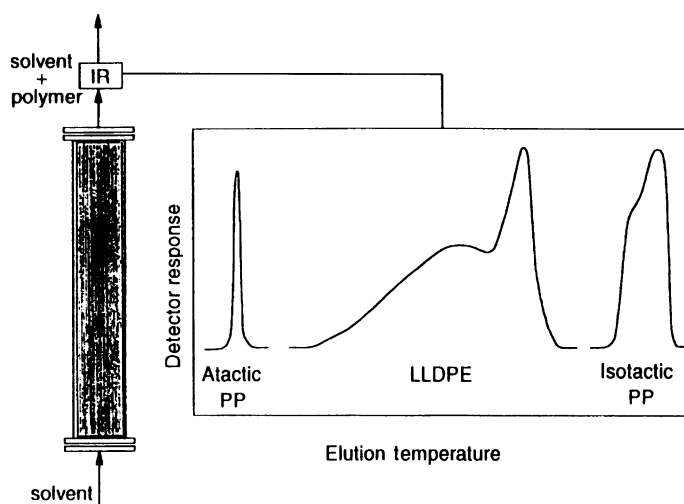
Fig. 4 Elution step of temperature rising elution fractionation (*Tref*) analysis and typical Tref profiles of different polymers [5]. *LLDPE* linear low-density polyethylene, *PP* polypropylene

tion period (Fig. 4). In this review, an overview of Tref operation will also
be given and relevant recent research findings related to Tref will be high-
lighted. More comprehensive reviews focusing solely on Tref are available in
the literature [5–9]. This review focuses on the fractionation of ethylene/α-
olefin copolymers by Crystaf and Tref, because these techniques have been
used more often to analyze this class of polymers. Extensions to other types
of semicrystalline polymers, however, will also be discussed when required.

2
Theoretical Background

The fractionation mechanism of Crystaf and Tref relies on differences of
chain crystallizabilities in dilute solution: polymer chains with high crys-
tallizabilities will be fractionated at higher temperatures, while chains with
low crystallizability are fractionated at lower temperatures. In this section,
we review the basic theory of polymer crystallization in dilute solutions to
explain how solvent type, polymer volume fraction, molecular weight, and
comonomer content affect chain crystallizabilities and equilibrium melting
temperatures. The theory describing the CCD of copolymers will also be sum-
marized.

2.1
Thermodynamic Considerations for Homopolymer Solutions

The Flory–Huggins equation for the free energy of mixing can be used to de-
scribe the thermodynamic equilibrium of a concentrated polymer solution
assuming a uniform distribution of solvent and polymer segments [10, 11].
The decrease in the equilibrium melting temperature of the polymer due to
the presence of solvent and the number of chain segments is given by

$$\frac{1}{T_m} - \frac{1}{T_m^0} = \left(\frac{R}{\Delta H_u}\right)\left(\frac{V_u}{V_l}\right)\left[-\frac{\ln\left(v_2\right)}{x} + \left(1 - \frac{1}{x}\right)v_1 - \chi_1 v_1^2\right], \tag{1}$$

where T_m^0 is the melting temperature of the pure polymer, T_m is the equi-
librium melting temperature of the polymer in solution, ΔH_u is the heat of
fusion per repeating unit, V_u and V_l are the molar volumes of the polymer
repeating unit and diluent, respectively, v_1 and v_2 are the volume fractions of
the diluent and polymer, respectively, x is the number of segments, and χ_1 is
the Flory–Huggins thermodynamic interaction parameter.

The crystallization step in Crystaf and Tref, however, occurs in dilute so-
lution. Theoretically, this situation is more complicated because polymer
segments are nonuniformly distributed through the solution. Strictly speak-
ing, for dilute solutions the Flory–Huggins free-energy function shown in

Eq. 1 is no longer valid. To account for the nonuniform segment distribution, the general theory for dilute solutions, where the chemical potential of the solvent is expressed in virial form, has to be considered. Fortunately, it has been found that the change in chemical potential of the polymer with increasing dilution is so small that it does not have any appreciable effect on its equilibrium melting temperature [12]. For practical purposes, Eq. 1 is obeyed over the complete concentration range of dilutions.

To examine the effect of chain length on the melting temperature of a polymer in a dilute solution, it is appropriate to rearrange Eq. 1 as follows:

$$\frac{1}{T_m} - \frac{1}{T_m^0} = \frac{R}{\Delta H_u} \frac{V_u}{V_1} \left(v_1 - \chi_1 v_1^2 \right) - \frac{R}{\Delta H_u} \left[\frac{\ln \left(v_2 \right)}{r} + \frac{v_1}{r} \right]. \tag{2}$$

Here, the number of repeating units per polymer chain (r) is used instead of the number of segments (x). The second term on the right-hand side quantifies the effect of chain length, indicating that the equilibrium melting temperature decreases with a reduction in molecular weight [13]. However, this term is only important for chains with low molecular weights, as clearly
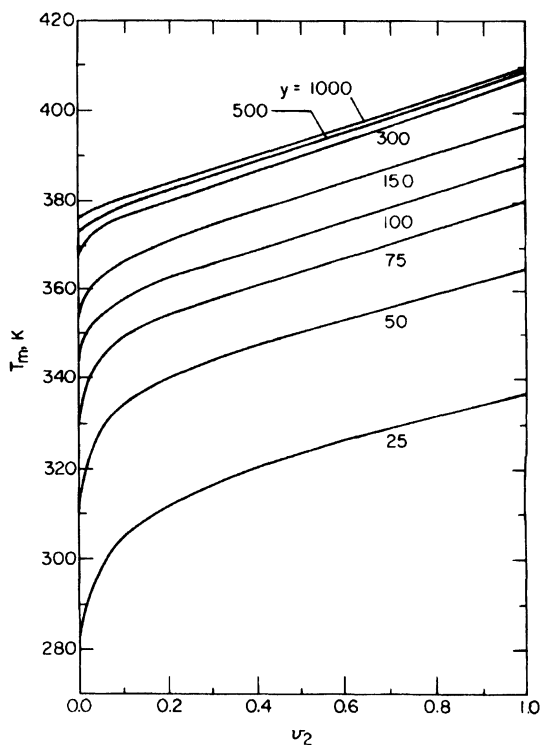
Fig. 5 Predicted melting temperatures for several chain lengths using Eq. 2 [13]

illustrated in Fig. 5. For large values of r, the case of polymers with high molecular weight, the melting temperature is relatively independent of chain length and Eq. 2 is reduced to the simpler form

$$\frac{1}{T_m} - \frac{1}{T_m^0} = \frac{R}{\Delta H_u} \frac{V_u}{V_1} \left(v_1 - \chi_1 v_1^2 \right) .$$ (3)

Equation 3 implies that all polymer chains having reasonably large molecular weights will crystallize at the same temperature, all other factor being the same. In other words, the effect of molecular weight on Crystaf or Tref profiles of high molecular weight polymers should be negligible. This is in good agreement with experimental observations for both Crystaf and Tref [14, 24].

2.2
Thermodynamic Considerations for Copolymer Solutions

In the case of copolymer solutions, the melting temperature also depends on interactions between the different monomeric units and the solvent. Considering the case in which the crystalline phase is pure (i.e., only monomeric units of a single type crystallize and no solvent is present in the lattice), the decrease in the melting temperature can be derived in a similar manner as for the homopolymer solution case using the Flory–Huggins theory with an appropriate modification [15]. To take into account the interactions between both comonomers and solvent, the net interaction parameter for binary copolymers should be calculated as follows:

$$\chi_1 = v_A \chi_{1A} + v_B \chi_{1B} - v_A v_B \chi_{AB} ,$$ (4)

where χ_1 is the interaction parameter of a binary copolymer with pure solvent, χ_{1A} and χ_{1B} are the interaction parameters of the corresponding homopolymers with the solvent, χ_{AB} is the interaction parameter between comonomers A and B in the copolymer chain, and v_A and v_B are the volume fractions of comonomers A and B in the copolymer molecules, respectively.

If the steric structures of both comonomer units in random copolymers are similar, the melting temperature depression equation will be the same as Eq. 1, with the interaction parameter calculated with Eq. 4. For a given copolymer, the crystallizabilities of copolymer chains in dilute solution strongly depend on the chain composition. From thermodynamic considerations, this can be explained from the fact that changes in copolymer composition alter the value of the interaction parameter defined by Eq. 4. For copolymers with two chemically similar comonomers, χ_{1A} will be very close to χ_{1B}, and χ_{AB} will approach zero. In this system, one can simply use Eq. 1 with $\chi_1 = \chi_{1A} \approx \chi_{1B}$.

2.3
Stockmayer's Bivariate Distribution

Stockmayer's bivariate distribution is an analytical expression describing the weight distribution of the kinetic chain length and the chemical composition for linear binary copolymers. This distribution quantifies the deviation from the average comonomer composition and molecular weight due to the statistical nature of copolymerization.

Stockmayer [16] derived this distribution with the aid of some approximations from a general theory of chain copolymerization described earlier by Simha and Branson [17]. Stockmayer's distribution has been found to be a useful tool for understanding chain microstructures of several copolymers [18–22].

Stockmayer's bivariate distribution for linear binary copolymers can be expressed by the simple equations,

$$w(r, y) = r\tau^2 \exp(-r\tau) \frac{1}{\sqrt{2\pi\beta/r}} \exp\left(\frac{-y^2}{2\beta/r}\right), \tag{5}$$

$$\beta = \overline{F}_1 \left(1 - \overline{F}_1\right) \sqrt{1 + 4\overline{F}_1 \left(1 - \overline{F}_1\right) \left(r_1 r_2 - 1\right)}, \tag{6}$$

where $\overline{F}_1$ is the average mole fraction of monomer type 1 in the copolymer, y is the chemical composition deviation from $\overline{F}_1$, r is the kinetic chain length, r_1 and r_2 are the reactivity ratios for copolymerization, and τ is the ratio of the transfer rate to the propagation rate. Stockmayer's distribution was first developed from a polymerization kinetics viewpoint but a similar distribution function can also be obtained using a statistical approach [23].

This distribution function provides important insights on the detailed composition distribution of linear binary copolymers. We will use it frequently to interpret Crystaf and Tref fractionation results in the next sections of this review. Therefore, it is useful to discuss some of its main characteristics in this section.

Figure 6 shows that copolymers with a tendency to form comonomer blocks ($r_1 r_2 > 1$) will have a broader CCD than copolymers having a tendency toward alternating comonomers ($r_1 r_2 < 1$). Note that $r_1 r_2 = 1$ is the condition of ideal copolymerization, which generates random copolymers. Considering copolymer chains with the same $r_1 r_2$ but different chain lengths, Stockmayer's distribution shows that short copolymer chains will have a broader composition distribution than long copolymer chains (Fig. 7). These simulation results are in fact intuitive: as the chain length of a copolymer approaches infinity, its composition should approach the average copolymer composition; similarly, a tendency to form alternating comonomer units ($r_1 r_2 < 1$) will forcibly result in copolymers with a 50/50 mol % comonomer composition and a very narrow CCD.
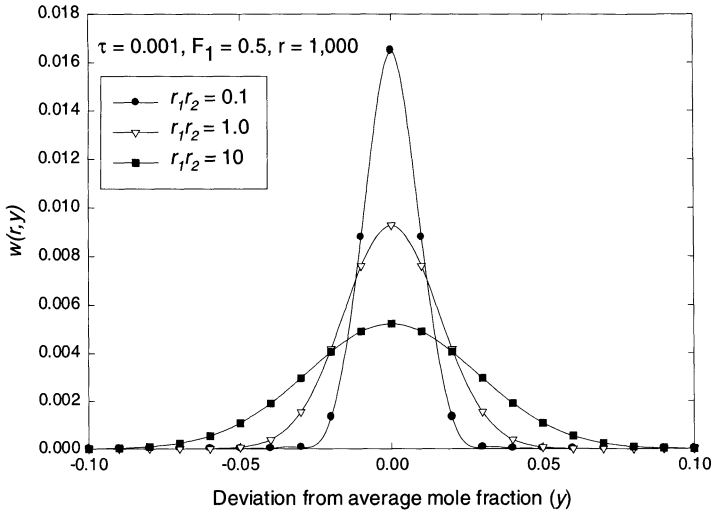
Fig. 6 Chemical composition distribution as a function of reactivity ratio product
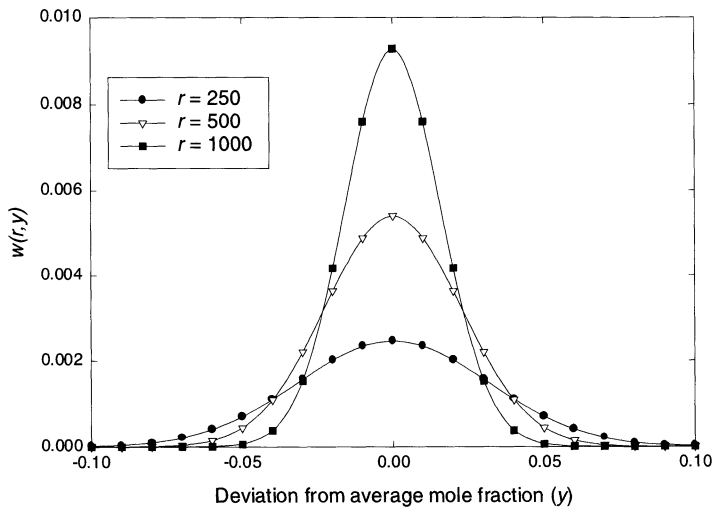
Fig. 7 Chemical composition distribution of copolymer chains with different chain lengths

Integrating Eq. 5 over all chain lengths, one obtains the equation describing the CCD component of Stockmayer's distribution, independently of chain length:

$$w(y) = \int\limits_{r=0}^{\infty} w(r,y)\, \mathrm{d}r = \frac{3}{4\sqrt{2\beta\tau}\left(1 + \frac{y^2}{2\beta\tau}\right)^{5/2}}. \tag{7}$$
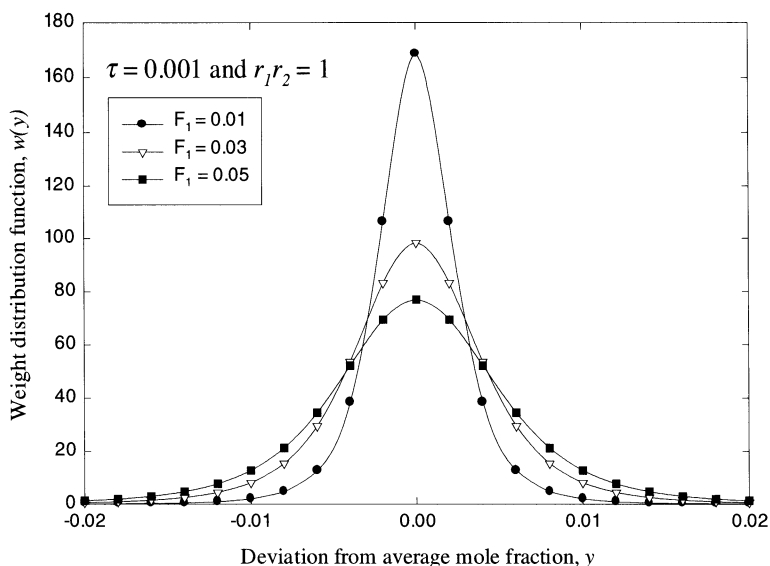
Fig. 8 Broadening of the chemical composition distribution due to increasing average comonomer content as predicted by Stockmayer's distribution, Eq. 7

Figure 8 illustrates how the CCD, predicted with Eq. 7, varies as a function of average mole fraction of monomer type 1. Notice that the CCD broadens with increasing average mole fraction of monomer type 1. This phenomenon will also be demonstrated experimentally later in this review.

3
Temperature Rising Elution Fractionation

Similarly to Crystaf, Tref is an analytical technique that fractionates semicrystalline polymers on the basis of chain crystallizabilities. However, Tref involves two consecutive steps, crystallization and elution, while Crystaf can perform a similar analysis in a single crystallization step.

Tref can be operated in analytical or preparative modes (A-Tref and P-Tref, respectively). Figures 9 and 10 show diagrams of experimental set-ups for both modes of operation [24, 25]. These two operation modes differ mainly in the elution step and sample size, which will be discussed later in more detail.
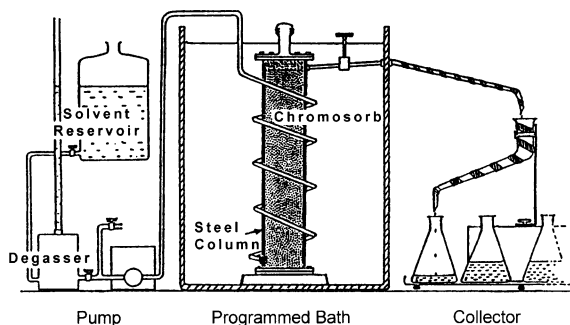
Fig. 9 Schematic diagram of preparative Tref (*P-Tref*) [25]
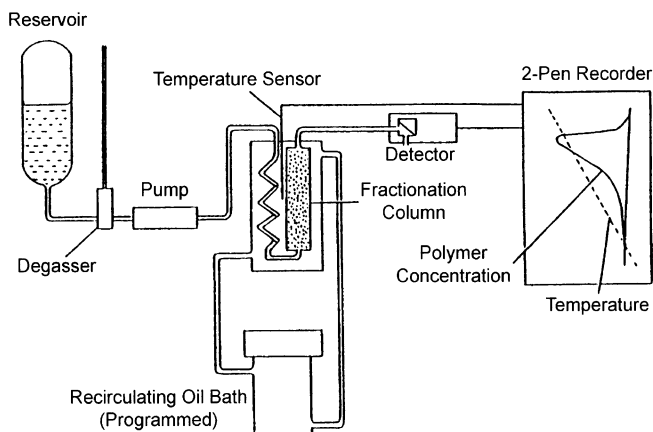
Fig. 10 Schematic diagram of analytical Tref (*A-Tref*) [24]

3.1
Basic Experimental Apparatus and Procedures

Tref operation can be briefly described as follows. First, the polymer sample is dissolved in a good solvent at high temperature and then introduced into a column containing an inert substrate, such as glass beads or steel shot. The temperature in the column is then decreased at a slow, constant cooling rate (CR). This step allows polymer chains to crystallize in an "orderly" fashion, from higher to lower crystallizabilities, i.e., from lower to higher comonomer contents. Alternatively, the crystallization step can be carried out in a temperature-programmable stirred vessel containing the inert substrate (Fig. 11) [8] and after precipitation is complete, the polymer-coated support is introduced into the Tref column. (The onion skin schematic depicted in Fig. 11 for the polymer precipitated onto the support is for illustrative purposes only; it most certainly does not correspond to the polymer phase distribution on the actual support.) For both A-Tref and P-Tref, the CR has to
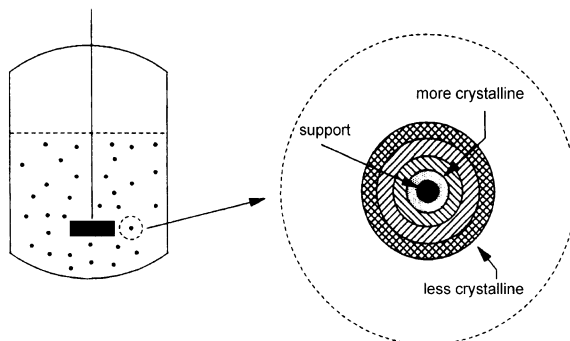
Fig. 11 Illustration of polymer layers on the support after the crystallization step in Tref. Layer dimensions are greatly exaggerated for illustration purposes [8]

be slow enough to ensure efficient polymer fractionation. The crystallization step is the most important one in Tref, as most of the polymer fractionation occurs during this period.

In the elution step, pure solvent is flowed through the column as the temperature is increased. As the dissolution temperature of the polymer is reached, the polymer outer layers dissolve back into the solvent in the reverse order they were precipitated. The elution step is carried out in different ways for A-Tref and P-Tref. Table 1 summarizes the most relevant characteristic of both methods [5].

In A-Tref, the column temperature in the elution step is increased at a slow, constant rate, while the polymer concentration in the eluent is monitored with an on-line mass-sensitive detector to obtain the Tref profile (the distri-

Table 1 Comparisons between analytical and preparative temperature rising elution fractionation (*A-Tref* and *P-Tref*) [5]

A-Tref	P-Tref
1. Fractions are collected continuously by gradually increasing the elution temperature.	1. Fractions are collected at predetermined temperature intervals. Continuous operation is less commonly used.
2. Information on macromolecular structure is obtained on-line by means of a calibration curve.	2. Information on macromolecular structure is obtained off-line by additional analytical techniques.
3. Requires smaller columns and smaller sample sizes.	3. Requires larger columns and larger polymer sample sizes.
4. Faster than P-Tref but generates less information about polymer microstructure.	4. Time-consuming but can generate detailed information about polymer microstructure.

bution of chain crystallizabilities in terms of the weight fraction of polymer eluted at each temperature). The CCD and the tacticity can be obtained from the Tref profile using a calibration curve.

P-Tref generally uses larger columns and samples sizes. In this case, the temperature is increased as a step function and all polymer eluting in a given temperature interval is recovered for further analysis by other techniques. P-Tref is more commonly used to prepare a series of fractions, each having narrower CCDs than the parent sample.

Tref can also be combined with other fractionation techniques, such as size-exclusion chromatography (SEC) or successive solution fractionation (SSF). These cross-fractionation techniques can provide a great wealth of information on chain microstructure. The applications of cross-fractionation techniques using Tref will be summarized later in this review.

3.2
Effect of Chain Microstructures and Operation Conditions

It is important to have a clear understanding on how chain microstructural characteristics and operation conditions influence Tref results in order to avoid data misinterpretation. Wild et al. [24] studied the effect of molecular weight on the fractionation process in Tref using linear polyethylene fractions with narrow molecular weight distributions (MWDs). They reported that molecular weight effects could be observed when polymers with low molecular weights (less than 10 000) were considered. Tref results become independent of chain length, however, for polyethylene samples with higher molecular weights. These experimental results are in agreement with the theory of crystallization from dilute solution discussed earlier.

Comonomer content significantly affects Tref profiles. This is to be expected, as the comonomer units are known to reduce chain regularity, thus lowering chain crystallizability [26, 27]. Linear relationships between average comonomer contents (CC) and elution peak temperatures are generally observed for ethylene/1-olefin copolymers [5, 6]. It is important that these relationships reflect only the influence of comonomer content because they are used as calibration curves to convert Tref profiles into CCDs.

Recently, Savitski et al. [28] investigated the effect of short-chain branch length on Tref using sets of ethylene/1-olefin copolymers. They reported that comonomer type could noticeably affect Tref profiles and change the slope of Tref calibration curves (Fig. 12). At the same comonomer content, the calibration curves are shifted to lower elution temperatures as the length of the short-chain branch increases. This can be explained from the fact that, as the length of the short branch increases, they become effective at disrupting the crystal regular packing and are more likely to be excluded from the lattice. Therefore, longer short branches more effectively decrease chain crystallizability. These results imply that, to estimate the CCD accurately, the branch
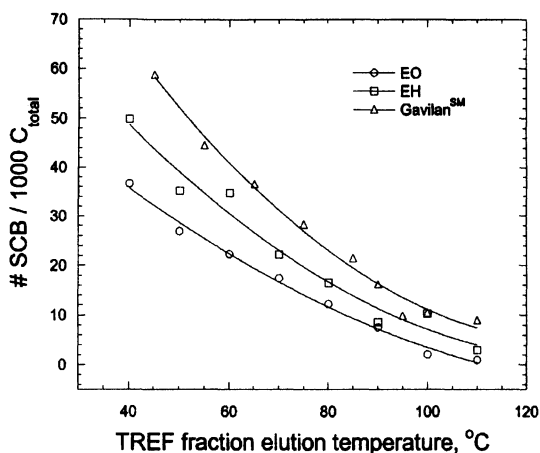
Fig. 12 Effect of comonomer type on Tref calibration curves [28]

type must be known a priori in order to choose an appropriate calibration curve.

Operation conditions also influence Tref results. Our recent work [29] showed that crystallization kinetics plays an important role in the fractionation process. The CR, the heating rate, and the solvent flow rate can affect Tref profiles to a large extent. We demonstrated that there is a general relationship between Tref profiles and the relative ratio among the CR, the heating rate, and the solvent flow rate:

1. A too fast CR can significantly reduce the fractionation efficiency, as polymer chains will not have sufficient time to separate according to their microstructures.
2. Since the solvent flow rate during the elution step determines the residence time of the polymer solution in the column, slow flow rates broaden Tref profiles and increase the Tref peak temperature, most likely due to an increase in residence time and axial dispersion in the column. Although higher solvent flow rates can help reduce axial dispersion, they also reduce the signal-to-noise ratio.
3. Fast heating rates can broaden Tref profiles, as a given volume of solvent will elute polymer over a wider range of crystallinities.

On the basis of these observations, we proposed that keeping a constant ratio of CR, heating rate, and solvent flow rate was required to cancel out the effects of the individual rates and generate very similar Tref profiles at different operation conditions. Figure 13 demonstrates that this approach is valid for the range of conditions investigated.

Cocrystallization is commonly studied by analyzing blends of two or more polymer samples. Cocrystallization is considered significant when the Tref profile for the blend cannot be superimposed onto the Tref profiles of the
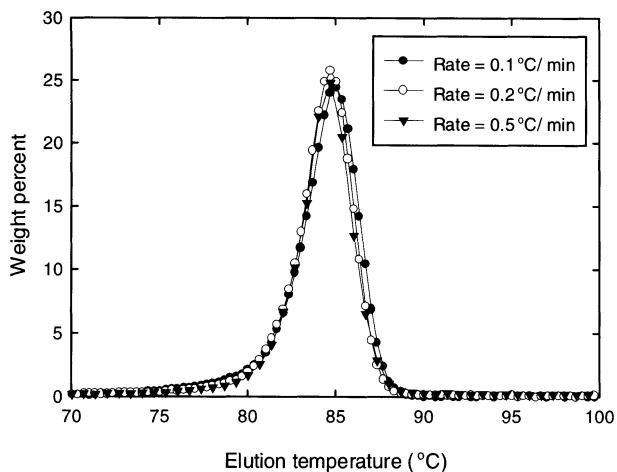
Fig. 13 Tref profiles for different operation conditions. The ratio of cooling rate : heating rate : solvent flow rate remains constant at 1 : 1 : 1 [29]
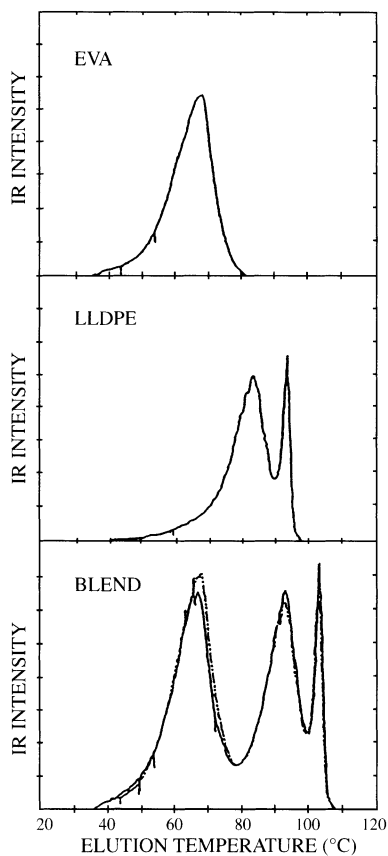
Fig. 14 Tref profiles of a polyolefin blend and its parent samples [30]
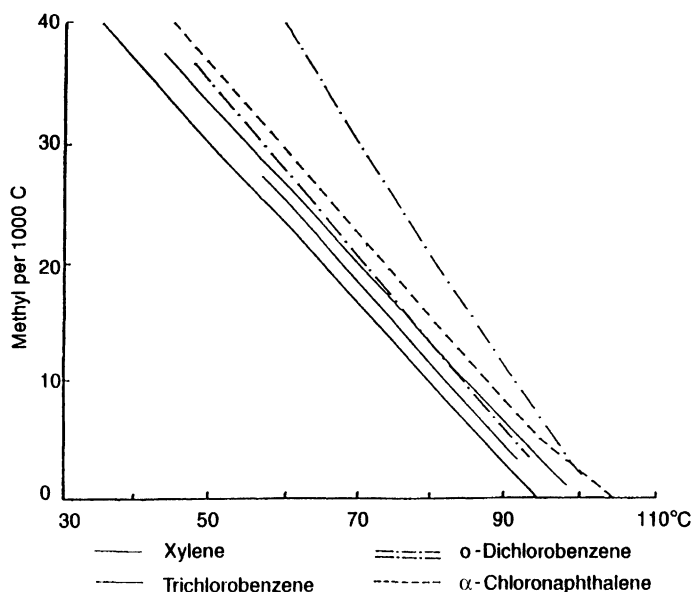
Fig. 15 Tref calibration curves for several solvent types [31]

blend components. Generally, cocrystallization during Tref analysis is reported to be very small (Fig. 14) [30]. However, our recent work [29] shows that fast CRs can promote significant cocrystallization during the analysis of ethylene/1-olefin blends, as will be discussed in more detail later in this review.

Within the range of commonly used initial polymer concentration (1–10 mg/mL), this operation parameter does not play a major role in the fractionation [29]. A high polymer concentration can help increase the signal-to-noise ratio, but too high a concentration can cause problems such as plugging of the lines, detector, and Tref column. The particular design of each Tref apparatus normally determines the range of appropriate initial concentrations.

Solvent type does not seem to affect the efficiency of the fractionation process in any significant way. Different solvent types simply shift Tref profiles to higher or lower elution temperatures depending on the interactions between polymer and solvent. Thermodynamically good solvents shift Tref profiles to lower elution temperatures, while poorer solvents do the opposite. Calibration curves prepared using different solvents were reported to be almost parallel (Fig. 15) [31], which indicates that the choice of solvent in Tref is of minor importance.

3.3
Use of Tref to Estimate the CCD of Copolymers

One of the main applications of Tref is determining the CCD of copolymers. The major difficulty of using Tref analysis to obtain quantitative CCDs is that the calibration curve depends on several operation conditions and on material type. Factors that affect Tref calibration curves are solvent type, CR, comonomer type, comonomer content, and comonomer sequence length distribution.

Comonomer type, fraction, and sequence length distribution can affect Tref calibration curves; therefore, calibration standards for samples with very broad and nonuniform CCDs, such as LLDPE made with heterogeneous Ziegler–Natta catalysts, are generally obtained by fractionating the parent resin with P-Tref. The compositions of these calibration standards have to be determined using other analytical techniques, such as ^{13}C NMR or Fourier transform IR (FTIR) spectroscopy, so that the comonomer composition versus elution temperature calibration curve can be determined for each sample type. Since this is a very time consuming method, most researchers simply opt for using calibration curves determined for similar polymers. Recently, standards made with metallocene catalysts have found wide application since they do not require fractionation by P-Tref. This approach, however, is quantitatively inaccurate when used to analyze polymers made with other cat-
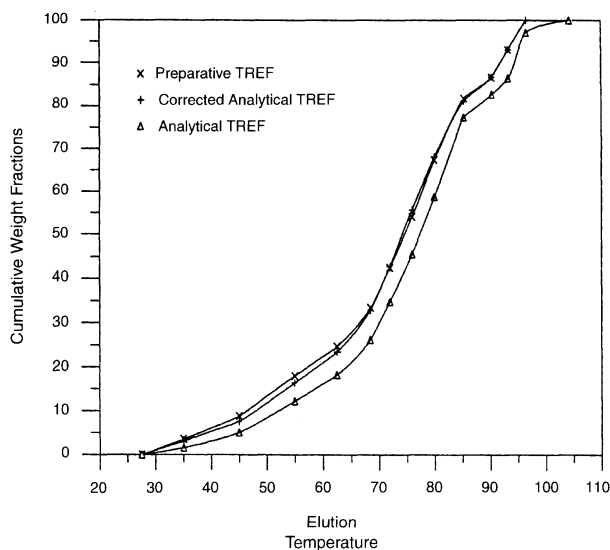
Fig. 16 Cumulative Tref profiles of A-Tref before correction, corrected A-Tref, and P-Tref [32]
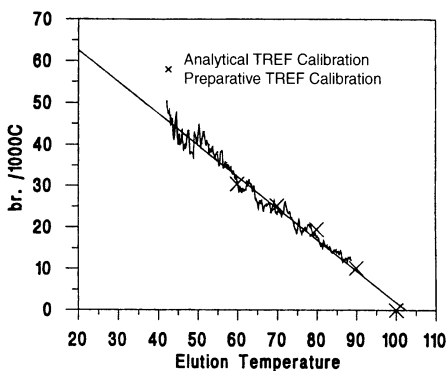
Fig. 17 Comparison between calibration curves obtained using a dual IR system in A-Tref and P-Tref [33]
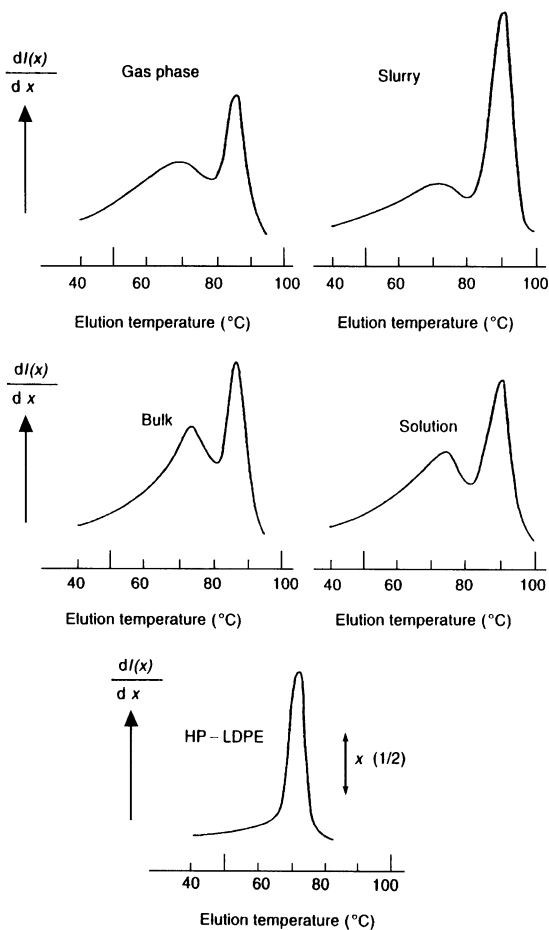
Fig. 18 Comparison of Tref profiles for LLDPE made in four different Ziegler–Natta polymerization processes and that of low-density polyethylene (*LDPE*) [34]

alysts, particularly if the "blockiness" of the sample and of the calibration standards differ considerably.

Pigeon and Rudin [32] reported the branching frequencies measured with A-Tref and P-Tref at the same elution temperature could be different (Fig. 16). Their results imply that a calibration curve produced from P-Tref cannot be used for converting raw A-Tref results to the CCD. It is necessary to correct the A-Tref results before applying the calibration curve by considering the elution time associated with the volume of the A-Tref and P-Tref columns.

To reduce the complexity of using P-Tref to obtain calibration curves, Pigeon and Rudin [33] proposed an alternative technique using A-Tref and a dual IR spectrometry detector. The dual IR system proposed allowed them to measure both concentration and branching frequency as a function of elution temperature. The calibration curve obtained by on-line dual IR spectrometry in A-Tref is identical to the one from P-Tref (Fig. 17). This eliminates the need to perform P-Tref on every sample and provides a fully quantitative Tref analysis.

Perhaps one of the greatest contributions of Tref to the understanding of olefin polymerization was the elucidation of the nature of active sites present on heterogeneous Ziegler–Natta catalysts. The systematic application of Tref to ethylene/1-olefin copolymers made with heterogeneous Ziegler–Natta catalysts in different polymerization processes has shown that all these resins have a signature bimodal Tref peak that can only be explained by the presence of two or more distinct types of active sites on the catalyst [34]. In contrast, low-density polyethylene (LDPE) made with the free-radical mechanism has a much narrower and unimodal Tref profile (Fig. 18), as expected from a free-radical polymerization mechanism.

3.4
Cross-Fractionation

Cross-fractionation is a combination of two or more fractionation techniques, each of which separates polymer chains according to a different microstructural characteristic. By combining different techniques, cross-fractionation can probe information on chain microstructure in greater detail than any single characterization technique and is an especially important tool for understanding polymers with complex chain microstructures. In this review, we considered only cross-fractionation techniques that involve chain crystallizability as one of the fractionation mechanisms. More details on a wide range of cross-fractionation techniques are available in the literature [35].

Besides being used to understand complex microstructural distributions, cross-fractionation can also be used for sample preparation. Before single-site-type catalysts were commonly available, it was extremely difficult to study the independent effect of molecular weight or comonomer composition on polyolefin properties, because polyolefins produced with Ziegler–

Natta catalysts have very broad and interdependent molecular weight and comonomer composition distributions (for these resins, the molecular weight decreases with increasing comonomer content).

SSF/solution crystallization fractionation [36] are old techniques used to prepare fractions with narrow molecular weights and comonomer composition distributions. Unfortunately, these techniques are very time consuming and generally require significant amounts of solvent. More recently, P-Tref/SEC apparatuses have been used to perform this type of cross-fractionation in a more efficient, but still rather involved, way [37–40].

In P-Tref/SEC cross-fractionation, copolymer chains are first fractionated according to comonomer composition into a series of fractions using P-Tref. Each fraction is then analyzed using SEC to obtain its MWD. P-Tref/SEC is a very powerful cross-fractionation technique because it provides information on the bivariate comonomer composition and MWD. Although the process is still time-consuming, the information obtained with P-Tref/SEC cross-fractionation provides an almost complete map of chain microstructures. This cross-fractionation technique has been used for various ethylene/1-olefin copolymers (1-butene, 1-hexene, 1-octene, and 1-pentene-4-methyl).

As is true for most complex techniques, caution should be taken when interpreting and quantifying the results from P-Tref/SEC because the fractionation mechanisms of P-Tref and SEC are not based solely on comonomer composition and molecular weight, respectively, but rather are based on chain crystallizabilities and hydrodynamic volumes.

Other common cross-fractionation techniques are SSF/A-Tref and SSF/P-Tref [41, 42]. In these techniques, polymers are first fractionated using SSF and the fractions are then further fractionated according to chain crystallizabilities using A-Tref or P-Tref. When P-Tref is used, further determination of comonomer content by ^{13}C NMR or FTIR spectroscopy is required. Figures 19 and 20 show 3D and contour plots of bivariate distributions of molecular weight and comonomer composition obtained by SSF/P-Tref cross-fractionation for an ethylene/1-pentene-4-methyl copolymer [42]. Comparing the contour plot with the equivalent contour plot of a LDPE sample (Fig. 21), one clearly notices significant differences between the bivariate distributions of these two samples.

Although the methods already mentioned can provide very detailed information on chain microstructure, they have the disadvantage of being very time consuming, which precludes their use in day-to-day analyses. Simpler approaches have been proposed by measuring one average microstructural property across the distribution of another property. For example, the average comonomer composition of polymers eluted from SEC columns can be measured as a function of molecular weight (or, more accurately, hydrodynamic volume) using on-line FTIR spectroscopy. This technique is a partial replacement for the more involved SEC/A-Tref cross-fractionation. Another possibility consists of measuring the average molecular weight of polymers
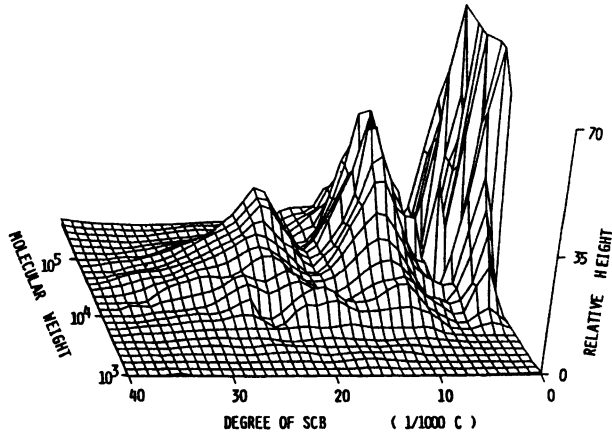
Fig. 19 Three-dimensional plot of the molecular weight distribution (*MWD*) and the CCD obtained from cross-fractionation of LLDPE [42]
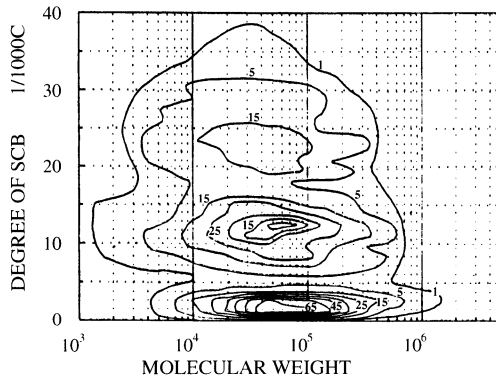
Fig. 20 Contour plot of the MWD and the CCD obtained from cross-fractionation of LLDPE [42]
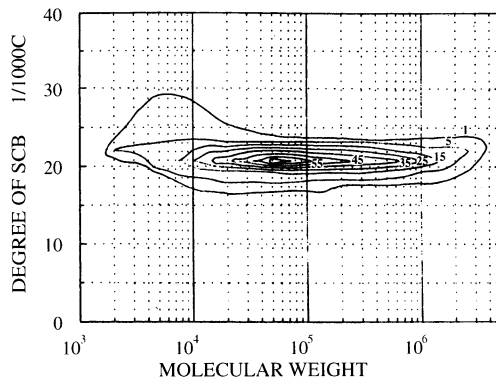
Fig. 21 Contour plot of MWD and CCD obtained from cross-fractionation of LDPE [42]

eluted from Tref columns using a light scattering detector to replace the more complex P-Tref/SEC combination. However, these two methods (SEC/FTIR and P-Tref/light scattering) are not true cross-fractionations because one of the characterization techniques merely measures average microstructural characteristics.

In the case of SEC/FTIR characterization, a method for recovering the full distribution from the average comonomer composition was proposed based on a polymerization kinetics model and the deconvolution of the MWD [43]. It was found, however, that both SEC/FTIR and P-Tref/light scattering techniques generally lose part of the information on the bivariate distribution of molecular weight and comonomer composition [44].

Besides the cross-fractionation of molecular weight and comonomer composition, another group of cross-fractionation techniques focus on the cross-fractionation of comonomer composition and chain sequence length. This group includes a combination of P-Tref and differential scanning calorimetry (DSC) with successive nucleation/annealing (SNA) [45, 46].

DSC is a widely used thermal analysis technique for studying polymer crystallization. DSC instruments contain two sample holders, each connected to their own heat source. A polymer sample is placed in one of the holders, while the other sample holder is left empty as a reference cell. By changing the temperature of both holders at a constant rate, the difference in the energy extracted from both holders to keep them at the same temperature is recorded,
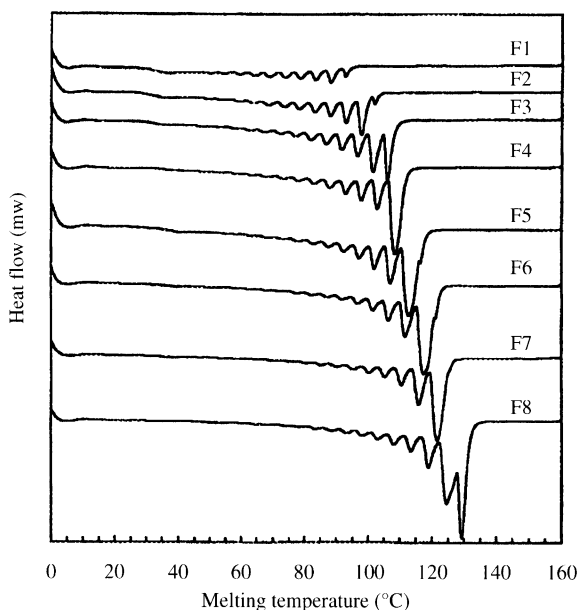
Fig. 22   P-Tref/successive nucleation/annealing cross-fractionation of Ziegler–Natta LLDPE [46]

providing the thermogram of the heat flow as a function of temperature. As the lengths of the polymer segments that can crystallize are related to the temperature, the DSC thermogram can be related to the comonomer sequence length distribution of the polymer.

When DSC is performed in SNA mode, instead of using a constant CR, the temperature program is subjected to a series of heating–annealing–cooling cycles. This process involves recrystallization and reorganization of polymer sequences and is found to be much more efficient and to offer higher resolution compared with the conventional DSC mode of operation. Therefore, P-Tref/DSC/SNA cross-fractionation is also a useful technique to understand the intermolecular and intramolecular heterogeneity of copolymers (Fig. 22).

3.5
Mathematical Modeling of Tref

Because of the complexity of the fractionation mechanism, not many mathematical models have been proposed to describe separation with Tref. Soares and Hamielec [47] used Stockmayer's distribution (Eq. 7) to simulate the CCD of linear binary copolymers synthesized with multi-site-type catalysts. Under the assumption that the fractionation process of Tref was controlled only by comonomer composition, the CCD was directly converted into the Tref profile using a calibration curve. For the case of ethylene/1-olefin copolymers made with multiple-site catalysts, the CCD of the whole polymer is described as the weighted summation of the CCDs of the copolymers produced by each active site:

$$\overline{w}(y) = \sum_{i=1}^{n} m_i w_i(y) \,, \tag{8}$$

where $\overline{w}(y)$ is the CCD for the whole polymer, m_i is the mass fraction of polymer produced on site i, $w(y)$ is the CCD for the individual site i (Eq. 7), and n is the total number of site types. Equation 8 is very useful to represent the effect of multiplicity of active sites on the CCD, but other alternative models are also possible [48]. Since Eq. 8 permits the most straightforward description for the CCD of polymers made with multiple-site catalysts, it will be the only model used in this review to illustrate Tref and Crystaf fractionation.

Figure 23 shows a simulated Tref profile for a LLDPE model sample made with a five-site-type catalyst [47]. By solving the inverse problem, this approach has been used to deconvolute experimental Tref profiles and provide information on the number of active-site types present on the catalyst (Fig. 24) [49]. This model, however, has the serious limitation of not accounting for peak broadening in Tref. Peak broadening in Tref has been reported to be significant (Fig. 25) [50].
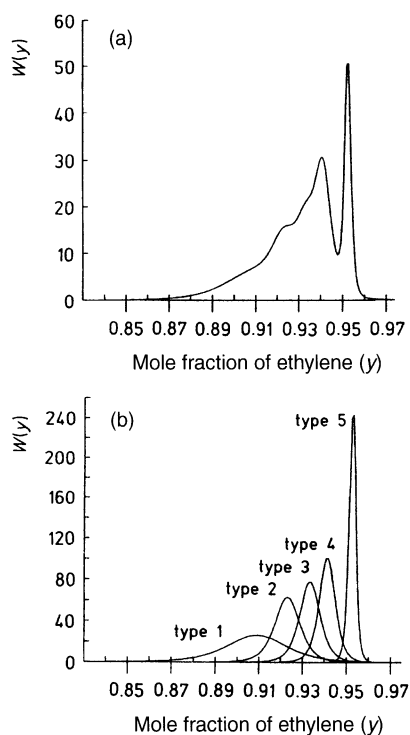
Fig. 23 (**a**) Simulated Tref profile of LDPE made by a five-site-type catalyst. (**b**) Simulated Tref profiles of LLDPE made by each catalytic-site type in a five-site-type catalyst [22]
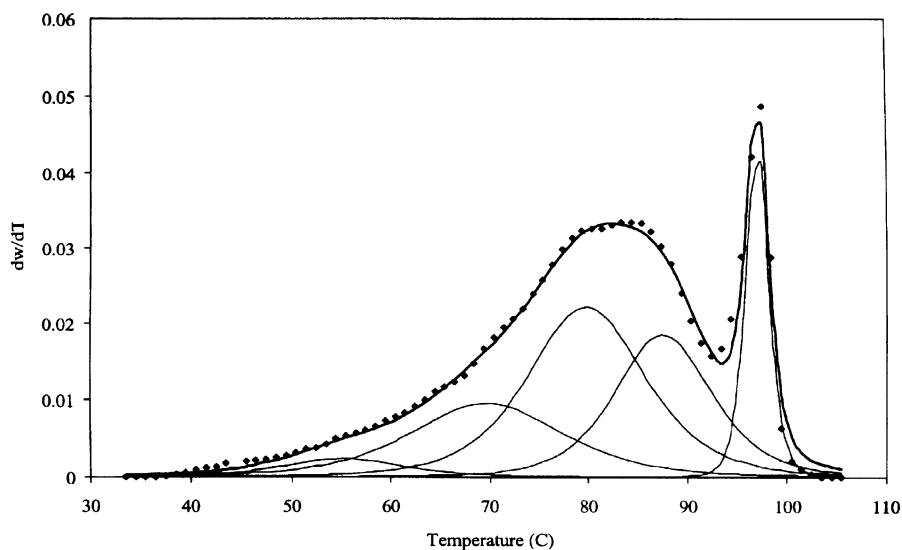
Fig. 24 Deconvolution of the CCD to determine the active-site types of a heterogeneous Ziegler–Natta catalyst [49]
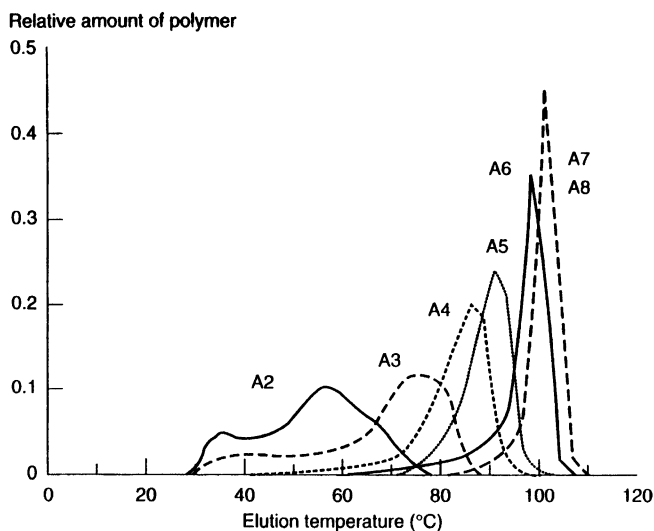
Fig. 25 A-Tref profiles of P-Tref fractions obtained at 3 °C intervals. Significant broadening can be observed [50]

Borrajo et al. [51] and Eliçabe et al. [52, 53] proposed a thermodynamic model for Tref based on the Flory–Huggins theory. They attempted to relate the distribution of crystallizable chain lengths with the elution temperature profile. Their model was validated only for the limiting case of low molecular weight high-density polyethylene (HDPE) with a narrow MWD. Since the model assumes extended-chain crystallization, it cannot adequately explain the results when long polymer chains are considered, as chain-folding effects during crystallization are found to play an important role in this case.

4
Crystallization Analysis Fractionation

4.1
Basic Experimental Apparatus and Procedures

Figure 26 shows a schematic diagram of one Crystaf crystallization vessel. The commercial version of Crystaf (Polymer Char, Spain) has five crystallization vessels that are placed inside a temperature-programmable oven. The vessels can be used in parallel to analyze up to five samples simultaneously (Fig. 27). The vessels are made of stainless steel and are provided with stirring units. The crystallization vessels are connected to a nitrogen line, a waste line, and a sampling line attached to an in-line filter. The sampling lines are connected
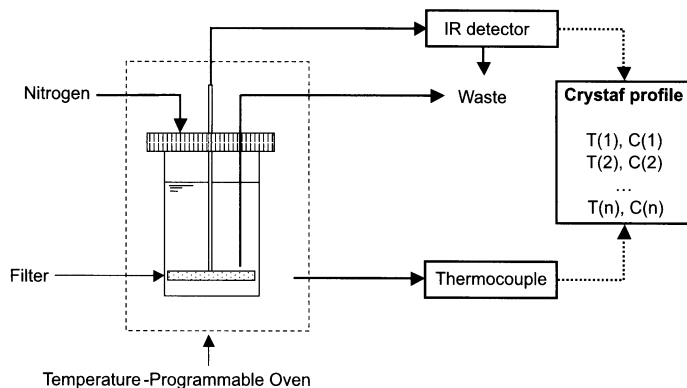
Fig. 26 Schematic diagram of a crystallization vessel in Crystaf
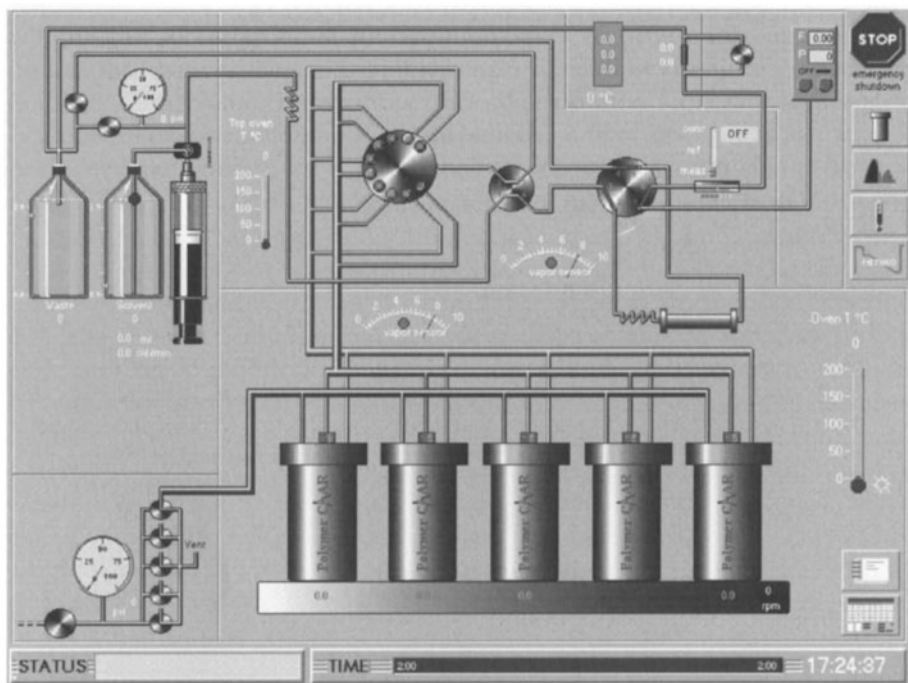
Fig. 27 Schematic diagram of a commercial Crystaf unit (Polymer Char, Spain)

to an on-line IR detector used to measure the polymer solution concentration as a function of crystallization temperature.

Prior to the fractionation or crystallization step, the polymer sample is dissolved at high temperature in a good solvent inside a crystallization vessel to ensure complete dissolution. For analyzing polyolefins, 1,2,4-tricholobenzene is generally the solvent of choice. Dilute solutions (0.1–0.5 mg/mL) are recommended to avoid effects from chain-to-chain interactions and cocrystal-

lization, but solutions with too low initial concentrations (below 0.1 mg/mL) might lead to poor resolution owing to low signal-to-noise ratios.

The dissolution step is followed by the stabilization period, when the temperature of the polymer solution is kept a few degrees above the initial crystallization temperature. The exact value of the stabilization temperature is, of course, determined by the polymer of interest. A stirring rate of approximately 200 rpm is commonly used during both dissolution and stabilization periods; however, the stirring rate is reduced to approximately 100 rpm for the subsequent crystallization steps to minimize shear-induced chain scission. Notice, however, that a small degree of chain scission is tolerable, since Crystaf is not significantly affected by molecular weight. Stirring during the crystallization step is necessary to ensure a uniform polymer concentration distribution and avoid filter plugging.

During the crystallization step, the temperature of the solution is decreased at a slow, constant CR, typically of 0.1–0.2 °C/min. This allows the polymer chains with the highest crystallizabilities to precipitate first at high temperatures, followed by the chains with lower crystallizabilities. A slow CR is essential to minimize undesirable crystallization kinetics and cocrystallization effects. At predetermined temperature intervals during the crystallization, a small aliquot of polymer solution is removed from the crystallization
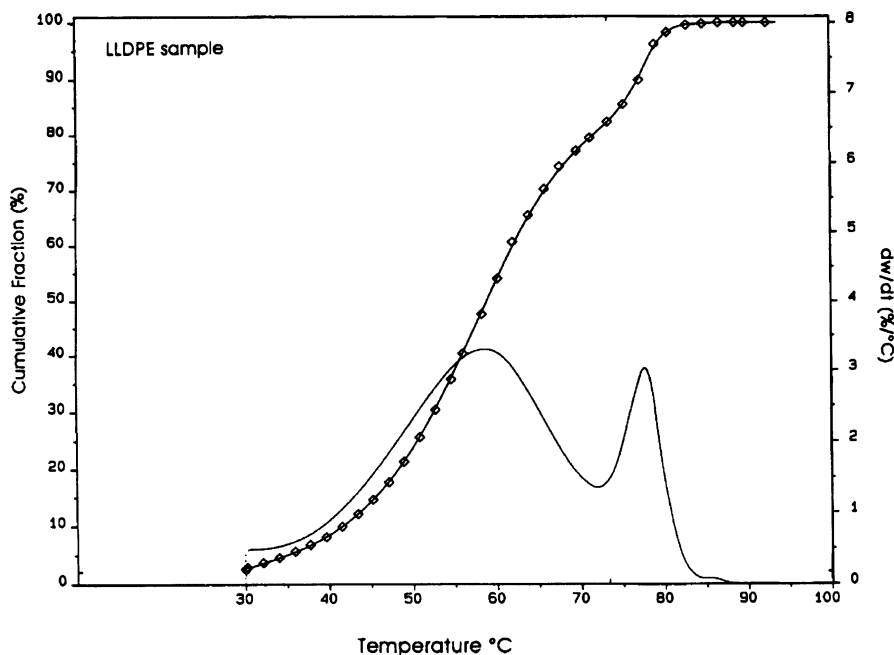
Fig. 28 Typical cumulative (or integral) and derivative Crystaf profiles of LLDPE synthesized with a Ziegler–Natta catalyst [1]

vessel by increasing the nitrogen pressure in the vessel and forcing the poly-
mer solution through the filter. (The in-line filter in the sampling line avoids
polymer crystallites from being sampled with the polymer solution.) The
concentration of polymer in solution as a function of crystallization tempera-
ture is then monitored through the on-line IR detector and recorded by the
data acquisition software.

The plot of solution concentration as a function of crystallization tem-
perature is called the cumulative or integral Crystaf profile (Fig. 28) [54]. The
amount of polymer crystallizing at each temperature can be determined by
differentiation of the integral Crystaf profile at that temperature. The plot of
the amount of polymer crystallized as a function of crystallization tempera-
ture (called the derivative Crystaf profile or simply the Crystaf profile, also
shown in Fig. 28) is the most commonly reported form of Crystaf results.

4.2
Comparison Between Crystaf and Other Characterization Techniques

Crystaf has often been compared to other techniques, specifically Tref and
DSC [1, 2, 54–56]. It is generally accepted that Crystaf and Tref profiles dif-
fer mainly by a temperature shift due to the supercooling effect in Crystaf,
similar to what is observed between the heating and cooling cycles in DSC.

Gabriel et al. [56] compared Crystaf, Tref, and DSC profiles for LLDPE syn-
thesized with a Ziegler–Natta catalyst (Fig. 29). Their results provide excellent
validation of Crystaf analysis. Special care should be taken, however, when
comparing results from different characterization techniques, because of dif-
ferences in the typical operation conditions from one technique to another.
The comparison with DSC is particularly difficult to make because DSC mea-
sures the heat of crystallization in the polymer melt where effects of chain
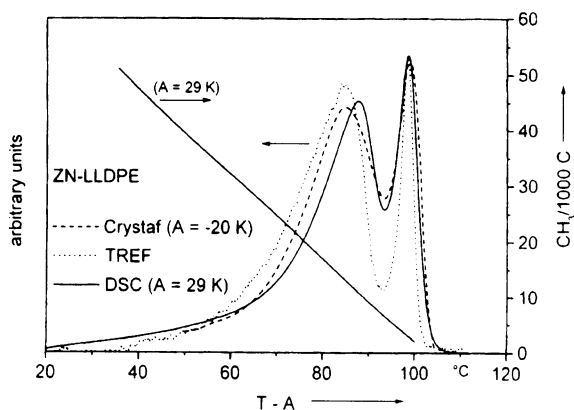
Fig. 29 Comparison of results obtained from Crystaf, Tref, and differential scanning
calorimetry (*DSC*) [56]. Peaks are shifted to allow superposition

entanglement, secondary crystallization, and cocrystallization play a more important role than in Crystaf or Tref.

For some samples, the comparison between Crystaf and Tref results is not so straightforward. Britto et al. [54] compared Crystaf and Tref results for various LLDPE and HDPE samples and found that although the two techniques agreed for most samples, they could also differ for some resins at the high-crystallinity region of the profiles. Although Tref could clearly detect a high-crystallinity double peak, this peak was absent from the Crystaf profiles (Fig. 30). The appearance of this double peak may be attributed to recrystallization and also appears during DSC analyses.

To provide an unbiased comparison between Crystaf and Tref, we used these two techniques at the same CR to analyze polyolefin blends with known
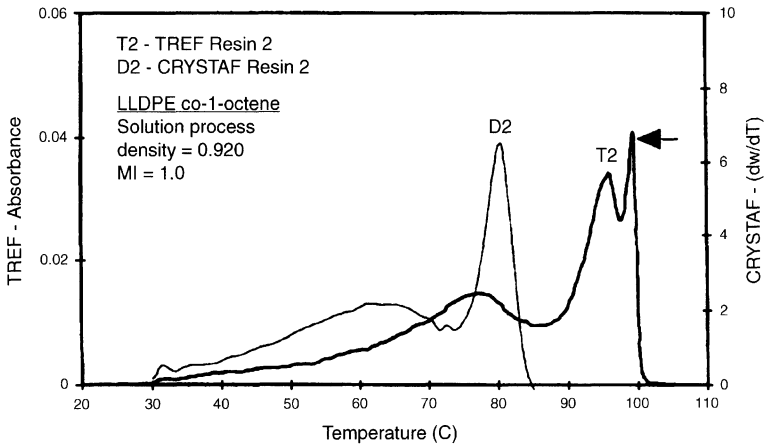
Fig. 30 Comparison between Crystaf and Tref profiles of LLDPE [54]
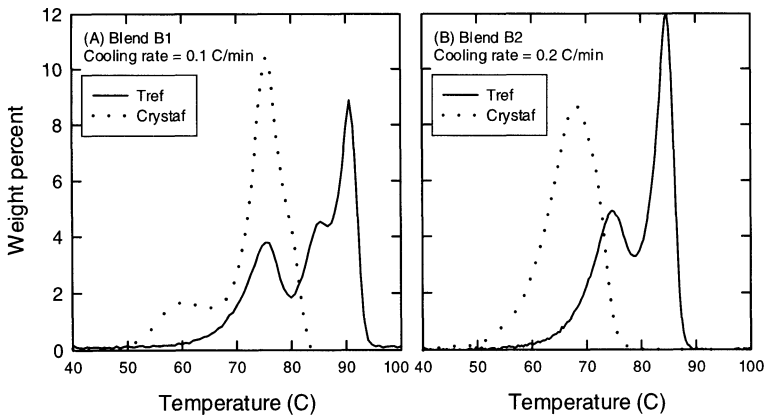
Fig. 31 Comparison between Crystaf and Tref profiles of blends of ethylene/1-hexene copolymers with known multimodal CCD measured at the same cooling rate [29]

multimodal CCDs in our recent study (Fig. 31) [29]. We found that, for the same CR, Tref can better resolve the peaks of multimodal polyolefin blends than Crystaf. It should be kept in mind, however, that the peak resolution of Crystaf can be significantly improved by using a slower CR, while still retaining the advantage of a shorter analysis time. This phenomenon will be discussed in more detail in Sect. 4.5.

Crystaf relies on the fitting (generally using splines) of 40–50 experimental points acquired for the cumulative curve. The fitted data are then used to calculate the differential Crystaf curve, as discussed before. To avoid the appearance of "false" peaks during the differentiation, curve-smoothing is sometimes required. Unfortunately, this procedure may also lead to some loss of resolution during Crystaf analysis, especially for samples containing sharp peaks. Tref is not subject to this limitation, since it directly measures the differential profile during the polymer elution step.

4.3
Effect of Chain Microstructure

All microstructural features impacting chain crystallizability can potentially influence the Crystaf fractionation process. The main microstructural properties of interest are: (1) number average molecular weight, (2) CC, and (3) comonomer type. Each of these factors will be discussed below.

4.3.1
Effect of Molecular Weight

Nieto et al. [14] investigated the effect of chain length on Crystaf profiles using a series of ethylene homopolymers with different molecular weights. A plot of Crystaf peak temperatures versus number-average molecular weights indicates that the crystallization temperature decreases with molecular weight below a certain chain length threshold (Fig. 32) [14]. However, at a reasonably high molecular weight, the crystallization temperature is independent of molecular weight. These findings are supported by the theoretical model discussed earlier for polymer solutions, as described by Eq. 2.

In addition, Crystaf profiles of polyethylene resins were reported to broaden with decreasing molecular weight averages (Fig. 33) [57], which is also in agreement with Eq. 2. As the crystallization temperature becomes independent of chain length for the samples with higher molecular weight averages, the Crystaf profiles become narrower as all chains crystallize at approximately the same temperature. On the other hand, for the samples with lower molecular weight averages, the Crystaf profiles broaden because the crystallization temperatures of the shorter chains in the sample are affected by their length.
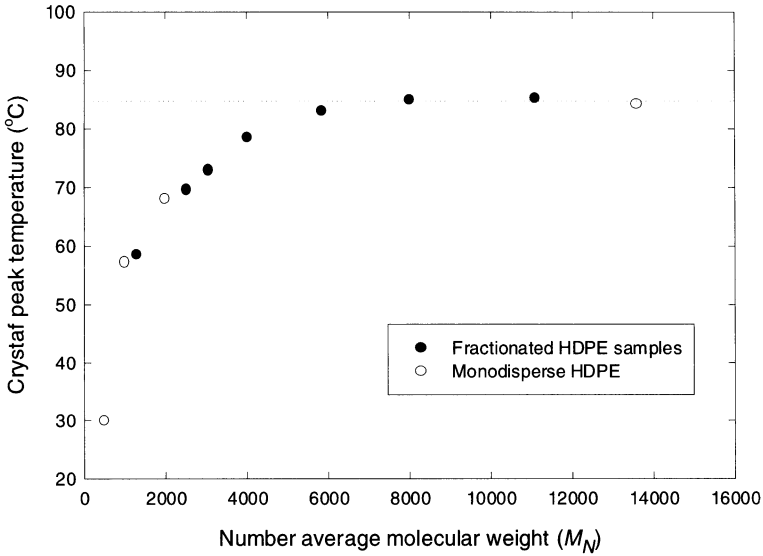
Fig. 32 Effect of chain length on the crystallization temperature of high-density polyethylene (*HDPE*) [14]
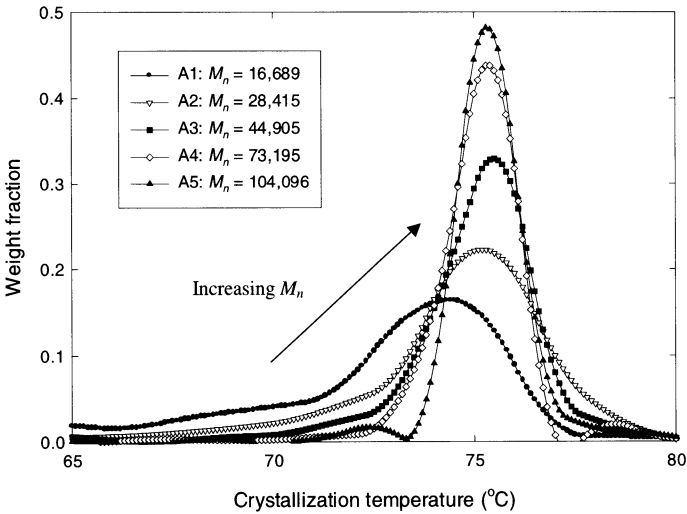
Fig. 33 Effect of number-average molecular weight on Crystaf profiles. Each sample is a fraction of ethylene/1-hexene copolymers. Fractionation was carried out using solvent/nonsolvent extraction; therefore, these samples have distinct molecular weights and contain similar amounts of 1-hexene [57]

These results have two important implications. First, Crystaf profiles will be influenced by the MWD when samples with low molecular weight averages are considered. Luckily, as shown in Fig. 33, the Crystaf peak temperature is not significantly affected unless samples with very low molecular weight aver-

ages are analyzed. This is a reassuring result, since Crystaf peak temperatures are used to create calibration curves. Second, if the sample contains chains with very low molecular weights its Crystaf profile can be significantly broadened towards the low crystallinity end of the distribution. If this factor is neglected during data interpretation and attributed to a higher fraction of comonomer, the estimated CCD will be much broader than the actual CCD.

4.3.2
Effect of Comonomer Content

The fraction of comonomer units in the copolymer chains is the most important factor affecting chain crystallizability and, therefore, crystallization temperature. This is due to the fact that comonomers act as chain defects, interrupting chain regularity and greatly lowering chain crystallizability.

Sarzotti et al. [58] investigated the effect of comonomer content on Crystaf profiles using a series of ethylene/1-hexene copolymers with different comonomer contents but approximately the same molecular weight, effectively eliminating any possible misinterpretations that might arise because of molecular weight effects (Fig. 34) [58]. As expected, Crystaf peak temperatures are dramatically influenced by the CC of the copolymer chains. Moreover, the Crystaf profiles become broader with an increase in comonomer content.

The decrease in Crystaf peak temperature can be simply explained with Eq. 4, as the chain composition alters the thermodynamic interaction parameter for the copolymer, χ_1. To understand the broadening of the distribution,
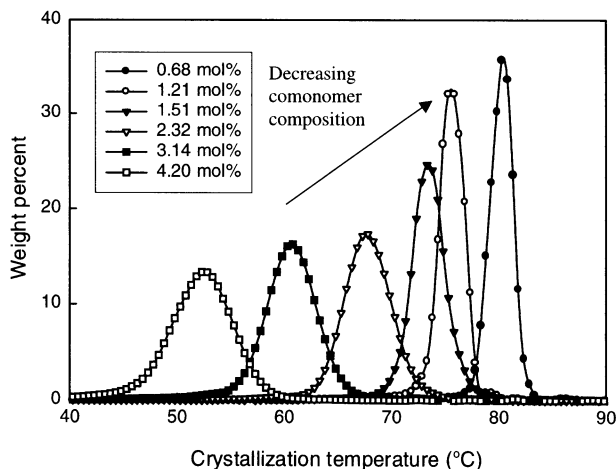
Fig. 34 Effect of comonomer content on Crystaf profiles. These samples are ethylene/1-hexene copolymers synthesized using a single-site-type catalyst. All samples have similar molecular weights [58]

however, it is more appropriate to consider Stockmayer's bivariate distribution. As previously discussed in this review, high comonomer contents will broaden the CCD of copolymers, following Stockmayer's bivariate distribution, Eq. 7. This phenomenon is elegantly illustrated in Fig. 8 from a theoretical point of view.

4.3.3
Effect of Comonomer Type

The effect of comonomer type was studied by Brull et al. [59] using propylene/1-olefin copolymers with several comonomer types (1-octene, 1-decene, 1-tetradecene, and 1-octadecene). They reported that, for their set of samples, not only Crystaf peak temperatures but also melting and crystallization temperatures measured by DSC were independent of comonomer type but depended strongly on comonomer content.

More recent work by the same research group [60] has investigated the effect of comonomer type using a series of ethylene/1-olefin copolymers (1-decene, 1-tetradecene, and 1-octadecene). Notice that ethylene instead of propylene was used in this particular study. Once more, they reported that Crystaf peak temperatures were practically independent of comonomer type (Fig. 35).

These two results are interesting because earlier work by da Silva Filho et al. [49] showed that ethylene/1-butene and ethylene/1-octene copolymers had significantly different crystallization temperatures for the same
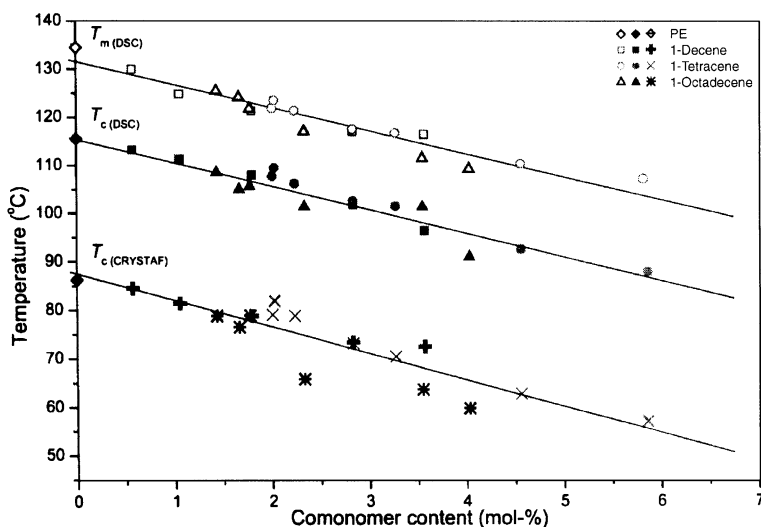
Fig. 35 Effect of comonomer type on Crystaf peak temperature and cooling and melting DSC peak temperatures [60]

comonomer content. The trend observed in their work is also in good agreement with previous investigations examining the effect of comonomer type on Tref calibration curves for ethylene/1-hexene and ethylene/1-octene copolymers (Fig. 12) [28].

Therefore, it seems that Crystaf peak temperatures are independent of comonomer type when comonomers are longer than 1-octene (1-decene, 1-tetradecene, and 1-octadecene), but depend on comonomer type for shorter comonomers (1-butene, 1-hexene, and 1-octene). We can rationalize this observation by assuming that 1-olefin comonomers longer than 1-octene are always excluded from the crystallites and therefore have the same effect on chain crystallizability. Contrarily, 1-olefin comonomers that are shorter than 1-octene can be partially incorporated into the crystallites (the shorter the comonomer, the higher the degree of crystal inclusion) and will depress the crystallization temperature to a lesser extent. This is in contrast to several experimental observations indicating that side groups larger than methyl are not significantly incorporated into the crystal structure [61–64]. It may be speculated that the comonomer effect seen in Crystaf is, therefore, related to the nonequilibrium crystallization nature of this fractionation technique.

4.4
Effect of Cooling Rate

Ideally, it would be preferable to operate Crystaf in conditions that fractionate the polymer chains according to their crystallizabilities at thermodynamic equilibrium in order to eliminate any crystallization kinetics effects. Practically, this idealized condition is untenable because very long analysis times would be required. Recent investigations [29] have shown that the fractionation process in Crystaf is, in fact, very far from thermodynamic equilibrium.

As the effect of crystallization kinetics becomes unavoidable, it is important to understand its impact on Crystaf profiles. Figure 36 shows how the Crystaf peak temperatures vary as a function of CR for three ethylene/1-hexene copolymers [29]. It is clear that the CR can have a dramatic effect on Crystaf peak temperatures even at very low CRs. The Crystaf profiles are significantly shifted to higher temperatures when slower CRs are used. Empirical linear relationships can be established between the Crystaf peak temperature of each polymer sample (T_P) and the natural logarithmic of the CR, as shown in Fig. 36.

It is important to keep in mind that the typical CR used in Crystaf analysis, 0.1 °C/min, is in fact far from thermodynamic equilibrium. This can be easily noticed as further lowering of the CR can still significantly shift the Crystaf profiles. Notice that for sample B in Fig. 36, the peak temperature is still increasing even at the prohibitively slow CR of 0.001 °C/min. Even though this should by no means be considered a limitation when comparing resins with different CCDs or measuring CCs in copolymers, it makes the development
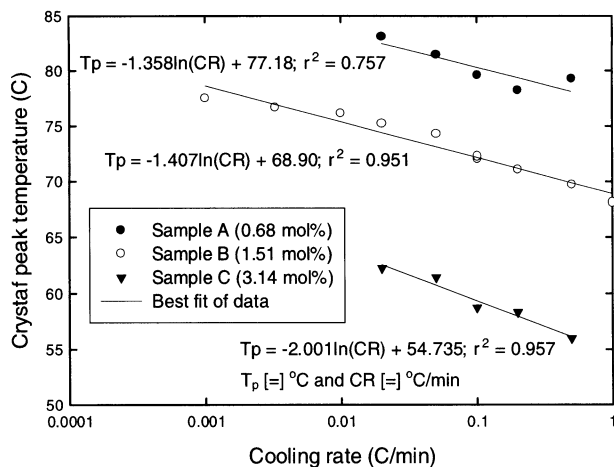
Fig. 36 Relationship between Crystaf peak temperature and cooling rate for various ethylene/1-hexene copolymers [29]

of mathematical models for Crystaf a much more challenging task since it requires that crystallization kinetics effects be taken into consideration.

4.5
Effect of Cocrystallization

Cocrystallization during Crystaf analysis can be investigated by comparing experimental Crystaf profiles of blends with their predicted Crystaf profiles, assuming the absence of cocrystallization. The Crystaf profiles of the blends in the absence of cocrystallization can be estimated as the summation of the Crystaf profiles of each parent sample, measured alone, multiplied by its weight fraction in the blend. Deviations from the predicted profile are a measure of the extent of cocrystallization taking place during the analysis.

When a blend is made of polymers with very different crystallizabilities, cocrystallization is minimal and does not have a significant effect on Crystaf profiles [1, 65, 66]. However, cocrystallization can be significant when the components of the blend have similar crystallizabilities [67]. In this case, cocrystallization can be so dramatic as to distort the shape of the measured Crystaf profile for the blend and completely mislead its interpretation.

Two factors were found to regulate cocrystallization in Crystaf: (1) CR [29] and (2) the similarity of chain crystallizabilities [67]. Figure 37 shows the effect of CR on cocrystallization of a trimodal blend of ethylene/1-hexene copolymers. Fast CRs can induce cocrystallization and distort the experimental Crystaf profile. It is important to note that this phenomenon exists even at the typically used CR of 0.1 °C.
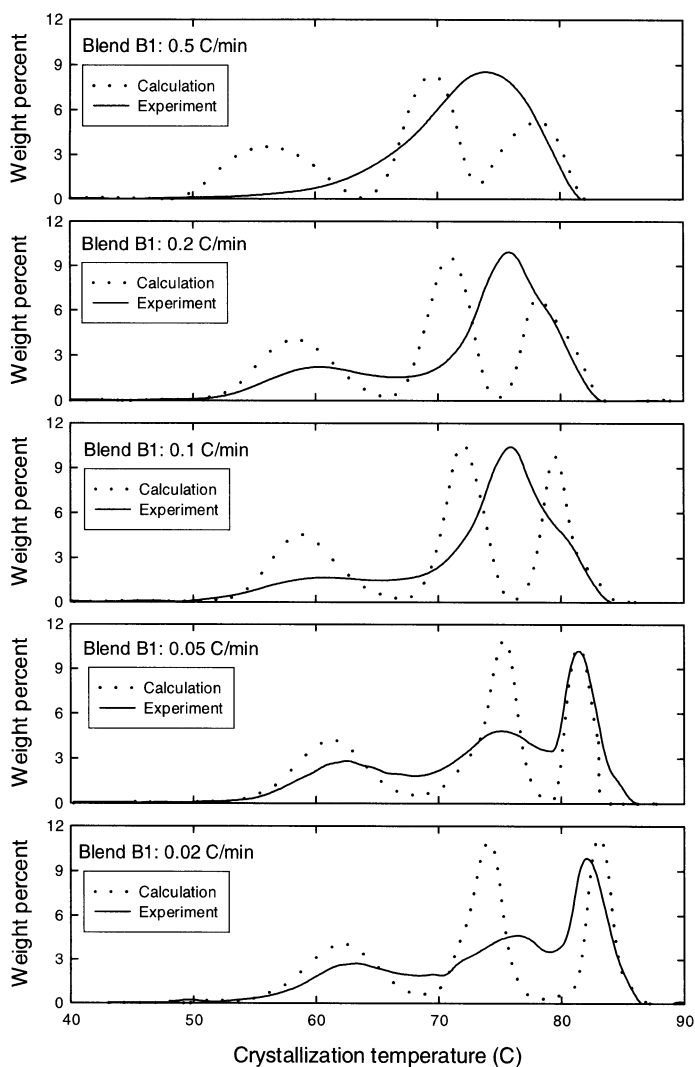
Fig. 37 Effect of cooling rate on cocrystallization during Crystaf analysis [29]

Another important factor affecting cocrystallization is the similarity of chain crystallizabilities, which can be quantified by the difference between the Crystaf peak temperatures of the parent samples, ΔT_C. By varying ΔT_C, changes in cocrystallization behavior can be easily observed (Fig. 38). Similarity of chain crystallizabilities, as indicated by a small ΔT_C, strongly induces cocrystallization during the analysis; a similar criterion could have been defined using density or crystallinity differences to access the importance of cocrystallization for these polymers.
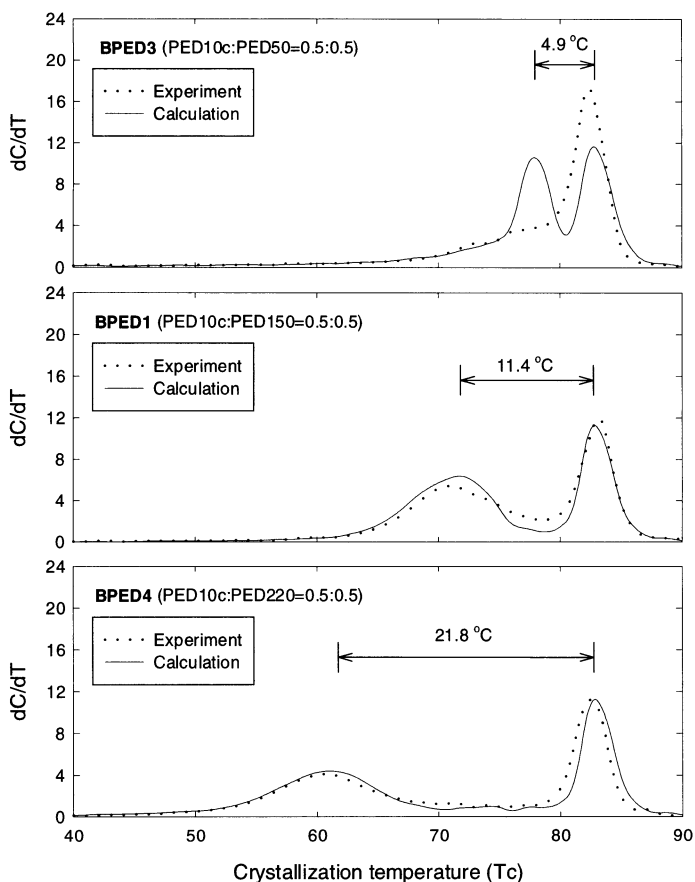
Fig. 38 Similarity of chain crystallizabilities (measured as Crystaf peak separation) induces cocrystallization in Crystaf analysis [67]

In our recent work [67], we investigated the effect of comonomer type on cocrystallization using a series of ethylene/1-olefin copolymers with four comonomer types: propylene, 1-hexene, 1-octene, and 1-dodecene. Four blends, one for each copolymer type, were prepared such that they crystallized at the same temperature range and had similar ΔT_C to eliminate the effect of similarity of chain crystallizabilities. The Crystaf results of these blends indicated that the comonomer type of the parent samples did not appreciably influence their cocrystallization behavior, as illustrated in Fig. 39.
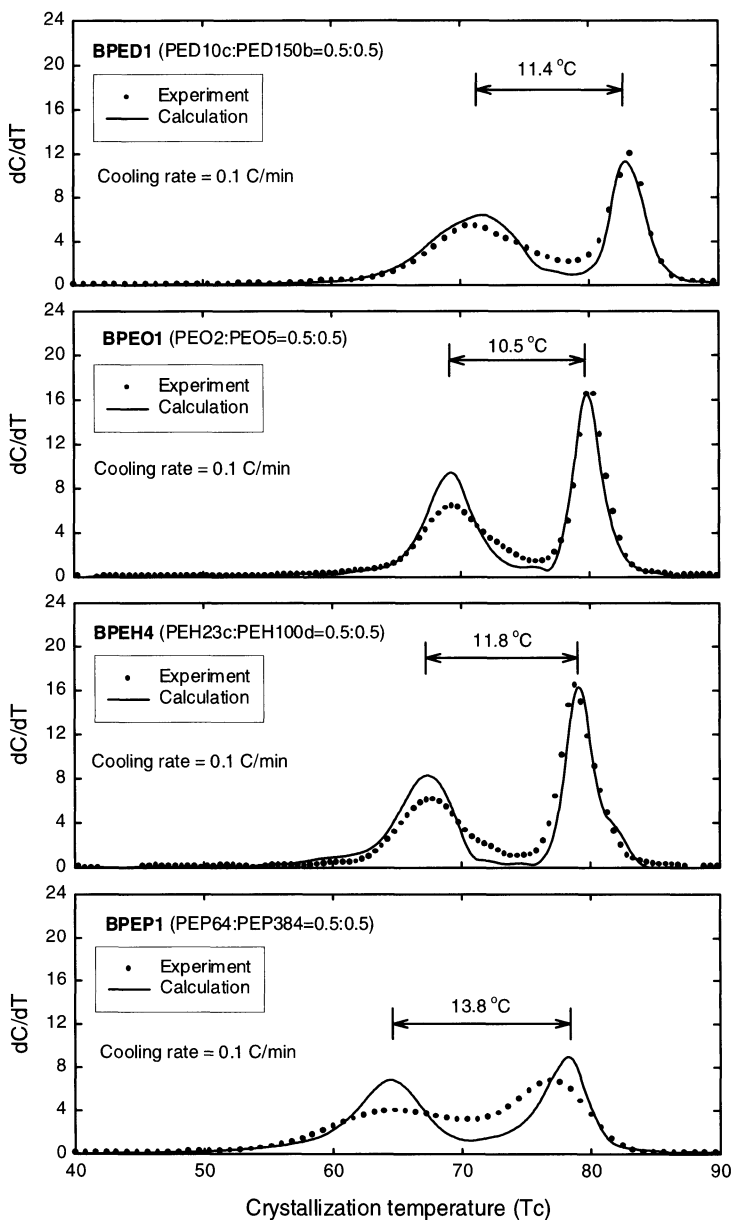
Fig. 39 Effect of comonomer type on cocrystallization at a cooling rate of 0.1 °C/min for blends with the same comonomer type. *BPED* blend of ethylene/1-dodecene copolymers, *BPEO* blend of ethylene/1-octene copolymers; *BPEH* blend of ethylene/1-hexene copolymers, *BPEP* blend of ethylene/propylene copolymers [67]

5
Crystaf Applications

5.1
Estimation of CC and CCD of Copolymers

One of the main applications of Crystaf analysis is the estimation of the CCD of semicrystalline copolymers, specifically LLDPE. The CCD of copolymers can be obtained from the Crystaf profile with the help of a calibration curve relating the CC and the crystallization temperature. For routine analysis, a calibration curve can also give a quick estimation of the CC from the Crystaf peak temperature. Evidently, because of the crystallization kinetics and cocrystallization effects described before, in general only an approximation of the actual CCD is possible with Crystaf and Tref.

Two methods for preparing the calibration curve have been reported. Both methods were done by performing Crystaf analysis in a series of narrow-CCD copolymer samples with known comonomer contents with crystallizabilities covering a broad range of crystallization temperatures. The only difference between these two methods is the type of samples used in the calibration. The first method uses a series of polymer samples synthesized with single-site-type catalysts [58, 68], while the second method uses a series of fractions from broad-CCD Ziegler–Natta copolymers obtained with P-Tref [1, 49]. After the whole series of samples has been analyzed, the relationship between Crystaf peak temperature and CC is used as the calibration curve.

A number of calibration curves have been reported for Crystaf (Table 2, Fig. 40). Unfortunately, similar to calibration curves for Tref, calibration curves for Crystaf depend on polymer type, solvent type, CR, and method of sample preparation. Published calibration curves should only be used if care is taken in trying to replicate as closely as possible the conditions under which they were obtained.

The calibration curve is significantly influenced by the CR, as should be expected from our previous discussion. We have recently proposed the following generalized calibration curve for random ethylene/1-hexene copolymers taking into account the effect of the CR [29],

$$CC = 10.0 - 0.1216 \times T_P - 0.1653 \times \ln(CR), \tag{9}$$

where CC is in mole percent, T_P is the Crystaf peak temperature in degrees Celsius, and the CR is in degrees Celsius per minute. This empirical equation was fitted using the data from Sarzotti et al. [58] and Anantawaraskul et al. [29] and it is applicable for CR = 0.003–2 °C/min and CC = 0.68 – 4.2 mol %. The equation fits well all the experimental data with a coefficient of determination (r^2) of 0.993.

With the help of a calibration curve, Crystaf profiles can be converted to the CCD. This quantitative CCD is useful for establishing structure–property

Table 2 Summary of reported calibration equations with their applicable ranges and experimental conditions

Copolymer	Method of preparing calibration samples	Range of applicable comonomer content (mol %)	Cooling rate (°C/min)	Calibration equation	Reference (best linear fit)
PE/1-octene	Fractionation using P-Tref	0.86–4.66	0.2	CC = −0.0968 T_C + 8.6321	Monrabal [1]
PE/1-octene	Synthesis using single-site-type catalysts	0.637–6.985	0.2	CC = −0.1651 T_C + 13.684	Monrabal et al. [64]
PE/1-octene	Fractionation using P-Tref	0.3–6.4	0.2	CC = −0.1248 T_C + 10.633	da Silva Filho et al. [48]
PE/1-hexene	Synthesis using single-site catalysts	0–4.234	0.1	CC = −0.1270 T_C + 10.86	Sarzotti [57]
PE/1-butene	Fractionation using P-Tref	1.2–8.9	0.2	CC = −0.1690 T_C + 14.36	da Silva Filho et al. [48]
PP/1-olefin	Synthesis using single-site catalysts	0–3.43	0.1	CC = −0.0670 T_C + 4.7074	Brull et al. [58]

PE polyethylene, *PP* polypropylene
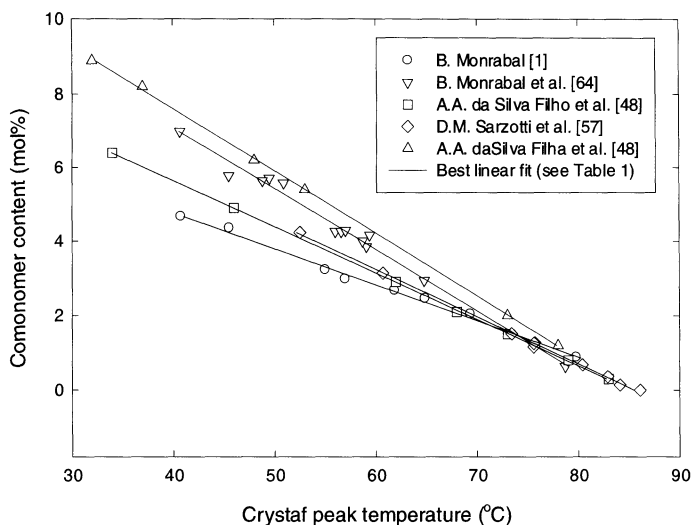
Fig. 40 Calibration curves reported for ethylene/1-olefin copolymers (see Table 2 for details of applicable range and conditions)

relationships [69, 70] and elucidating several issues in polymer reaction engineering.

5.2
Polymer Reaction Engineering

Tref has been used for many years in polymer reaction engineering investigations. For instance, Tref was one of the most important analytical techniques to determine the presence of multiple-site catalysts on heterogeneous Ziegler–Natta catalysts used for olefin polymerization, as previously illustrated in Fig. 18. Crystaf, with a much shorter analysis time than Tref, permits the routine determination of the CCD in polymer reaction engineering projects.

CCDs obtained with Crystaf have shed light on various topics in the area of polymerization and polymer degradation mechanisms. Similarly to Tref, Crystaf can be used to identify the nature of active site types in Ziegler–Natta catalysts, as proposed by da Silva Filho et al. [49].

Crystaf has been used to provide important insights on polymerization conditions affecting CCD [71–78]. For example, Fig. 41 shows how the CCD of ethylene/1-hexene copolymers made with a silica-supported binary metallocene catalyst is influenced by the relative amounts of each metallocene in the mixture [74]. This understanding leads to the ability to manipulate the CCD and allows us to tailor-make copolymers with predetermined microstructures through the combination of catalysts, cocatalysts, and/or support treatments.
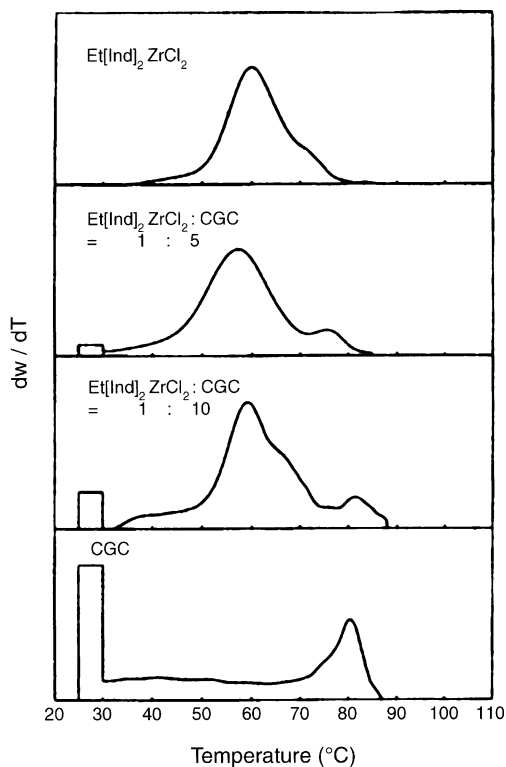
Fig. 41 Effect of catalyst type and catalyst combinations on the CCDs of ethylene/1-hexene copolymers measured by Crystaf [74]
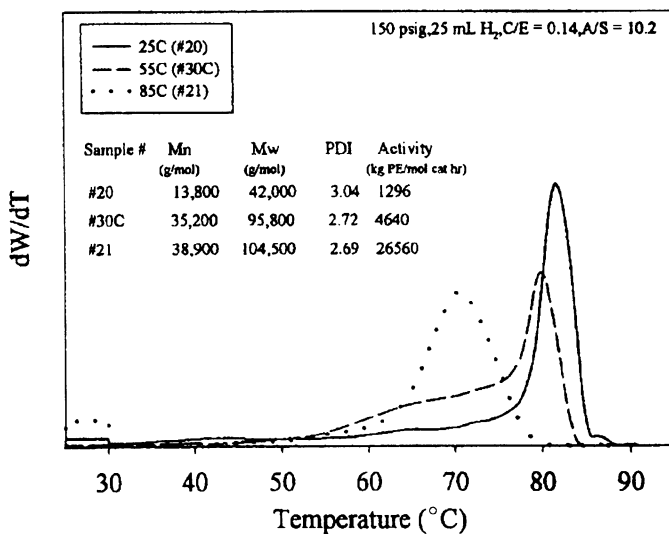
Fig. 42 Effect of polymerization temperature on the CCD of ethylene/1-hexene copolymers as measured by Crystaf [78]
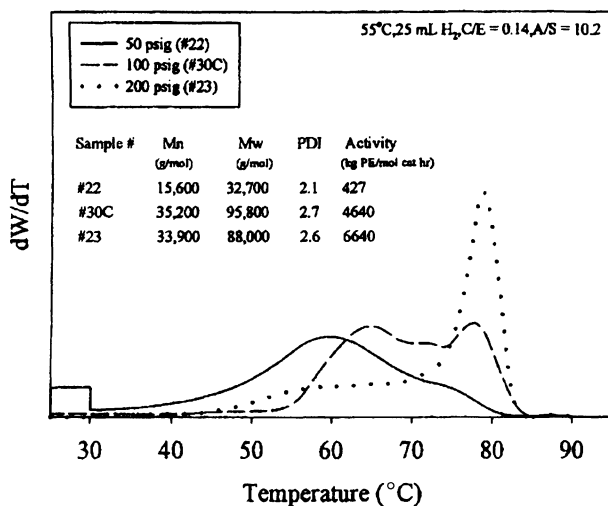
Fig. 43 Effect of polymerization pressure on the CCD of ethylene/1-hexene copolymers measured by Crystaf [78]
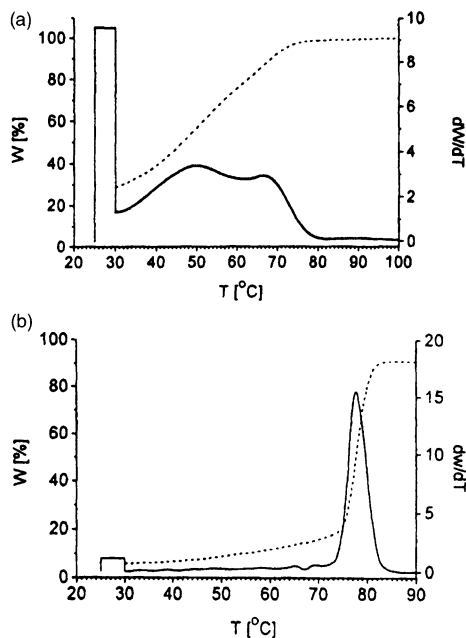
Fig. 44 Broadening of chemical heterogeneity due to thermo-oxidative degradation as revealed by Crystaf: (**a**) PP held at 110 °C for 4 days; (**b**) PP held at 130 °C for 1 day [79]

Using a careful factorial experimental design, the effect of polymerization temperature, polymerization pressure, amount of hydrogen, and the comonomer-to-monomer feed ratio on Crystaf profiles can be identified [78].

Figures 42 and 43 show the effect of polymerization temperature and pressure on the Crystaf profiles of ethylene/1-hexene copolymers produced with an in situ supported Ni diimine catalyst in the presence of chain-walking.

Recently, Crystaf has also found applications in the area of polymer degradation. de Goede et al. [79] used Crystaf to monitor the change in chemical heterogeneity during the thermo-oxidative degradation of polypropylene. Crystaf clearly reveals the broadening of chemical heterogeneity, decreasing of peak crystallization temperature, and increasing of the amount of the soluble fraction, as the degradation proceeds (Fig. 44). Crystaf analysis of the polymer taken at different distances from surface of the sample can additionally provide information about the gradient of degradation from the surface to the core of the sample, thus quantifying the spatial heterogeneity of the degradation process.

5.3
Analysis of Blend Compositions

Although several previous investigations considered the Crystaf analysis of blends, they merely intended to quantify the limitations of Crystaf due to cocrystallization [1, 2]. Only more recently has Crystaf been used to provide quantitative information on blend compositions [55, 65, 66].
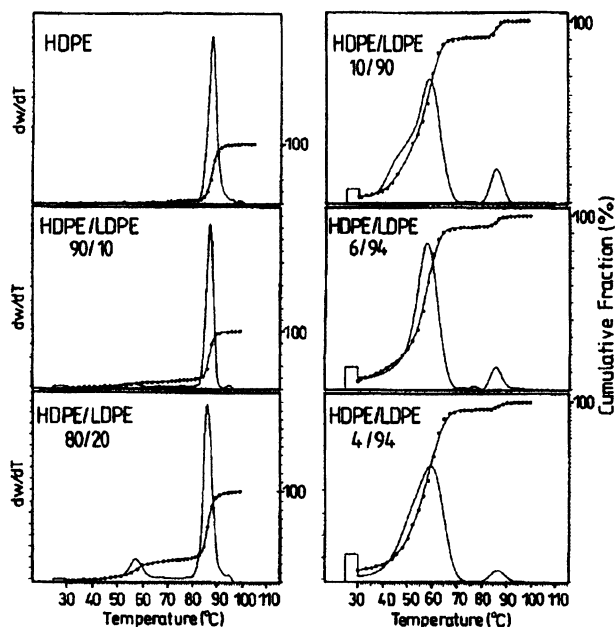
Fig. 45 Crystaf analyses of blends of commercial HDPE and LDPE [55]
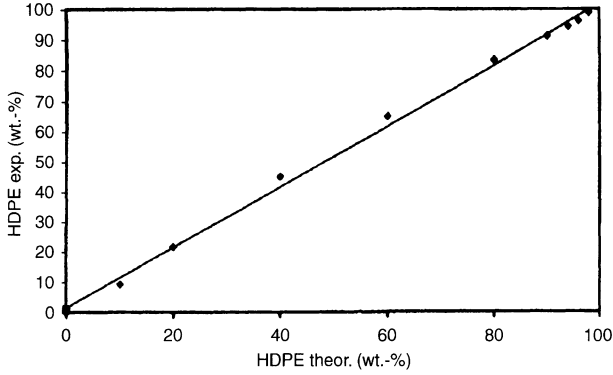
Fig. 46 Comparison between known HDPE composition in HDPE/LDPE blends and the ones measured by Crystaf [55]
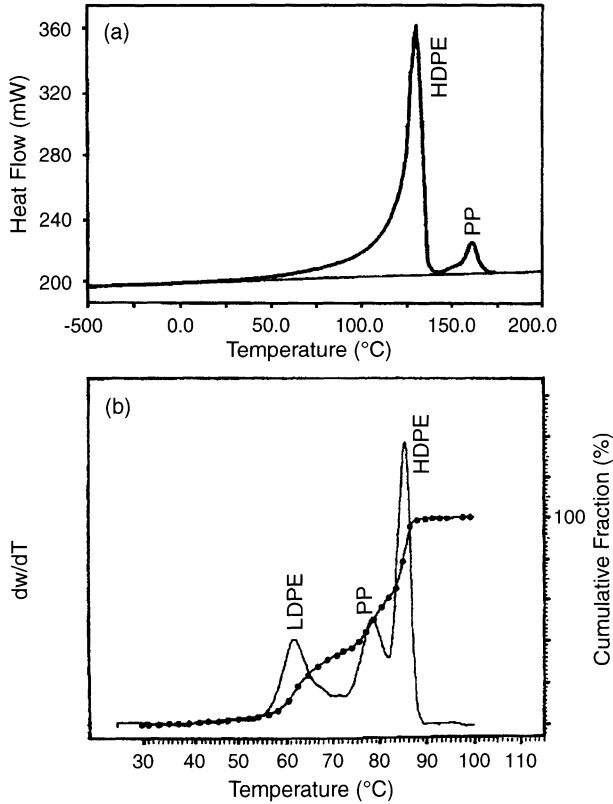
Fig. 47 DSC and Crystaf analysis of waste plastics [55]

Figure 45 shows Crystaf analyses of blends of commercial HDPE and LDPE reported by Pasch et al. [55]. By comparing the known composition of the blends with the composition measured by Crystaf (Figs. 45, 46), they

found that Crystaf was quantitatively accurate over a very wide range of compositions. For instance, Crystaf could detect blend components present in amounts as small as 5 wt %. In the analysis of waste plastic samples, Crystaf was found to be better than the conventional DSC method for providing information on blend compositions (Fig. 47).

The application of Crystaf analysis for detecting blend composition is, of course, limited by cocrystallization, particularly if accurate quantitative information is required. As previously discussed, cocrystallization is found to be significant when two chain populations crystallize at relatively close temperature ranges (small ΔT_C), even for very slow CRs. Therefore, the use of Crystaf for determining blend compositions will be more adequate when the blend components have distinctly separated Crystaf peak temperatures (large ΔT_C). Preferably, the difference between Crystaf peak temperatures should be more than 10 °C, particularly in the case where the blend components have similar molecular structures.

6
Mathematical Modeling of Crystaf

Although Crystaf has been established as a good alternative to Tref during the last decade, accurate quantitative models for describing the Crystaf fractionation process are still unavailable. Incidentally, they are equally unavailable for Tref. The main difficulty in achieving a generalized mathematical model is the complexity of the crystallization mechanism and fractionation process taking place in these two techniques, as discussed at length in this review.

Two main approaches have been proposed to model Crystaf fractionation: (1) models based on Stockmayer's bivariate distribution [58, 80], and (2) models based on the distribution of chain crystallizabilities using Monte Carlo simulation [57, 81].

6.1
Stockmayer's Bivariate Distribution Models

Sarzotti et al. [58] used Stockmayer's distribution, Eq. 7, and a calibration curve to model Crystaf profiles (Fig. 48). The two variables in Eq. 7, $\overline{F}_1$ and τ, were used as adjustable parameters to minimize the sum of the squares of the residuals between model and experimental profiles. Even though the model fitted the experimental profiles adequately, the molecular weights calculated from the model (easily obtained as $1/\tau$) were significantly lower than the ones measured by SEC, indicating that the model was not theoretically sound and only worked as a convenient empirical fit of the experimental data.
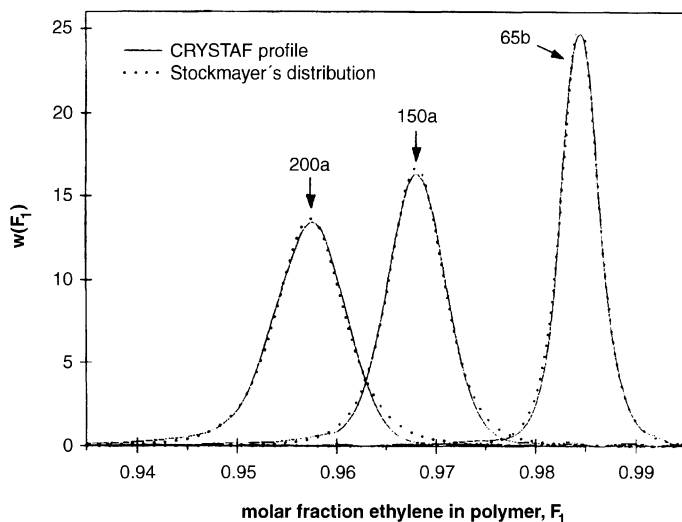
Fig. 48 Comparison between experimental Crystaf profiles and Stockmayer's bivariate distribution [58]

Soares et al. [80] proposed a model using Stockmayer's distribution with additional help from a generic instrumental spreading function to account for the instrumental peak broadening in Crystaf. Again, although the model could fit the experimental profiles well, the parameters used in the spreading function were considered purely empirical.

Although these models are not rigorously correct, the fact that they can fit well the experimental profiles is surprising, considering that using Stockmayer's distribution to model the CCD obtained from Crystaf is based on a number of rather severe simplifying assumptions. These models assume that (1) the polymer is prepared under uniform polymerization conditions (i.e., in the absence of compositional drift and other reactor nonuniformities), (2) the fractionation process in Crystaf is controlled only by the average copolymer composition per chain, (3) cocrystallization is absent during the analysis, (4) the fractionation process is independent of molecular weight even for the short chains, and (5) crystallization kinetics does not influence Crystaf profiles or, in other words, the fractionation takes place at thermodynamic equilibrium.

Unfortunately, most of these assumptions have recently been proved to be inaccurate [14, 29]. Even though modeling Crystaf profiles with Stockmayer's distribution can provide an adequate fit of the data, these models are, at best, only semiempirical. It is clear that a truly phenomenological model of the Crystaf fractionation process is essential to obtain the details of the correct distribution.

6.2
Monte Carlo Models

Monte Carlo simulation is a technique for solving stochastic problems that is widely used in the area of polymer science and engineering. Specifically for studies of polymer microstructures, it has been used to predict the CCD of copolymers and the distribution of stereoregularity [82, 83]. One of the advantages of this technique is that one can obtain detailed statistical information of chain structures simply from relatively easy to measure polymer properties such as the CC and the molecular weight.

Beigzadeh et al. [81] proposed the first Monte Carlo model for simulating Crystaf profiles. They assumed that the crystallization of a copolymer chain during Crystaf was solely governed by the length of its longest crystallizable monomer sequence. For the particular case of ethylene/1-olefin copolymers, the longest ethylene sequence per chain was assumed to govern the crystallization process in Crystaf. They proposed that Crystaf profiles could be calculated from the distribution of the longest ethylene sequence, instead of the CCD, and used Monte Carlo simulation to obtain this distribution. A modified Gibbs–Thompson equation [81] was used as the thermodynamic equilibrium relationship between the crystallization temperature and the length of the longest ethylene sequence, which was assumed to be proportional to the lamella thickness

$$T_C = \frac{T_S^\circ(\mathrm{LS} - \alpha)}{\mathrm{LS}} - \beta, \qquad (10)$$

where T_C is the crystallization temperature measured by Crystaf, T_S° is the equilibrium melting temperature of a chain with infinite chain length, α is a constant proportional to $1/\Delta H_u$, LS is the longest ethylene sequence, and β is the supercooling temperature in Crystaf.

They obtained good agreement with the experimental Crystaf profiles for their limited sample set of ethylene/1-octene copolymers. Later, Costeux et al. [23] derived an analytical expression for this distribution of the longest monomer sequences. This analytical solution can be used to dramatically shorten the computational time required for Crystaf modeling using the method of Beigzadeh et al. [81].

The model of Beigzadeh et al. was later applied to a series of ethylene/1-hexene copolymers covering a wider range of molecular weights and comonomer contents [57]. Unfortunately, it was found that the model based on the distribution of the longest monomer sequences could not accurately describe all the resins investigated.

We proposed a modified Monte Carlo model [57] based on the distribution of average ethylene sequence lengths, which was found to better represent the Crystaf profiles for a wider range of ethylene/1-olefin copolymers. Figure 49 compares the experimental Crystaf profiles with results from the proposed
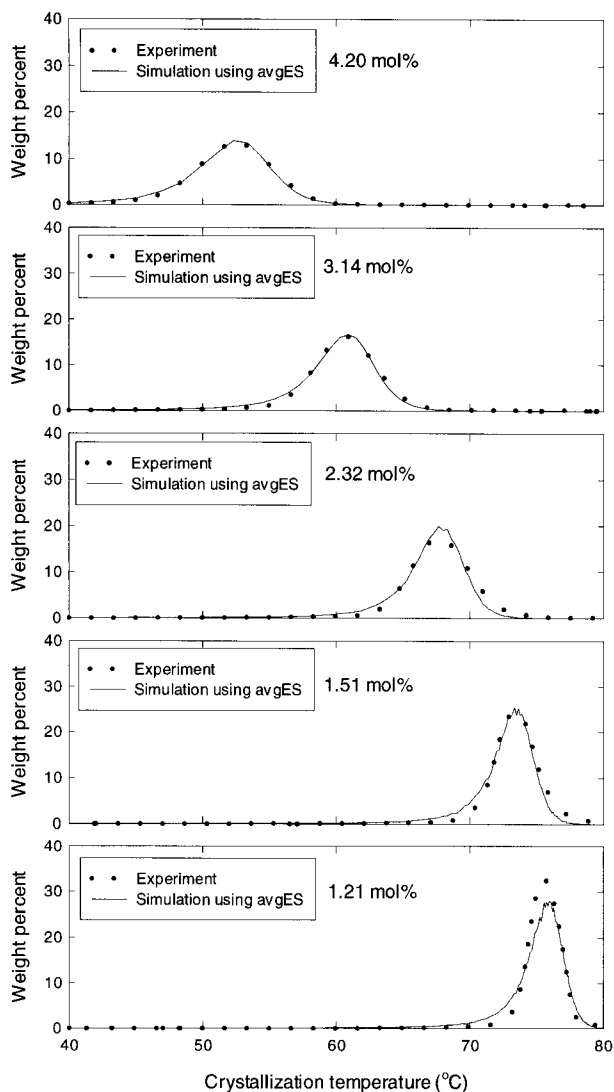
Fig. 49 Comparison between experimental and simulated Crystaf profiles of ethylene/
1-hexene copolymers with different comonomer contents [57]

model. It was speculated that the distribution of average ethylene sequence
lengths might provide a better representation of Crystaf profiles owing to
the fact that Crystaf fractionation takes place far from thermodynamic equi-
librium. In this way, using the average ethylene sequence lengths instead of
the longest ethylene sequence lengths would be an indirect (and clearly em-
pirical) way of accounting for the complex phenomena taking place during
crystallization in Crystaf.

Although these Monte Carlo models can explain qualitatively the effects of molecular weight and comonomer content on Crystaf profiles, they are unable to take into account crystallization kinetics and cocrystallization effects that have recently been reported as significant factors affecting Crystaf profiles [29, 67]. More work is required to quantify these important effects. Such a model, if developed, would be invaluable to obtain a universal calibration curve for Crystaf and Tref.

7
Conclusion and Future Trends

After only approximately a decade since it was developed, Crystaf has become one of the most important analytical techniques in polyolefin characterization laboratories. It can provide fast and crucial information required for the proper understanding of polymerization mechanisms and structure–property relationships. In industry, it has been established as an indispensable tool, together with Tref, for product development and product quality monitoring.

Nonetheless, compared with its older cousin Tref, Crystaf is still in its early stage of development. Improvements not only in terms of a better theoretical understanding, but also from the viewpoint of instrumentation, might lead to a more efficient fractionation process. For example, the recent development of a triple detector (IR/light scattering/viscometer) for Crystaf, the so-called Crystaf 3D, can provide a wealth of information on polymer microstructure at each crystallization temperature.

So far, Crystaf has been mostly limited to the analysis of LLDPE and some polypropylene resins. Certainly, there are many other semicrystalline copolymers that could greatly benefit from the information on CCD provided by Crystaf. In fact, the direct extension of Crystaf analysis for these polymers might be expected in a short time, considering the easy and fully automated use of Crystaf.

Crystaf has also started to gain recognition as an efficient technique to analyze polyolefin blends quantitatively, as it is considered to be superior to the conventional DSC method. It is quite certain that its use for blend analysis will become more common in the near future.

Cocrystallization is one of the limitations in Crystaf analysis. It seems that Tref is more appropriate for analyzing copolymers with complex CCD, especially if one needs more quantitative results. This is due to the fact that Tref analysis seems to be less affected by cocrystallization for the same CR. The fact that Tref also measures the differential profile directly, without the use of curve fitting and differentiation required in Crystaf, is responsible for the fact that Tref profiles generally appear sharper and more resolved than the equivalent Crystaf ones.

Although various mathematical models have been proposed recently to describe Crystaf and Tref, none can account for important phenomena such as crystallization kinetics and cocrystallization effects during the fractionation. From an academic viewpoint, the understanding of the fractionation mechanism operative in both techniques and the development of good phenomenological models is still a challenging task.

In conclusion, it can be said that both techniques are complementary in nature and will be used side by side for the better understanding of semicrystalline copolymers, combining the faster and easier use of Crystaf with the sharper resolution of Tref.

References

1. Monrabal BJ (1994) Appl Polym Sci 52:491
2. Monrabal B (1996) Macromol Symp 110:81
3. Cady LD (1987) Plast Eng 25
4. Gownder MJ (2001) Plast Film Sheeting 17:53
5. Soares JBP, Hamielec AE (1999) Temperature rising elution fractionation. In: Pethrick RA, Dawkins JV (eds) Modern techniques for polymer characterization. Wiley, New York, pp 15–55
6. Wild L (1990) Adv Polym Sci 98:1
7. Wild L, Blatz C (1993) Development of high performance tref for polyolefin analysis. In: Chung TC (ed) New advances in polyolefins. Plenum, New York, pp 147–157
8. Soares JBP, Hamielec AE (1995) Polymer 36:1639
9. Fonseca CA, Harrison IR (1999) Temperature rising elution fractionation. In: Pethrick RA, Dawkins JV (eds) Modern techniques for polymer characterization. Wiley, New York, pp 1–14
10. Flory PJ (1949) J Chem Phys 17:223
11. Flory PJ (1953) Principles of polymer chemistry, 1st edn. Cornell University Press, Ithaca, p 495
12. Mandelkern L (2002) Crystallization of polymers, 2nd edn. Cambridge University Press, Cambridge, p 90
13. Prasad A, Mandelkern L (1989) Macromolecules 22:4666
14. Nieto J, Oswald T, Blanco F, Soares JBP, Monrabal B (2001) J Polym Sci Part B Polym Phys 39:1616
15. Mandelkern L (2002) Crystallization of polymers, 2nd edn. Cambridge University Press, Cambridge, p 224
16. Stockmayer WH (1945) J Chem Phys 13:199
17. Simha R, Branson H (1944) J Chem Phys 12:253
18. Stejskal J, Kratochvil P, Strakova D (1981) Macromolecules 14:150
19. Stejskal J, Kratochvil P, Jenkins AD (1987) Macromolecules 20:181
20. Stejskal J, Kratochvil P (1987) Macromolecules 20:2624
21. Tacx JCJF, Linssen HN, German AL (1988) J Polym Sci Part B Polym Chem 26:61
22. Soares JBP, Hamielec AE (1995) Macromol Theory Simul 4:305
23. Costeux S, Anantawaraskul S, Wood-Adams PM, Soares JBP (2002) Macromol Theory Simul 11:326
24. Wild L, Ryle D, Knobeloch D, I Peat (1982) J Polym Sci Part B Polym Phys 20:441

25. Wild L, Ryle T (1977) Polym Prepr Am Chem Soc 18:182
26. Shirayama K, Kita S-I, Watabe H (1972) Makromol Chem 151:97
27. Burfield DR, Kashiwa N (1985) Makromol Chem 186:2657
28. Savitski EP, Caflisch GB, Killian CM, Meadows M, Merkley JH, Huff BJ (2003) J Appl Polym Sci 90:722
29. Anantawaraskul S, Soares JBP, Wood-Adams PM (2003) J Polym Sci Part B Polym Phys 41:1762
30. Kelusky EC, Elston CT, Murray R (1987) Polym Eng Sci 27:1562
31. Glockner GJ (1990) J Appl Polym Sci Appl Polym Symp 45:1
32. Pigeon M, Rudin A (1993) J Appl Polym Sci 47:685
33. Pigeon M, Rudin A (1994) J Appl Polym Sci 51:303
34. Usami T, Gotah Y, Takayama S (1986) Macromolecules 19:2722
35. Pasch H (2000) Adv Polym Sci 150:1
36. Springer H, Hengse A, Hinrichsen G (1990) J Appl Polym Sci 40:2173
37. Mirabella FM, Ford EA (1987) J Polym Sci Part B Polym Phys 25:777
38. Mingozzi I, Nascetti S (1996) Int J Polym Anal Character 3:59
39. Nakano S, Goto Y (1981) J Appl Polym Sci 26:4217
40. Zhou XQ, Hay JN (1993) Eur Polym J 29:291
41. Schouterden P, Groeninckx G, Van der Heijden B, Jansen F (1987) Polymer 28:2099
42. Hosoda S (1988) Polym J 20:383
43. Soares JBP, Abbott RF, Willis JN, Liu X (1996) Macromol Chem Phys 197:3383
44. Faldi A, Soares JBP (2001) Polymer 42:3057
45. Kim Y-M, Kim C-H, Park J-K, Kim J-W, Kim T-I (1996) J Appl Polym Sci 60:2469
46. Zhang M, Lynch DT, Wanke SE (2000) J Appl Polym Sci 75:960
47. Soares JBP, Hamielec AE (1995) Polymer 11:2257
48. Soares JBP (1998) Polym React Eng 199:1917
49. da Silva Filho AA, Soares JBP, de Galland GB (2000) Macromol Chem Phys 201:1226
50. Defoor F, Groeninckx G, Schanterden P, Van der Heijden B (1992) Polymer 33:3878
51. Borrajo J, Cordon C, Carella JM, Toso S, Goizueta G (1995) J Polym Sci Part B Polym Phys 33:1627
52. Elicabe G, Carella J, Borrajo J (1996) J Polym Sci Part B Polym Phys 34:527
53. Elicabe G, Cordon C, Carella J (1996) J Polym Sci Part B Polym Phys 34:1147
54. Britto LJD, Soares JBP, Penlidis A, Monrabal B (1999) J Polym Sci Part B Polym Phys 37:539
55. Pasch H, Brull R, Wahner U, Monrabal B (2000) Macromol Mater Eng 279:46
56. Gabriel C, Lilge D (2001) Polymer 42:297
57. Anantawaraskul S, Soares JBP, Wood-Adams PM, Monrabal B (2003) Polymer 44:2393
58. Sarzotti DM, Soares JBP, Penlidis A (2000) J Polym Sci Part B Polym Phys 40:2595
59. Brull R, Pasch H, Raubenheimer HG, Sanderson R, van Reenen AJ, Wahner UM (2001) Macromol Chem Phys 202:1281
60. Graef SM, Brull R, Pasch H, Wahner UM (2003) e-Polymers, no 05
61. Alamo RG, Viers BD, Mandelkern L (1993) Macromolecules 26:5740
62. Alamo RG, Domszy RC, Mandelkern L (1991) Macromolecules 24:6480
63. Richardson MJ, Flory PJ, Jackson JB (1963) Polymer 4:221
64. Shida M, Ficker HK, Stone IC (1966) J Polym Sci Polym Lett 4:346
65. Pasch H (2001) Macromol Symp 165:91
66. Brull R, Grumel V, Pasch H, Raubenheimer HG, Sanderson R, Wahmer UM (2002) Macromol Symp 178:81
67. Anantawaraskul S, Soares JBP, Wood-Adams PM (2004) Macromol Chem Phys 205:771

68. Monrabal B, Blanco J, Nieto N, Soares JBP (1999) J Polym Sci Part A Polym Chem 37:89
69. Simon LC, de Souza RF, Soares JBP, Mauler RS (2001) Polymer 42:4885
70. Soares JBP, Abbott RF, Kim JD (2000) J Polym Sci Part B Polym Phys 38:1267
71. Chu KJ, Shan CLP, Soares JBP, Penlidis A (1999) Macromol Chem Phys 200:2372
72. Chu KJ, Soares JBP, Penlidis A, Ihm SK (1999) Macromol Chem Phys 200:1298
73. Kim JD, Soares JBP (1999) Macromol Rapid Commun 20:347
74. Chu KJ, Soares JBP, Penlidis A (2000) Macromol Chem Phys 201:340
75. Kim JD, Soares JBP (2000) J Polym Sci Part A Polym Chem 38:1427
76. Shan CLP, Chu KJ, Soares JBP, Penlidis A (2000) Macromol Chem Phys 201:2195
77. Simon LC, Patel H, Soares JBP, de Souza RF (2001) Macromol Chem Phys 202:3237
78. Shan CLP, Soares JBP, Penlidis A (2002) J Polym Sci Part A Polym Chem 40:4426
79. de Goede S, Brull R, Pasch H, Marshall N (2003) Macromol Symp 193:35
80. Soares JBP, Monrabal B, Nieto J, Blanco J (1998) Macromol Chem Phys 199:1917
81. Beigzadeh D, Soares JBP, Duever TA (2001) J Appl Polym Sci 80:2200
82. Cheng HN, Tam SB, Kasehagen LJ (1992) Macromolecules 25:3779
83. Cheng HN, Kasehagen LJ (1993) Macromolecules 26:4774

Editor: Akihiro Abe

Chemical Composition of Polymer Surfaces Imaged by Atomic Force Microscopy and Complementary Approaches

G. Julius Vancso (✉) · Henrik Hillborg · Holger Schönherr

MESA+ Institute for Nanotechnology and Faculty of Science and Technology,
Department of Materials Science and Technology of Polymers, University of Twente,
P.O. Box 217, 7500 AE Enschede, The Netherlands
g.j.vancso@tnw.utwente.nl

Abstract In this article we review the recent developments in the field of high reso-
lution lateral mapping of the surface chemical composition of polymers by atomic force
microscopy (AFM) and other complementary imaging techniques. The different AFM ap-
proaches toward nanometer scale mapping with chemical sensitivity based on chemical
force microscopy (CFM) are discussed as a means to unravel, for instance, the lateral
distribution of surface chemistry, the stability of various types of functional groups in
various environments, or the interactions with controlled functional groups at the tip sur-
face. The applicability and current limitations of CFM, which allows one to image chem-
ical functional group distributions with a resolution in principle down to the 10–20 nm
scale, are critically discussed. In addition, complementary imaging techniques are briefly
reviewed and compared to the AFM-based techniques. The complementary approaches
comprise various spectroscopies (infrared and Raman), secondary ion mass spectrome-
try (SIMS), matrix-assisted laser desorption/ionization mass spectrometry (MALDI-MS),
X-ray photoelectron spectroscopy (XPS or ESCA), and near-field optical techniques used
for imaging.

1
Introduction

1.1
The Scope of Atomic Force Microscopy
in Polymer Surface Characterization

The Atomic Force Microscope [1] with its various imaging modes, and the
related Scanning Probe Microscopy techniques have changed the scientific
landscape during the last 15 years. Atomic force microscopy (AFM) and re-
lated scanned probe techniques have become enabling methods (platforms)
in cutting-edge nanotechnology. These instruments at the same time func-
tion also as a "workhorse" in scientific laboratories and are being used to
assist solving materials science problems covering a wide range of issues. It
is not the purpose of this review to introduce AFM, its operational princi-
ples, and the various imaging modes used in polymer research. Instead, the
reader is referred to other reviews introducing AFM imaging [2–14], AFM-
based studies, and force measurements using force-distance curves [15, 16].

We only mention here that the probe used in AFM is a sharp tip, which is attached to a flexible microbeam (microcantilever). In AFM various forms of interactions between the apex of the tip (with a radius between approximately 10–100 nm) and the sample surface are measured, either as a function of tip location with respect to the surface, or at a fixed (x, y) position as a function of the cantilever deflection or tip-sample distance. In most conventional instruments the cantilever-tip assembly is attached to a piezo controller, which positions the tip in the (x, y) scanned plane and adjusts the vertical position (piezo travel) to accommodate sample height, or to measure tip-sample force curves. The latest generation instruments can also be equipped with active x-y-z distance feedback control loops, which enable one to perform lithography, vertical positioning of the tip (e.g. for single molecule force spectroscopy), etc.

Whereas scanned probe techniques are being continuously developed, some applications have reached a relative maturity. At the beginning of AFM in the eighties emphasis in AFM-related research was put on surface topology imaging of structures from the 100 micrometer to the nanometer size domains. Distinct advantages of AFM, e.g., its capability to deliver "true" 3-D surface topology information, have been described in ample detail in the literature. A great deal of excitement was caused by nanometer-scale studies making use of the AFM's ability to visualize molecular packing in regular structures from a true nanometer scale perspective. Corresponding research was soon followed by work aiming at surface property studies on the nanoscale (tribology, adhesion by surface force measurements using AFM cantilevers as nanoscale force sensors, nanomechanics). With developments in imaging speed and stability, and with inventions enabling environmental control (temperature, imaging media, including gases and solvents) studies of processes (physical and chemical) and nanofabrication approaches are also gathering momentum (Fig. 1).

The chemical functionalization of AFM tips allows one, in principle, to map functional groups at surfaces, to pick up and deliver single molecule reactants, and to study force responses of (macro)molecules under mechanical tension, or exited by external fields (e.g. light). Various tip functionalization approaches have been described in the literature. By now, some of these can be considered as robust enough for being routinely used in research laboratory environments to study interaction forces between (functionalized) tips and sample surfaces in a simple manner. AFM tips with simple functional groups attached (e.g. in the form of a self-assembled monolayer of the functional molecules) can even be commercially purchased. The surface forces measured by AFM, of course, always include contributions by London dispersion forces. However, when functional groups are attached to tip surfaces, e.g., by AFM tip modifications, these can interact with surface groups via system-specific forces (H-bonding and other hydrophilic interactions, hydrophobic forces, acid/base type interactions, etc.) in addition to London
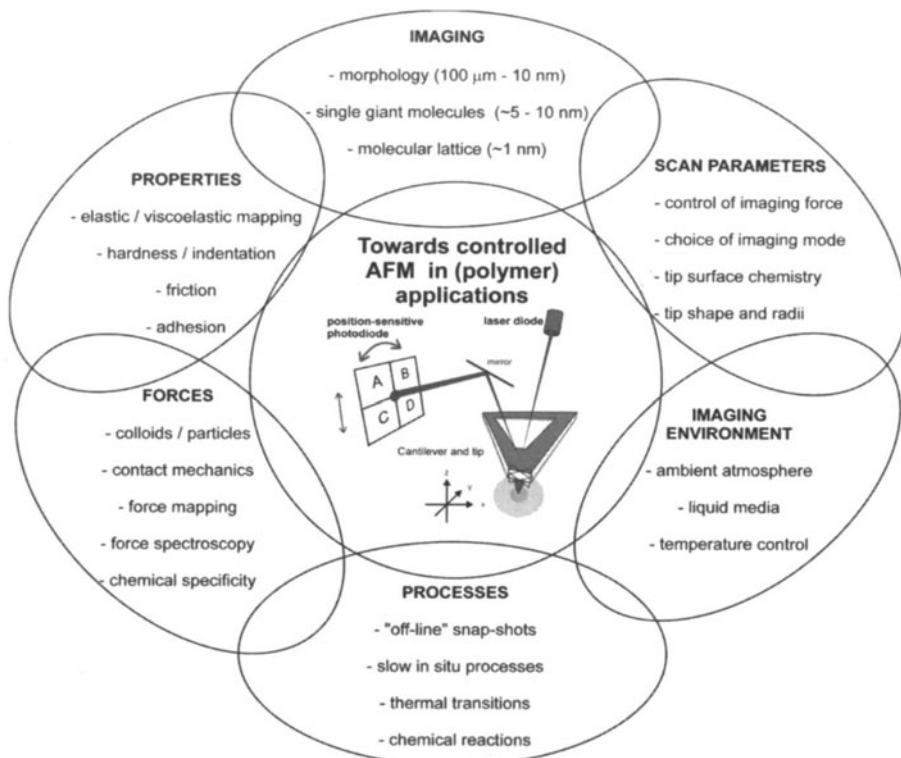
Fig. 1 Towards controlled AFM in (polymer) applications

forces. The tip force-distance curve characteristics measured reflect the sum of all of the specific and non-specific contributions.

As a result of the high lateral resolution of AFM when sharp probes and appropriate imaging conditions are used, in theory, lateral mapping of surface chemical groups can be performed with near nanometer (several tens of nm) resolution. This mapping involves measurements of the local variation of interaction forces either in the surface normal or in the surface tangential direction. Surface normal forces and forces at which AFM tips get disengaged in the surface normal direction give information about adherence,[1] while surface tangential forces are related to tribological properties (static and dynamic friction). By measuring local variations of normal and lateral forces, in ideal situations (for ideally smooth surfaces and without surface (visco)elastic deformation under the load of the AFM tip) one would image the lateral dis-

---

[1] We use here "adherence" to describe the practical work of adhesion to emphasize differences between its value and the magnitude of thermodynamic adhesion. The latter, if expressed in work of adhesion, corresponds to the reversible free energy change per unit surface area when two contacting surfaces are moved apart from contact to infinite distance of separation. Thus, adherence also includes the energy dissipated during separation of the contacting surfaces from each other.

tribution of chemical groups at the sample surface, hence the related method has been named "Chemical Force Microscopy" (CFM).[2] This nomenclature has been introduced by one of the first groups of authors [17] describing mapping of functional groups in self-assembled monolayes (SAMs) of end-functionalized alkanethiols. These authors mapped the spatial arrangement of different functional end groups exposed at the surface of the SAMs using chemically specific contrast between the tip and the SAM surface (see Sect. 5.1).

In this review we shall focus on "true" imaging with chemical sensitivity, with the main focus of using forms of AFM, which utilize and control chemically specific contrast between tip and sample, e.g., by controlled modification of the tip surface. AFM as a near-field technique has a limited field of depth, which can be significant (several tens of nanometers) only if soft, rubbery or viscoelastic polymers are studied. Hence, for smooth surfaces (i.e. without the perturbation of surface topological features and roughness) the interactions between tip and sample are dominated by the surface chemistry and surface mechanical properties. Thus, questions that one can raise regarding surface chemical composition include the lateral distribution of surface chemistry, the stability (e.g. for charged surfaces in electrolytes) of various types of functional groups in various environments, interactions with controlled functional groups at the tip surface, etc. CFM allows one to image chemical functional group distributions with a resolution, in principle, down to the 10–20 nm scale. However, chemical imaging is by no means routine, and one should carefully evaluate experimental strategies and data for lateral mapping of chemical groups. To this end, it is very essential to consider CFM as a complementary technique to the other surface imaging approaches, including spectroscopies (infrared – IR –, and Raman), secondary ion mass spectrometry (SIMS), X-ray photoelectron spectroscopy (XPS or ESCA), etc. Hence, these imaging techniques will also be reviewed in this article, albeit shortly, and differences and complementary approaches with CFM will be emphasized and discussed whenever appropriate.

Emphasis is laid in this review naturally on polymer specific problems. It is not our purpose to give a full encyclopedic account of the literature up to date. We shall rather focus on typical selected applications and introduce briefly the underlying physical and chemical concepts. We try to sketch the power and the limitations of CFM at the current state-of-the-art of the technological developments of CFM. The choice of the examples discussed reflects our preferences and scientific taste, but omissions may have also occurred by accident. We regret if we left out (by accident or by choice) articles from

---

[2] Chemical force microscopy (CFM) will be used as a synonym for "AFM using defined surface chemistry, for instance self-assembled monolayer functionalization, on AFM probe tips in order to measure differences in surface chemical composition" (using friction or adhesion differences related to interactions between functional groups or atoms exposed on both tip and sample surface as contrast) throughout this review article.

the literature which the corresponding authors would miss and we offer our apologies to those who consider these omissions as negligence on our part. We cannot provide justice to everyone.

1.2
The Case and Need of Surface Treatment of Polymers

In applications, such as coatings, adhesives and biomaterials, the surface properties, as well as good bulk mechanical properties, of polymers are equally important for their success. Since polymers often do not possess the required surface properties, various treatment techniques have been developed to modify their chemical or physical characteristics. Introducing functional groups, or modifying the surface morphology, for increased adhesion or decreased hydrophobicity are classical examples for these treatments. A limiting factor for biomaterials is, for example, non-specific protein interactions, often leading to undesirable responses from the host. These undesirable reactions are driven by surface-protein interactions. One method to enhance biocompatibility is by chemical modification of the surface by grafting biologically active molecules, such as peptides, proteins or polysaccharides. These surface modifications can be achieved by different techniques making use of either physical adsorption or covalent binding. Functional groups can be grafted by various techniques, such as plasma modification, gamma radiation grafting, photochemical reactions as well as exposure to oxidizing agents in solution.

With the recent development of various advanced surface characterization techniques, our understanding of polymer surfaces has been significantly improved, as well as our ability to control and even to tailor surface characteristics for specific applications down to sub-micrometer dimensions. Techniques for controlling the lateral distribution of functional groups on surfaces have a wide range of potential applications such as in biosensors, cell guidance, molecular electronics, wetting, membranes, etc. Regarding a general reference on polymer surfaces, the reader is referred to the book of Garbassi et al. [18]. Complementary microspectroscopic imaging is dealt with in the monograph of Koenig [19].

1.3
Homogeneous vs. Heterogeneous Distributions
of Functional Groups at Surfaces

In thermodynamics of polymers (solutions, mixtures, etc.) radial pair distribution functions are of central importance as they contain information about the global character of intermolecular interactions and describe the structure on the atomic (segmental) ensemble level. Pair distribution functions and spatial distribution in heterogeneous (e.g. two component) systems

can also be statistically described and averages, such as preferential solvation and clustering, can be quantitatively derived. Once the pair distribution functions are known, average measurable thermodynamic quantities (derivatives of the corresponding thermodynamic potentials) can be calculated. Scattering experiments, as well as other thermodynamic measurements, such as "inverse" gas chromatography, can be used to derive statistical structure (and property) characteristics (see e.g. [20–23]). In principle, for heterogeneous surfaces similar surface-specific formalisms can be introduced. It has been recognized that surface chemical heterogeneities for multicomponent systems have a profound influence on surface-related phenomena, such as adsorption [24]. For a statistical description of surfaces, particle distribution functions should be specified to describe (average) values and distributions of surface-sensitive properties down to the characteristic observation depths from the (geometrical) surface into the bulk. Once the distribution function and the averaging processes (characteristic moments over the particle distribution functions) for the given property that depend on the spatial heterogeneity are known, the appropriate ensemble mean values (measurable) of the property in question can be derived. Although for the bulk such statistical treatments are standard, there is surprisingly very little described in the literature regarding statistical treatments of surface-related atomistic structures and properties (and related distributions). One important example is related to thermodynamic adsorption on heterogeneous surfaces, or interfaces. For heterogeneous surfaces [heterogeneous materials, surface treated (polymer) particles] adsorption sites can have different (free) energies and correspondingly a site energy distribution can be defined (and measured). For example, energy site distributions at the surface of xerographic toner particles (with heterogeneous average compositions) were characterized with success [21].

For heterogeneous surfaces in multicomponent systems it is surprising that virtually no quantitative description is usually given with respect to exact lateral distributions of surface (functional) groups down to quantity-dependent characteristic depths. One usually characterizes heterogeneous surfaces by number average concentrations of atoms or molecular fragments (XPS, SIMS) or patch sizes and shapes for surface phase-separated structures. For a quantitative description of surface structure and properties such distributions must eventually be introduced. However, there are only few experimental techniques, which give (in real space) adequate information about the atomic (or segmental) distribution of different species. Surface scattering (in Fourier space) could be used, but this falls beyond the scope of this review as we focus here on non-average local imaging of spatial heterogeneities of functional groups (in real space) and not on ensemble averaging. In the following sections it will become clear that a tremendous experimental and theoretical effort is needed until rigorous surface structure distributions for heterogeneous surfaces (and ultimately a first-principles based treatment of surfaces) can be given with atomistic details.

Polymer surfaces are often expected to show spatially heterogeneous distributions of functional groups as a result of, e.g., widely-applied surface treatment procedures and surface chemical reactions. The analysis of the spatially heterogeneous chemistry and the direct relation of this heterogeneous surface chemistry with related properties have been only recently addressed in detail. This lack of knowledge that we have just begun to overcome has been in part caused by the unavailability of suitable characterization tools that allow one to map the respective distributions on the sub 100 nm length scale.

The knowledge of the spatially heterogeneous distributions of functional groups is of widespread importance in polymer science and of striking relevance in the biochemical field. It is well known that, for instance, cell adhesion depends critically on the spacing of (poly)peptide sequences on functionalized substrates. For example, the effect of surface coverage of RGD protein sequences, which was at that time only indirectly related to lateral spacings, has been investigated in detail [25]. A minimum spacing of 440 nm was concluded to be necessary for spreading of cells, while focal point formation required minimal spacings of 140 nm. In an extension of this type of work, the direct control of spacing between adhesion islands was shown by Chen et al. to control cell growth or cell death [26]. More recently, the nanoscale clustering of RGD was unraveled [27], which clearly proves and exemplifies the importance of micro- and nanoscale analysis of the distribution of chemical functional groups at surfaces. Many of these and related biological and biochemical processes rely on biopolymers, such as proteins and peptides, in so far they can be considered part of polymer science. In addition, the interaction of man-made polymers and biological species is of crucial importance in for instance drug discovery and tissue engineering [28, 29], and hence the understanding of the underlying processes down to the molecular scale clearly requires advanced local chemically sensitive analysis and imaging methodologies, as discussed in this review.

In addition to the obvious impact of nanometer scale distributions of recognition units in controlling cell adhesion, the lateral heterogeneity of functional groups at polymer surfaces plays a centrally important role in many surface-related properties and processes, for example in the well-known phenomenon of wetting of surfaces. In most instances a liquid placed on a solid does not wet the surface, but remains as a drop having a definite angle of contact between the liquid and the solid phase. The idealized situation for a homogeneous, flat surface is illustrated in Fig. 2.

The contact angle θ is geometrically defined as the angle formed by the intersection of the two planes tangent to the liquid and solid interfaces at the perimeter of the contact between the two phases and the third surrounding phase, which is typically air or vapor. The change in surface free energy, ΔG, accompanying a small displacement of the liquid such that the change in area
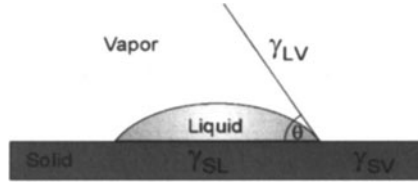
Fig. 2 Contact angle between a liquid placed on a solid surface and the surface; γ is the interfacial energy (or interfacial tension), and LV, SV, and SL in the subscripts refer to liquid-vapor, solid-vapor, and solid-liquid interfaces, respectively

of solid covered is ΔA, can be written as

$$\Delta G = \Delta A \left(\gamma_{SL} - \gamma_{SV} \right) + \Delta A \gamma_{LV} \cos(\theta - \Delta \theta) \tag{1}$$

where γ is the interfacial energy (or interfacial tension), and LV, SV, and SL refer to liquid-vapor, solid-vapor, and solid-liquid interfaces, respectively.
    At equilibrium

$$\lim_{\Delta A \to 0} \frac{\Delta G}{\Delta A} = 0$$

and Eq. 1 becomes:

$$\gamma_{SV} - \gamma_{SL} = \gamma_{LV} \cos \theta \tag{2}$$

In combination with the definition of thermodynamic work of adhesion:

$$w_{SLV} = \gamma_{SV} + \gamma_{LV} - \gamma_{SL} \tag{3}$$

we can write Eq. 2 as

$$w_{SLV} = \gamma_{LV}(1 + \cos \theta) \tag{4}$$

Equation 2 was stated in quantitative form by Young in 1855 [30]; the equivalent (Eq. 4) was stated in algebraic form by Dupré in 1869 [31], along with the definition of work of adhesion.
    By contrast, real surfaces can be rough and/or heterogeneous in composition [24]. In the following we will briefly discuss as an illustrative example how the wettability and the contact angles measured will depend on the surface composition. For instance, the surface can be composed by domains of different composition. The effect of a patchy structure on the Young equation was described by Cassie, who proposed the following equation (Cassie equation) for a two component, heterogeneous surface [32]:

$$\cos \theta = f_1 \cos \theta_1 + f_2 \cos \theta_2 \tag{5}$$

where f_1 and f_2 are the fraction of the surface having inherent contact angles θ_1 and θ_2. Equation 5 constitutes a simple arithmetic mean, weighted by the respective surface fractions of the components. The Cassie treatment of heterogeneous surfaces was reviewed by Israelachvili and Gee [33], who

modified Eq. 5 in order to account for heterogeneities close to atomic and molecular dimensions:

$$(1 + \cos\theta)^2 = f_1 \left(1 + \cos\theta_1\right)^2 + f_2 \left(1 + \cos\theta_2\right)^2 \tag{6}$$

Equation 6 replaces Eq. 5 whenever the sizes of the chemically heterogeneous patches approach molecular or atomic dimensions. In the latter treatment, polarizabilities, dipole moments and surface charges are averaged, owing to the very low dimension of heterogeneity, instead of cohesion energies as in the Cassie equation. Experiments on mixed monolayers of alkanethiols showed that the Cassie equation fits the variation of angle with surface fraction better than the Israelachvili–Gee equation [34], while for other systems the deviations were to within the experimental error [35]. While these treatments describe the effect of chemical composition on equilibrium contact angles, it is obvious that other techniques, in particular the imaging techniques discussed in this review, may provide differently weighted information.

Apart from wettability and the related spreading of liquids, chemically heterogeneous surface composition has a profound impact on adhesion and its respective failure mechanisms and defects [24]. Further relevant areas comprise release surfaces, corrosion, lubrication, as well as chemical surface functionalization in coatings, sensors and biomedical applications (stealth surfaces) [18]. These important phenomena together with related applications in miniaturized devices, where the tolerances for defects and lateral heterogeneities are rapidly decreasing, are in the focus of the microscopic techniques reviewed in this article.

An emerging area of applicability is the field of sub-micron and nanopatterning, where there is a clear need to analyze the chemical composition of patterns at the relevant length scales. Many of these applications are again ultimately located at the interface between polymer surface science and life science. For example, protein patterning of polymer surfaces via e-beam lithography [36], bioactive molecular patterning in the fabrication of biosensors [37] and high-throughput combinatorial chemistry analytical techniques [38], as well as light-directed, spatially addressable, stepwise chemical synthesis of bioactive biopeptides are target areas [39]. Other examples include applications in microfluidic devices for localized drug applications to cell cultures [40] and DNA analysis [41], and investigations on neuron networks [42, 43]. For fundamental understanding of these interface-related processes, knowledge on a sub-micrometer level is required.

In addition to the mentioned widespread phenomena related to polymer surface chemical composition, applications outside the life sciences are located e.g. in the area of semiconducting polymers [44], e.g. for the fabrication of polymeric light emitting diodes. For this particular topic, the efficiency of polymeric light emitting diodes has been shown to be dependent of the nucleation processes (referred to as nanometer-sized clusters) in conjugated polymer films. These phenomena can be successfully studied on

a sub-micrometer scale by a combination of Near-Field Scanning Optical Microscopy and AFM [45].

2
How can Polymer Surfaces be Modified?

The purpose of this chapter is to focus on controlled surface modifications of polymers, with emphasis on the advances achieved during the past decade or so. The commonly used techniques generally mentioned include corona discharge, plasma, UV, laser, and electron beam treatments. Lateral patterning techniques utilizing soft lithography, which is the collective name for a number of techniques where a patterned elastomer is used as mold, stamp or mask to generate or transfer patterns with sub-micrometer resolution, will not be covered in this chapter, since several comprehensive reviews focused on these techniques have been recently published [46, 47].

2.1
Plasma Treatment

The term "plasma" denotes a partially ionized gas containing a mixture of positive and negative charge carriers and neutral components. The overall charge of the plasma is neutral. Plasmas used for surface modification of polymers are generally not in a thermal equilibrium, but are generated by an external electric field applied over the gas mixture. This means that the gas temperature is usually hardly above room temperature even though the temperature of the electrons is much higher ($10\,000-100\,000$ K) and is only maintained as long as the external electric field exists. The reason for the low gas temperature is that the electrons make up only a very small part of all particles present and that the energies of positive ions and neutral species are only negligibly increased by the electric current within the plasma. By exposing a polymer surface to a plasma, it is exposed to this complex mixture of reactive species such as ions, electrons, as well as to UV radiation. Generally, the effects can be classified as follows [48]: (1) Surface reactions between gas-phase species and surface species introduce functional groups and crosslinks at the surface, (2) plasma polymerization, which involves the formation of a thin film via polymerization of an volatile organic monomer, and (3) etching, where materials are removed from the polymer surface by physical etching forming volatile by-products. There exists a large body of literature on surface modification of synthetic polymers by plasma treatments or plasma polymerization [49–55]. The advantage of the plasma processes is that the modification is limited to the top surface layer and does not affect the bulk properties of the polymer.

By using different types or mixtures of gases in the plasma, different surface functionalities can be obtained. Oxygen containing plasmas are the most frequently used treatments and these very effectively increase the surface energy of polymers by introduction of oxygen-containing species, such as hydroxyl, carbonyl, carboxyl and ether groups. Plasma treatments in noble gases, such as argon or helium, also result in a significant increase of oxygen containing groups. This is probably due to the exposure of the freshly treated, reactive surfaces to atmospheric oxygen after treatment or originates from trapped oxygen on the reactor walls [50] or oxygen dissolved within the polymer. Nitrogen containing plasmas can be used to introduce functionalities, such as amino groups. Fluorine containing plasmas are used to increase the hydrophobicity of polymer surfaces by the introduction of fluorine. Different functional groups can also be obtained by plasma polymerization using different monomers. For example, poly(ethyleneterephthalate) was functionalized in a glow discharge plasma by: $- OH$ (using allyl alcohol), $- NH_2$ (using allyl amine), $- CF_3$ (using perfluorohexene) and siloxyl groups (using hexadimethylsilane) [56].

Reports on the lateral distribution of the induced functional groups on polymer surfaces by plasma treatments have only been published recently. For example, using AFM with chemically functionalized tips, the lateral distribution of functional groups in plasma-polymerized allylamine films was investigated [57]. These measurements indicated the presence of a heterogeneous local environment of the amino groups formed, where patches exhibiting differences in hydrophobicity on a sub-50 nm scale were detected. In another study it has been shown that surface treatments of isotactic polypropylene with fluorine-containing gases resulted in an inhomogeneous distribution of the hydrophobicity on length scales below 50 nm [58].

Plasma-induced chemical micropatterning for cell growth is a new field of plasma surface modification of polymers. The advantages are the flexibility concerning type and density of introduced functional groups and the possibility to modify the morphology of the surface [59]. Moreover, the technique provides sterile surfaces and can be scaled to high outputs. Disadvantages are the low pressure and the UV-component which may cause denaturation and generation of multiple surface functionalities [59]. Another recent application of the plasma technique is mass production of disposable microfluidic devices by plasma etching (using an oxygen plasma) [60]. In most of these applications aiming at a lateral homogeneity of the introduced functionalities is obvious as is the need to develop suitable high resolution analysis methods.

2.2
UV-Radiation and UV-Laser Ablation

UV-radiation, generally in the range between 250–400 nm, can be used for lateral surface modification of polymer surfaces. The radiation causes

photon-activated fragmentation, or crosslinking, of the surface, where UV-sensitizers can be added to enhance the photon yield of the process. The characteristic penetration depth of the UV usually does not exceed a few hundred nanometers [61]. The technique can be used with lateral control of the functionalized groups using different atmospheres [62]. Polymer surfaces were irradiated by UV in different reactive gas atmospheres, where BrCN introduced nitrile functionalities, N_2H_4 introduced amino functionalities and $SO_2 + O_2$ introduced a mixture of thioureas and derivatives of sulfonic acids. Projection techniques allowed patterned modification of the surfaces to be made. Another application is improved micro-wear resistance of polymer surfaces [63]. Conducting patterns in 1-4-polybutadiene, doped by iodine, were made by UV-photolithography [64]. Conducting polymers are of interest for many potential applications in polymer batteries, integrated circuits, field-effect transistors, optical memory storage devices and electrochromic displays [65]. The microlithographic formation of conducting patterns is a key prerequisite for most of these applications [64].

UV lasers are photon sources characterized by energy and spatial coherence, whose energies can be in the watt range. The energies can be delivered in pulses and the narrow wavelength spread can be tuned to the maximum absorption of a polymer, making the treatments an energy-efficient process for patterning the surface. The photoablation process involves absorption of short-duration laser pulses, which excites and fragments the polymer chains. The resulting shock wave ejects the decomposed fragments (C_2, CO_2, CO) leaving behind a photoablated cavity [66]. Thus the method can be used as a dry etching technique. Special polymers, based on cinnamylidenemalonic acid ester groups, have been tailored for higher sensitivity to the laser ablation [67]. They exhibited high sensitivity, stability to wet etching (acids), high quality film formation properties and high resolution ablation structures. Prototyping can be performed using UV-laser ablation because of the flexibility of the direct writing [60]. A pulsed UV-excimer laser was used for photoablation of polymer surfaces, making fluid-handling microchannels with high aspect ratios for the fabrication of microdiagnostic devices [66, 68]. Bilayers of UV-absorbing and optically transparent polymer films were irradiated by UV-laser pulses. The UV-absorbing polymer was selectively photolyzed, and covalently crosslinked onto the transparent film. Fine surface patterns of the formed crosslinked film-layers were obtained by pulsed irradiation through a projection mask [69]. By using this method two dimensional patterns consisting of hydrophilic domains ($\approx 150\,\mu m \times 150\,\mu m$) of crosslinked poly(N,N-dimethylacrylamide) on hydrophobic polyethylene were created.

2.3
Electron/Ion Beam Treatment

Polymer surfaces can also be laterally modified using electron beam lithography. A focused beam of high-energy electrons is used to pattern a layer of electron-sensitive polymers, mostly poly(methyl methacrylate) [70]. By this process line widths < 5 nm have been achieved [71]. Using e-beam lithography, high resolution patterning of protein features on (poly(*tert*-butyl-methacrylate-*co*-methyl-methacrylate) with a resolution of 125 nm has been obtained [36]. Ion beams also contain high energy species, but these only affect the surface regions due to their higher mass. Ion beams are used in high-resolution patterning of polymeric surfaces, such as patterning of protein features on (poly(*tert*-butyl-methacrylate-*co*-methyl-methacrylate) [36]. Enhancement of interfacial adhesion between polypropylene and polyamide by functionalization of the polypropylene surface by low-energy ion beam irradiation has also been performed [72]. The modification depth was < 70 nm. Lithography with neutral metastable atoms has several advantages compared to electron and ion beams: thanks to the short wavelength (< 0.01 nm) the neutral beam can be focused to a spot that is limited by the size of one atom and the effects of diffraction will be very small even for lithography through masks with 10 nm scale features [73]. By exposing self-assembled monolayers (SAMs) on gold substrates to metastable argon atoms, the SAMs were sensitized to etching by an aqueous ferricyanide solution, which etched patterns into the gold.

2.4
Surface Grafting

Polymer surface grafting offers versatile means for surface modification. The advantages of the grafting technique are the easy and controllable introduction of new polymer chains with a high surface density and precise localization at the surface, while keeping the bulk properties unchanged [74]. If the surface to be modified possesses reactive groups, modification can be conducted by a chemical coupling reaction. If no functional groups are present they can be created by irradiation of the surface, generating radicals as surface sites for graft polymerization. Graft polymerization is usually achieved by the formation of highly reactive radical-generating species, such as trapped polymer radicals or peroxide groups, via γ-irradiation [75], UV irradiation [76–79], plasma, glow discharges or ozone treatments [53], followed by a subsequent radical polymerization at elevated temperatures in solution. By using tethered diblock copolymers (PS-*b*-PMMA), whose blocks can self-assemble, ordered arrays or patterns on the surface can be fabricated [80]. These nano patterns can be controlled by the degree of grafting, molecular weight of the blocks, volume fraction of diblock copolymer

and the Flory–Huggins interaction parameter [80, 81]. For example, well-defined poly(*tert*-butyl acrylate) brushes were prepared by a surface-initiated polymerization on silicon wafers [82]. The brushes were then patterned using photolithographic techniques yielding novel patterned polymer surfaces exhibiting well-defined hydrophobic and hydrophilic domains. Features as small as 1 μm could be reproducibly obtained [82]. Patterned polymer brushes of poly(caprolactone) were prepared from micro-contact printed gold surfaces. The key feature of this approach was to use the surface-initiated polymerization to chemically amplify the patterned SAM into a patterned macromolecular film. The benefit of this approach was the formation of patterned polymeric thin films without the need for photolithographic tools. This method is also tolerant to initial imperfections within the original monolayer structure [82].

Surface block-graft-copolymerization, based on the photochemistry of N, N-diethyldithiocarbamate has been applied to precisely design biocompatible and functional surfaces (patterns of immobilized heparin or proteins), as well as block-grafted surfaces on polystyrene [83]. Polystyrene surfaces have also been patterned by immobilization of poly(N-isopropylacrylamide) by photolithography, and subsequently used for regiospecific cell attachment [84]. Surface modification of polydimethylsiloxane microfluidic devices by UV induced polymer grafting improved the stability of the electroosmotic mobility and improved electrophoretic resolution of peptides [85].

2.5
Surface Patterns Originating from Physical Instabilities

Another class of methods for achieving patterning of polymer surfaces on a length scale of micrometers or less relies on a physical instability with an intrinsic length scale. Examples of such processes, which will not be further discussed in this review, include dewetting [86, 87], buckling produced by stresses arising from dispersion forces [88, 89] or residual mechanical stress [65]. Further approaches exploit the amplification of capillary waves by various means [90, 91].

3
Surface Tension and Surface Tension Models

In this section a brief introduction to the concept of surface tension and surface tension models for the determination of surface tension of solids is given. The surface tension (γ) is the tangential stress (mN m^{-1}) in the surface layer and is a direct measure of the intermolecular forces at the surface [92]. A number of empirical and semi empirical methods, based

on contact angle measurements, have been developed for determining surface tension of solids. Among these are the critical surface tension [93–95], the Good–Girifalco equation [96, 97], the equation of state by Wu [98, 99], Fowkes theory [100] and its extensions [101, 102], and Lewis acid/base interactions [103]. Controversies and discussions concerning the validity of these methods can be found in literature and have been reviewed by a number of authors [98, 104, 105].

3.1
Single Surface Tension Theories

The fundamental equation for the measurement of solid surface tension by using contact angle measurements is the Young's equation:

$$\gamma_{SV} - \gamma_{SL} = \gamma_{LV} \cos\theta \tag{7}$$

where γ_{SV}, γ_{SL} and γ_{LV} are the interfacial tensions between solid/vapor, solid/liquid and liquid/vapor respectively, and θ is the equilibrium contact angle. The γ_{SV} may be considerably less than the surface tension of the solid in vacuum (γ_S), as a result of absorption of vapor on the surface. The amount of reduction in the surface tension of the solid caused by this absorption is referred to as the equilibrium spreading pressure π_e:

$$\pi_e = \gamma_S - \gamma_{SV} \tag{8}$$

A stable equilibrium is obtained if the surface is ideally smooth, uniform and non-deformable. If the surface is rough or heterogeneous, the system may reside in one of many metastable states, and the measured angle is a metastable contact angle. In this instance, the contact angle is not only dependent of surface tension, but also on the surface roughness and the drop volume [98].

The concept of critical surface tension was proposed by Fox and Zisman [93–95]. An empirical, linear relation was found when plotting between the cosine of the advancing angle and the surface tension of a series of homologous liquids (referred to as a Zisman plot). The critical surface tension (γ_C) equals the surface tension of the liquid, when it is extrapolated to a zero contact angle on the solid:

$$\gamma_C = \lim_{\theta \to 0} \gamma_{LV} = \gamma_S - \left(\gamma_{SL} + \pi_e\right) \tag{9}$$

Since both the interfacial tension and spreading pressure will vary with the testing liquid, values of the critical surface tensions must be used with great caution [92, 98]. Non-linear relations are often observed if specific interactions (such as hydrogen bonding) between liquid and surface are present [94]. Moreover, it may not be sufficient to measure only the advancing angle, thereby losing information from the contact angle hysteresis [104].

Good et al. formulated a theory of interfacial tension between two phases using the geometric mean of the surface tension of each phase and suggested a general equation, known as the Good–Girifalco equation [96, 97]. When substituted into the Young's equation, neglecting the spreading pressure, this leads to [105]:

$$\gamma_{SV} = \gamma_{LV}(1 + \cos\theta)^2/4\Phi^2 \tag{10}$$

where Φ is an interaction parameter, characteristic of the molecular properties of a given system. The interaction parameter can be determined from a liquid homologue of the solid, or from molecular constants [98]. Based on the critical surface tension and the Good–Girifalco theory, Wu proposed an equation of state, which gives accurate values of surface tension [98, 99]. The contact angle of a series of testing liquids with known surface tension (γ_{LV}) is used to obtain a number of critical surface tensions ($\gamma_{C,\Phi}$).

$$\gamma_{C,\Phi} = \Phi^2\gamma_S - \pi_e = \frac{1}{4}(1 + \cos\theta)^2\gamma_{LV} \tag{11}$$

The $\gamma_{C,\Phi}$ is plotted against γ_{LV} to obtain a curve (the equation of state plot) whose maximum value ($\Phi \approx 1$) corresponds to the surface tension of the solid (γ_S). The maximum value is attained by matching the polarities of the testing liquids and the surface.

3.2
Theories Based on Multi-Component Surface Tension Models

These theories are based on the assumption that the surface tension can be considered as a sum of a number of independent components, each representing a particular intermolecular force [92]:

$$\gamma = \gamma^d + \gamma^p + \gamma^h + \gamma^i + \gamma^{ab} + \dots \tag{12}$$

where γ^d, γ^p, γ^h, γ^i, and γ^{ab} are the contributions from London dispersion forces, polar forces, hydrogen-bonding forces, induction (Debye) forces and acid-base forces, respectively. Fowkes made the assumption that the surface tension was based on the sum of the hydrogen bonding and dispersive forces and derived an expression for the surface tension of a liquid on a solid in which only dispersion forces were common to both phases [100]:

$$\gamma_{SL} = \gamma_S + \gamma_L - 2\sqrt{\gamma_S^d\gamma_L^d} \tag{13}$$

This theory was then further complemented with polar contributions to the surface tension, for example by inserting the geometrical mean of polar components [101, 102] or by use of the reciprocals of the dispersive and polar surface tension components [106, 107]. Assuming that the geometrical mean could describe both polar and dispersion interactions Owens and

Wendt [102] proposed the following equation:

$$\gamma_{SL} = \gamma_{SV} + \gamma_{LV} - 2\sqrt{\gamma_{SV}^{d}\gamma_{LV}^{d}} - 2\sqrt{\gamma_{SV}^{P}\gamma_{LV}^{P}} \qquad (14)$$

By inserting γ_{SL} into the Young's equation the two unknown solid surface tension components can be obtained via the measurement of the equilibrium contact angles of two liquids of known surface tension components, for example by using water and diiodomethane [102]:

$$1 + \cos\theta = 2\sqrt{\gamma_{S}^{d}}\left(\frac{\sqrt{\gamma_{L}^{d}}}{\gamma_{LV}}\right) + 2\sqrt{\gamma_{S}^{h}}\left(\frac{\sqrt{\gamma_{L}^{h}}}{\gamma_{LV}}\right) \qquad (15)$$

Van Oss et al. [103, 108, 109] combined γ^{d}, γ^{P} and γ^{i} into a single component, which they called the apolar or Lifshitz-van der Waals component (γ^{LW}). The hydrogen bond (γ^{h}) and acid-base (γ^{ab}) components were described by electron acceptor-electron donor (Lewis acid/base) interactions of the polar component (γ_{i}^{AB}). The electron acceptor-electron donor parameters of the surface tension of a compound i are expressed as γ_{i}^{+} (acidic term) and γ_{i}^{-} (basic term) according to: $\gamma_{i}^{AB} = \sqrt{\gamma_{i}^{+}\gamma_{i}^{-}}$ [108, 109]. The total surface tension is then obtained by the addition of the apolar and polar components. By combining this approach with the Young–Dupré equation the following equation is obtained [108]:

$$\gamma^{tot} = \gamma^{LW} + \gamma^{AB} = (1 + \cos\theta)\gamma_{L} = 2\left(\sqrt{\gamma_{S}^{LW}\gamma_{L}^{LW}} + \sqrt{\gamma_{S}^{+}\gamma_{L}^{-}} + \sqrt{\gamma_{S}^{-}\gamma_{L}^{+}}\right) \qquad (16)$$

Thus by contact angle measurements using three different liquids (L), of which two must be polar, with known γ_{L}^{LW}, γ_{L}^{+}, and γ_{L}^{-} values, the γ_{S}^{LW}, γ_{S}^{+} and γ_{S}^{-} of any solid (S) can, in principle, be determined. The value of γ_{L} must be known or determined independently [108]. The apolar component of the surface tension of solids (γ_{S}^{LW}) can be determined by contact angle measurements using strictly apolar liquids for which $\gamma_{L} = \gamma_{L}^{LW}$. These surface tension components can be related to experimentally determined pull-off forces between chemically modified AFM tips and an oxyfluorinated isotactic polypropylene surface in CFM approaches [110]. It was observed that the pull-off force measured with carboxylic acid tips in ethanol depended linearly on the basic term of the surface tension (γ_{i}^{-}) on the modified polymer surface.

3.3
Contact Angle Hysteresis

The most commonly used method for the determination of surface tension of polymers is the sessile drop technique. A droplet of a purified liquid is placed on a surface using a syringe. The angle formed by adding liquid to the

droplet, causing it to advance over the surface is termed the advancing contact angle. The angle formed by removing liquid from the droplet, causing it to recede over the surface, is termed the receding contact angle. The difference between the advancing and the receding contact angles is referred to as the contact angle hysteresis. Its value depends on the surface roughness and the surface heterogeneity [98]. Generally, the influence of the surface roughness on contact angle hysteresis is insignificant if the asperities are $< 0.5\,\mu m$ or if heterogeneous phases present with characteristic dimensions in the range of $< 0.15\,\mu m$ [98]. Cosines of equilibrium contact angles $(\cos\theta)$ of liquids on heterogeneous surfaces with well-defined surface regions obey the Cassie equation which predicts a linear dependence on the surface composition, as mentioned previously (Eq. 5) [32].

Agreement with the Cassie equation has been obtained for contact angle measurements on surfaces micropatterned using $-CH_3$ and $-COOH$ groups [111]. Johnson and Dettre performed a theoretical analysis of a two-region surface consisting of circular, low $(\theta_1 = 120°)$ and high $(\theta_2 = 0°)$ surface energy regions, ranging between 100 to $25\,\mu m$ in diameter [112]. They found that the advancing angles were associated with the low-surface-energy regions, whereas the receding angles were associated with the high-surface-energy regions. Furthermore, the contact angle hysteresis was found to increase with decreasing diameter of the phases. They concluded that both the advancing and receding angles must be measured to obtain reliable data describing surface heterogeneities [112]. Other phenomena that may cause a contact angle hysteresis on polymer surfaces include the dynamic nature of the polymer network (reorientation of functional groups) [53, 104] or swelling and liquid penetration by the probing liquid [18]. Critical measurements of the contact angle hysteresis and its time dependence offer a valuable help to understand the nature of polymer surfaces, especially in combination with other surface sensitive techniques [104].

4
Techniques to Measure Ensemble Average Distributions

4.1
Surface Forces

The chemical nature of surfaces determines most of their characteristics such as surface tension and adhesion. In the previous Section we discussed the basic definitions and experimental techniques for studies of surface tension in polymer systems. We have seen that the outmost atomic layers with a characteristic action radius determine the magnitude of the various components of the different types of interactions, which contribute to the excess free energy

of surfaces. A typical atom in the bulk is surrounded by its neighbors and experiences forces in all directions due to interatomic (chemically specific) interactions. The resulting interatomic force fluctuates in equilibrium (without additional external forces) around a zero value. In contrast, if atoms (or other specii) are at the geometrical surface of the body under consideration, they are only interacting by the atoms below or beside them (disregarding the gas and vapor molecules present above the surface). The net resulting force is pointing towards the interior and its value depends on pair- and multiatomic forces within an action radius. Whereas the first neighbors make the strongest contributions, there are non-zero force contributions also from the second, third, etc. coordination spheres below the particular surface atom being considered. These make an effective contribution to surface forces (hence to surface tension) up to a characteristic distance of a few atomic (molecular) layers. Thus macroscopic surface tension techniques result in values averaged over a characteristic action radius with a typical value in the range of up to a few nanometers. In addition, for multicomponent systems (with different atoms and molecules) all the different pairs of the mixed type interactions contribute to macroscopic surface tension. Hence these techniques average over chemical composition, as well as the characteristic action radius of the corresponding surface forces.

Differences in surface tension (surface free energy) and in adhesion for different substances are a result of different interatomic (intermolecular) forces. These (surface) forces are also responsible for the work required when two contacting bodies are separated from contact to infinite distance. Although the physical origin of all relevant intermolecular forces from a physical chemistry point of view stems from electromagnetic interactions, it is customary to group these in categories based on characteristic phenomena which dominate the essential physical behavior. Thus one speaks of ionic (monopole), dipole-dipole, ion-dipole interactions, induced dipolar forces, van der Waals (London dispersive) interactions, hydrophobic and hydrophilic, solvation, structural, and hydration forces, steric and fluctuation forces, etc. The reader finds an in-depth description and review of all these interactions in the book of Israelachvili [113]. Disregarding London dispersive forces, in cases when forces between a pair of complementary specii depend on the choice and the nature of these, one speaks of specific (molecule-specific) interactions. For example, strong dipole-dipole interactions occur when a hydrogen atom bonded to an electronegative atom in a given molecule interacts with the lone electron pair of a nearby electronegative atom, bonded in another molecule. The complementarity here is obvious such as in ligand-receptor (key-lock), or antibody-antigen type interactions for entirely specific pairs that bind together in biological molecules (e.g. for biotin and avidin, with an interaction energy of 35 kT which is one of the highest known for ligand-receptor systems) [113]. It should be mentioned that for H-bonded and some other

ligand-receptor pairs the term specificity does not always mean exclusivity for the choice of a given pair (no obvious need for a geometrical fit).

For polymer surface properties controlled by the chemical composition, thermodynamic (equilibrium), non-equilibrium, and technical terms and definitions play an important role. These are not always used in a consistent way, hence a short recapitulation seems appropriate. The thermodynamic work of adhesion (W_A) is defined as the reversible work (the free energy change) required to separate two phases with unit area of contact, from contact to infinity. The corresponding work of adhesion (and cohesion for similar bodies) can be easily expressed with surface tension values. In general, for surfaces of two intimately contacting solids ("1"and "2", respectively) each with a unit area, are separated in a medium ("3"), a work W_{132} is required which can be expressed as:

$$W_{132} = W_{12} + W_{33} - W_{13} - W_{23} \tag{17}$$

This equation is easy to understand as one new 1–3 and one new 2–3 unit surface areas are created at the expense of breaking up the unit area 1–2 contact and expanding the fluid by two unit areas to cover both sides of the originally contacting bodies. This expression is valid for processes that occur through quasi-equilibrium steps, i.e. when energy dissipation (e.g. due to surface or interface molecular relaxation and other processes) is negligible. This is, however, often not the case, i.e. net rearrangements of surface-proximity atoms, groups of atoms or molecules accompany approach or withdrawal. In addition, stored elastic energy (due to molecular stress fields) will also relax and gets dissipated by internal atomic and molecular scale friction. These dissipative processes, i.e. surface molecular rearrangements and internal stress relaxation give rise to differences in adhesion for outbound and inbound movement cycles and result in hysteretic behavior. Further contributions to dissipative processes can originate in surface topology (e.g. roughness) effects. Adherence is experimentally easier to access (as opposed to adhesion) and is used to describe the energy required to separate the two contacting surfaces during a mechanical test. The value of adherence (which can be determined by specific experimental techniques) is usually greater that the (presumed) value of adhesion e.g. due to contributions by viscoelastic dissipation, plastic deformation and other forms of dissipated energy [114].

The basic concept in chemical force microscopy is to scan forces of adherence, from pixel to pixel in AFM experiments with chemically specific contrast. As force in general is a vectorial quantity, for a full characterization its magnitude and direction are both needed. However, in AFM instead of fully measuring both, the lateral and the normal components are separately recorded. Here we assume the usual measurement geometry i.e. the sample surface being horizontal, and the AFM tip mounted above the specimen (with a cantilever long axis making a shallow angle with the sample surface). The magnitude of the lateral component, i.e. the friction force, de-

pends on the normal load. The normal (vertical) component is the sum of the vertical (pre-set) load (which can be positive upon pushing the tip into the sample, or negative, upon pulling the tip away from the surface) and the normal component of the surface (adhesion) and elastic (deformation) forces, respectively. As discussed in section 5, during a tip-sample approach cycle at snap-on the tip jumps in contact as the gradient of attractive forces overcomes the cantilever spring constant and the magnitude of the net at-tractive normal forces (including the elastic bending force of the cantilever) becomes negative at a characteristic tip-sample distance. The opposite hap-pens at withdrawal when at increasing piezo displacement (thus increasing bending of the cantilever-spring and increasing negative normal force) the tip jumps out of contact. This pull-off happens when the cantilever spring constant overcomes the gradient of attractive forces and the total force on the tip (surface, adhesion, and tip-elastic contributions) crosses zero and becomes positive. At this point the tip jumps out of contact. The magni-tude of the snap-on (pull-on) and pull-off forces are usually different as the sample-cantilever tip mechanical system is bistable and exhibits an inherent hysteresis loop. This hysteresis and the basics of lever mechanics, lever-tip sample contact and non-contact interactions are nicely described by Sarid in one of the first reference books on AFM [5]. It should be mentioned that the lever hysteresis and the adhesion hysteresis have different origins; i.e. lever hysteresis can be present for ideal, non-dissipative sample-tip systems, as well.

For imaging with chemical sensitivity (either based on adhesion, or on friction force contrast arising from chemical composition differences) it is relevant to understand the physical origins of the pull-off forces. Naturally, during an AFM force-distance cycle, a contact between tip and sample (in general, within a medium, e.g. in a fluid cell) is first established during ap-proach and then broken during withdrawal. The radius of the contact areas between AFM tip and sample are small (typically in the range of tip radii of several tens of nanometers for imaging i.e. low normal force conditions). It is of interest to consider theories of (continuum) contact mechanics as start-ing point which quantitatively describe the pull-on and pull-off forces and related work of adhesion. It is also of interest to consider whether the corres-ponding macroscopic contact mechanics theories break down at the level of only a few contacting (effectively interacting) pairs of atoms (or molecules) in AFM. Another reason for discussing adhesion is due to interrelations between friction and adhesion. In friction force microscopy (sometimes referred to as Lateral Force Microscopy) forces of friction (lateral forces) are measured by detecting the torsion of AFM cantilevers. Intuitively, one anticipates correla-tions between adhesion and friction as surface forces are being broken (and formed) during both processes. Related studies e.g. by the surface forces ap-paratus (SFA) [115, 116] showed that the static friction force to start a sliding motion is related to the thermodynamic work of adhesion. However, kinetic

friction also depends on the irreversible component (i.e. energy dissipation) of the adhesion work. Hence, adhesion hysteresis (which can be measured e.g. in contact mechanics cycles) yields information about kinetic friction.

We summarize below the most relevant results of contact mechanics theories due to their relevance for AFM adhesion (and thus chemical mapping) research.

4.2
Adhesion Force and Work of Adhesion between Solids

The physical foundation of any treatment dealing with adhesion and friction forces is the knowledge of interatomic (intermolecular) potentials. If the pairwise (two-body) potential between two specii is described by a potential $V(r)$ as a function of the distance, r, between the particles, the force $F(r)$ and the potential are related through simple differential (integral) equations:

$$- F(r) = \frac{dV(r)}{dr} \tag{18}$$

$$V(r) = - \int_{r}^{\infty} F\left(r'\right) dr' = \int_{\infty}^{r} F\left(r'\right) dr' \tag{19}$$

The potential energy for a pair of atoms at a separation distance of r can be obtained as the integral (area) under the force-distance curve between infinity and the distance r (see Fig. 3).

The pairwise potential energy $V(r)$ between two non-bonded intermolecular pairs (strictly speaking atoms) as a function of intermolecular separation, r, can be obtained by summing repulsive and attractive potentials which are often approximated by the "6–12" Lennard–Jones potential:

$$V(r) = 4\varepsilon \left[\left(\frac{\sigma}{r}\right)^{12} - \left(\frac{\sigma}{r}\right)^{6} \right] \tag{20}$$

where σ is the equilibrium intermolecular separation and ε is the depth of the potential well at equilibrium separation (see Fig. 3).

The values of the power exponents can differ from "6–12" for various cases (see reference [113]); for example for H-bonded systems a "12–10" potential gives a better description. Various other functional forms are used to describe the pairwise potential energy, for details the reader is referred to the literature.

For van der Waals potentials the values of the two parameters, i.e. σ and ε, must be known. If the concrete forms of the interatomic potential functions (including all different types of London dispersion, dipole, induced dipole, etc. forces) are known, the usual treatment of calculating net forces between objects includes a "pairwise" summation of the interaction forces between atoms (molecules). Here we neglect multibody interactions, which can be
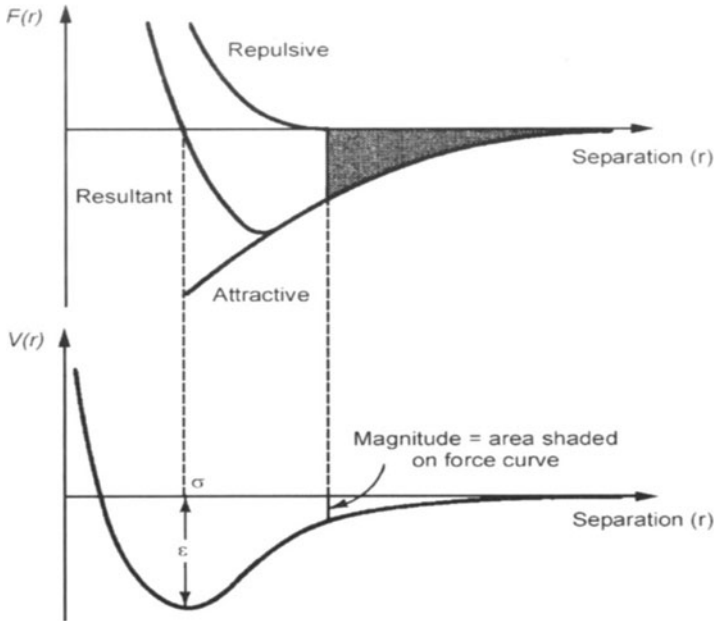
Fig. 3 Potential energy $V(r)$ and force $F(r)$ for two interacting atoms ("point-like" molecules) as a function of separation distance r

considered, e.g. by Green-function formalisms. Additivity is assumed during calculations of pairwise interactions and retardation effects for interactions are usually neglected. In addition to the knowledge of the two-body interaction potential energy functions, the exact geometry of the interacting bodies (e.g. sphere and a semi-infinite planar object) must also be known. The corresponding so-called Hamaker summation method [113, 117] is well described in texts and references and also in AFM-related references [5]. Regarding the interaction energy $W(d)$ of a sphere with a semi-infinite planar object made of two different types of materials (i.e. having the number density of atoms "ϱ_1" and "ϱ_2", respectively), it has the following form as a function of gap distance "d" between the sphere and the flat:

$$W(d) = -\frac{AR}{6d} \tag{21}$$

where R is the radius of the sphere and "A" is the Hamaker constant defined as:

$$A = \pi^2 C \varrho_1 \varrho_2 \tag{22}$$

keeping only the attractive part of the van der Waals potential $w(r) = -C/r^6$ ($C = 4\varepsilon\sigma$) between the corresponding pairs of atoms of the sphere and the semi-infinite flat, respectively. In Figs. 4 and 5 we depict typical examples of
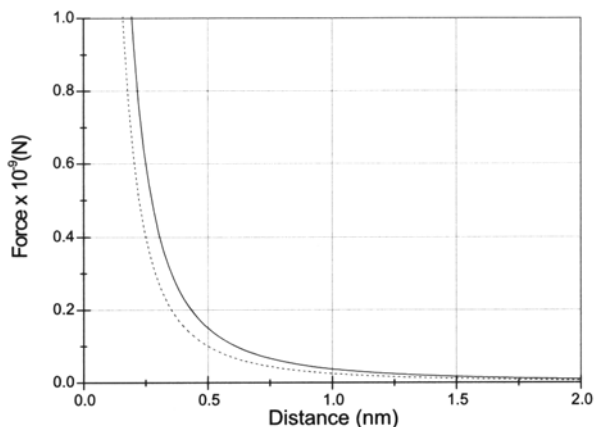
Fig. 4 Intermolecular forces vs. distance between a sphere (with a radius of 50 nm) and flat surfaces. *Solid curve*: both sphere and planar surface are terminated by hydrocarbon groups across water as a medium, with a Hamaker constant of 4.5×10^{-21} J ([113], pg 189). *Dashed curve*: both sphere and planar surface are modified with bilayer surfaces composed of the uncharged sugar-headgroup lipid, monogalactosyl diglyceride in 0.15 M NaCl, with a Hamaker constant of 3.5×10^{-21} J ([113], pg 396) (source: Zou S., private communication)
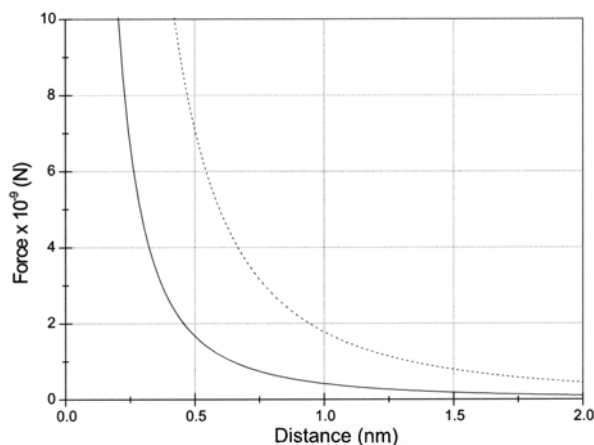
Fig. 5 Intermolecular forces vs. distance between a sphere (with a radius of 50 nm) and flat surfaces. *Solid curve*: both sphere and planar surface are terminated by hydrocarbon groups across vacuum as a medium, with a Hamaker constant of 0.5×10^{-19} J ([113], p 178). *Dashed curve*: silicon nitride/silicon scenario, with a Hamaker constant of 2.13×10^{-19} J [118] (source: Zou S., private communication)

the van der Waals forces for different surfaces as a function of separation distance in different media.

Interactions between atoms and molecules are usually described by potential energies as a function of separation distance as the directly measured

quantities are usually of thermodynamic nature. In force microscopy the negative differential of the potential energy function, i.e. force-distance – is measured, hence we should now relate force and potential. For two general curved surfaces with radii of curvature R_1 and R_2 the force $F(D)$ as a function of distance of separation, D, is related to the energy per unit area of two planar surfaces at the same separation (Derjaguin approximation, Israelachvili) [113]:

$$F(D) \approx 2\pi \left(\frac{R_1 R_2}{R_1 + R_2} \right) W(D) \qquad (23)$$

The most useful consequence of the Derjaguin approximation is that it allows one to obtain a force law (by considering local curvatures of any curved surface) for any given geometry of two interacting bodies. If the work of adhesion between two bodies (in a third medium) is given by W_{132} then the adhesion force between two infinitely stiff (non-deformable) spheres of respective radii of curvature R_1 and R_2 of the given materials has the following form:

$$F = 2\pi \left(\frac{R_1 R_2}{R_1 + R_2} \right) W_{132} \qquad (24)$$

Upon approach (or withdrawal) of objects surface forces can be determined (surface forces apparatus, AFM). To estimate forces for a typical AFM experiment, let us consider a sphere with a radius of 1 μm (replacing an AFM probe) at a distance of 1 nm from a surface. A characteristic value of the constant $C = 4\sigma\varepsilon = 5 \times 10^{-78}$ Jm^6 with $\varrho_1 = \varrho_2 = 3 \times 10^{28}$ m^{-3}. In this case a Hamaker constant $A = 1 \times 10^{-19}$ J was used and the corresponding force obtained had a value of 1.6×10^{-8} N (16 nN). In reality, the tip radii of AFM probes are much smaller (on the order of 10–20 nm) and the tip-sample distance varies depending on AFM operating conditions. Typical values of contact forces (at pull-off) in characteristic AFM experiments are in the range of 10 pN–10 nN.

Infinitely stiff spheres do not deform when brought in contact and pressed together. Hence the contact between them is a point contact. If the Young's modulus of the contacting spheres is finite, then the contact point becomes a contact circle with a radius "a". The value of the contact radius "a" depends in such cases on the elastic properties of the spheres, on the Young's moduli E_1 and E_2, and on the Poisson's ratios v_1 and v_2, of the two contacting materials, respectively. The value of the contact radius "a" can be calculated from the following formula:

$$a^3 = \frac{3}{4} \left(\frac{1 - v_1^2}{E_1} + \frac{1 - v_2^2}{E_2} \right) \frac{R_1 R_2}{R_1 + R_2} L \qquad (25)$$

with the load L pressing the two spheres together. For this simplest case no surface forces were assumed, and the "flattening out" of the contact area from a geometrical point to a circle is fully due to elastic deformation under

load. The corresponding expressions were derived by Hertz, hence the name
"Hertzian contact". Naturally, if one of the surfaces (say R_1) is planar, then
$R_1 = \infty$ and $R_2 = R$; or if one of the surfaces is rigid $E_1 = \infty$ and $E_2 = E$. If
the contacting sphere is rigid (stiff AFM tip pressing against an elastic, planar
surface) then the contact radius is written:

$$a^3 = \frac{3}{4}\left(1 - v^2\right)\frac{RL}{E} \tag{26}$$

However, when surface (adhesive) forces are present, the shape of the con-
tacting spheres in the vicinity of the rim of the contact area will further be
deformed. Due to van der Waals attraction, this additional deformation of the
elastic body will pull the two contacting objects closer together and hence
further increases the contact radius with regard to the Hertzian value.

It was Johnson, Kendall and Roberts (JKR) who described the area of con-
tact of two spheres including surface energy under the combined external
load and the load of adhesion forces [119]. Figure 6 shows the contacting
geometry for an infinitely stiff (rigid) surface and an elastic sphere for the
Hertzian (dashed line) and JKR (solid line) contacts, respectively. Near the
contact the vertical arrows at the dashed contour represent the surface forces
which cause an additional deformation of the elastic sphere thus increasing
the contact radius from a_H (Hertz) to a_{JKR} (JKR). The contact radius for the
JKR model is a function of the external load, the work of adhesion, the radius

(a)   (b)

Hertzian elastic contact   JKR adhesive contact
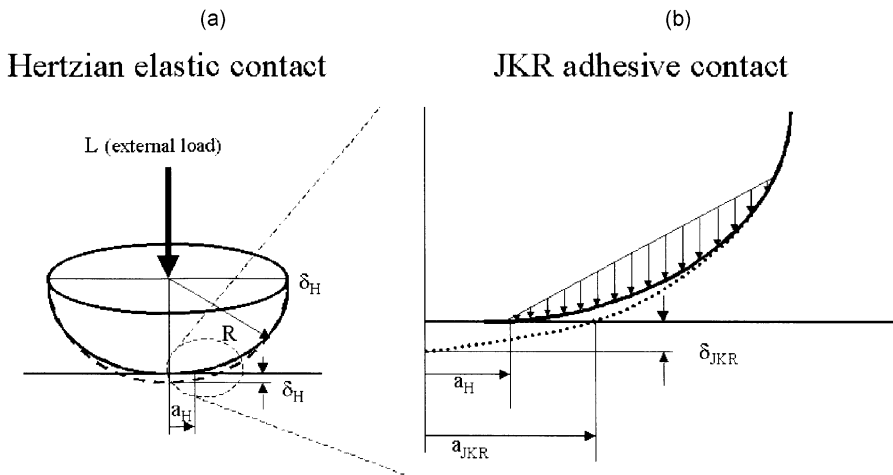
Fig. 6 Comparison of elastic Hertzian contact (*left*) and adhesive JKR contact (*right*).
(**a**) Hertzian contact: *Dashed line* (sphere): shape of contacting spherical lens prior to
pressing to the flat by force L. Hertzian contact profile shown by *solid line*, with radius
under external load $L : a_H$; (**b**) JKR contact: Schematic of adhesion force (adhesive "zone"
model, forces schematically indicated by vectors) further deforming a spherical lens from
Hertzian contact (*solid line*) to JKR contact (*dotted line*) with radius a_{JKR}

of the contacting sphere (or if two different spheres are contacting, the reduced radii) and the elastic constant K (a combination of the Young's moduli and the Poisson's ratios of the contacting materials), defined as:

$$\frac{1}{K} = \frac{3}{4}\left(\frac{1 - \nu_1^2}{E_1} + \frac{1 - \nu_2^2}{E_2}\right) \tag{27}$$

written as:

$$a_{JKR}^3 = \frac{R}{K}\left[L + 3\pi W_{123}R + \left(6\pi W_{123}RL + \left(3W_{123}\pi R\right)^2\right)^{\frac{1}{2}}\right] \tag{28}$$

The value of a_{JKR}^3 can only become zero (at rupture of contact) if the normal force is negative, i.e. if the contacting sphere is pulled up (away from the flat). If this is the case, a physical solution can only exist if

$$6\pi W_{132}RL \leq \left(3W_{132}\pi R\right)^2 \tag{29}$$

When the contacting sphere is about to "jump off", the force that is necessary to separate the sphere from the flat plane, L_{pf}, is written as

$$L_{pf} = -\frac{3}{2}\left(W_{132}\pi R\right) \tag{30}$$

For the Hertzian contact no force is needed to pull away the contacting sphere from the flat plane in excess of the weight of the sphere. However, for the JKR contact, due to adhesion forces, this does not hold. The value of the non-zero pull-off force represents the adhesion of the contacting sphere with the flat. Strictly speaking, this force corresponds to adherence of the surfaces as energy dissipation, surface relaxation, etc. also influence its value. It should be stressed, that the value of the JKR *pull-off force* only depends on the sphere (lens) radius and the work of adhesion (adherence) in the medium in which the JKR experiment is conducted. Thus the contact area and mechanical properties do not play a role for its value.[3]

All the above considerations for contact mechanics were based on pairwise additivity of molecular forces. The role of the medium in which contacting and pull-off is performed, has not been discussed so far. However, the surroundings obviously influence surface forces e.g. via effective polarizability effects (essentially multi $\nu > 0$-body interactions e.g. by the presence of a third atom and its influence via instantaneous polarizability effects). These

---

[3] Several other contact mechanics theories have been put forward, which are not described in detail in this contribution. The most important ones of these theories for AFM applications include the Derjaguin-Muller-Toporov (DMT), the Burnham-Colton-Pollock (BCP) and the Maguis mechanics, see in 15,16. These theories differ in the assumptions (and limitations) and yield different expressions for the pull-off force. For example, the DMT theory, which assumes that long-range surface forces act only outside the contact area (as opposed to JKR, where adhesion forces only inside the contact area are assumed), predicts a pull-off force of $2\pi RW$; compare with the JKR expression of Eq. 30.

effects can become noticeable in condensed media (liquids) when the pair-wise additivity of forces can essentially break down. One solution to this problem is given by the quantum field theory of Lifshitz [120], which has been simplified by Israelachvili [113]. The interaction is expressed by the (frequency-dependent) dielectric constants and refractive indices of the contacting macroscopic bodies (labeled by 1 and 2) and the medium (labeled by 3). The value of the Hamaker constant A_{total} is considered as the sum of a term at zero frequency ($\nu = 0$, dipole-dipole and dipole-induced dipole forces) and London dispersion forces (at positive frequencies, $\nu > 0$).

$$A_{\text{total}} = A_{\nu=0} + A_{\nu>0} \approx \frac{3}{4}kT \left(\frac{\varepsilon_1 - \varepsilon_3}{\varepsilon_1 + \varepsilon_3} \right) \left(\frac{\varepsilon_2 - \varepsilon_3}{\varepsilon_2 + \varepsilon_3} \right)$$

$$+ \frac{3h\nu_e}{8\sqrt{2}} \frac{\left(n_1^2 - n_3^2 \right) \left(n_2^2 - n_3^2 \right)}{\left(n_1^2 + n_3^2 \right)^{0.5} \left(n_2^2 + n_3^2 \right)^{0.5} \left[\left(n_1^2 + n_3^2 \right)^{0.5} + \left(n_2^2 + n_3^2 \right)^{0.5} \right]} \quad (31)$$

Here ν_e is the main electronic absorption frequency in the UV, typically around 3×10^{15} s^{-1} [113]. An analysis of the above equation shows some interesting consequences. A close match between the dielectric constants of the interacting bodies leads to diminishing values of the first term. The second term (determined by the refractive index values) shall then play the dominant role in the surface forces in this case. This effect can be utilized in "force spectroscopy" to maximize pull-off forces. On the other hand, interaction forces can also be minimized by a proper choice of the medium. Both these aspects will be important later for AFM-based force spectroscopy.

5
Atomic Force Microscopy with Chemically Functionalized Tips ("Chemical Force Microscopy", CFM)

As mentioned in the introduction, chemical force microscopy (CFM)[4] is an AFM-based technique, which allows one to determine and map the distribution of chemically distinct functional groups. Owing to the small tip-sample contact area, this mapping can be performed down to the sub-50 nm level [17]. The technique is based on the controlled chemical modification/functionalization of AFM probe tips in order to control the interaction between tip and the sample surface. Depending on the exposed functional groups and the medium, attractive or repulsive van der Waals forces, forces between dipoles, H-bonding, and electrostatic repulsion, among other forces,

---

[4] Chemical force microscopy (CFM) is used as a synonym for "AFM using defined surface chemistry, for instance self-assembled monolayer functionalization, on AFM probe tips in order to measure differences in surface chemical composition" (using friction or adhesion differences related to interactions between functional groups or atoms exposed on both tip and sample surface as contrast) throughout this review article.

may occur (see Sect. 4). The chemical contrast necessary for "imaging" is achieved by exploiting the spatial or temporal variations of these forces in quantitative measurements of the pull-off and/or friction forces between the tip and selected areas on the surface of interest. This approach is in particular promising for high resolution studies of functional group distributions in surface-treated polymers [57, 58, 110, 121–138].

5.1
The Case of Chemically Sensitive Imaging of Surfaces by Atomic Force Microscopy

5.1.1
Atomic Force Microscopy

Atomic force microscopy has developed into a mature technique for quantitative topography imaging of solid materials, including polymers. In the basic mode, called contact mode AFM, a very sharp probe tip, which is attached to a cantilever (typical spring constant of 1.0–0.1 N/m), is scanned across the sample surface (Fig. 7). The accurate positioning of the tip or, as shown in Fig. 7, the sample under a stationary tip, is achieved by piezo actuators. While the tip is scanned over the sample surface, the deflection of the cantilever is measured using a position-sensitive photodiode. A feedback loop holds a preset cantilever deflection constant by adjusting the piezo extension ("constant force mode"). A graphic representation of the adjustment of the piezo actuator's vertical extension as a function of lateral position yields the sample
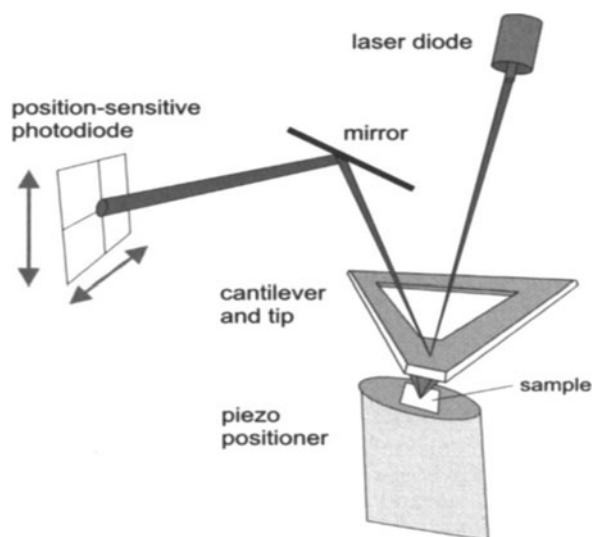
Fig. 7 Schematic diagram of contact mode AFM. (Adapted with permission from [143])
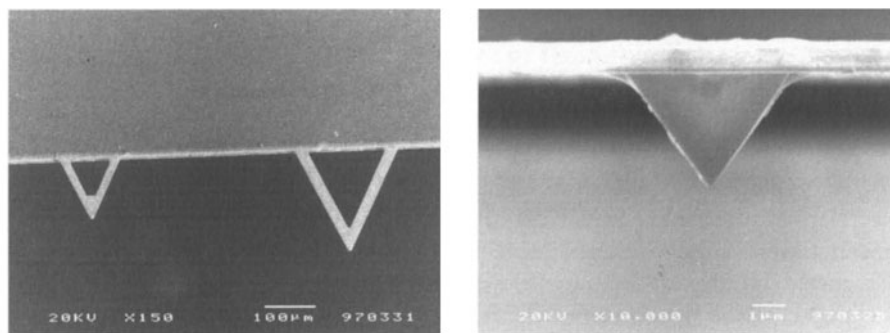
Fig. 8 SEM image of contact mode AFM cantilevers (*left*) and tip (*right*) (Reprinted with permission from [143])

topography (surface profile). The deflection of the cantilever is a result of the (repulsive and attractive) interactions between the atoms of the tip and the atoms of the sample surface, hence the name *force* microscopy. The nature of the various tip - sample interactions and their dependence on the tip - sample distance have been discussed in the literature [113, 116].

AFM tips, which are often made of silicon or silicon nitride, possess a radius of curvature at the apex between ca. 10 and (several) 100 nm nanometers. SEM images of two typical cantilevers and a tip are shown in Fig. 8. The tip radius, which ultimately limits the true lateral resolution [139], can also be determined based on high resolution SEM images or calibration gauges such as $SrTiO_3$ crystals [140]. AFM experiments are often performed in ambient conditions, however under these conditions a contamination layer (including water) gives rise to sometimes significant capillary forces [141]. AFM experiments can also be performed in other gases, in liquids, or in (high) vacuum. By performing measurements in liquids utilizing a liquid cell, the problem of capillary forces can be conveniently eliminated [142].

5.1.2
AFM-Based Force Measurements

Chemically sensitive imaging can be achieved in a general sense if a particular mode of AFM is sensitive to differences in a materials properties, which are then related to certain chemical functionalities exposed at or near the surface.

Differences in, for instance, modulus can give rise to excellent materials contrast in force modulation mode AFM or intermittent contact mode AFM phase imaging [144–146]. However, since this imaging contrast is not directly related to exposed functional groups and rather depends only on mechanical properties (including different indentation depths or energy dissipation), these and related approaches will not be considered here as chemically sensitive imaging [2, 147].

By contrast, normal forces and in some case lateral (friction) forces between the AFM probe tip and the sample surface are intimately related to exposed functional groups and will hence be treated in detail. CFM utilizes predictable and often specific interactions between functional groups in order to detect and identify functional groups with sub-100 nm resolution (see Sect. 5.1.3). The central idea of CFM is to control the interaction between tip and sample surface by chemically modifying the tip (Scheme 1). The interaction between such chemically modified tips and well-defined model surfaces composed of monolayers on gold, which expose different functional groups at the surface, was shown to depend on the nature of the interacting functional groups. These observations were consistently made in both pull-off force and friction measurements [17].

Pull-off force experiments and friction mode AFM with unmodified tips can be utilized to measure differences on chemically heterogeneous surfaces and have been shown to differentiate between chemically distinct phases in phase separated LB films, etc. However, the tip functionality cannot be varied and therefore, this approach is inherently limited [148].

In a standard contact mode AFM set up both repulsive and attractive forces between sample and surface can be measured with a high accuracy (force-displacement curves, force-distance curves, force spectroscopy). Examples include electrostatic forces, electrostatic double layer forces, hydrogen bonding, van der Waals interactions, and magnetic forces. The resolution limit for an optical detection system and typical commercial spring constants has been estimated to be in the order of 10^{-11} N [149]. Depending on the detection system, the force constant, the stiffness, and the resonance frequency of the cantilever even smaller forces are in principle measurable using designer cantilever-tip assemblies [150, 151].
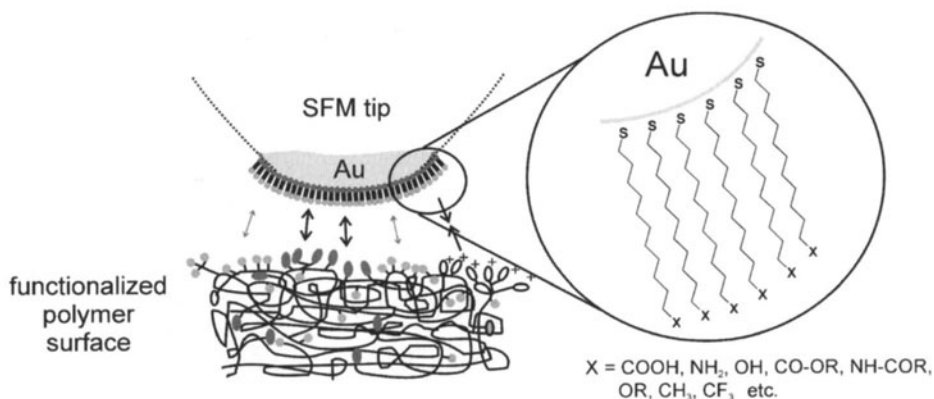
Scheme 1 Schematic drawing of monolayer-modified SFM tip used for CFM and interactions between exposed functional groups on the contacting surfaces (Adapted with permission from [143])

In a standard force displacement experiment the sample is moved up and down (in and out of contact with the tip) at a fixed position (x, y) [15, 152]. In Fig. 9, the corresponding movements of piezo (sample) and cantilever deflection, and the resulting force displacement curve are schematically depicted. The adhesion is characterized by the so-called pull-off or pull-out force (sudden jump of force when the tip breaks free from the surface). This force is related via the corresponding surface free energies to the functional groups exposed on the contacting surfaces and also the medium in which the experiment takes place (see below). A quantitative determination of forces requires a thorough calibration of the cantilever spring constant [15, 152–155].

A second viable option to perform chemically sensitive AFM imaging in a general sense is using the lateral force, or friction mode. This is based on the "semi-quantitative" relationship between adhesion (adherence, pull-off) and friction. In contact mode AFM, friction forces can be measured simultaneously with topography imaging in constant force mode. In order to maximize the sensitivity of friction force measurements the sample is scanned in an angle of 90° with respect to the long axis of the cantilever. The torsion of the cantilever around its long axis is measured with a 4-quadrant photodiode (for schematic see Fig. 7). A representative example for the corresponding output of the photodiode signal is shown in Fig. 10. The so-called friction loop displayed here allows one to calculate the friction force from the difference of the trace and retrace line multiplied by 0.5. In order to improve the statistics one typically acquires a complete scan simultaneously for both relative scan directions (trace and retrace) and calculates the mean friction forces from the corresponding difference image.
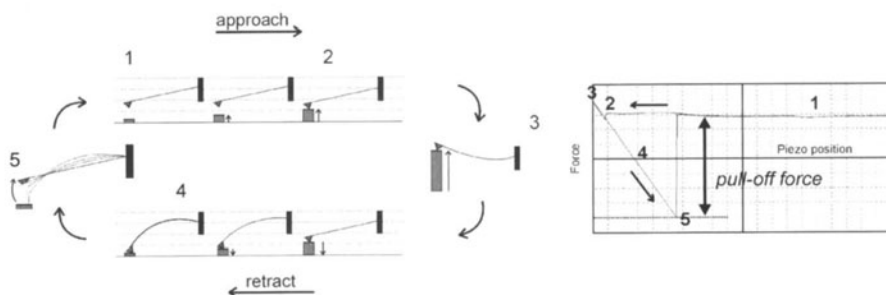
Fig. 9 Measurement of force distance curves (*left*); Schematic force-distance plot (*right*): The sample is approaching the tip (1, top); at some distance the gradient of the force overcomes the cantilever spring constant and the tip jumps into contact (2); further movement up causes a deflection of the cantilever (3); during retraction the tip "sticks" usually much longer to the surface (4) and snaps off when the spring constant overcomes the force gradient (5). The adhesion between tip and sample is characterized by the so-called pull-off or pull-out [156] force (snap off). (Adapted with permission from [143])
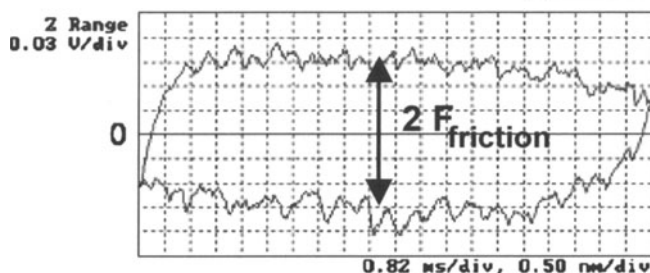
Fig. 10 Friction loop (friction force vs. scanned distance plot) measured perpendicular to the polymer chain direction of oriented polyethylene with a – CF_3 modified tip [131]. The photodiode output signal in Volts is directly proportional to the friction force (Reprinted with permission from [143])

Quantitative measurements of friction forces are complicated by the geometry in the case of triangular shaped cantilevers, variations of photodiode sensitivity, the dependence of the photodiode output signal on laser alignment and the difficulty of accurate calibration of the lateral force spring constant [157]. Furthermore, since the friction forces are related to energy dissipation, these forces may depend on factors other than the chemical nature and variation of the functional groups exposed. Examples include polymer specimens with orientational order on various length scales (molecular, lamellar) or monolayer systems, which possess differences in conformational order (see below).

In order to utilize pull-off forces obtained in force-displacement measurements, or friction forces in lateral force microscopy (LFM) measurements for chemically sensitive imaging, the relation of these forces and chemical functionality must be established. For pull-off forces, (continuum) contact mechanic theories, including the JKR theory, have yielded a satisfactory description of the experimental data [119]. For the idealized geometry of a sphere with radius R interacting with a flat planar surface, the JKR theory predicts that the contact area is a function of R, the moduli of the sphere and surface material (through the reduced modulus K, see Eq. 27), the surface energy per unit area W_{123} (Eq. 17) and load L (compare Eq. 28). The pull-off force thus derived (Eq. 30) depends only on the sphere radius and the surface energy per unit area/work of adhesion W_{12}, which may be expressed as a function of the surface free energies of the tip (γ_1), the sample γ_2, and the corresponding interfacial free energy γ_{12} (Eq. 32). If the experiment is carried out in a medium, the γ_i refer to the surface free energy for the surface i in contact with the corresponding medium.

$$W_{12} = \gamma_1 + \gamma_2 - \gamma_{12} \tag{32}$$

As mentioned, the central idea behind CFM is to exploit differences in long and short range forces via (a) the control of the tip chemical composition by assembly of a functionalized monolayer (see below), thus via control of the

surface free energy of the tip, and (b) via control of the medium.[5] By corre-
lating the forces obtained in force-displacement measurements with surface
energies based on these equations it is possible to discriminate between dif-
ferent materials and specimens of a given material with different surface en-
ergies. This approach can be combined with spatially resolved adhesion force
imaging by sequential pull-off force data acquisition. As an example for spa-
tially resolved adhesion data we show in Fig. 11 the spatially resolved friction
and force data measured on a solution-grown polyethylene (PE) lamella de-
posited on mica. The interaction between the Si_3N_4 tip and the hydrophobic
PE crystal is weaker than the interaction between the tip and the underlying
mica substrate. As this data were acquired in air, the contribution of capillary
forces must be considered as well. Typically, CFM measurements are carried
out in a liquid environment to eliminate these forces. The friction contrast in
the lateral force mode image shown on the left, however, is dominated by the
difference in friction force due to the different orientation of folds in different
fold sectors.

   The localization of different functional groups exposed at various polymer
surfaces is more challenging. For chemically complex polymer surfaces, such
as surface-treated polymers, the variation in chemical nature of the func-

---

[5] For a discussion of manipulation of the sum of van der Waals forces via an appropriate choice of
solvent, see [125].
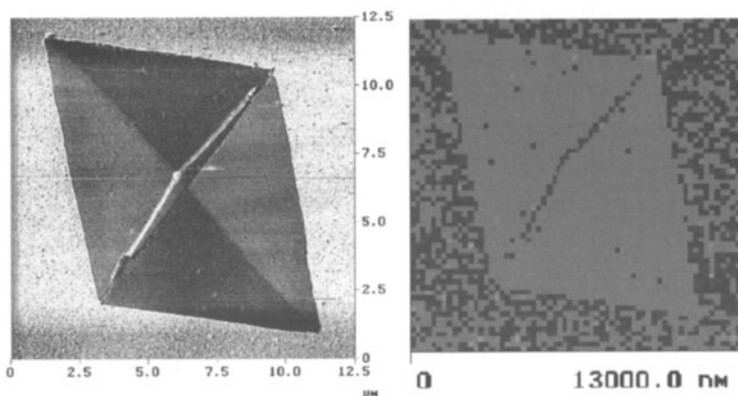
Fig. 11 Friction force micrograph of PE lamella on mica (*left*, friction forces increase
from dark to bright contrast) and laterally resolved adhesion forces (*right*, dark: − 80 nN,
bright: − 50 nN pull-off force) collected in the so-called force-volume (FV) mode (see
Sect. 5.2.2). Since the measurement was carried out in air, the forces are dominated by
capillary forces. The contrast in the friction force micrograph is related to the orientation
of the folds on the polymer lamella surface, which are oriented along the crystal edge in
each sector. (Reprinted with permission from [158]. Copyright 1999 American Chemical
Society)

tional groups exposed will result in many different interactions with the tip (Scheme 1). If these different interactions can be understood, the detection of chemically distinct species with high spatial resolution becomes feasible. The spatial resolution is limited by the range of the operating forces or by the sharpness of the probe tip. In a first approximation we can state the contact area at pull-off A_0 according to the JKR theory. For typical values we obtain an area of < 10–$100\,\text{nm}^2$, i.e. < 50–500 molecules of a monolayer (see below).

$$A_0 = \pi \left(\frac{3\pi R^2 W_{12}}{2K} \right)^{\frac{2}{3}} \tag{33}$$

5.1.3
AFM Probe Functionalization, Surface Imaging and Surface Chemistry

The standard AFM tip materials silicon (rather SiOx) and silicon nitride, as well as various metal and oxide coatings applied by evaporation or sputtering, can be used in conjunction with different liquid environments to vary the interaction between tip and surface in a controlled way. While these tip functionalities may be useful in CFM experiments, a much richer variety of tip functionalities is in many cases required, to allow for instance for (specific) hydrogen-bonding, hydrophobic or hydrophilic interactions. Thus, the need to control and deliberately vary the surface free energy of the tip (e.g. γ_1) can be met by procedures for controlled tip functionalization. Among the requirements for tip functionalization procedures are ease and reliability of preparation, chemical and mechanical robustness of the deposited layers, and a wide variety of functionality (different functional groups). These requirements are met by using self-assembled monolayers (SAMs). These are monomolecular layers, which are formed by spontaneous adsorption and organization at the solid-liquid or solid-gas interface. These layers are highly ordered, thus the alkane chains possess conformational order, the end groups that dominate the corresponding surface energy are exposed at the layer surfaces, and the anchoring headgroups are bound to the tip. The most popular procedures will be briefly explained.

The free hydroxyl groups exposed on standard AFM tip materials SiOx and silicon nitride can be directly functionalized using chloro- or ethoxy-substituted alkanesilane chemistry (Fig. 12 left). When proper reaction conditions are used, SAMs can be deposited onto the tip. These procedures are complicated by crosslinking reactions for the typically used trichloro- or triethoxysilanes, by variations in the number of silanol groups exposed on the tip surface, and details of the derivatization procedure.

A severe limitation is related to the limited number of functional groups, which can be introduced in the ω-position of the alkane substituent due to unwanted side reactions. An alternative approach relies on the forma-
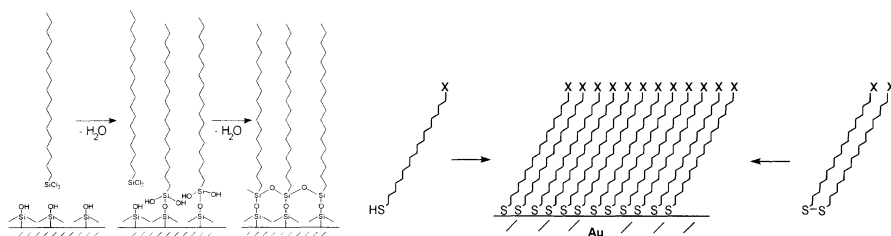
Fig. 12 *Left*: Schematic drawing of the idealized condensation reaction of trichlorosilanes on oxidized silicon, which leads to an internally cross linked SAM. *Right*: Schematic drawing of self-assembly of n-alkanethiols and disulfides on gold. Thiol and disulfide molecules which are functionalized in the ω-position, can be utilized leading to functionalized SAMs. (Reprinted with permission from [143])

tion of SAMs on noble metals, such as gold. AFM tips can be coated by a thin layer of Au (one to few nm of Cr or Ti is used as an adhesion promoting layer between Au and the tip), which is then simply immersed into a solution of a ω-functionalized alkanethiol or disulfide. After several hours of assembly the tip can be rinsed and dried, and is reliably functionalized. Many functional groups are compatible with this chemistry, thus $-CH_3$, $-CF_3$, $-CO-OCH_3$, $-CH_2-OCH_3$, $-CO-NH_2$, $-NH_2$, $-OH$, $-COOH$ and many other groups can be incorporated. The caveat of this procedure is the increase in mean tip size. The evaporated Au layers are granular (Fig. 13).

The SAMs used for tip modification, being versatile in terms of surface chemistry (exposed functional groups), homogenous, and practically defect-free, are ideal model systems for interfacial studies and thus served as model systems for the first CFM studies. In the histograms shown in Fig. 14 the differences in pull-off force between a $-COOH$ functionalized tip and two different pairs of surfaces is summarized. The mean pull-off forces calcu-
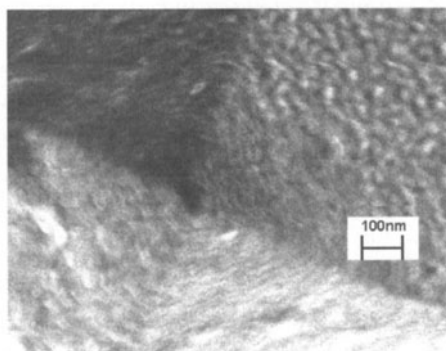
Fig. 13 High resolution SEM image of a gold/SAM coated AFM tip. (Reprinted with permission from [143])
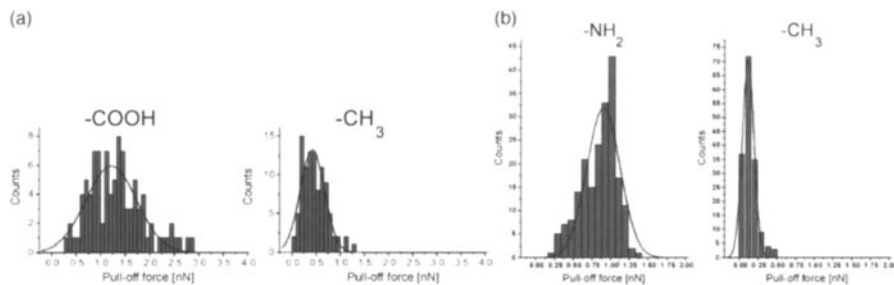
Fig. 14 (**a**) Histograms of pull-off forces measured with a – COOH tip on – COOH (*left*) and – CH₃ terminated SAMs (*right*) in ethanol (*curves*: Gaussian fits). The average pull-off forces are 1.21 ± 0.51 nN (– COOH) and 0.42 ± 0.25 nN (– CH₃); (**b**) Histograms of pull-off forces measured with a – COOH tip on – NH₂ (*left*) and – CH₃ terminated SAMs (*right*) in ethanol (*curves*: Gaussian fits). The average pull-off forces are 0.90 ± 0.22 nN (– NH₂) and 0.12 ± 0.08 nN (– CH₃) (Reprinted with permission from [57]. Copyright 2000 American Chemical Society)

lated from the histograms show that carboxyl groups and methyl groups, and amino groups and methyl groups, respectively, can be differentiated in force measurements in ethanol.

From the force histograms it is evident that areas in monolayer systems, which expose different chemically distinct functional groups, can be differentiated in pull-off force measurements. In Fig. 15, the first example of CFM force imaging published by the Lieber group is shown [17]. Here a patterned SAM exposing – CH₃ and – COOH groups was imaged (friction contrast) with a – CH₃ and a – COOH terminated tip in ethanol. The friction contrast shows in accordance with adhesion measurements that the interaction between carboxylic acid groups in ethanol is stronger than the mixed interaction between methyl and carboxyl groups.
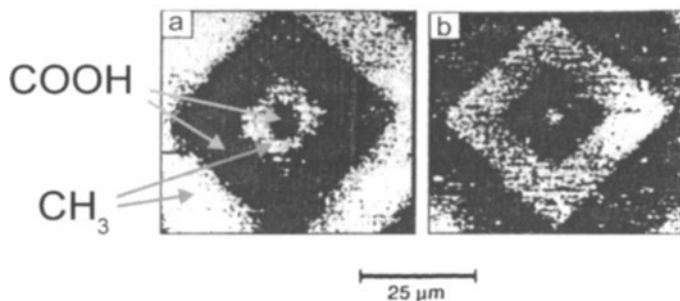
Fig. 15 Friction force image recorded on a patterned – CH₃/– COOH monolayer sample with (**a**) a – CH₃-terminated tip and (**b**) a – COOH-terminated tip in ethanol. The friction forces, which increase from dark to bright contrast, show a contrast reversal. (Adapted/reprinted with permission from [17]. Copyright 1994 AAAS)
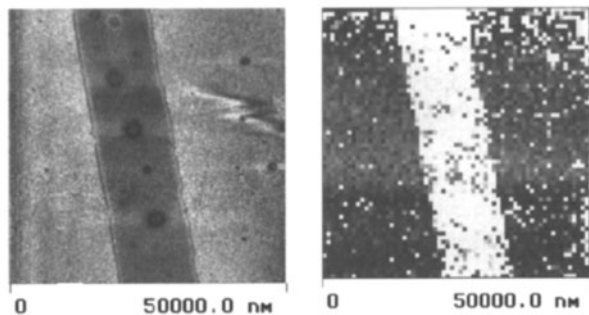
Fig. 16 AFM friction force micrograph (*left*, $z = 0.2$ V) and FV (see Sect. 5.2.2) force image (*right*, $z = -20$ nN) measured with a $-CH_3$ modified tip on patterned SAM exposing a hydrophilic $-OH$ stripe in a hydrophobic cholesterol-terminated matrix in water. In the FV image darker color corresponds to higher pull-off forces. (Reprinted with permission from [163]. Copyright 1999 American Chemical Society)

Rapidly after the first report, a number of groups have reproduced the original contact mode results and complemented the observations and the results of the Lieber group [57, 58, 110, 125–132, 134, 135, 137, 138]. One of the spectacular results is the chiral recognition reported by McKendry et al. [134] A very closely related field is the so-called single molecule force spectroscopy [121, 159, 160]. Here AFM tips are functionalized e.g. with ligand molecules. Specific interactions with surface-immobilized receptors are measured. Examples include exclusively relatively large molecules, often with biological relevance, such as DNA, cell adhesion molecules, or streptavidin [121, 159]. This method can also be extended to measure individual supramolecular host-guest interactions of small molecules, which possess fast unbinding kinetics [121, 161, 162].

A second example for CFM imaging is shown in Fig. 16. Here a hydrophobic $-CH_3$ terminated tip is used to differentiate between hydrophilic and hydrophobic regions in a microcontact printed SAM in friction and adhesion (pull-off) force measurements in water [163].

In addition to chemically sensitive imaging, the control of tip-sample interactions by means of tip functionalization has been exploited by various authors to improve the imaging forces and thus force contrast [164–166].

We can summarize at this point that the forces measured in AFM adherence force (and frequently friction) measurements depend crucially on the chemistry of the AFM tip and the surface of interest, as well as the medium in which the contact takes place. Hence by systematic variation of the tip chemistry via chemical modification/functionalization and of the medium chemical contrast spatially resolved chemical imaging becomes possible.

5.2
CFM on Polymers – Friction and Pull-Off Force Imaging/Mapping

Reports on CFM-based imaging by force mapping of well-defined model surfaces, mainly composed of SAMs, are abundant in the literature. By contrast, there are much fewer reports on the application of CFM imaging on polymers. Expanding on the basic features of the friction force and pull-off force data acquisition, the simplified interpretation based on continuum contact mechanics, and the discussion of various examples of CFM data based on force-displacement (f-d) curves and pull-off forces discussed above, we will shift our focus here to the spatially resolved acquisition of force and friction data on polymers. Since the "tip functionality" of any tip material can very well be defined and may offer the basic requirement of CFM regarding chemical contrast, we will also treat some results obtained with "unmodified" tips.

5.2.1
Friction Force Imaging

CFM friction imaging using modified AFM tips is, as far as the imaging technique and data acquisition are concerned, the same as conventional friction force or lateral force imaging in contact mode AFM. In order to maximize sensitivity, the relative scanning direction of the tip with respect to the sample is carried out such that the scanning direction is perpendicular to the long axis of the cantilever (compare Fig. 7). The image contrast, correctly derived from a difference image of retrace subtracted from trace divided by 2, can be predicted in the case that adhesive interactions are dominant. The magnitude of the friction force is proportional to the contact area A, which can be calculated as a function of work of adhesion following e.g. Equation 28. Based on this equation, a local increase in work of adhesion leads to an increase in magnitude of the measured friction force.

One early example described by Sinniah et al. [138] shows that AFM tips functionalized with various alkanethiols can be utilized to differentiate polyamide-rich regions from poly(ethylene glycol)-rich regions in a blocky segmented copolymer in water (Fig. 17). In this particular case, the friction forces observed with the more hydrophobic methoxy-terminated tips on the polyamide-rich domains exceed the forces measured on the PEG-rich domains. Using amide-terminated tips, the contrast is significantly reduced, which implies imaging with predictable contrast.

A similarly clear and predictable contrast has been reported by Feldman et al. for a phase separated blend of polystyrene (PS) and poly(methyl methacrylate) (PMMA) imaged with gold-coated and silicon oxide coated tips in perfluorodecalin (Fig. 18) [125]. Here the contrast is dominated by the dispersive van der Waals interactions, which have been selectively amplified by
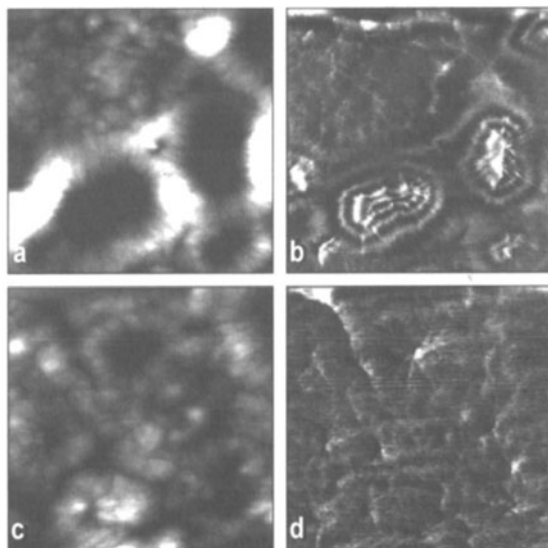
Fig. 17 Solvent-exclusion contribution to image contrast is demonstrated with scanning force data acquired on a co-block-polyethylene glycolpolyamide (Nylon-12) surface (PEBAX 1074), prepared by melting/resolidification. (**a**) Topographic image in water, methoxy tip termination (15 μm × 15 μm); (**b**) friction image in water, methoxy tip termination (15 μm × 15 μm); (**c**) topographic image in water, amide tip termination (7.5 μm × 7.5 μm); (**d**) friction image in water, amide tip termination (7.5 μm × 7.5 μm). (Reprinted with permission from [138]. Copyright 1996 American Chemical Society)
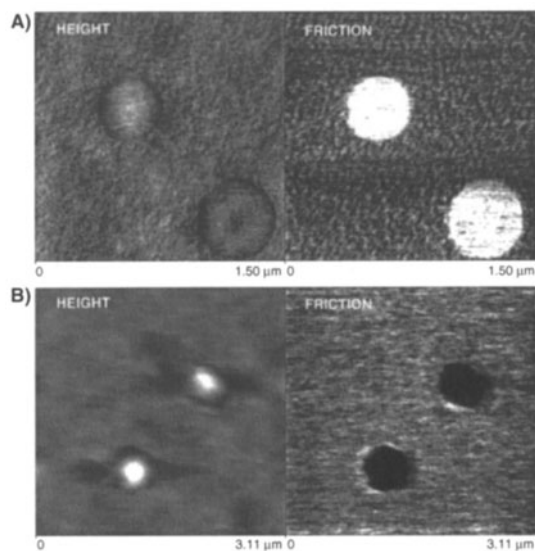
Fig. 18 Height (AFM) and friction (LFM) images of a spin-cast polystyrene/poly(methyl methacrylate) polymer blend [PS/PMMA (1 : 10 w/w)], obtained with (**a**) gold-coated and (**b**) SiO$_x$ tips under perfluorodecalin. (Reprinted with permission from [125]. Copyright 1998 American Chemical Society)

a clever choice of the solvent as discussed above. The gold-coated tip experiences higher friction forces on the PS compared to PMMA, while the silicon oxide terminated tip shows an inverted contrast. This example shows how the Lifshitz theory earlier mentioned can be successfully applied to predict the chemical contrast for various apolar polymers imaged by different tips in cases where the optical constants of the materials in question are known or can be determined. The chemical contrast on (more) polar surfaces, including polymers that have undergone an oxidative surface modification, cannot be predicted in a similar way (see below).

The resolution of friction imaging is limited by the effective tip-sample contact area and thus by the sharpness of the chemically modified probe (the contact area in principle varies with the variation of surface composition due to changes in the JKR forces). This sharpness can be described by a tip radius of 10–100 nm, depending on the procedure used. Werts et al. have reported on successful CFM imaging of a microphase-separated block copolymer (PS-PVP hetero-arm star copolymer), which implies a lateral resolution of better than ~ 30 nm [167]. On thin microtomed sections of microphase-separated polymer films the friction contrast measured in an argon atmosphere was pronounced with a carboxylic acid-functionalized tip, as shown in Fig. 19, while methyl-terminated tips yielded no contrast between the microphase separated domains. This observation was interpreted by the authors as chemical contrast, i.e. polystyrene and poly(2-vinylpyridine) can be differentiated owing to the strong interactions between the carboxylic acid groups on the tip and the pendant pyridine groups of the 2-PVP block.

The clear advantage of friction imaging compared to pull-off force mapping is the ease of the experiment and the relatively rapid data acquisition. Scan velocities of several micrometers per second are feasible, hence typical images can be recorded within one to a few minutes and possible instru-
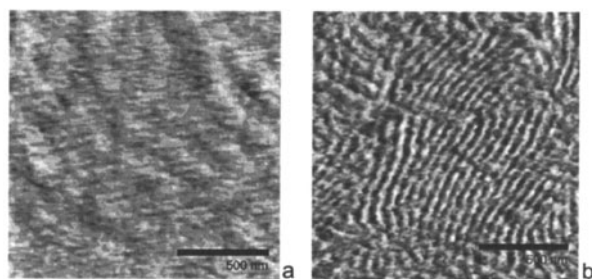
Fig. 19 Friction force images ($1.5 \,\mu m \times 1.5 \,\mu m$) obtained by means of CFM (**a**) with a – CH$_3$ tip and (**b**) with a – COOH tip. Since the friction coefficients determined with a – CH$_3$ tip are nearly the same on PS as PVP, the lamellar structure is not visible in (**a**). With a – COOH tip the friction coefficient is higher for the PVP part of the copolymer, which reveals the morphology as the alternating bright (high friction, PVP) and dark (low friction, PS) areas. (Reprinted with permission from [167]. Copyright 1998 Wiley-VCH)

mental drift in liquid media can be tolerated to a certain extent. Possible disadvantages include an increased tip-sample contact area (compared to the situation at pull-off in a f-d experiment, see Eqs. 33 and 28) and a contact area variation at a constant load due to variations of the JKR forces. Hence lower lateral resolution, and the possibility of tip or sample damage as a result of significant shear forces may arise. The interpretation of experimental data is sometimes complicated by friction forces, which are not dominated by adhesive interactions. Alignment on the molecular scale (polymer chains in crystalline areas [131, 168, 169] or at the fold surface of solution-grown lamellar crystals, see also Fig. 11 left) [158, 170–172] may lead to pronounced friction anisotropy; we have for instance measured differences in friction signal of a factor of > 4 depending on the orientation of PTFE chains with respect to the stationary scanning direction of the tip [169, 170]. Further, variations in modulus (Eq. 28) may dominate over the work of adhesion and render interpretation of the image contrast difficult without additional experimental data or independent knowledge. The most serious limitation is the intrinsic difficulty to perform truly quantitative friction imaging, which is required to obtain values of surface free energy similar to the data extracted from f-d curve measurements. Besides the calibration of the lateral spring constant of the cantilever, the calibration of the photodiode (sensitivity) is a major challenge [157]. The best option is obviously to analyze friction force data and subsequently captured pull-off force data (for an example see below).

5.2.2
Pull-Off Force Imaging

The alternative imaging mode for laterally visualizing chemical or compositional differences in CFM involves spatially resolved f-d curve data acquisition. As briefly mentioned above, several approaches as to how to tackle this experimental challenge have been proposed [173–178]. The basic approach is to record f-d curves for each pixel of a mesh of pixels. A simple method is the display of the data as a so-called force volume (FV) image. In this approach the deflection data are sliced and sorted in deflection values that are larger and smaller than some arbitrarily chosen value. Since this mode displays the deflection values with respect to a reference point and not true pull-off forces, care must be taken when such data are interpreted. For instance, f-d curves displaying a large hysteresis may show a strongly negative (deflection = force) value in the force volume image, which may erroneously imply large pull-off forces. The best way to analyze and display the data is by an automated software procedure in which each force-displacement curve recorded for each single pixel is analyzed off-line. The corresponding data, e.g. magnitude of the pull-off force, can be displayed on a 2-D map of forces (adhesion map) or can be treated statistically to yield a mean value of the pull-off force. In

the latter case an image with a limited number of pixels, e.g. 64×64 points^2, yields a mean of 4096 force-distance measurements [179].

A comparison with subsequently recorded height images can be useful to exclude some well-known artifacts. The interpretation of force data on the basis of the continuum contact mechanics (e.g. JKR theory, see Sect. 4.2) relies on the idealized situation of a spherical tip interacting with a flat surface; however, in practice, surfaces are in most cases "rough" [132, 133]. Protrusions on the sample surface lead to a local variation in tip-sample contact area. Depending on the geometry near the area of contact, i.e. non-conformal tip-sample contact or contact between tip side-wall and a protrusion, this may lead to an underestimate, or an overestimate, respectively, of the "true" pull-off forces [132]. Two illustrative examples are shown in Figs. 20 and 21.

In Fig. 20, a height and a corresponding force volume image are shown, which were recorded with a $- CH_3$ terminated tip on an octadecanethiol SAM on a granular gold surface. In force-volume images the pull-off forces can be graphically displayed in a layered image. Pull-off forces larger than a certain value are displayed in a gray scale. As an attractive force has per definition a negative sign, the scaling ranges from dark tones (high pull-off force) to bright tones (low pull-off force). The influence of the tip-sample contact area is clearly seen. The pull-off forces are smallest on top of the grains, where the contact area is minimized, while the highest forces are measured between the grains. The differences in contact area on this chemically absolutely homogeneous, but granular, surface (rms roughness on this image scale 3–5 nm) can already give rise to artifacts in CFM.

Artifacts due to contact area variations can also be observed, when features with sizes of several hundred nanometers are imaged. In order to illustrate this problem, poly(vinyl alcohol) (PVA) fibers, prepared by elec-
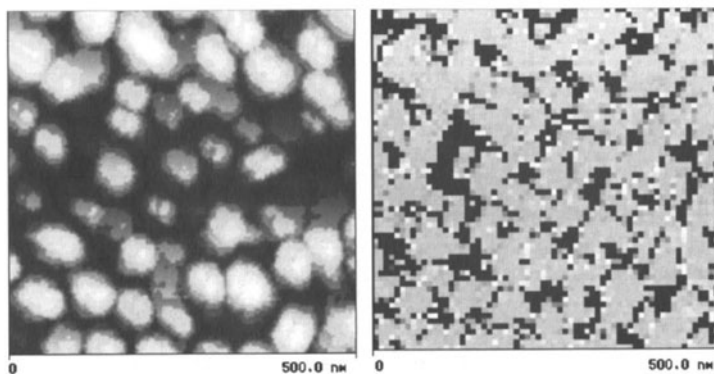
Fig. 20 Height (*left*) and FV images (*right*) of octadecanethiol SAM on granular gold surface obtained with $- CH_3$ terminated tip in air. The gray scale denotes: bright (low forces) to dark (high forces), $- 5$ nN to $- 21$ nN. (Reprinted with permission from [143])

trospinning [180, 181], were imaged on SAMs using functionalized tips. The pull-off force differences between the polymer and the substrates varied systematically when fibers with a diameter of one or several micrometer were imaged [143]. For thinner fibers the pull-off force images revealed a clear inhomogeneous pull-off force on the polymer fiber itself (Fig. 21).

The occurrence of areas of high and low adhesive forces, which are oriented parallel to the PVA fiber axis, can be attributed to an increased and decreased effective contact area between the side of the tip as compared to the tip apex. As the fiber shape is not a priory known, no definite conclusions about the chemical contrast can be obtained. However, a careful comparison of topography and force data clearly reveals the artifact. These observations demonstrate that force maps, and force data in general, must be interpreted carefully. In particular, attention must be paid to avoid coupling of the topography into the force images.

The first example for the study of polymer surfaces by "adhesion force" mapping known to us is the report by Mizes et al., who studied polycarbonate with a conventional Si_3N_4 tip [173]. On the polycarbonate film depicted in Fig. 22, a clear contrast in the adhesion image is seen.

All methods based on the capture of individual force-distance, f-d, curves are conceptually similar to this first reported method. The acquisition of f-d data in a pixel-per-pixel fashion is intrinsically slow compared to friction imaging since the tip must be lifted out of contact for each pixel. In liquids the corresponding viscous drag forces limit data acquisition to rates of typically few pixels per second, thus, an image of 64 pixels × 64 pixels takes on the order of 8–12 min. For high resolution work, thermal and instrumental drift may therefore become serious problems. However, these drawbacks are often overcome by a much more straightforward data inter-

0   1000.0 nm   0   1000.0 nm
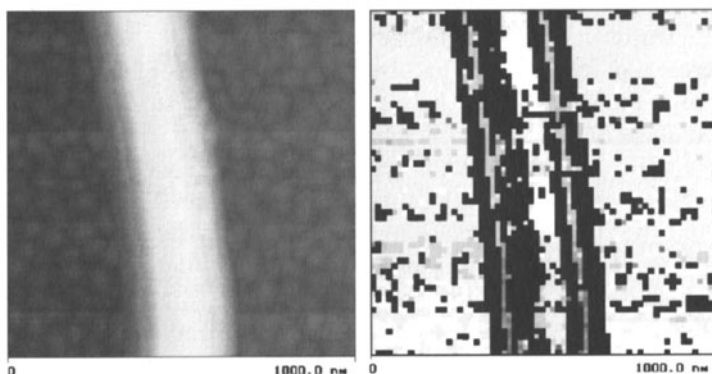
Fig. 21 Height (*left*) and FV force images (*right*) of electrospun fiber of PVA on SAM of octadecanethiol. The gray scale denotes: bright (low forces) to dark (high forces), − 4 nN to − 30 nN. (Reprinted with permission from [143])

(a)   (b)

← —————— 2 µm —————— →   ← —————— 2 µm —————— →
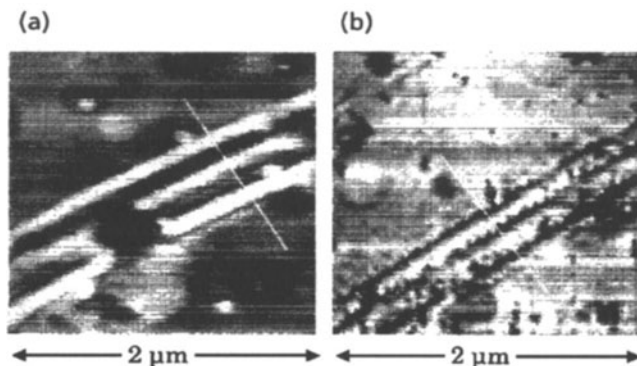
Fig. 22 (**a**) Topography of an undoped polycarbonate film; (**b**) Spatial variation in adhesion over approximately the same area. The adhesion ranges from 7.6 to 36.3 nN. (Reprinted with permission from [173]. Copyright 1991 American Institute of Physics)

pretation (as discussed above the pull-off forces do not depend on modulus, but only on tip radius and work of adhesion) and a significantly less complicated calibration of the cantilever spring constants and photodiode sensitivities [15, 16, 153–155, 157].

An improved experiment has been proposed and commercialized by the group of Marti [182]. In the so-called "pulsed force" mode, the sample is modulated sinusoidally (∼ 1 kHz) during a conventional contact mode AFM scan with an amplitude, which is just large enough to overcome the adhesive interactions. Hence the tip contacts, indents, and breaks free from the surface with a frequency of ∼ 1 kHz during scanning. Instead of digitally recording the complete f-d curve, only the four points are captured, the baseline, the maximum repulsive force, the maximum adhesion force and a point that can be used with the maximum repulsive force to define the slope in the loading regime, respectively (Fig. 23). CFM data using this technique have been reported by Fujihira et al. on SAMs [183].

As mentioned in the introduction, the application of CFM on surface-treated polymers promises to be particularly useful to determine the lateral distribution of surface functional groups in liquid environments on the nanometer scale. Owing to the complexity of the conventional functionalization procedures, the imaging of particular functional groups is, however, difficult and the data interpretation may become challenging. The presence of many different functional groups with widely varying contributions to the intermolecular interactions discussed above, limits the successful mapping to phase-separated blends or morphologies (see examples above) on the one hand, and to "addressable" functional groups, such as acidic or basic groups, on the other hand. For the latter functional groups, it is possible to change the chemical character of the group in situ in the liquid cell of the AFM simply by changing the pH. Thus, while all interactions of pH-independent functional
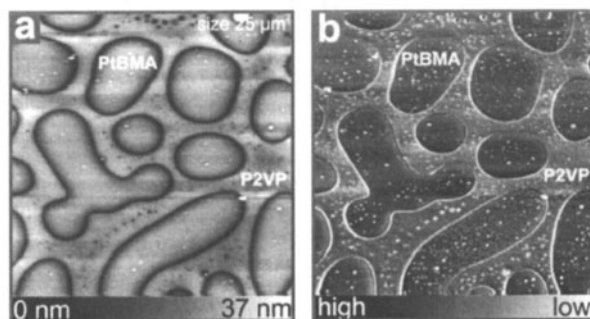
Fig. 23 Pulsed force mode measurement on two homopolymers spincoated on silicon from THF solution of a mixture of P2VP and PtBMA. The pulsed force mode AFM images clearly distinguish the PtBMA islands from the surrounding P2VP in both topography (**a**) and in adhesion (**b**). (Reprinted with permission from [184]. Copyright 2000 American Institute of Physics)

groups are unchanged or at worst predictably altered, the addressable groups change their behavior and become charged (or uncharged). This feature can be exploited in selective CFM imaging.

As an illustrative example we show below the surface of two modified (oxyfluorinated) isotactic polypropylene films [185] imaged in force-volume mode with a hydroxy-functionalized tip. The hydroxy end group of the alkanethiol used for tip modification shows pH-independent adhesive properties [124] and, owing to the low surface energy, the adhesion in aqueous medium is minimized on all surfaces. As shown in Figs. 24–26, the pull-off forces of various oxyfluorinated iPP films depend on the pH of the imaging solution (Fig. 24). This behavior is attributed to the deprotonation of the carboxylic acid groups introduced by the surface modification [57, 58, 110].

From an analysis of FV images of these specimens it becomes clear that the forces are heterogeneously distributed over the film surface at low and intermediate pH, while at high pH exclusively electrostatic repulsion is observed with no discernible pull-off force. A careful comparison with the additionally captured height images ensures that the observed differences in pull-off force are not due to differences in effective contact area. The areas in which attractive interactions are measured at pH 6.1 were interpreted to contain carboxylic acid groups with a higher "pK_a" compared to the regions where repulsion is observed. This observation was attributed to a difference in local hydrophobicity, in accordance with data reported by the Lieber group on SAMs [124]. The most hydrophobic local environments will be the areas where the deprotonation of carboxylic acid groups is least favored. Consequently, these areas will be more protonated at pH 6.1 compared to the more hydrophilic areas, thus areas with a high density of – COOH and – OH functionalities [58].
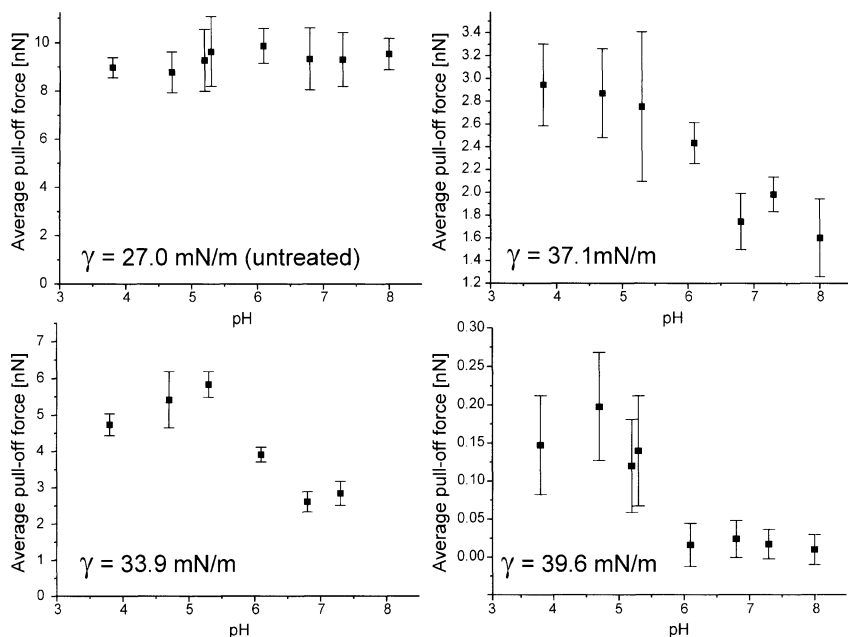
Fig. 24 Force titration of an untreated iPP (*top*, *left*) and three oxyfluorinated iPP films using OH-terminated SFM tips. The total surface tension values are indicated. The error bars correspond to the standard deviation of the average value calculated from the corresponding histograms. (Reprinted with permission from [58]. Copyright 2000 American Chemical Society)

A qualitatively similar observation was made on plasma polymerized al-lylamine films on oxidized Si (Fig. 27) [57, 121]. The force titration behavior was found to agree with the presence of primary amino groups that were identified independently by FT-IR spectroscopy and XPS. The shift in force pKa ($\sim$ 5.7) with respect to the solution pKa ($\sim$ 10.5) was attributed similarly to the above mentioned behavior of carboxylic acid groups to the effect of the hydrophobic environment; the more hydrophobic the local environment, the higher is the free energy of creating a charged amino group. The locally more hydrophobic environments will resist protonation stronger than hydrophilic areas and hence correspond to the areas of high pull-off force.

Another recent example of the use of CFM for polymer surfaces is force-volume mapping of stabilized polypropylene films (process stabilizers, UV-stabilizers and antioxidants) [186, 187]. The mapping was performed using methyl- or hydroxy- functionalized tips in water or in nitrogen atmosphere. Differences in the pull-off forces between the additives and polypropylene al-lowed imaging with sub-micrometer resolution of the lateral distribution of the additives present on the surface. By performing pull-off measurements on spin-coated films of pure additives, characteristic pull-off force values were obtained, which made it possible to discriminate between the antioxidant,
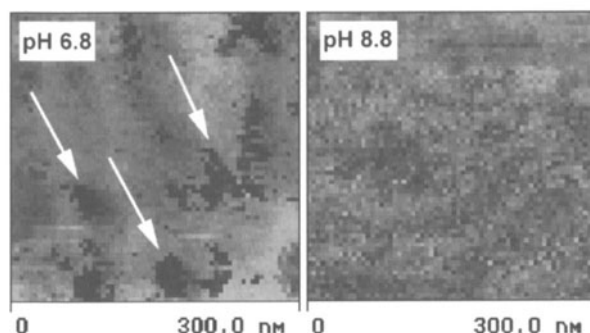
Fig. 25 FV images of oxyfluorinated iPP ($\gamma = 39.6$ mN/m) at pH 6.8 (*left*) and pH 8.8 (right). Dark color indicates high adhesion (-0.3 nN for pH 6.8, ≈ 0 nN for pH 8.8), bright color indicates low adhesion (0 nN for pH 6.8 and pH 8.8). The arrows indicate areas of high pull-off forces, which were attributed to domains with the most hydrophobic character, i.e. lower density of polar $-$ COOH and $-$ OH functional groups introduced by the oxyfluorination). (Reprinted with permission from [58]. Copyright 2000 American Chemical Society)
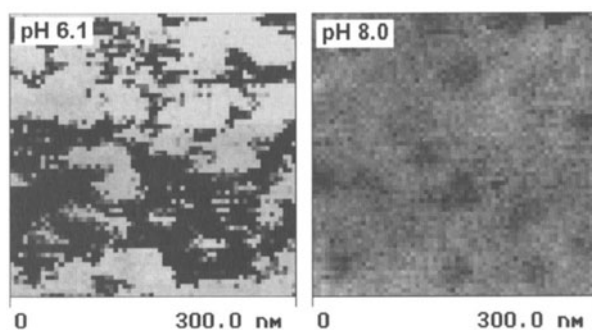
Fig. 26 FV images of oxyfluorinated iPP ($\gamma = 37.1$ mN/m) at different pH. In the force images dark color indicates high adhesion (-1.3 nN, -0.4 nN for pH 6.1 and pH 8.0, respectively), bright color indicates low adhesion (-0.2 nN and ≈ 0 nN for pH 6.1, and pH 8.0, respectively). (Reprinted with permission from [58]. Copyright 2000 American Chemical Society)

which was more hydrophobic, and the UV-light stabilizers [187]. It was, however, pointed out that it was necessary to perform measurements using both tip modifications in both water and nitrogen atmosphere in order to identify an additive. Moreover, a gradual change of the average adhesion forces with aging time of the stabilized polypropylene films was correlated to a migration of additives from the bulk to the surface, gradually forming a film which made the surface less hydrophobic [186]. Time of flight (ToF) SIMS was used to confirm the presence of the additives, even though sub-micrometer resolution was not provided [187].
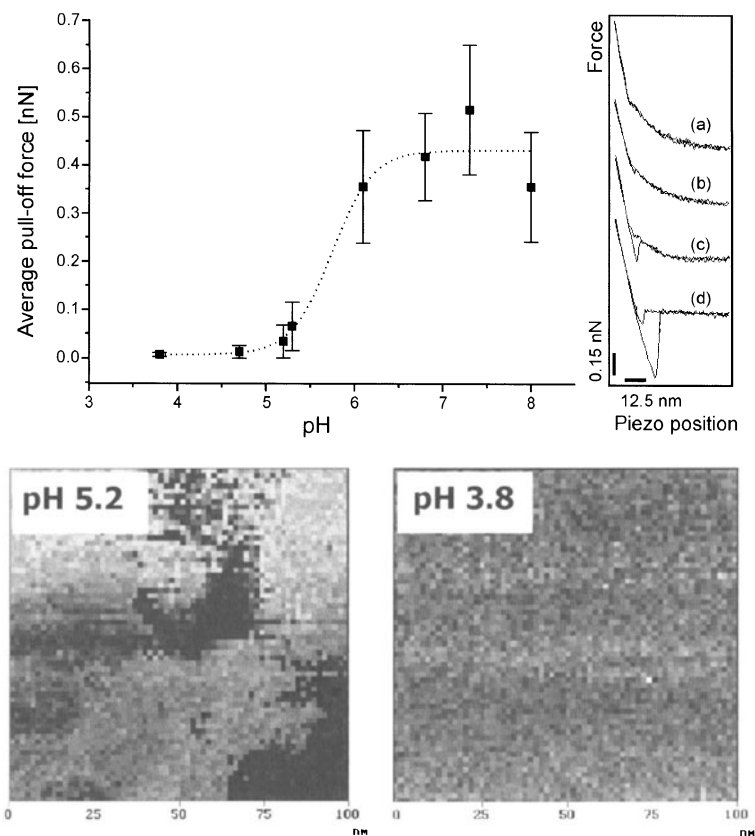
Fig. 27 *Top*: Force titration of plasma polymerized allylamine film (the *dotted line* has been added to guide the eye). To the right corresponding force-distance curves which display (depending on the pH of the buffered aqueous solution) (a) exclusively repulsive (pH 4.7), (b) and (c) repulsive and attractive (pH 5.3 and pH 6.2, respectively), or (d) exclusively adhesive interactions (pH 6.8). Bottom: FV images of corresponding plasma polymerized allylamine film at pH 5.2 (bright 0.0 nN, dark – 2.0 nN) and pH 3.8 (bright 0.0 nN, dark – 0.1 nN). (Reprinted with permission from [57]. Copyright 2000 American Chemical Society)

CFM using hydroxy- or methyl-terminated tips has been used to investigate the frictional properties of polystyrene films exhibiting different degrees of oxidation, ranging between 0–20 at. % oxygen by XPS [188, 189]. It was claimed that absolute friction values of the oxidized surfaces could be derived, if the torsional response of the tip cantilever and the resulting signal output of the photodiode were known. A linear increase in the coefficient of friction with increasing surface oxygen level (by XPS) and in the water contact angle were observed. The friction values of the oxidized surfaces obtained using the hydroxy-terminated tip were higher than those obtained using the methyl-terminated tip. It was suggested that this could be used

to follow approximate changes in polar free surface energy of polymer surfaces due to oxidation. Moreover the lateral resolution using this CFM approach was demonstrated using a model system consisting of a PS/PMMA blend. Little image contrast was obtained using an non-functionalized or a methyl-terminated tip since the friction difference between the two phases was too low (Fig. 28a). Using a hydroxy-functionalized tip a clear contrast was obtained, thus the increased friction contrast was chemical in nature and caused by an increased polar interaction between the tip and surface (Fig. 28b) [188].

Eaton et al. used FV mapping for imaging of a phase-separated blend of PMMA and poly(dodecyl methacrylate) (PDDMA) [190, 191]. Unmodified silicon nitride cantilevers were used in ambient conditions in air or in water using a liquid cell. Differences in pull-off forces correlated with features in topography, making it possible to distinguish between the PDDMA-rich
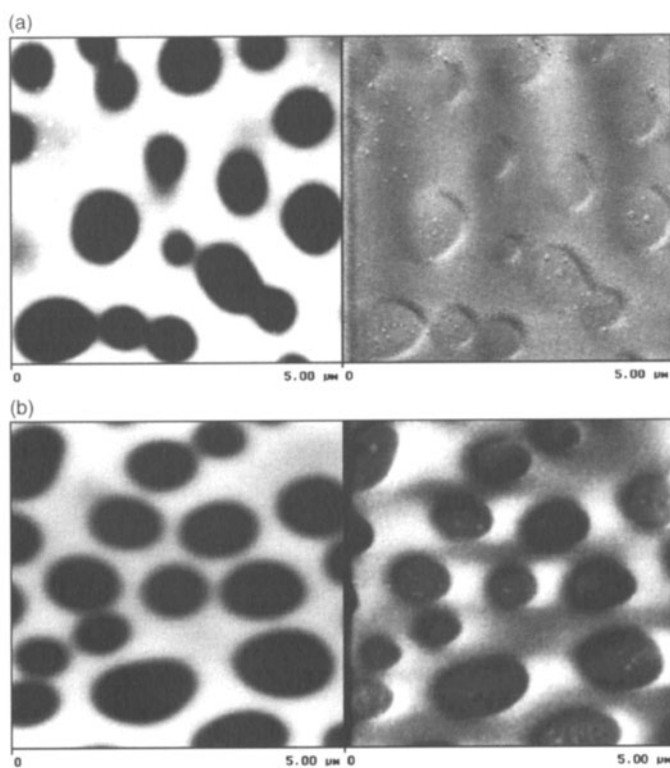
Fig. 28 Topographical (*left*, z range 150 nm) and frictional force (*right*, z range 0.2 V) images of a PS/PMMA blend using unfunctionalized (**a**) and hydroxy-terminated (**b**) tips. The continuous phase consists of PMMA. (Reprinted with permission from [188]. Copyright 2000 American Chemical Society)

domains (exhibiting higher adhesion) from the PMMA-rich domains (exhibiting lower adhesion). However, since the values of the adhesive force measured in the PDDMA-rich domains were lower than those determined for films of pure PDDMA, it was suggested that this was due to sub-micrometer-level domains of PMMA, even though no evidence for this hypothesis was provided. Particularly high adhesion forces were observed at the interface between the domains, originating from the increased contact area between the tip and the substrate [191]. It was suggested that indentation mapping, using a stiffer cantilever, could be used as a complimentary technique to the adhesion mapping, since it was less dependent of topographic features.

By performing adhesion mapping and friction force imaging of mechanically scratched structures on biaxially oriented polypropylene films with a conventional Si_3N_4 tip an increase in surface energy of the scratched regions was observed [192]. This was explained in terms of increasing density and orientation of polymer strands, as well as added energy by the work done by the mechanical scratching. The increase in the surface energy ("adhesion force") was comparable to that introduced by surface oxidation of the unscratched surface after 1 min UV/ozone exposure. The CFM approach was thus successfully used to create and assess local active sites of the surface in terms of surface energy increase or wettability improvement.

Furthermore, CFM was used in a study on the surface chemical properties of UV excimer laser irradiated polyamide to complement XPS and ToF-SIMS data [193], as well as in a study on the surface properties of modified poly(dimethyl siloxane) (PDMS) [194]. The surface hydrophobicity of UV/ozone-treated PDMS was also probed by Hillborg et al. using CFM and AFM indentation measurements, among other techniques, as a function of storage/recovery time [179]. The CFM data were acquired in the form of force volume images and were converted automatically into pull-off force images and the corresponding histograms (force distributions) using a custom-made software. Exposure times < 30 min resulted in laterally homogeneously oxidized surfaces, which are characterized by an increased modulus and a high segmental mobility of PDMS. As detected on a sub-50 nm level, the subsequent "hydrophobic recovery" was characterized by a gradual increase in pull-off forces and a decrease in normalized modulus, approaching the values of unexposed PDMS after 8–50 days. Longer exposure times (60 min) led to the formation of a hydrophilic silica-like surface layer. Under these conditions a gradual surface reconstruction within the silica-like layer occurred with time after exposure, where a hydrophilic SiO_x-enriched phase formed < 100 nm sized domains, surrounded by a more hydrophobic matrix with lower normalized modulus (Fig. 29).
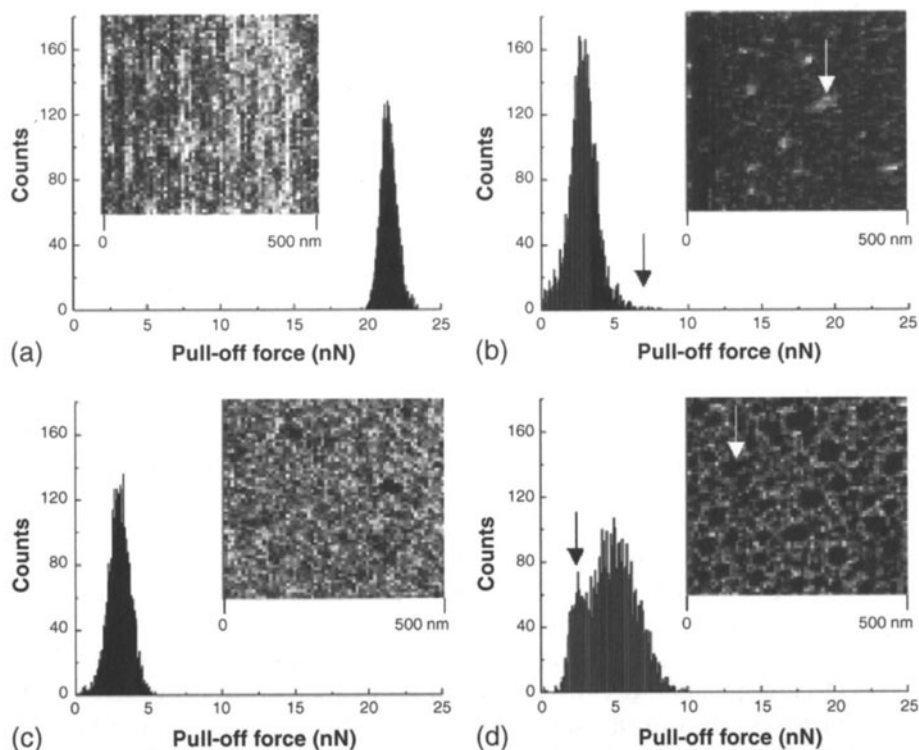
Fig. 29 Representative histograms of the pull-off forces and corresponding adhesion (pull-off force) images of: (**a**) unexposed PDMS and oxidized PDMS; (**b**) 0.1; (**c**) 8 and (**d**) 40 days after exposure to 60 min UV/ozone. In the adhesion images, the *gray scales* are individually scaled from dark (low pull-off) to bright (high pull-off). (Reprinted with permission from [179]. Copyright 2004 American Chemical Society)

6
Other Techniques to Image Chemical Functional Groups and their Lateral Distributions

In this section surface characterization techniques, which are capable of lateral imaging of polymer surfaces with sub micrometer resolution, are discussed. The following terms will be used: mapping is used when small regions of a single area of interest are sequentially sampled. These regions are then linked together via their spatial coordinates. The term imaging is used when the whole area of interest is sampled simultaneously, and the localized spatial resolution is achieved by other means [195].

6.1
Secondary Ion Mass Spectrometry

SIMS is based on the mass spectrometric analysis of secondary ions, generated by the interaction of a primary ion beam (usually Ga^+ or Ar^+) with the polymer surface. The emitted fragments of the molecules allow characteristic signatures of elements, isotopes and molecules to be identified. Generally, ToF analyzers are used due to their higher sensitivity, compared to quadrupole detectors. Of the currently available spectroscopic imaging techniques for non-conducting materials, time-of-flight secondary ion mass spectrometry imaging is a powerful method thanks to its combination of high sensitivity (femtomole-attomole), capacity to detect molecules as well as elements, and sub-micrometer lateral resolution [196–199]. There are two operational regimes in SIMS, which yield fundamentally different information and analytical features. The so-called dynamic SIMS involves use of a high primary ion current density on the sample that allows fast erosion so that in-depth concentration profiles can be measured. Static SIMS operates in principle the same primary ion guns, but at a lower primary ion current ($< 10^{13}$ ions cm^{-2}), where the basic idea is that each local environment in the sample is hit only once by the primary beam, thereby only acquiring data from the top 10–20 Å [196–199]. SIMS imaging can either be performed using an ion microscope or ion microprobe instruments [197, 198]: the ion microprobe uses a finely focused primary ion beam, which is raster-scanned point by point over a given area. The intensity of a given ion or a full mass spectrum is then acquired from each point. In the ion microscope mode, the entire area is irradiated by a less focused primary ion beam. The lateral distribution information is then obtained by the use of special ion optics and position-sensitive detection. Using the microprobe mode, the lateral resolution is defined by the beam diameter (around 20 nm using liquid metal ion guns) [198, 200]. In the microscope mode the lateral resolution of approximately 0.4 μm is determined by the ion optics of the instrument [197]. The drastically decreased sputter and ionization yield of secondary ions for higher molar mass polymers, however, reduces the lateral resolution compared with these values obtained at favorable conditions (single layers of molecules etc.) [197]. Thus, in imaging polymer surfaces a higher intensity, especially for the higher mass molecular peaks, in order to allow molecular imaging with the most characteristic ions, and shorter exposure times are desirable. The best theoretical resolution (Δl) is correlated according to the following equation:

$$\Delta l = \sqrt{\frac{\sigma}{Y}} \tag{34}$$

where σ is the damage cross section of the exposed surface layer and Y is the yield of secondary ions (the number of detected secondary ion species divided by the total number of applied primary ions). In this context, post-

ionization (of emitted neutral particles) techniques for molecular species and new primary ion beams in order to increase the yield are promising for the future development of SIMS. [197, 198, 201–204] Static SIMS imaging using cluster ion beams (for example Au_2^+) generated with a liquid metal ion source seems to be a promising approach for imaging organic surfaces [204].

Typical applications of imaging SIMS to polymers are characterization of Langmuir–Blodgett (LB) films [205, 206], self-assembled monolayers [207], polymer blends [208] and micro patterned surfaces [209, 210]. Molecular identification of active members of bead-bound combinatorial libraries is another application well suited to imaging SIMS. Femtomol quantities of different peptides attached to 30–60 μm PS beads have been determined [211, 212], even though the method provides fewer structurally informative fragments, compared to MALDI-MS [212]. At least two factors limit the spatial imaging of self-assembled monolayers and polymers as identified by a number of researchers [42, 202, 210, 213, 214]: firstly, organic molecules do not frequently give rise to unique molecular ions with an intensity that is sufficiently large to permit imaging below the static SIMS limit. Secondly, low mass atomic ions often have high enough intensity for ToF-SIMS imaging under static conditions, but can originate from different chemical species on the surface, ranging from the underlying substrate, as well as from other organic moieties. One solution to this problem is the use of specific labeling techniques, for example using isotopes [208, 215]. Stable isotope labeled proteins (^{15}N-labeled streptavidin) were utilized in ToF-SIMS imaging of biotin micro-patterns on polymer or gold surfaces. The imaging was based on the specific secondary ion ($C^{15}N^-$).

Leufgen et al. demonstrated the use of static ToF-SIMS to visualize two coexisting phases in LB films, prepared as a mixture of two fluorescent dyes: NBDPC and DPPC (nitrobenzooxadiazol- and dipalmitoyl-phosphatidylcholine) [216]. Images of the monolayer produced by mapping the detected intensities of specific secondary ions are shown in Fig. 30. The lateral resolution was approx. 1 μm. The distribution of the protonated molecular ions of NBDPC was enriched in a liquid-expanded phase (Fig. 30a), whereas the protonated DPPC molecular ions were enriched in the liquid-condensed phase (Fig. 30b). The domain structures seen in the images of the protonated molecules corresponded exactly to fluorescence data (not shown). The homogeneous distribution of the gold substrate ions is shown in Figure (Fig. 30c).

Bourdos et al. observed that the contrast of ToF-SIMS images of LB films was generated not only by chemical, but also by physical differences within the film on the substrate (packing of molecules in the liquid crystal phase) [206]. The lateral resolution obtained during the experiments was approximately 230 nm. The resolution was limited by the pixel raster used even though the physical limit determined by the ion beam was approximately 80 nm.
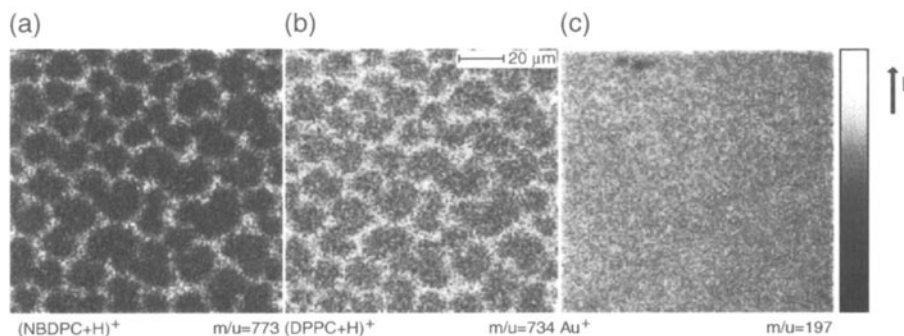
Fig. 30 Mass-resolved images by static TOF-SIMS ($120 \times 120 \ \mu m^2$). The secondary ion intensities are color coded, from dark to bright. Illustrated is the lateral distribution of the molecular ions of: (**a**) NBDPC, (**b**) DPPC, and (**c**) gold ions (substrate). (Reprinted with permission from [216]. Copyright 1996 American Chemical Society)

Static ToF-SIMS imaging of the morphology and miscibility of ethylene-tetrafluoroethylene copolymer/PMMA blends was successfully performed using the ion F^- ($m/z = 19$) as a distinct characteristic fragment. The lateral resolution was approx. 780 nm [217]. The corresponding images showed that slow cooling facilitated the phase separation between ETFE and PMMA domains. The dynamic rearrangement of bromine end groups ($^{79}Br^-$, $^{81}Br^-$, $m/z = 79, 81$) attached on amorphous or semi crystalline polymers prepared by condensation polymerization of Bisphenol A and 1,8-dibromooctane was investigated using static ToF-SIMS [218]. The images revealed that the bromine end groups were preferentially expelled to the surface of the lamellae during the crystallization process.

Static ToF-SIMS was also used to investigate the effects of various surface-engineering conditions on the lateral distribution of poly(L-lysine)- or poly(ethylene glycol) modified poly(lactic acid). However, the analysis of poly(ethylene glycol) and poly(lactic acid) surfaces did not produce distinguishing ions of a sufficient intensity, yielding high enough lateral contrast. During these conditions, imaging XPS (Sect. 6.2) was successfully used despite of the comparatively low lateral resolution ($25 \ \mu m$, compared to approx. $1 \ \mu m$ using SIMS) [219]. This combination of instruments was also successfully used for chemically micro-patterned surfaces, formed by plasma-polymerization [209]. Distinct regions of fluorine, carboxylic acid and hydrocarbon functionalities were imaged by ToF-SIMS, whereas mapping XPS was used to image the nitrogen content (using the N $1s$ peak) due to the lack of a unique nitrogen signal of allylamine [209]. Another application of imaging static ToF-SIMS described in literature is the characterization of surface diffusion of polymers on inorganic substrates [220]. It was observed that PS and PMMA did not exhibit any surface diffusion at room temperature, whereas poly(dimethylsiloxane) and a perfluorinated polyether exhibited high surface
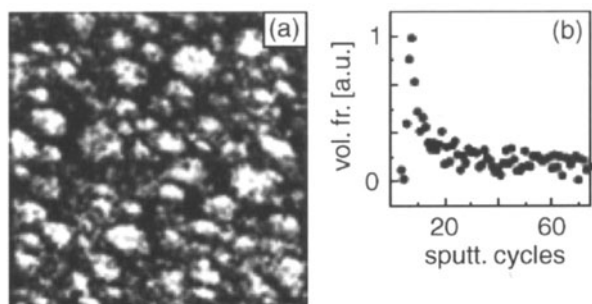
Fig. 31 Imaging by dynamic SIMS ($27 \times 27 \, \mu m^2$): (**a**) deuterated polystyrene (*white areas*, $m/z = 26$) distribution in a deuterated polystyrene/polyimide (50/50) blend; (**b**) corresponding profile of the polyimide fraction as function of distance from surface (1 sputtering cycle ≈ 0.5 nm). (Reprinted with permission from [208]. Copyright 2001 Wiley-VCH)

diffusion. Provided that a well-defined boundary between a covered and un-covered surface area can be produced, this technique can be applied to a wide variety of substrate-overlayer combinations [220].

By using dynamic mode SIMS the lateral distribution of phases in three dimensions can be resolved (Fig. 31). Thin films (thickness ca. 500 nm) of binary mixtures of deuterated or partially brominated PS, polyisoprene and poly(vinylpyridine) were investigated with a lateral resolution of approximately 120 nm and composition versus depth profiles with a resolution better than 10 nm [208]. The brominated PS formed continuous phase-domain structures in the interior of the films whereas they were encapsulated by deuterated PS layers at the interfaces. Moreover a very thin layer (ca. 3 nm) of polyisoprene covered the surface of a binary mixture of poly(isoprene)/deuterated PS [208].

Dynamic SIMS has also demonstrated the clustering of oxidized poly(pyrrole) into small granules (50–300 nm) embedded in a matrix of ferric stearate LB films after exposure to pyrrole vapors [221], and the surface enrichment of fluorinated chains in a poly(methyl methacrylate) matrix [222].

6.2
X-ray Photoelectron Spectroscopy

XPS is one of the most popular spectroscopic methods for surface analysis of polymers. It provides qualitative and quantitative information on the atomic composition down to a depth of typically 0.5–10 nm depending on the take-off angle. In an XPS instrument the sample is positioned in a high vacuum chamber and is irradiated with a monochromatic X-ray source (generally Al K_α or Mg K_α) resulting in an emission of photoelectrons from the exposed surface region. The XPS spectrum shows the number of photoelec-

trons as a function of their kinetic energy, which is characteristic of the element and its binding state (except for helium and hydrogen). The recent increase in instrumental sensitivity has led to the development of spatially resolved XPS [223, 224]. The spatial resolution of commercial instruments is in the order of 5–30 μm with acquisition times of minutes rather than hours [223, 225]. The lateral resolution is limited mainly due to the difficulty in focusing the X-ray beam. Although XPS imaging does not have the same spatial resolution as ToF-SIMS, the advantage of XPS is not only the determination of the atomic surface composition, but also the information it delivers on the electronic environment (often referred to as chemical shift) in a non-destructive manner [209, 219]. As is the case with SIMS, imaging can be made using two different main techniques: the first utilizes the X-ray beam to bombard the specimen very locally, i.e. an X-ray probe. The second method floods the specimen with X-rays and then images parts of the surface by manipulating the photoelectrons in a controlled manner [225].

A direct comparison of the spatial resolution of XPS and transmission infrared spectroscopy imaging on heterogeneous polymer blends of poly(vinyl chloride)/PMMA was presented by Artyushkova et al. [226] The spatial resolution of the XPS and infrared instruments was 2–3 μm and 7 μm, respectively. The comparable resolution of the instrumentation allowed for images and spectra from the same areas of the samples to be directly compared (Fig. 32).

The XPS image was based on the intensity of the Cl $2p$ peak, whereas the infrared image was based on the absorption at the band at 1333 cm^{-1}, used for identification of PVC. The PVC enriched (bright) areas in the images were

XPS, Cl 2p   FTIR-PVC band
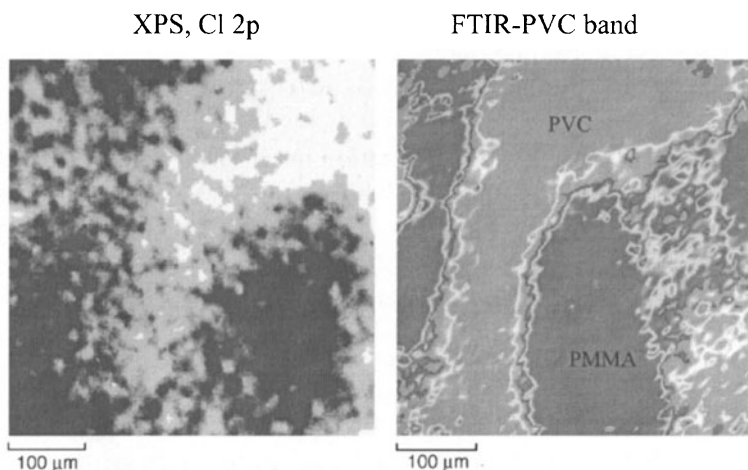
Fig. 32 Comparison of XPS Cl $2p$ and transmission FT-IR PVC (1333 cm^{-1}) images for a PVC/PMMA (25/75) blend. (Reprinted with permission from [226]. Copyright 2000 Society for Applied Spectroscopy)

similar in both shape and size. Since the XPS sampled approximately the top 10 nm, while the transmission infrared images were representative of the total film thickness (a few micrometers). This implied that the phase-separated regions extended well into the film (Fig. 32). This combination of different techniques thus provided a more complete method for characterizing complex polymers containing different surface and bulk combinations [226].

Owing to the sensitivity of the chemical surrounding, XPS imaging was used to study segregation effects of polyethylene glycol (PEG)-modified poly-lactic acid (PLA) systems, since it enabled a straightforward distinction of the two species [219]. Mapping of the signal intensity at a given binding energy (C 1s) as function of the position along a sample surface was performed with a lateral resolution of approx. 25 μm. The PLA generated three peaks each being separated by binding energy shifts of approx. 2 eV and 4 eV relative to the C 1s methyl group at 285.0 eV. The C 1s ether peak of PEG arose at 286.3 eV, enabling a straightforward deconvolution and determination of the relative intensities of the two polymers. The method was used to assess surface segregation of PEG and PLA, which were of the order of tens of microns [219]. Moreover imaging XPS and laterally resolved Raman microscopy were used to investigate the effects of laser-induced ablation of polyimide [227]. Both methods revealed the deposition of carbon surrounding the ablation craters (300 μm diameter).

Although spatially resolved XPS is constantly improving (increased intensity of the X-ray source, improved electron optics of the lenses, increased transmission of the energy analyzer) it is believed that SIMS will be at an advantage for probing inhomogeneous surfaces [225]. However, when the chemistry involved in the surfaces is complex, XPS offers unique capabilities owing to the chemical shifts in binding energies [225].

6.3
Matrix-Assisted Laser Desorption/Ionization Mass Spectrometry

Matrix-assisted laser desorption/ionization mass spectrometry (MALDI-MS) based imaging was first described in 1995, developed as a detection method for thin-layer chromatographic separations [228]. The images are obtained by acquiring mass spectra stepwise over the desired area of a surface. The mass of the ions of interest is then extracted and displayed at their correct spatial positions to produce the final image. The spatial resolution achieved was 250–500 μm even though the ultimate spatial resolution, based on matrix heterogeneity and minimum laser beam diameter to acquire a good signal intensity, was estimated to be in the order of 50 μm [228]. The spatial resolution of the imaging approach is moreover limited by the physical ability to focus and step the laser across the sample, spreading of the sample due to the addition of the liquid matrix, [228, 229] as well as by the software used for the scanning and acquisition process [230]. The capability of imag-

ing MALDI-MS has been demonstrated by the acquisition of mass spectra images of symbols printed by an ink-jet printer with a lateral resolution of 30 µm [230, 231]. Two letters were printed on top of each other using different inks [230]. Since the inks differed in molecular weight, the letters did not interfere with each other in the acquired images (Fig. 33). Moreover
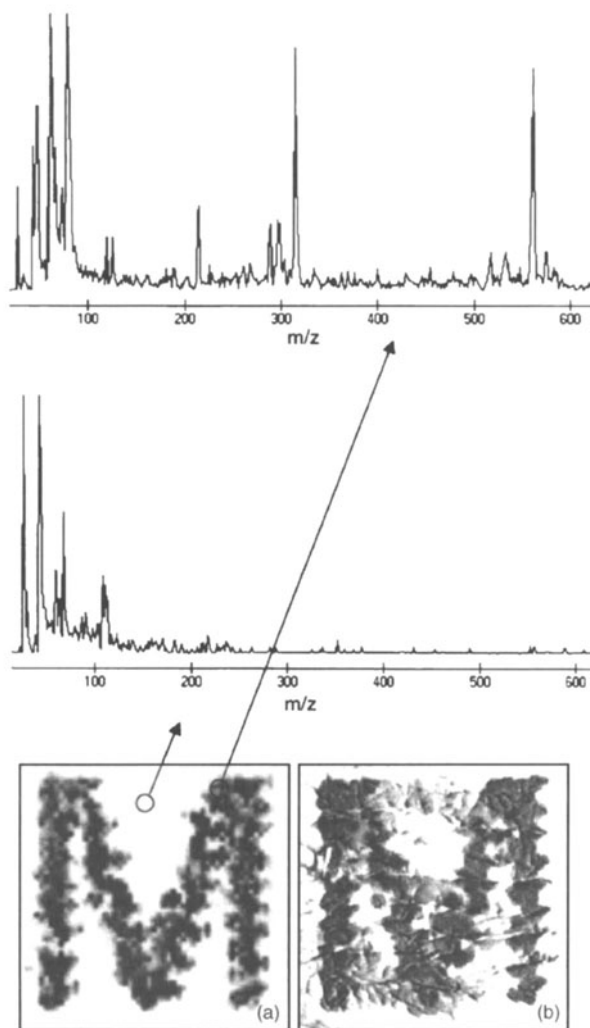
Fig. 33 (**a**) Mass spectrometry image ($m/z = 340$) by MALDI and (**b**) optical image of a letter printed with an ink printer. The size of the images are 1500×1500 µm². (Reprinted by permission of Elsevier Science from "Automated mass spectrometry imaging with a matrix-assisted laser desorption ionization time-of-flight instrument", by Stoeckli et al., Journal of the American Society for Mass Spectrometry, Vol. 10, pg 69, 1999, by the American Society for Mass Spectrometry)

the potential to perform quantitative analyses was demonstrated [230]. Since MALDI-MS imaging offers the possibility to detect significantly higher molar masses than SIMS, direct MALDI-based imaging is believed to become an important complement to other molecular imaging techniques [229].

6.4
Raman Microspectroscopy

Raman microspectroscopy is based on an optical microscope, where the spectral distribution of inelastically scattered light is detected by a Raman spectrometer/CCD detector, thereby microprobing an area with a spatial resolution of about 1 μm. The spatial resolution of Raman systems employing normal optical microscopes is limited to approximately the wavelength of the light (about 0.5 μm), because both the illuminating laser light and the Raman scattered light are collected in the optical far field (i.e. many wavelengths of light away from the scattering material). While the methods of image acquisition are diverse, each generates a two-dimensional map based on the intensity of a given Raman scattering band. By using Raman imaging, a widened laser beam provides a global illumination of the investigated area which is then imaged directly onto a CCD detector. A complete Raman spectrum can be collected for each pixel. Raman mapping is an equivalent procedure which uses point illumination to obtain the spectrum at single points, gathered in a grid pattern over an area of the sample. The addition of confocal filters can increase the lateral resolution and allows one to image at different depths. The theoretical performance of a confocal Raman microscope is mainly determined by the optical properties of the microscope objective (numerical aperture, magnification power, and focal length) and by the size of the pinhole placed in the back image plane of the microscope [232]. The depth of analysis in the confocal mode is in the order of 2–4 μm [232]. Recent developments in Raman spectrometers have led to great improvements in sensitivity and imaging capabilities [233, 234], allowing mapping of polymer surfaces with a lateral resolution of < 1 μm [235, 236]. Submicron spatial resolution using wide-field Raman imaging in the confocal mode has been demonstrated by imaging polystyrene spheres (2 μm diameter) with an interparticle distance of 200 nm [237]. The dominant criteria to take into account when obtaining a Raman image is the weakness of the Raman effect [234, 237]. Since the incident laser energy is focused on a very small area, low laser power must also be used to minimize local thermal expansion and sample degradation [237]. Moreover problems of sample fluorescence and photodamage may occur when mapping polymer surfaces [236, 238, 239]. Markwort et al. compared Raman imaging using global illumination with mapping by point illumination and concluded that lower spectral resolution, increased fluorescence and artifacts caused by sample shape were worse for the global illumination method [240]. These authors recommended the use

of point illumination with confocal light collection for the study of heterogeneous polymer surfaces.

A polypropylene/polyethylene copolymer containing a small amount of blended ethylene-propylene rubber (EPR) was characterized by confocal Raman microspectroscopic mapping with a spatial resolution of 1 μm. The surfaces exhibited micrometer-size domains with a higher content EPR in the copolymer matrix (Fig. 34a). However, since absorption bands originating from the copolymer were more or less dominant in all spectra, it was concluded that the EPR existed as submicrometer particles. Figure 34 shows the same surface after a surface modification by exposure to an argon-plasma. The regions containing higher amounts of EPR exhibited a slight increase in number and size suggesting that the EPR was less susceptible to damage due to its crosslinked nature [235]. Due to the poor sensitivity of Raman spectroscopy to polar functional groups it was not possible to map the oxygen functionality on the surface. However, by mapping using reflection infrared spectroscopy the presence of hydroxy groups was verified. The lateral resolution was, however, limited to 30–50 μm. After the plasma treatment, the surfaces were grafted using polystyrene. The lateral distribution of polystyrene was shown to be heterogeneous and corresponded to the areas of higher EPR concentration after the plasma treatment [235].

By combining Raman imaging with photoacoustic FT-IR and FT-IR microscopy three-dimensional maps of the heterogeneous degradation of epoxy and polyurethane films exposed to UV and water vapor were obtained [241]. Similarly, the phase separation in styrene/butylacrylate copolymers and latex films were analyzed [242]. Blakey and George used point illumination Raman mapping to investigate the surface of photooxidized PP with a lateral resolution of 1 μm and successfully mapped the distribution of both oxidation products (α,β-unsaturated ketones) and catalyst residues [239]. The distri-
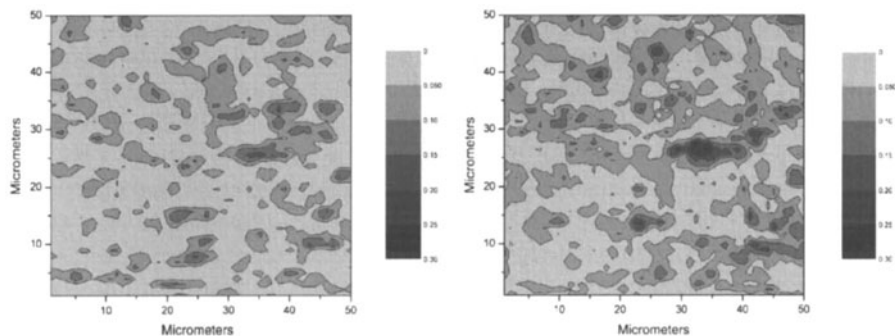
Fig. 34 Raman map of the surface distribution of EPR in a PP matrix (**a**) before and (**b**) after plasma treatment (the absorption band used for EPR was 1064 cm^{-1}, whereas 1220 cm^{-1} was used for PP). (Reprinted with permission from [235]. Copyright 2001 Society for Applied Spectroscopy)

bution of the oxidation products did not correlate with the distribution of the catalyst. It was suggested that the catalyst residues tended to stabilize the polymer in the immediate vicinity, but also formed reactive species that diffused away from the catalyst to initiate oxidation [239].

Raman confocal microprobe mapping was used to investigate the effect of a silica filler on the phase separation in binary blends of brominated poly(isobutylene-*co-p*-methylstyrene) and *cis*-1-4-polybutadiene with a lateral resolution of less than 1 μm [238]. The size of the polymer domains were less than one micrometer, even though some domains formed aggregates, which in some cases exceeded 5 μm. By using long (70 μm) linear scans the average size of these aggregates as a function of added silica filler was investigated. Using linear scans are less time consuming, but provide similar information. It was found that the average size of these aggregates decreased with increased concentration of silica: from 4–6 μm without silica, down to 2–2.5 μm at 45 phr (parts per hundred) silica as a result of the increasing shear deformations during the internal mixing process.

By using Raman imaging/mapping techniques with a lateral resolution of 1–2 μm inhomogeneous surface structures of a number of polymers were investigated including sub-microdomain structures of polycarbonate/ poly(styrene-*co*-acrylonitrile) blends [243], recrystallization of polyethylene blends [244], surface architecture of a chlorinated PP-primer in thermoplastic olefins [245], the effect of embedded PET fibers on the orientation of PP spherulites during crystallization [246], surface ablation/carbonization of polyimide by laser irradiation [227] and characterization of photoablated PET surfaces [247]. Furthermore, the chemistry and kinetics of holographic grating formation in a multicomponent photopolymer was also studied to directly image the submicron concentration variations responsible for the hologram diffraction [236].

An interesting approach describing the combination of the lateral resolution of near-field scanning optical microscopy with Raman spectroscopy to attempt material-specific surface characterization on the nanoscale [233, 248, 249]. However, long acquisition times (approx. 10 h) and attendant instrumental drift severely limit the advantage in resolution [250]. A strongly increased Raman signal from molecules attached to metallic nanostructures have attracted considerable attention since this effect, referred to as Surface Enhanced Raman Scattering (SERS) shows promise in overcoming the low-sensitivity problems inherent in Raman spectroscopy [251, 252]. Surface-enhanced Raman mapping has been used to produce images of patterned self-assembled monolayers of molecules, differing only in the terminal functional groups, on silver or gold surfaces with a resolution of approximately 2 μm [250, 253, 254]. The technique combines chemical selectivity with the ability to be used under ambient conditions or even in the presence of a liquid, as in an electro-chemical cell containing an aqueous electrolyte [250].

6.5
Near Field Scanning Optical Microscopy

Near field scanning optical microscopy (NSOM) is a scanning probe microscopy technique, which can simultaneously collect nanoscale topographic and fluorescence images by scanning with a force feedback mechanism in the near-field using a fiber optic probe with a sub-wavelength aperture. Thus this technique is not diffraction limited, which allows one to obtain optical (spectroscopic) information in the sub-wavelength length scale. In a region very close to the aperture, there is an evanescent electric field, whose lateral extent is confined by the size of the aperture, which is typically on the order of 25–150 nm [255, 256]. By keeping the sample-probe separation constant within this near-field region (approx. 7–15 nm), an image of the sample is formed with a resolution of ~ 100 nm. The NSOM probe is used to excite the sample and the transmitted light or the excited fluorescence is collected together with topographic data in either transmission or reflection mode. Absorbance and fluorescence spectroscopies provide detailed chemical information while polarization spectroscopy can be used to determine molecular orientation. An important consideration in reflection NSOM is the effect of contributions to the signal from the bulk of the samples. However, the evanescent modes of the NSOM tip will only excite the sample to a depth of approximately 100 nm giving NSOM its surface sensitivity [257].

The application of NSOM to characterization of polymer surfaces has been so far mainly limited to thin conjugated polymer films [255, 257–266]. Spectroscopic studies have revealed strong heterogeneities in the emission from these films [255, 257, 260], while others have observed a homogeneous emission [266]. A direct correlation between the nanometer-scale topography of a conjugated polymer film and the local electronic properties was found by NSOM: thin films of poly(p-phenylene vinylene) exhibited polymer aggregates in the size of 100–200 nm, which correlated to areas with lower photoluminescence (Fig. 35) [257, 262]. Furthermore thin films of substituted polyfluorene also exhibited polymer aggregates in the size of 50–150 nm, which correlated to regions with lower fluorescence [255, 259, 260]. It was suggested that these aggregates were caused by partial insolubility of the polymer in solution prior to casting [255, 259, 260]. It is believed that these aggregated species may be responsible for the reduced fluorescence efficiency of polymeric light emitting devices (LEDs) [264].

However, when thin films of a substituted poly(p-phenylene vinylene) were studied by NSOM no aggregated domains above the resolution limit of 50 nm were found [266]. With careful evaluation of both the spectroscopy and morphology using NSOM, new polymers with superior properties for improved device performance can be created by tailoring the molecular structure in order to avoid aggregation [259, 260, 264, 265].
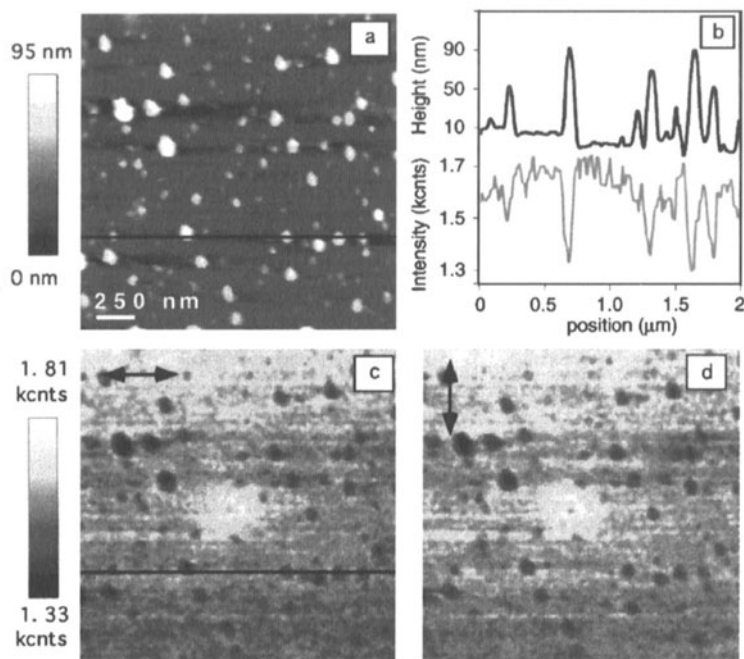
Fig. 35 Near field scanning optical microscopy (NSOM) images ($2 \times 2\ \mu m^2$) of a thin conjugated polymer film: (**a**) topography, (**b**) line scans of lines shown in (**c**) and (**d**), (**c**) and (**d**) NSOM fluorescence images at orthogonal polarizations. (Reprinted with permission from [45]. Copyright 2000 American Chemical Society)

NSOM has also been used to pattern thin polymer films with resolution below 100 nm by photo-oxidation [262]. Moreover, time-correlated single photon counting has been successfully integrated with NSOM to image chemical species with different fluorescence lifetimes with a spatial resolution of < 100 nm [267]. The method was used to follow a photochemical degradation of a thin conjugated polymer film [267]. In addition, infrared absorption spectroscopy has been successfully integrated with NSOM for the analysis of polymer surface phenomena [268, 269]. The chemical specificity of infrared spectroscopy, combined with near-field sub-wavelength resolution was used to characterize transport phenomena in a polymeric photoresist during a UV-lithographic process [268].

7
Outlook

Based on the current state of the art, as reviewed in this article, it is obvious that much work needs to be done in order to approach surface analysis of

polymers with true nanometer scale spatial resolution combined with exact chemical information. For crystalline solids, in an ideal (ultrahigh vacuum) environment great progress has been made following the advent of related real-space imaging techniques, such as the scanning tunneling microscope (for metals and semiconductors). In such cases true atomic (or sub-atomic) information in direct space can be obtained on the sub-nanometer scale. These ordered systems can also be successfully studied down to the atomic level by high-resolution transmission electron microscopy. Polymers, unfortunately, exhibit in general a very complex structural hierarchy and the degree of order typical for inorganic and metallic crystals is virtually unknown in the world of macromolecular systems. The complex structural architecture is obviously reflected also by the surfaces and interfaces of these materials. In addition, due to the large size molecular building blocks the definition of surface as such is not that straightforward as it is for e.g. metallic crystals.

AFM-based approaches for high resolution lateral mapping of the surface chemical composition of polymers have made their debut, expanding resolution limits in favorable cases down to the 20–30 nm level. These approaches, which exploit the use of chemically functionalized tips, can be considered relatively mature in terms of mapping differences in surface and interfacial energies (hydrophilic/hydrophobic) in the sub-micrometer to sub-100 nm regime on flat polymer specimens of known origin or treatment. However, the chemical information is still indirect and limited, and does not match in quality the exact composition information provided on the ensemble average level (without high spatial resolution) by established spectroscopic and spectrometric methods.

The question can be posed: can the problem of exact and accurate surface analysis of polymers be solved and if yes, when? This problem has two facets: a principal, theoretical one, and an experimental, instrumental one. A full theoretical solution means that the problem is solved, when the position and type of each particle (atom) in space and time at (or near) the surface would be known. Problems like this, including the description of atomistic and molecular systems with a high degree of freedom, are treated by statistical mechanics. There are practical and technical problems with an exact atomistic description, including the amount of information and the amount of data that is absolutely necessary. Statistical mechanics treats systems with a high degree of freedom by various means over partition functions for the different ensembles. For such a description the surface must be first defined. As a pure geometrical definition for non-crystalline materials (polymers) is not possible, one option is to define surfaces to within a given depth of field by the technique used to measure composition. For example, surface tension is sensitive to the few top molecular (or atomic) layers due to cutoff in effective pair interaction functions, while XPS (depending on the escape depth and electron take off angle) can look into the surface to a thickness of up to 10 nm, and infrared reflection spectroscopy for surface characterization gathers informa-

tion from a top surface layer with a few to 10 μm depth. For validation of statistical averaging structural information (on the ensemble level) is usually used in the Fourier space. In this review we focused on direct space imaging and direct space local determination of structural heterogeneities, and left surface scattering out from our treatment. For the average description of surfaces the relationship between these two approaches still needs to be established.

If we set out to unravel surface chemical functionalities with high spatial resolution down to atomic detail, we also encounter various practical (technical) problems. It is fair to say that the technique development for direct space analysis (again, we exclude Fourier space methods) is still lagging much behind. Chemical force microscopy can be considered as a first step in the direction of a true description of surface chemical functionalities with high spatial resolution in polymers, primarily based on the chemically sensitive analysis of AFM data via adhesion mapping. At this point the detailed theory for force spectroscopy is not developed beyond the description of London forces. The consideration of the effect of polar functional groups in force spectroscopy (similar to difficulties with solubility parameter and surface tension approaches for polar forces, as well as specific interactions) is still in its infancy. Instead, one must still rely on continuum contact mechanics to couple measured forces and surface free energies.

Clearly, the briefly reviewed complementary spectroscopic techniques are important to approach these current shortcomings in a rational manner for practical purposes. For future progress significant technical refinements for, e.g. XPS and SIMS imaging, will enhance the spatial resolution and will lead to new opportunities. However, the costs for the equipment and instrumentation may limit the widespread application of these approaches compared to AFM-based techniques.

So far we have not considered surface dynamics and time-dependent relaxation processes. These can alter surfaces and thus time averaging must also be considered. At the same time, the speed with which the different approaches gather information about lateral distributions of surface chemical groups must be recognized. Finally, another very essential variable is the chemical environment (solution, gases, etc.). For ionizable surfaces to describe their stability and lateral chemical structure, domain stability of charged heterogeneous patches (usually different from the bulk), differences in ionization behavior, conformational changes and molecular relaxation, which drive dynamic surfaces towards different equilibria in different mediums, must be considered.

It is of course difficult to predict future developments, however, a number of directions can be identified. These comprise the development of the next generation force microscopy instruments (advanced analysis of the behavior of resonating levers), which would deliver topological, physical, as well as chemical information on surfaces in a parallel fashion, with high reso-

lution, fabrication of smaller, sharper probe tips (to increase the resolution and attainable scan rates, with more robust chemical functional coatings), manufacturing small probes with high resonance frequencies and using them with fast and robust electronics to increase imaging speed and systems for robust imaging under full environmental control. These developments will likely lead to a significant broadening of the possible applications and attainable lateral resolutions, which in turn will allow one to bring many more systems and approaches from the academic level to everyday routine, which is of relevance for the practitioners in industry and R&D. This anticipated development must be complemented by simultaneous theoretical advances to enable one to tackle problems with increased complexity. Corresponding developments will likely be complemented by the advancement of other techniques, such as those briefly mentioned, as well as others, which possess the potential to provide new, complementary information about chemistry on the nanoscale.

References

1. Binnig G, Quate CF, Gerber C (1986) Phys Rev Lett 56:930
2. Munz M, Cappella B, Sturm H, Geuss M, Schulz E (2003) Filler-reinforced elastomers scanning force microscopy. Springer, Berlin Heidelberg New York
3. Colton RJ, Engel A, Frommer JE, Gaub HE, Gewirth AA, Guckenberger R, Rabe J, Heckl WM, Parkinson B (1988) Procedures in scanning probe microscopies. Wiley, New York
4. Sheiko SS (2000) New developments in polymer analytics II. Springer, Berlin Heidelberg New York
5. Sarid D (1991) Scanning force microscopy: with applications to electric, magnetic and atomic forces. Oxford University Press, Oxford
6. Wiesendanger R (1994) Scanning probe microscopy and spectroscopy: methods and applications. Cambridge University Press, Cambridge
7. Magonov SNW (1996) Surface analysis with STM and AFM: experimental and theoretical aspects of image analysis. VCH, Weinheim

8. Ratner BD, Tsukruk VV (1998) ACS symposium series, vol. 694. American Chemical Society, Washington, DC

9. Tsukruk VV, Wahl KJ (1999) ACS symposium series, vol. 741. American Chemical Society, Washington, DC

10. Goh MC (1995) In: Prigogine I, Rice SA (eds) Advances in chemical physics, vol. 91. Wiley, New York

11. Hamers RJ (1996) J Phys Chem 100:13 103

12. Miles M (1997) Science 277:1845

13. Miles MJ (1994) In: Spells (ed) Advances in the characterization of solid polymers. Chapman and Hall, London, p 17

14. Frommer J (1992) Angew Chem Int Ed 31:1298

15. Cappella B, Dietler G (1999) Surf Sci Rep 34:1

16. Burnham NA, Colton RJ, Pollock HM (1993) Phys Rev Lett 70:247

17. Frisbie CD, Rozsnyai LF, Noy A, Wrighton MS, Lieber CM (1994) Science 265:2071

18. Garbassi F, Morra M, Occhiello E (2000) Polymer surfaces: From physics to technology. Wiley, New York

19. Koenig JL (1998) Microspectroscopic imaging of polymers. Oxford University Press, Oxford

20. Kirkwood JG, Buff FP (1951) J Chem Phys 19:774

21. Segeren L, Wouters MEL, Bos M, Van den Berg JWA, Vancso GJ (2002) J Chromatogr A 969:215

22. Tan ZJ, Vancso GJ (1997) Macromolecules 30:4665

23. Wendorff JH, Fischer EW (1973) Kolloid-ZuZ Polymere 251:876

24. Adamson AW, Gast AP (1997) Physical chemistry of surfaces. Wiley Interscience, New York

25. Massia SP, Hubbell JA (1991) J Cell Biol 114:1089

26. Chen CS, Mrksich M, Huang S, Whitesides GM, Ingber DE (1997) Science 276:1425

27. Maheshwari G, Brown G, Lauffenburger DA, Wells A, Griffith LG (2000) J Cell Sci 113:1677

28. Craighead HG, James CD, Turner AMP (2001) Curr Opin Solid State Mater Sci 5:177

29. Goessl A, Bowen-Pope DF, Hoffman AS (2001) J Biomed Mater Res 57:15

30. Young T (1855) In: Murray PGJ (ed) Miscellaneous works, vol. 1, London, p 418

31. Dupré A (1869) Théorie mécanique de la chaleur. Gauthier-Villars, Paris

32. Cassie ABD (1948) Discuss Faraday Soc 3:11

33. Israelachvili JN, Gee ML (1989) Langmuir 5:288

34. Laibinis PE, Whitesides GM (1992) J Am Chem Soc 114:9022

35. Schönherr H, Feng CL, Shovsky A (2003) Langmuir 19:10 843

36. Nicolau DV, Taguchi T, Taniguchi H, Yoshikawa S (1999) Langmuir 15:3845

37. Morgen H, Pritchard DJ, Cooper JM (1995) Biosens Bioelectron 10:841

38. Gallop MA, Barrett RW, Dower WJ, Fodor SPA, Gordon EM (1994) J Med Chem 37:1233

39. Fodor SPA, Read JL, Pirrung MC, Stryer L, Lu AT, Solas D (1991) Science 251:767

40. Thiebaud P, Lauer L, Knoll W, Offenhausser A (2002) Appl Surf Sci 17:87

41. Effenhauser CS, Bruin GJM, Paulus A, Ehrat M (1997) Anal Chem 69:3451

42. Makohliso SA, Leonard D, Giovangrandi L, Mathieu HJ, Ilegems M, Aebischer P (1999) Langmuir 15:2940

43. Takano H, Sul JY, Mazzanti ML, Doyle RT, Haydon PG, Porter MD (2002) Anal Chem 74:4640

44. Granlund T, Nyberg T, Roman LS, Svensson M, Inganas O (2000) Adv Mater 12:269

45. Teetsov J, Vanden Bout DA (2000) J Phys Chem B 104:9378

46. Xia YN, Whitesides GM (1998) Angew Chem Int Ed 37:551
47. Xia YN, Rogers JA, Paul KE, Whitesides GM (1999) Chem Rev 99:1823
48. Yasuda HK, Yeh YS, Fusselman S (1990) Pure Appl Chem 62:1689
49. Shenton MJ, Lovell-Hoare MC, Stevens GC (2001) J Phys D: Appl Phys 34:2754
50. Klages CP (1999) Materialwiss Werkstofftech 30:767
51. Hollahan J, Bell A (1974) Wiley, New York
52. Chan CM, Ko TM, Hiraoka H (1996) Surf Sci Rep 24:3
53. Yasuda H (1985) Plasma polymerization. Academic Press, Orlando
54. Gupta B, Anjum N (2003) Radiation effects on polymers for biological use. Springer, Berlin Heidelberg New York
55. Meek JM, Craggs JD (1978) Electrical breakdown of gases. Wiley, New York
56. Tang LP, Wu YL, Timmons RB (1998) J Biomed Mater Res 42:156
57. Schönherr H, Van Os MT, Forch R, Timmons RB, Knoll W, Vancso GJ (2000) Chem Mater 12:3689
58. Schönherr H, Hruska Z, Vancso GJ (2000) Macromolecules 33:4532
59. Ohl A, Schroder K (1999) Surf Coat Technol 119:820
60. Rossier J, Reymond F, Michel PE (2002) Electrophoresis 23:858
61. Skurat VE, Dorofeev YI (1994) Angew Makromol Chem 216:205
62. Feiertag P, Kavc T, Meyer U, Gsoels I, Kern W, Rom I, Hofer F (2001) Synth Met 121:1371
63. Vasilets VN, Nakamura K, Uyama Y, Ogata S, Ikada Y (1998) Polymer 39:2875
64. Dai LM, Griesser HJ, Hong XY, Mau AWH, Spurling TH, Yang YY, White JW (1996) Macromolecules 29:282
65. Bowden N, Brittain S, Evans AG, Hutchinson JW, Whitesides GM (1998) Nature 393:146
66. Roberts MA, Rossier JS, Bercier P, Girault H (1997) Anal Chem 69:2035
67. Lippert T, Wei J, Wokaun A, Hoogen N, Nuyken O (2000) Appl Surf Sci 168:270
68. Schwarz A, Rossier JS, Roulet E, Mermod N, Roberts MA, Girault HH (1998) Langmuir 14:5526
69. Nakayama Y, Matsuda T (1996) J Appl Phys 80:505
70. Dobisz EA, Brandow SL, Bass R, Shirey LM (1998) J Vac Sci Technol B 16:3695
71. Yasin S, Hasko DG, Ahmed H (2001) Appl Phys Lett 78:2760
72. Kim HJ, Lee KJ, Seo Y (2002) Macromolecules 35:1267
73. Berggren KK, Bard A, Wilbur JL, Gillaspy JD, Helg AG, McClelland JJ, Rolston SL, Phillips WD, Prentiss M, Whitesides GM (1995) Science 269:1255
74. Uyama Y, Kato K, Ikada Y (1998) Grafting/characterization techniques/kinetic modeling (Advances in Polymer Science), vol. 137. Springer, Berlin Heidelberg New York
75. Chapiro A (1981) EPJ 19:859
76. Ogiwara Y, Kanda M, Takumi M, Kubota H (1981) J Polym Sci, Part B:Polym Phys 19:457
77. Oster G, Shibata O (1957) J Polym Sci 26:233
78. Uchida E, Uyama Y, Ikada Y (1989) J Polym Sci, Part A: Polym Chem 27:527
79. Tazuke S, Kimura H (1978) J Polym Sci, Part B: Polym Lett 16:497
80. Zhao B, Brittain WJ (2000) Prog Polym Sci 25:677
81. Zhao B, Brittain WJ, Zhou WS, Cheng SZD (2000) J Am Chem Soc 122:2407
82. Husemann M, Morrison M, Benoit D, Frommer KJ, Mate CM, Hinsberg WD, Hedrick JL, Hawker CJ (2000) J Am Chem Soc 122:1844
83. Nakayama Y, Matsuda T (1999) Langmuir 15:5560
84. Ito Y, Chen GP, Guan YQ, Imanishi Y (1997) Langmuir 13:2756
85. Hu SW, Ren XQ, Bachman M, Sims CE, Li GP, Allbritton N (2002) Anal Chem 74:4117

86. Herminghaus S, Jacobs K, Mecke K, Bischof J, Fery A, Ibn-Elhaj M, Schlagowski S (1998) Science 282:916
87. Higgins AM, Jones RAL (2000) Nature 404:476
88. Sharp JS, Jones RAL (2002) Phys Rev E 66:11 801
89. Dalnoki-Veress K, Nickel BG, Dutcher JR (1999) Phys Rev Lett 82:1486
90. Schaffer E, Thurn-Albrecht T, Russell TP, Steiner U (2000) Nature 403:874
91. Schaffer E, Harkema S, Roerdink M, Blossey R, Steiner U (2003) Adv Mater 15:514
92. Chan CM (1994) Polymer surface modification and characterization. Hanser Gardner, München
93. Fox HW, Zisman WA (1950) J Colloid Sci 5:514
94. Fox HW, Zisman WA (1952) J Colloid Sci 7:109
95. Fox HW, Zisman WA (1952) J Colloid Sci 7:428
96. Good RJ (1964) Adv Chem Ser 43:74
97. Good RJ, Girifalco LA (1960) J Phys Chem 64:561
98. Wu S (1982) Polymer interface and adhesion. Marcel Dekker, New York
99. Wu S (1980) J Colloid Interface Sci 73:590
100. Fowkes FM (1962) J Phys Chem 66:382
101. Kaelble DH (1970) J Adhes 2:66
102. Owens DK, Wendt RC (1969) J Appl Polym Sci 13:1741
103. Van Oss CJ, Good RJ, Chaudhury MK (1986) J Colloid Interface Sci 111:378
104. Morra M, Occhiello E, Garbassi F (1990) Adv Colloid Interface Sci 32:79
105. Kloubek J (1992) Adv Colloid Interface Sci 38:99
106. Wu S, Brzozowski KJ (1971) J Colloid Interface Sci 37:686
107. Wu S (1971) J Polym Sci C34:19
108. Van Oss CJ, Chaudhury MK, Good RJ (1988) Chem Rev 88:927
109. Van Oss CJ, Chaudhury MK, Good RJ (1987) Adv Colloid Interface Sci 28:35
110. Schönherr H, Hruska Z, Vancso GJ (1998) Macromolecules 31:3679
111. Drelich J, Wilbur JL, Miller JD, Whitesides GM (1996) Langmuir 12:1913
112. Johnson REJ, Dettre RH (1964) J Phys Chem 68:1744
113. Israelachvilli JN (1991) Intermolecular and surface forces. Academic Press, London
114. Bistac S, Brogly M (2002) In: Somasundaran P (ed) Encyclopedia of surface and colloid science. Marcel Dekker, New York, p 108
115. Chen Y-L, Helm C, Israelachvilli JN (1991) J Phys Chem 95:10 736
116. Israelachvilli JN, Chen Y-L, Yoshizawa H (1995) In: Rimai DS, Demejo LP, Mittal KL (eds) Fundamentals of adhesion and interfaces. VSP, Utrecht, p 261
117. Hamaker HC (1937) Physica 4:1058
118. Rabinovich YI, Adler JJ, Ata A, Singh RK, Moudgil BM (2000) J Colloid Interface Sci 232:17
119. Johnson KL, Kendall K, Roberts AD (1971) Proc R Soc London, Ser A 324:301
120. Lifshitz EM (1995) Soviet Physics JETP-USSR 2:73
121. Schönherr H, Beulen MWJ, Bugler J, Huskens J, Van Veggel FCJM, Reinhoudt DN, Vancso GJ (2000) J Am Chem Soc 122:4963
122. Noy A, Frisbie CD, Rozsnyai LF, Wrighton MS, Lieber CM (1995) J Am Chem Soc 117:7943
123. Noy A, Sanders CH, Vezenov DV, Wong SS, Lieber CM (1998) Langmuir 14:1508
124. Vezenov DV, Noy A, Rozsnyai LF, Lieber CM (1997) J Am Chem Soc 119:2006
125. Feldman K, Tervoort T, Smith P, Spencer ND (1998) Langmuir 14:372
126. Thomas RC, Tangyunyong P, Houston JE, Michalske TA, Crooks RM (1994) J Phys Chem 98:4493

127. Thomas RC, Houston JE, Crooks RM, Kim T, Michalske TA (1995) J Am Chem Soc 117:3830
128. Akari S, Horn D, Keller H, Schrepp W (1995) Adv Mater 7:549
129. Green JBD, McDermott MT, Porter MD, Siperko LM (1995) J Phys Chem 99:10 960
130. Van der Vegte EW, Hadziioannou G (1997) J Phys Chem B 101:9563
131. Schönherr H, Vancso GJ (1997) Macromolecules 30:6391
132. Schönherr H, Vancso GJ (1998) J Polym Sci, Part B: Polym Phys 36:2483
133. McKendry R, Theoclitou ME, Abell C, Rayment T (1998) Langmuir 14:2846
134. McKendry R, Theoclitou ME, Rayment T, Abell C (1998) Nature 391:566
135. Green JBD, McDermott MT, Porter MD (1996) J Phys Chem 100:13 342
136. Noy A, Vezenov DV, Lieber CM (1997) Annu Rev Mater Sci 27:381
137. Van der Vegte EW, Hadziioannou G (1997) Langmuir 13:4357
138. Sinniah SK, Steel AB, Miller CJ, ReuttRobey JE (1996) J Am Chem Soc 118:8925
139. Weihs TP, Nawaz Z, Jarvis SP, Pethica JB (1991) Appl Phys Lett 59:3536
140. Sheiko SS, Moller M, Reuvekamp E, Zandbergen HW (1993) Phys Rev B 48:5675
141. Binggeli M, Mate CM (1994) Appl Phys Lett 65:415
142. Weisenhorn AL, Hansma PK, Albrecht TR, Quate CF (1989) Appl Phys Lett 54:2651
143. Schönherr H (1999) From Functional Group Ensembles to Single Molecules: Scanning Force Microscopy of Supramolecular and Polymeric Systems, Ph. D. Thesis, University of Twente
144. Bar G, Thomann Y, Brandsch R, Cantow HJ, Whangbo MH (1997) Langmuir 13:3807
145. Bar G, Brandsch R, Whangbo MH (1998) Langmuir 14:7343
146. Bar G, Thomann Y, Whangbo MH (1998) Langmuir 14:1219
147. Krausch G, Hipp M, Boltau M, Marti O, Mlynek J (1995) Macromolecules 28:260
148. Overney RM, Meyer E, Frommer J, Brodbeck D, Luthi R, Howald L, Guntherodt HJ, Fujihira M, Takano H, Gotoh Y (1992) Nature 359:133
149. Putman CAJ, De Grooth BG, Van Hulst NF, Greve J (1992) J Appl Phys 72:6
150. Viani MB, Schaffer TE, Chand A, Rief M, Gaub HE, Hansma PK (1999) J Appl Phys 86:2258
151. Viani MB, Schaffer TE, Paloczi GT, Pietrasanta LI, Smith BL, Thompson JB, Richter M, Rief M, Gaub HE, Plaxco KW, Cleland AN, Hansma HG, Hansma PK (1999) Rev Sci Instrum 70:4300
152. Burnham NA, Colton RJ, Pollock HM (1992) Phys Rev Lett 69:144
153. Hutter JL, Bechhoefer J (1993) Rev Sci Instrum 64:1868
154. Sader JE (1998) J Appl Phys 84:64
155. Tortonese M, Kirk M (1997) Proc SPIE 3009:53
156. Weisenhorn AL, Maivald P, Butt HJ, Hansma PK (1992) Phys Rev B 45:11 226
157. Carpick RW, Salmeron M (1997) Chem Rev 97:1163
158. Vancso GJ, Schönherr H (1999) In: Tsukruk VV, Wahl KJ (eds) Microstructure and microtribology of polymer surfaces (ACS Symposium Series), vol. 741. American Chemical Society, New York, p 317
159. Hugel T, Seitz M (2001) Macromol Rapid Commun 22:989
160. Janshoff A, Neitzert M, Oberdorfer Y, Fuchs H (2000) Angew Chem Int Ed 39:3213
161. Zapotoczny S, Auletta T, De Jong MR, Schönherr H, Huskens J, Van Veggel FCJM, Reinhoudt DN, Vancso GJ (2002) Langmuir 18:6988
162. Auletta T, De Jong MR, Mulder A, van Veggel FCJM, Huskens J, Reinhoudt DN, Zou S, Zapotoczny S, Schönherr H, Vancso GJ, Kuipers L (2004) J Am Chem Soc 126:1577
163. Jenkins ATA, Boden N, Bushby RJ, Evans SD, Knowles PF, Miles RE, Ogier SD, Schönherr H, Vancso GJ (1999) J Am Chem Soc 121:5274

164. Alley RL, Komvopoulos K, Howe RT (1994) J Appl Phys 76:5731
165. Howald L, Luthi R, Meyer E, Guthner P, Guntherodt HJ (1994) Z Phys B: Condens Matter 93:267
166. Akari S, Schrepp W, Horn D (1996) Langmuir 12:857
167. Werts MPL, Van der Vegte EW, Grayer V, Esselink E, Tsitsilianis C, Hadziioannou G (1998) Adv Mater 10:452
168. Vancso GJ, Snétivy D, Schönherr H (1998) In: Ratner BD, Tsukruk VV (eds) Scanning probe microscopy of polymers (ACS Symposium Series), vol. 694. American Chemical Society, New York, p 67
169. Vancso GJ, Förster S, Leist H (1996) Macromolecules 29:2158
170. Nisman R, Smith P, Vancso GJ (1994) Langmuir 10:1667
171. Smith PF, Nisman R, Ng C, Vancso GJ (1994) Polym Bull 33:459
172. Pearce R, Vancso GJ (1998) Polymer 39:6743
173. Mizes HA, Loh KG, Miller RJD, Ahuja SK, Grabowski EF (1991) Appl Phys Lett 59:2901
174. Joyce SA, Houston JE, Michalske TA (1992) Appl Phys Lett 60:1175
175. Van der Werf KO, Putman CAJ, De Grooth BG, Greve J (1994) Appl Phys Lett 65:1195
176. Baselt DR, Baldeschwieler JD (1994) J Appl Phys 76:33
177. Berger CEH, Van der Werf KO, Kooyman RPH, De Groot BG, Greve J (1995) Langmuir 11:4188
178. Radmacher M, Cleveland JP, Fritz M, Hansma HG, Hansma PK (1994) Appl Surf Sci 66:2159
179. Hillborg H, Tomczak N, Olah A, Schönherr H, Vancso GJ (2004) Langmuir 20:785
180. Jaeger R, Bergshoef MM, Batlle CMI, Schönherr H, Vancso GJ (1998) Macromol Symp 127:141
181. Jaeger R, Schönherr H, Vancso GJ (1996) Macromolecules 29:7634
182. Krotil HU, Stifter T, Waschipky H, Weishaupt K, Hild S, Marti O (1999) Surf Interface Anal 27:336
183. Okabe Y, Furugori M, Tani Y, Akiba U, Fujihira M (2000) Ultramicroscopy 82:203
184. Krotil HU, Stifter T, Marti O (2000) Rev Sci Instrum 71:2765
185. Hruska Z, Lepot X (2000) J Fluorine Chem 105:87
186. Duwez AS, Nysten B (2001) Langmuir 17:8287
187. Duwez AS, Poleunis C, Bertrand P, Nysten B (2001) Langmuir 17:6351
188. Ton-That C, Teare DOH, Bradley RH (2000) Chem Mater 12:2106
189. Ton-That C, Campbell PA, Bradley RH (2000) Langmuir 16:5054
190. Eaton PJ, Graham P, Smith JR, Smart JD, Nevell TG, Tsibouklis J (2000) Langmuir 16:7887
191. Eaton P, Smith JR, Graham P, Smart JD, Nevell TG, Tsibouklis J (2002) Langmuir 18:3387
192. Nie HY, Walzak MJ, Berno B, McIntyre NS (1999) Langmuir 15:6484
193. Yip J, Chan K, Sin KM, Lau KS (2003) Appl Surf Sci 205:151
194. Wang B, Chen L, Abdulali-Kanji Z, Horton JH, Oleschuk RD (2003) Langmuir 19:9792
195. Bhargava R, Wall BG, Koenig JL (2000) Appl Spectrosc 54:470
196. Benninghoven A (1994) Angew Chem Int Ed 33:1023
197. Van Vaeck L, Adriaens A, Gijbels R (1999) Mass Spectrom Rev 18:1
198. Adriaens A, Van Vaeck L, Adams F (1999) Mass Spectrom Rev 18:48
199. Hagenhoff B (2000) Mikrochim Acta 132:259
200. Chabala JM, Soni KK, Li J, Gavrilov KL, Levisetti R (1995) Int J Mass Spectrom Ion Processes 143:191
201. Kotter F, Benninghoven A (1998) Appl Surf Sci 133:47

202. Leonard D, Mathieu HJ (1999) Fresenius J Anal Chem 365:3
203. Stapel D, Thiemann M, Benninghoven A (2000) Appl Surf Sci 158:362
204. Stapel D, Benninghoven A (2001) Appl Surf Sci 174:261
205. Hagenhoff B, Deimel M, Benninghoven A, Siegmund HU, Holtkamp D (1992) J Phys D: Appl Phys 25:818
206. Bourdos N, Kollmer F, Benninghoven A, Sieber M, Galla HJ (2000) Langmuir 16:1481
207. Frisbie CD, Wollman EW, Wrighton MS (1995) Langmuir 11:2563
208. Bernasik A, Rysz J, Budkowski A, Kowalski K, Camara J, Jedlinski J (2001) Macromol Rapid Commun 22:829
209. Bullett NA, Short RD, O'Leary T, Beck AJ, Douglas CWI, Cambray-Deakin M, Fletcher IW, Roberts A, Blomfield C (2001) Surf Interface Anal 31:1074
210. Yang ZP, Belu AM, Liebmann-Vinson A, Sugg H, Chilkoti A (2000) Langmuir 16:7482
211. Brummel CL, Lee INW, Zhou Y, Benkovic SJ, Winograd N (1994) Science 264:399
212. Brummel CL, Vickerman JC, Carr SA, Hemling ME, Roberts GD, Johnson W, Weinstock J, Gaitanopoulos D, Benkovic SJ, Winograd N (1996) Anal Chem 68:237
213. Pacholski ML, Winograd N (1999) Chem Rev 99:2977
214. Cannon DM, Pacholski ML, Winograd N, Ewing AG (2000) J Am Chem Soc 122:603
215. Belu AM, Yang ZP, Aslami R, Chilkoti A (2001) Anal Chem 73:143
216. Leufgen KM, Rulle H, Benninghoven A, Sieber M, Galla HJ (1996) Langmuir 12:1708
217. Weng LT, Smith TL, Feng JY, Chan CM (1998) Macromolecules 31:928
218. Li HW, Huck WTS (2002) Curr Opin Solid State Mater Sci 6:3
219. Quirk RA, Briggs D, Davies MC, Tendler SJB, Shakesheff KM (2001) Surf Interface Anal 31:46
220. Deimel M, Rulle H, Liebing V, Benninghoven A (1998) Appl Surf Sci 134:271
221. Gerardi C, DeRiccardis F, Milella E (1998) Mater Sci Eng, C 5:203
222. Marien J, Ghitti G, Jerome R, Teyssie P (1993) Polym Bull 30:435
223. Fulghum JE (1999) J Electron Spectrosc Relat Phenom 100:331
224. Turner NH, Schreifels JA (2000) Anal Chem 72:99R
225. Drummond IW (1996) Philos Trans R Soc London, Ser A 354:2667
226. Artyushkova K, Wall B, Koenig J, Fulghum JE (2000) Appl Spectrosc 54:1549
227. Lippert T, Ortelli E, Panitz JC, Raimondi F, Wambach J, Wei J, Wokaun A (1999) Appl Phys A 69:S651
228. Gusev AI, Vasseur OJ, Proctor A, Sharkey AG, Hercules DM (1995) Anal Chem 67:4565
229. Garden RW, Sweedler JV (2000) Anal Chem 72:30
230. Stoeckli M, Farmer TB, Caprioli RM (1999) J Am Soc Mass Spectrom 10:67
231. Krause J, Stoeckli M, Schlunegger UP (1996) Rapid Commun Mass Spectrom 10:1927
232. Tabaksblat R, Meier RJ, Kip BJ (1992) Appl Spectrosc 46:60
233. Mulvaney SP, Keating CD (2000) Anal Chem 72:145R
234. Pappas D, Smith BW, Winefordner JD (2000) Appl Spectrosc Rev 35:1
235. Keen I, Rintoul L, Fredericks PM (2001) Appl Spectrosc 55:984
236. Kagan CR, Harris TD, Harris AL, Schilling ML (1998) J Chem Phys 108:6892
237. Schaeberle MD, Morris HR, Turner JF, Treado PJ (1999) Anal Chem 71:175A
238. Appel R, Zerda TW, Waddell WH (2000) Appl Spectrosc 54:1559
239. Blakey I, George GA (2000) Polym Degrad Stab 70:269
240. Markwort L, Kip B, Dasilva E, Roussel B (1995) Appl Spectrosc 49:1411
241. Kim H, Urban MW (2000) Langmuir 16:5382
242. Zhao YQ, Urban MW (2000) Macromolecules 33:2184
243. Schmidt P, Kolarik J, Lednicky F, Dybal J, Lagaron JM, Pastor JM (2000) Polymer 41:4267

244. Morgan RL, Hill MJ, Barham PJ, Van der Pol A, Kip BJ, Ottjes R, van Ruitein J (2001) Polymer 42:2121
245. Morris HR, Munroe B, Ryntz RA, Treado PJ (1998) Langmuir 14:2426
246. Fernandez MR, Merino JC, Gobernado-Mitre MI, Pastor JM (2000) Appl Spectrosc 54:1105
247. Rossier JS, Bercier P, Schwarz A, Loridant S, Girault HH (1999) Langmuir 15:5173
248. Narita Y, Tadokoro T, Ikeda T, Saiki T, Mononobe S, Ohtsu M (1998) Appl Spectrosc 52:1141
249. Jahncke CL, Paesler MA, Hallen HD (1995) Appl Phys Lett 67:2483
250. Yang XM, Tryk DA, Hashimoto K, Fujishima A (1998) J Raman Spectrosc 29:725
251. Kneipp K, Kneipp H, Itzkan I, Dasari RR, Feld MS (1999) Chem Rev 99:2957
252. Campion A, Kambhampati P (1998) Chem Soc Rev 27:241
253. Yang XM, Tryk DA, Hasimoto K, Fujishima A (1996) Appl Phys Lett 69:4020
254. Yang XM, Tryk DA, Ajito K, Hashimoto K, Fujishima A (1996) Langmuir 12:5525
255. Teetsov JA, Vanden Bout DA (2001) J Am Chem Soc 123:3605
256. Dunn RC (1999) Chem Rev 99:2891
257. DeAro JA, Weston KD, Buratto SK, Lemmer U (1997) Chem Phys Lett 277:532
258. Stevenson R, Granstrom M, Richards D (1999) Appl Phys Lett 75:1574
259. Teetsov J, Vanden Bout DA (2001) Macromol Symp 167:153
260. Teetsov J, Vanden Bout DA (2002) Langmuir 18:897
261. DeAro JA, Moses D, Buratto SK (1999) Appl Phys Lett 75:3814
262. DeAro JA, Lemmer U, Moses D, Buratto SK (1999) Synth Met 101:300
263. DeAro JA, Gupta R, Heeger AJ, Buratto SK (1999) Synth Met 102:865
264. Nguyen TQ, Martini IB, Liu J, Schwartz BJ (2000) J Phys Chem B 104:237
265. Nguyen TQ, Schwartz BJ, Schaller RD, Johnson JC, Lee LF, Haber LH, Saykally RJ (2001) J Phys Chem B 105:5153
266. Huser T, Yan M (2001) Synth Met 116:333
267. Kwak ES, Kang TJ, Bout DAV (2001) Anal Chem 73:3257
268. Dragnea B, Preusser J, Szarko JM, McDonough LA, Leone SR, Hinsberg WD (2001) Appl Surf Sci 175:783
269. Dragnea B, Preusser J, Schade W, Leone SR, Hinsberg WD (1999) J Appl Phys 86:2795

Editor: Hans-Henning Kausch

Nano-Imaging of Polymers by Optical Microscopy

Shinzaburo Ito (✉) · Hiroyuki Aoki

Department of Polymer Chemistry, Graduate School of Engineering,
Kyoto University, Katsura, 615-8510 Kyoto, Japan
sito@photo.polym.kyoto-u.ac.jp

Abstract The developments of laser scanning confocal microscopy (LSCM) and scanning near-field optical microscopy (SNOM) have expanded the application range of optical microscopy from micron to nanometer dimensions, in which the molecular and macromolecular materials exhibit intrinsic fundamental characteristics closely related to their functionality. Although atomic force and electron microscopes have often been utilized for observing materials in nanometer dimensions, the world of the critical length (10–100 nm) of nano-technology and science is now illuminated by "light", and is revealed as real optical images from different points of view associated with not only morphology but also spectroscopic, analytical, time-resolved and opto-electrical responses in a local space. This article reviews the recent findings made by LSCM and SNOM mainly in terms of morphology of polymeric materials; particular concerns are in the phase-separated structures of polymer blends, conformation and morphology of a single polymer chain, and also two-dimensional ultra-thin polymer films. These optical techniques will become an indispensable tool for understanding molecular and biological systems.

Abbreviations

AFM	atomic force microscopy
BAM	Brewster angle microscopy
BS	beam splitter
DNA	deoxyribonucleic acid
DUV	deep ultraviolet
Eo	eosin
FWHM	full width at half maximum
IPN	interpenetrating polymer network
LB	Langmuir-Blodgett
LSCM	laser scanning confocal microscopy
LSCFM	laser scanning confocal fluorescence microscopy
NA	numerical aperture
OM	optical microscopy
PB	polybutadiene
PDF	poly(9,9-dialkylfluorene)
Pe	perylene
PiBMA	poly(isobutyl methacrylate)
PMMA	poly(methyl methacrylate)
PODMA	poly(octadecyl methacrylate)
PPV	poly(p-phenylenevinylene)
PS	polystyrene
Py	pyrene
R6G	rhodamine-6G
SBR	poly(styrene-ran-butadiene)
SD	spinodal decomposition
SEM	scanning electron microscopy
SNOM	scanning near-field optical microscopy
STED	stimulated emission depletion
SWNT	single wall carbon nanotube
TEM	transmission electron microscopy
TIR	total internal reflection

1
Introduction

Optical microscopy (OM) has played essential roles in science, particularly for biological and medical research. This is due to the great advantage of OM; that is, real images of materials are easily observable at an ambient temperature and the atmospheric pressure, although the spatial resolution is limited to a micron scale due to the diffraction of light. In spite of a low magnification, optical techniques have reserved indispensable positions so far when the

objectives are so-called "soft materials" such as cells, micelles, membranes and a variety of organic molecular assemblies. This is also the case for observation of polymeric materials. Electron microscopes such as TEM and SEM have been widely employed for studying morphology of polymers, because the real space images provide unambiguous evidence on nano-structures of various polymer systems with a high resolution. Although it is often very hard for the samples to be selectively stained and to withstand the severe irradiation of electron beams in vacuo, the information obtained by the real images is superior to that from scattering methods using light, neutron, and X-ray etc., in particular for studying amorphous polymers. The growing interest in recent years in nano-science and technology has raised strong demands on nano-imaging in real space, and many researchers in materials science have awaited the developments of high resolution and convenient OM, applicable to soft materials and polymers. Here, we review the rapid progress made in the last decade on nano-imaging of polymer samples mainly by laser scanning confocal microscopy and scanning near field optical microscopy.

2
Nano-Imaging with Laser Scanning Confocal Microscopy

2.1
Instruments

Laser scanning confocal microscopy (LSCM) has been developed as a novel microscopic instrument, possessing the full merits of the optical techniques mentioned above. It is a kind of scanning microcopy technique that measures only one point in an object at a time by focusing the laser light on the small volume and scans it point by point to make an image [1, 2], whereas a conventional microscope can obtain an entire image of an object in the field of view at once. Figure 1a shows a typical optical system for confocal microscopy. The light from a point source is focused by an objective lens to illuminate a small point in the object. The optical response such as scattering, reflection, and fluorescence from the point illuminated, is collected by the same lens, and its intensity is measured by a photo-detector equipped with a pinhole. The confocal pinhole acts as a spatial filter for the selective detection of signals from the focal point, resulting in enhancement of the image contrast and improvement of the spatial resolution. The presence of the confocal pinhole is effective especially in improving the resolution in the depth direction. The stray light from the point out of the focal plane does not focus on the confocal pinhole and cannot be detected by the photo-detector, as indicated by a dashed line in Fig. 1a. Thus, a cross sectional image of the object can be obtained at the focal plane with a very shallow focal depth in the order of several
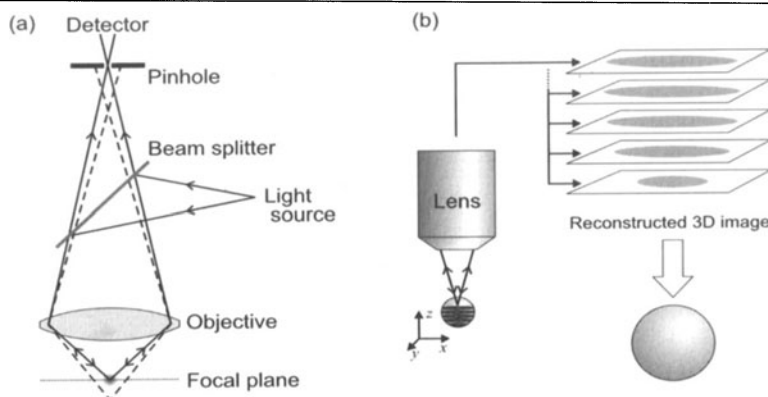
Fig. 1 (**a**) Schematic illustration of a typical optics for confocal microscopy and (**b**) a three-dimensional imaging process. The light from a point source is focused on a tiny point in an object. The signal is collected by the same lens and guided to a detector (*solid path* in *panel a*). The illumination and detection point is scanned point by point to make a microscopy image. The stray light from the point out of the focal plane is rejected by a pinhole put in front of the detector (*dashed line* in *panel a*). Stacking the images at different depths yields a three-dimensional image of the object

hundred nanometers without contribution of surrounding planes. The depth-discrimination with high contrast indicates the ability to observe the object three-dimensionally as shown in Fig. 1b. A set of individual images sliced at different levels affords a three dimensional image over the entire specimen through the reconstruction by image processing on a computer. This is the most striking advantage of confocal microscopy.

In OM, the spatial resolution both lateral (parallel to the focal plane) and axial (perpendicular to the focal plane) is always a critical issue. As to the lateral resolution, laser scanning confocal fluorescence microscopy (LSCFM) has a high resolution of $0.42\lambda/NA$, where NA is the numerical aperture; hence, the use of a large NA objective with blue laser light allows one to achieve a high resolution of less than 200 nm [3]. Polymer films containing coumarine-labeled latex particles with diameters of 500, 220, or 100 nm were examined to estimate the resolution of LSCFM [4]. The measurement of a single latex particle proved that the accuracy of the setup was in the order of 200 nm laterally and 400 nm axially.

2.2
Phase Separation Structures of Polymer Blends

This technique has been successfully applied to investigate phase-separated structures of polymer blends [5, 6]. Li et al. studied surface and bulk morphologies of polystyrene (PS)/poly(methyl methacrylate) (PMMA) blend films and found marked differences in the structure as a function of depth
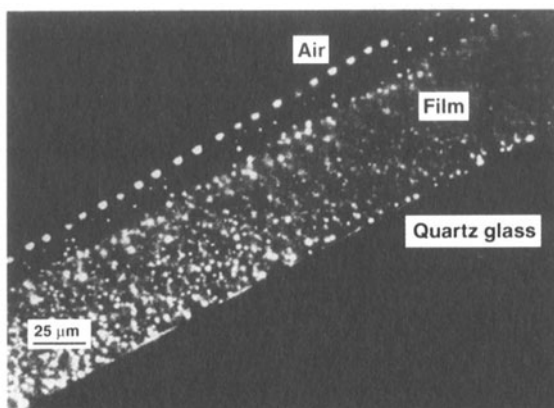
Fig. 2 Cross section morphology of a PS/PMMA blend (9/1) film prepared by casting the solution in toluene at a slow evaporation rate. Bright domains represent the dye-labeled PMMA-rich phase. Reprinted with permission of [7], copyright (1997) American Chemical Society

from the surface [7]. Because interfacial effects are usually dominant for determining the stability of systems particularly in the proximity of the interface, the effects tend to propagate into the bulk and often affect the phase-separation mechanism of the whole film. However, under a slow solvent evaporation rate, the mono-disperse PMMA-rich domains show a highly periodic distribution at the surface. Figure 2 shows a cross-section image of the blend film. There is a depletion layer between the surface and the bulk, in which PMMA molecules are diffusively transferred from the liquid-like bulk to the surface, resulting in a depletion layer free from PMMA-rich particles in between. As this work shows, LSCM provides invaluable information on three-dimensional morphologies even for wet samples containing a liquid phase.

LSCFM has been extensively employed for investigating various polymer systems such as interpenetrating polymer networks (IPN) and polymer latex films. Harmon *et al.* studied thermo-responsive hydrogel networks composed of a crosslinked poly(N-isopropylacrylamide) and a linear polymer of N-alkylacrylamide, and discussed the relationship between the kinetics of the volume phase transition and the phase separated morphology of the semi-IPN [8]. Winnik and coworkers have published many articles on the coalescence process of polymer latex. For example, using a series of sliced images of LSCFM, they visualized the depth profile from the top surface. Consequently the real images successfully clarified the distribution of particles, the size of each domain, and the morphology of blend films in the course of coalescence or segregation of the component polymers [9–11].

2.3
Time Dependent Observation

Another advantage of LSCM and LSCFM is that time evolution of structural changes can be followed. If the temperature of a binary polymer blend is suddenly shifted from the single-phase region to the spinodal region of the phase diagram, the system becomes thermodynamically unstable and starts separating into two phases. This demixing process is well known as spinodal decomposition (SD). The SD process proceeds in the order of 1) early stage, 2) intermediate stage, and 3) late stage. The blend shows a bicontinuous sponge-like structure during the whole stages, while keeping continuous growing of the phase separated structure. The time evolution at each stage has been extensively studied by both scattering methods and microscopic measurements, the latter mostly performed using electron microscopy and LSCFM. Although the structure in the early stage is too small to be visible on LSCFM, the morphology in the intermediate and late stages can be clearly observed in a wide range of dimensions from sub-microns to a millimeter scale at the maximum [12]. For example, Jinnai and coworkers reported a detailed analysis for the time evolution of bicontinuous interface of a phase separated polymer blend in the late stage of SD, using a binary mixture of deuterated polybutadiene (DPB) and polybutadiene (PB) [13, 14]. The latter polymer was labeled with anthracene chromophores in order to obtain a contrast enhancement in fluorescence microscopy. Figure 3 depicts typical LSCFM images showing the growing structure of the phase separated DPB/PB mixture with the elapse of time. Only the PB-rich phase is visible owing to the selective la-
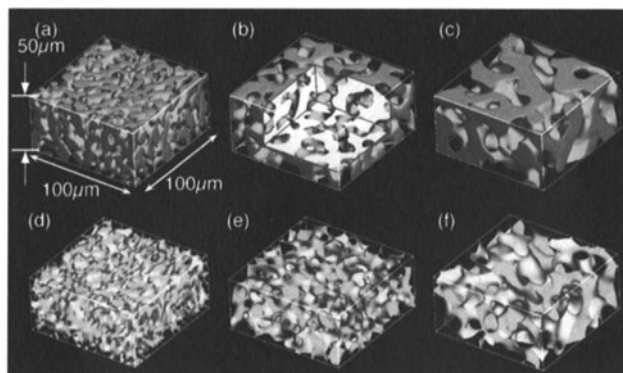
Fig. 3 Time evolution of bicontinuous structures in the DPB/PB blend at the critical composition. The LSCFM images were taken at (**a**) 1675, (**b**) 2880, and (**c**) 4860 min after the onset of SD. These images show only the PB-rich phase labeled with anthracene. Parts (**d**) to (**f**) represent the interface between two coexisting phases for the 3D volume corresponding to (**a**) to (**c**) , respectively. Reprinted with permission of [13], copyright (2000) American Chemical Society

beling with anthracene. On the other hand, the DPB-rich phase is shown as a dark or empty part. From these three-dimensional images, the local curvatures of the interfaces were quantitatively analyzed as a function of time, and it was confirmed that the phase separation process of this mixture well agreed with the prediction of theoretical equations.

Numerous articles have been published over the last decade with emphasis on the time evolution of the SD in binary polymer blends [15–18]. The dynamics could be clarified based on the visual images in three dimensions, owing to the technical development of LSCM and LSCFM.

2.4
Contrast

As shown in the previous figures, labeling is one of important keys for taking excellent images by OM. One needs considerable support of synthetic chemistry to introduce fluorescent probes selectively at a desired position of a polymer chain or to one component of polymer blends. Since each probe has its intrinsic excitation and emission wavelengths, one can get a high sensitivity and contrast in comparison to the non-labeled portion by choosing an appropriate set of the excitation laser light and the detection optical filters. This means that the use of different wavelength light for a given sample allows one to depict selectively one of the components in a multi-colored image, depending on the mechanism of contrast, the source of the signal, and the kind of chemicals etc. For example, an Ar laser (364, 458, 488, and 514 nm) and a He-Ne laser (543 and 633 nm) are often used as convenient light sources supplying various wavelengths. Figure 4 shows again a phase separated morphology of poly(styrene-*ran*-butadiene) (SBR) and polybutadiene (PB) blends [18]. These images were taken by irradiating the sample with two different wavelength light at 488 nm for panel a and 364 nm for the

(a)   (b)   (c)

Reflection LSCM image   Fluorescence LSCM image   Superposition of (a) and (b)
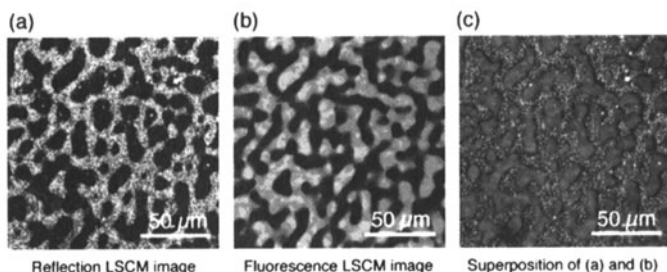
Fig. 4 LSCM images at a depth of 20 μm from the surface of the phase-separated SBR/PB (50/50) blend film. (**a**) Reflection LSCM image observed with λ = 488 nm (**b**) LSCFM image of the same field as in image (**a**) observed using λ = 364 nm (**c**) Superposition of the two images, (**a**) and (**b**) PB was labeled with anthracene. Reprinted with permission of [18], copyright (2001) American Chemical Society

middle panel b. Only the latter 364 nm light excited the anthracene labels attached to PB. Hence, the bright part of the middle image indicates the PB-rich domain. At 488 nm, both SBR- and PB-rich domains should be transparent. However, panel a of Fig. 4, which was taken in the reflection mode of LSCM at 488 nm, shows a bicontinuous phase separated structure with a sufficient contrast. These two images are complementary to each other, providing a perfectly superposed image as shown in panel c of Fig. 4. Therefore, the bright area of panel a must be assigned to the SBR-rich domain. This result suggests that the SBR-rich domain has inhomogeneous refractive index with a scale of the wavelength, resulting in a higher reflectivity to the laser light compared to the PB-rich phase. Thus, in addition to the selection of fluorescent probes, LSCM possesses tunability in choosing the wavelength of light to fit with optical properties of the objectives that we intend to see the interior.

2.5
Observation of a Single Polymer

The spatial resolution of LSCFM is still limited to a sub-micron scale. However, it is accessible to a specified volume on the image, in which a small objective can be subjected to fluorescence spectroscopy by means of the optical systems with the intense excitation laser and a highly sensitive light detection apparatus. The fluorescence spectra, time-resolved decay curves, fluorescence polarization, can be observed at a focal point under a microscope. Even in a liquid solution, in which all the solutes rapidly diffuse by Brownian motion, nano-particles of polymer latex and micelles of block copolymers in D_2O are optically trapped, and then their individual fluorescence characteristics can be measured one by one [4]. Since the diameter of a single latex bead or the size of a single micelle is far smaller than the spatial resolution of the microscope, it appears as a tiny bright spot like a star in the picture. It is impossible to see the shape of the particle. However, if the particle is isolated from the others at a sufficiently diluted concentration, LSCFM becomes a powerful tool for spectroscopic studies on a single particle, a single polymer chain, a single molecule etc.

Single molecule fluorescence spectroscopy by LSCFM has often been applied to conjugated polymer molecules, because much attention has been paid to their electro- and photo-functions that is used in light-emitting diodes and other applications such as thin film transistors, sensors, displays, and non-linear optics. Besides these applications, conjugated polymers are suited for LSCFM from a technical point of view, because the large fluorescence intensity from a single chain composed of multiple chromophores allows one to investigate the particular photochemistry and photophysics of the single chain. Poly(p-phenylenevinylene) (PPV) and its derivatives (Scheme 1) have been extensively studied so far [19–25]. A spin-cast film of polystyrene containing extremely diluted PPV-type polymers exhibits small spots
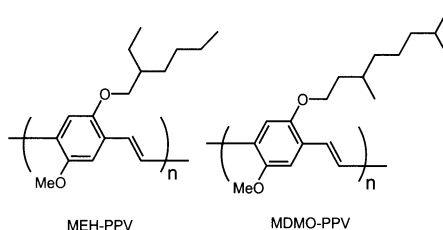
Scheme 1 Chemical structures of Poly(*p* –phenylenevinylene) (PPV) derivatives

of ca. 300 nm in diameter, which are resulted from fluorescence of individual polymer molecules, but blurred by the diffraction limit of light. These spots were assigned to single chains because the density, the number of spots per unit area, varied linearly with the concentration of PPV in the spin-cast solution.

Surprisingly, each spot showed discrete jumps of fluorescence intensity in the transient measurement; the intensity was intermittent and switched rapidly "on" and "off" states as shown in Fig. 5a. This behavior is often found in single molecule spectroscopy due to photobleaching of the chromophore
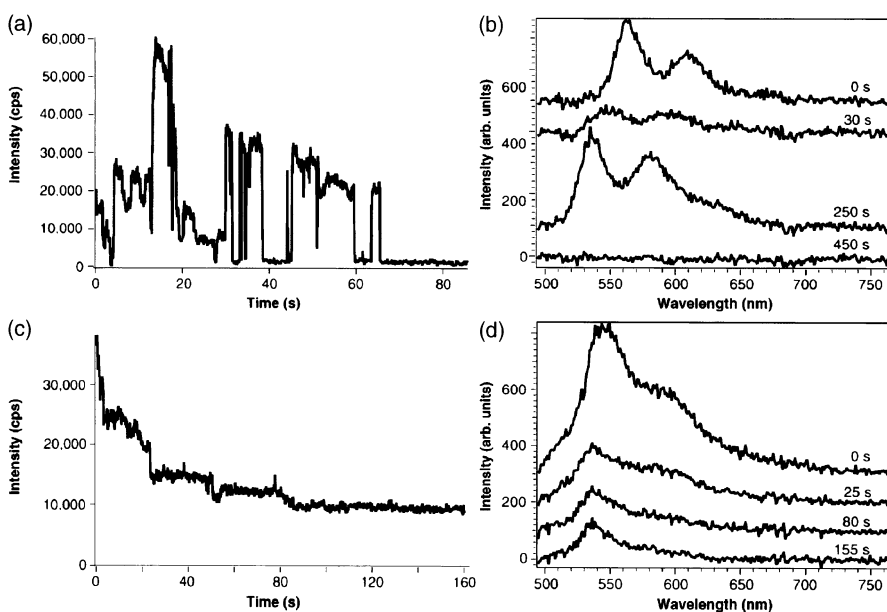
Fig. 5 (**a**), (**c**) Fluorescence intensity transients of a single conjugated polymer (MEH-PPV) spun from toluene and chloroform solution, respectively. (**b**), (**d**) Time-evolution of spectra of a MEH-PPV molecule spun from toluene and chloroform, respectively. Spectra are offset in vertical direction and labeled with the time at which they were taken. Reprinted with permission of [20], copyright (2001) Elsevier

or temporary conversion to a long-lived transient species like a triplet state. However, since the polymer has many chromophores in the chain, it is very hard to understand such a stepwise alteration. To explain this discrete jump, we need to assume that all of the chromophores in the single polymer behave like one molecule. Energy migration along the polymer chain has been suggested to be sufficiently rapid within the lifetime of the excited state (ca. 200 ps), and the excitation energy to collide efficiently with a quenching site produced in the polymer chain. This site could be generated with a photochemical process. For example, photoinduced charge separation occurs easily between an electron-donating chromophore and an acceptor molecule, and the radical cations and radical anions thus produced are known to be efficient quenchers for the excited state of chromophores. A pair of separated charges is a temporary species, which can return to the original state with the charge recombination process. Consequently, the spot intensity of fluorescence reverts back to the initial level.

In addition to this temporary quenching, a permanent defect may be produced by photochemical reactions such as photodecomposition, photo-oxidation, and photo-isomerization. Once the reaction occurs somewhere in a polymer chain, the bright spot will immediately disappear irreversibly from the image. Fluorescence spectra of the single spot can be measured by LSCFM equipped with an imaging monochromator and a liquid nitrogen cooled CCD [20, 21]. Figure 5b shows time-evolution of fluorescence spectra of a PPV-type molecule adsorbed on a cover glass. At the beginning, the first vibronic band appears around 570 nm, but the spectra shift to the blue side up to 50 nm during continuous excitation at 488 nm. This behavior indicates dispersion of the excitation energy levels in the polymer chain probably due to the local conformation of polymer segments. Energy migration takes place from the high energy level chromophores to the low level sites. Since the lowest site occupies the excitation energy longer than the high level site, it will be first subjected to photoreactions that yield photochemical defects. After consumption of all chromophores at the low levels, the remaining high-energy sites start emitting the fluorescence. Thus the spectral shift indicates temporal changes of the excited state of a single polymer, showing efficient communication among multiple chromophores through rapid energy transfer along the chain.

The discrete behavior of PPV polymers depends on the conformation of polymer chain. If the polymer sample was prepared from a good solvent, or if PPV was embedded in a matrix of low molecular weight PS, the fluorescence intensity transient revealed quite different characteristics from those previously mentioned. The spot showed a gradual decrease in intensity without discrete jumps to the dark level. The fluorescence spectra also gradually decreased in intensity while keeping the peak positions and the vibronic bands as shown in Fig. 5d. These results are usually expected for a multi-chromophoric system, in which the individual chromophores are in-

dependent of each other, and being gradually eliminated one by one from the system by the photobleaching reaction. The different fluorescence behavior is attributed to the difference of conformation of the single polymer chain. When a chain takes an extended conformation, the interaction between adjacent chromophores becomes weak, and then energy migration along the chain is prohibited. Consequently, the polymer emits fluorescence from the multiple chromophores. Thus, the transient and spectroscopic studies by using LSCFM can provide significant insight into the fundamental photophysics occurring in each one of single polymer molecules.

2.6
Single Molecule Spectroscopy

The fluorescence spectrum and its temporal profile provide us extensive information not only on the dye molecule itself but also on the local environment of the surroundings, such as molecular conformation, orientation, and local polarity around the molecule. Therefore, fluorescent dyes have been widely used to probe the local information in the system: various properties of the system is evaluated through the analysis of the fluorescence behavior of the dye molecules introduced [26]. In the conventional fluorescence probe methods, the observed fluorescence was the ensemble average over the numerous molecules which probably show different properties depending on their individual circumstances, histories, and locations. Single molecule spectroscopy allows us to evaluate various characteristics such as distribution, correlation, and time trajectories of the objectives, which are hidden through the process of ensemble averaging. In the single molecule experiment, however, we encounter the difficulty in the signal detection because the fluorescence from a single molecule is extremely weak. Therefore, the highest signal detection efficiency is an absolute requirement for the apparatus. Recent developments in optics with high throughput and sensitivity allow one to perform spectroscopic measurements for a single fluorescent molecule with a large absorption coefficient, a high emission quantum yield, and also high photo-stability such as rhodamine and carbocyanine dyes [27–32]. The single molecule fluorescence probe method has usually been used for dyes dispersed at an extremely low concentration, in order to observe individually molecules by confocal microscopy with a resolution of the diffraction limit. Vallee et al. studied the segmental dynamics of polymers in a glass state through the emission behavior of single 1,1′-octadecyl-3,3,3′,3′-tetramethlindodicarbocyanine (DiD) molecules [28, 30, 31], which were dispersed in a polymer film at a concentration of $< 10^{-9}$ mol L^{-1}. Figure 6a shows the fluorescence image of single DiD molecules, indicating the random orientation of the transition dipole. The fluorescence decay profile for each molecule was observed by a time correlated single photon counting technique. The molecules had different decay rates, indicating the hetero-

geneity of the polymeric glass. In addition to the spatial inhomogeneity, the fluorescence lifetime was temporally heterogeneous, that is, the lifetime fluctuated in time for a given dye molecule. Figure 6b depicts the fluorescence decay curves for the same molecule at different times. As shown in panel c, the fluorescence lifetime varied in time, whereas the fluorescence intensity was almost constant. The fluorescence lifetime of the DiD dye is insusceptible to the molecular conformation and is mainly dependent on the local dielectric constant of the polymeric matrix surrounding the probe molecule [29]. The local polarity at the location of the fluorophore varied in time due to the fluctuation of the free volume generated by segmental motions of the matrix polymer, resulting in the fluctuation of the fluorescence lifetime. The length scale of the cooperative motions responsible for the variation of fluorescence lifetime was evaluated by the theory of Simha and Somcynsky, and the effect of the polymer film thickness on the segmental dynamics was examined. The scale of the cooperative segmental motion decreased with the decrease of the film thickness in the range of < 50 nm, whereas it was constant for the polymer matrix thicker than 50 nm as shown in Fig. 7. This result indicates that the segmental dynamics become faster near the surface. Single molecule spectroscopy is a powerful tool for probing dynamics of polymers because it reveals the various molecular level characteristics hidden in the conventional ensemble averaged measurements. It has a large potential for obtaining insight into the polymer structure and dynamics in a nanometric scale.
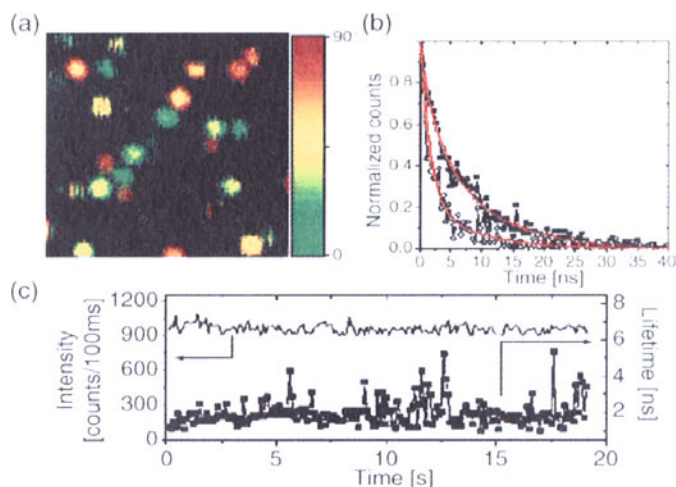
Fig. 6 (**a**) Fluorescence image of single DiD molecules embedded in a polystyrene film ($5 \times 5\ \mu m^2$). The pseudo color scale shows the polarization direction of the fluorescence, indicating the molecular orientation (**b**) Fluorescence decay curves for one DiD molecule at different times. The red lines are the single-exponential functions fitted to the data (**c**) Time traces of fluorescence intensity and lifetime with 100 ms time interval. Reprinted with permission of [30], copyright (2004) American Chemical Society
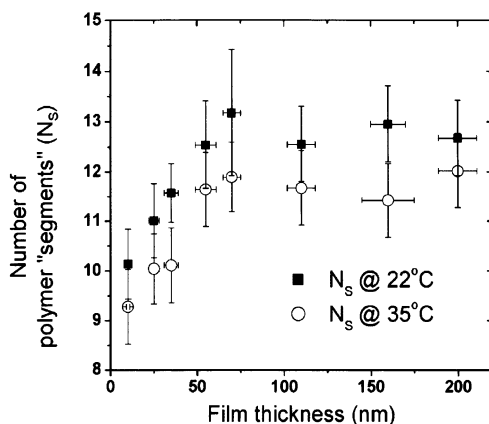
Fig. 7 Film thickness dependence of the number of segments, N_s, involved in the rearrangement volume evaluated by the Simha-Smocynski equation of state. Reprinted with permission of [30], copyright (2004) American Chemical Society

2.7
Recent Advances in Optical Microscopy

The theoretical limitation of the spatial resolution of optical microscopy is defined as the size of the smallest focus area of light. This limitation is called the diffraction limit, which predicts that the spatial resolution of optical microscopy is limited to $\sim \lambda/2$ [33]. The above criterion is based on the assumption that the signal intensity from the object is proportional to the incident power. When the interaction between light and the object is non-linear, this is not the case. The dashed line in Fig. 8 depicts the intensity profile of a diffraction-limited spot. When the object emits signals proportional to the square of the input light intensity, the intensity profile is given by the solid line in Fig. 8. This indicates that the width of the main peak and the intensity of the side-robes decrease for the case of quadratic interaction. Thus, the area emitting the signal light can be reduced by the non-linear optical interaction
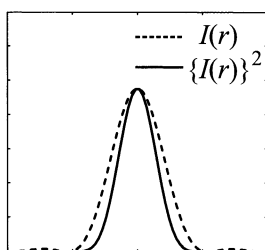
Fig. 8 Radial profiles of linear and quadratic intensity of a diffraction-limited spot, which are indicated by the *dashed* and *solid lines*, respectively

such as harmonic generation and multi-photon absorption, resulting in the improvement of the spatial resolution.

Two-photon excitation fluorescence can be used to improve the resolution of optical microscopy [34–36]. A fluorescent molecule is generally excited from the S_0 state to the S_1 state by absorbing a photon with the energy corresponding to the $S_1 - S_0$ level difference, $\Delta E = h\nu$. In a high photon flux density, the fluorophore can absorb two photons simultaneously. In a two-photon absorption process, the transition probability is proportional to the square of the photon density, resulting in the reduction of the excited area. Simultaneous absorption of two photons by a fluorophore requires the illumination by temporally and spatially confined light with the photon flux density in the order of 10^{30} photons $cm^{-1} s^{-1}$, which can be obtained by tightly focusing a femtosecond pulse from a mode-locked laser. The fluorescent molecule absorbs two photons at a frequency of $\nu/2$ and is excited to the S_1 state. Therefore, the fluorophore with an absorption band in an ultraviolet-visible range (400–500 nm) can be excited by near-infrared light at a wavelength of 800 to 1000 nm. The infrared excitation beam can penetrate deep into a thick medium without scattering because the scattering efficiency of light is proportional to λ^{-4}. This feature has an important role especially in three-dimensional imaging, which distinguishes the two-photon fluorescence microscopy from other techniques.

Another approach to higher spatial resolution in confocal microscopy is the stimulated emission depletion (STED) scheme [37–40]. The STED technique uses two light sources at different wavelengths. All fluorescent molecules are excited in the diffraction-limited excitation spot of the first source at λ_{ex}, and another beam at a longer wavelength λ_{STED} illuminates the outer part of the excitation focal spot to quench the fluorophore therein. The sequence of the pulses to excitation and depletion with appropriate shapes shrinks the point spread function of the microscope. Figure 9 shows the mechanism of STED. The fluorophore is instantaneously excited to an S_1 state by a first short laser pulse. Immediately after the excitation, the second STED pulse (as long as the fluorescence lifetime) is incident to the excited fluorophore. The STED pulse induces the stimulated emission from the lowest S_1 state to a high vibrational state of S_0 as shown in the Jablonski diagram of Fig. 9a, and the spontaneous emission other than λ_{STED} is detected from the area unirradiated by the STED beam. An appropriate shaping of the STED beam quenches the fluorescence at the outer part of the first excitation spot, and the fluorescence in a gray-scaled range in Fig. 9a is detected only from the very center of the first spot as shown in panel b. Figure 10 shows the fluorescence image of single molecules of rhodamine derivative observed by confocal and STED configurations. In the confocal microscopy image, the single molecules were observed as circular spots with a diameter of 234 nm. On the other hand, the STED microscopy can observe a single molecule in a $\sim$ 140-nm circular shape and clearly distinguish the two molecules sepa-
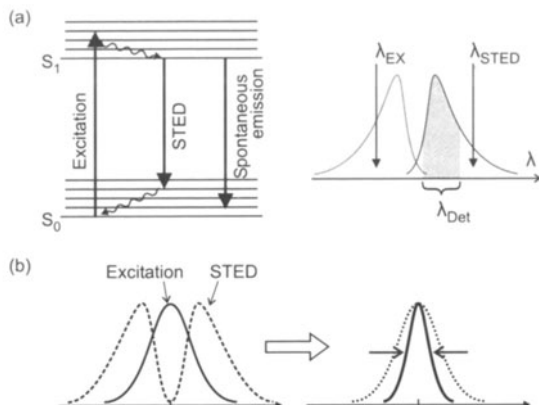
Fig. 9 Schematic illustration of STED. (**a**) Jablonski diagram indicating the S_0 and S_1 state of a molecule (*left*). A femtosecond pulse excites the fluorophore from S_0 to a high vibrational level in S_1. The following slow STED pulse induces the stimulated emission from the lowest S_1 level to a high vibrational level in S_0. The STED pulse depletes the S_1 state and quenches the fluorescence. The corresponding wavelength diagram is shown on the right-hand side: the *dotted* and *solid lines* are the absorption and emission spectra, respectively. The spontaneous emission at λ_{Det} is detected as the signal in the microscopy measurement. (**b**) The combination of the diffraction-limited excitation spot and the engineered STED pulse yields a narrowed point spread function
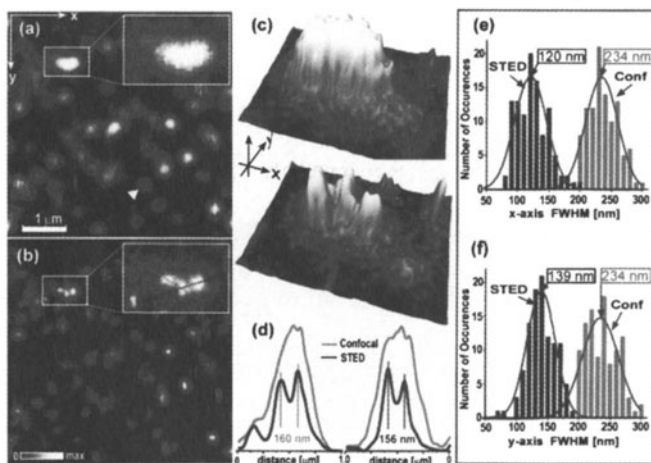
Fig. 10 Fluorescence images of single fluorescent molecules in the same area observed by conventional confocal (**a**) and STED configurations (**b**), and the rectangular areas in both images are enlarged (**c**). Panel d indicates the cross-section profiles for panel (**c**). The STED microscopy clearly resolves the three molecules separated by ~ 160 nm, which were observed as one ellipsoidal spot by the confocal setup. The histograms of the full width at half maximum (FWHM) of the observed fluorescence spots for the *x*- (**e**) and *y*-directions (**f**) indicate the sharpening of the focal spot in the STED configuration. Reprinted with permission of [40], copyright (2003) American Institute of Physics

rated by 160 nm, indicating the high spatial resolution of $\lambda/5$. By the further optimization of the optics and the combination with other techniques such as two-photon fluorescence, the STED microscopy has potential for the super-resolution microscopy in three dimensions and with high detection sensitivity down to the single molecule level. It would be a powerful tool for the structural analysis of biological and polymer materials.

The strategy to achieve a high resolution described above is based on the diffraction-limited optics. The optical microscopy in the next generation utilizes the non-propagating "light". An example of the spatially confined light is the evanescent field generated in a total internal reflection condition. In Fig. 11a, the incident light from the medium 1 with a refractive index n_1 penetrates into the medium 2 with a refractive index n_2, where $n_1 > n_2$. At the interface, total internal reflection occurs at the incident angle θ, given that the angle θ satisfies the condition, $\sin\theta > n_2/n_1$. Under this condition, the incident light slightly penetrates across the interface and reflected. The penetrated light has an imaginary component of the wavenumber vector in the direction normal to the interface, that is, the light cannot propagates in the z-direction but is confined at the interface within a distance of ~ 100 nm, which is called the evanescent light. Total internal reflection (TIR) microscopy illuminates a sample by the evanescent light generated at the sub-
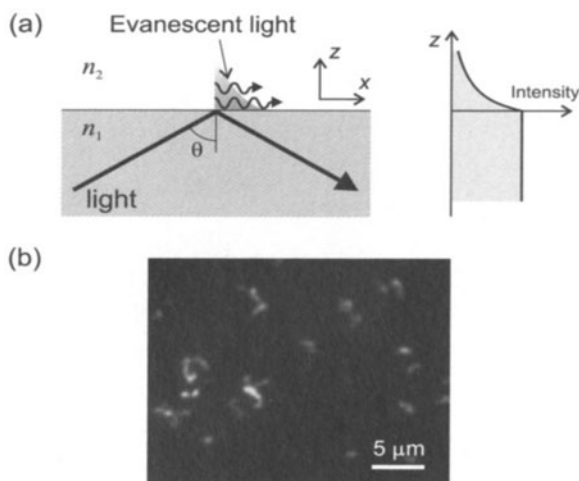
Fig. 11 Schematic drawing of the evanescent field generated in a total internal reflection condition (**a**). When the light is incident from a medium 1 with a high refractive index n_1 to a medium 2 with lower refractive index n_2, total internal reflection occurs in a condition of $\sin\theta > n_2/n_1$. In this situation, the incident light slightly penetrates to medium 2 across the interface, and the penetrating light is called the evanescent light. The evanescent wave propagates in the x-direction and decays rapidly in the z-direction as shown in the intensity profile in the right-hand side. The evanescent light is able to selectively illuminate the specimen at the interface; for example, single DNA molecules adsorbed on a cationic substrate (**b**)

strate surface, and the emission from the specimen was imaged by usual microscopy optics; therefore, the spatial resolution is diffraction-limited in the lateral dimensions. On the other hand, the height resolution is as high as 100 nm at the interface because of the selective excitation of the fluorophore within the region where the evanescent field is confined. The total internal reflection microscopy is suitable for studying dynamic processes at an interface such as the adsorption of single DNA chains onto a solid substrate [41, 42]. Figure 11b presents an example of a TIR microscope image for DNA at a solid/liquid interface.

In total internal reflection microscopy, the light is confined only to the z-direction, resulting in the diffraction-limited resolution in the xy-plane. In the last two decades a novel optical microscopy has been developed aiming at high spatial resolution by the three-dimensionally localized optical field, "optical near-field". Details on the structural analysis using the near-field microscopy is described in the next section.

3
Nano-Imaging with Near Field Optics

3.1
Outlook of SNOM

Scanning near-field optical microscopy (SNOM) is a new methodology for achieving a high spatial resolution free from the conventional theoretical limitation [43–49]. When the light is incident to a smaller object than its wavelength, there arise not only a propagating field such as scattered light but also a non-propagating electric field restricted around the object, which is called "optical near-field". The non-propagating optical near-field has information on the local structure smaller than the wavelength; therefore, the near-field component can achieve a high spatial resolution beyond the diffraction limit. The basic concept of SNOM was originally suggested more than 70 years ago [50]; however, due to technical difficulties such as the fabrication of a sub-wavelength aperture and the exact position control on a nanometric resolution, it was actually realized only after the invention of scanning probe microscopy in the early 1980's [51, 52]. SNOM is a scanning probe microscopic technique using a probe with a subwavelength-sized aperture. The light incidence to the aperture generates an optical near-field restricted to the vicinity of the probe end as shown schematically in Fig. 12. It allows one to illuminate the specimen and to obtain optical response from the nanometric area, and the raster-scan of the probe builds up the microscopy image with a resolution as high as the aperture size. In many cases, the apertured SNOM probe is fabricated from an optical fiber [46, 47, 53]. The optical fiber
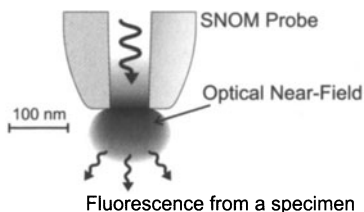
Fig. 12 Schematic illustration of near-field optical microscopy. The optical near-field confined in a nanometric area generates around an aperture much smaller than the wavelength of light

is sharpened mechanically and/or chemically, and the side of the tapered part is metal-coated to leave a small aperture at the sharpened end. As mentioned above, because the near-field intensity rapidly decays with increasing distance from the probe end, the gap between the SNOM probe and the sample surface must be kept constant at a few nanometers while the raster-scanning of the probe. This indicates that SNOM can obtain a topographic image of the sample simultaneously with the optical image. The block diagram of the SNOM system is shown in Fig. 13. The illumination light is coupled to the cleaved end of the fiber probe and guided to the aperture to generate the optical near-field at the sharpened end. The probe end is set above the sample by a force feed-back mechanism similar to AFM. The signal from the specimen is collected by an objective lens behind the substrate, and its intensity is measured by various photo-detectors as a function of the probe position. SNOM has attracted the attention of researchers in many fields of physics, biology, and material science, because it enables one to observe optical properties by spectroscopy in a time-resolved manner, and make polarization measurements
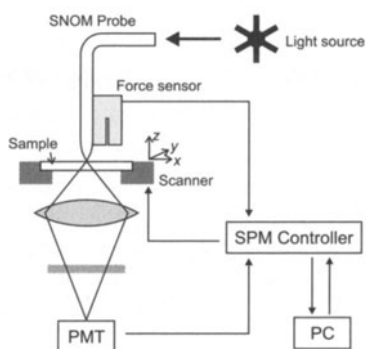
Fig. 13 Block diagram of a SNOM apparatus. The SNOM probe is attached to a piezo-electrics and the force interaction with the sample surface as the measure of the probe-sample distance. The signal light is collected by an objective lens and detected by a photo-multiplier (PMT) through filters or a spectrograph

of single molecule with high sensitivity. The combination of SNOM and the fluorescence method provides the detailed information of the structure and dynamics of the polymer systems with a nanometric spatial resolution.

3.2
Imaging of a Single Polymer Chain

There are many basic and important issues on the morphology of a single polymer chain. Conformation, orientation, end-to-end distance, radius of gyration, elastic modulus, and mobility, all characteristics of a single polymer chain are always fascinating research objects in polymer science. Therefore, many studies aiming at direct imaging of a single polymer chain have been preformed so far to discuss the relationship between the chain morphology and physical properties of polymers. There are various sophisticated works on DNA imaging by means of OM, because a DNA chain is easily visualized by conventional microscope and LSCM owing to the huge molecular weight and the very long chain length over $10\,\mu m$. In addition, OM is superior to other types of high-resolution microscopies such as TEM and SEM, since the observation at ambient and biologically relevant conditions is crucial for studying bio-macromolecules like DNA. SNOM has also been used for imaging DNA chains, which are embedded in a lipid membrane, cultured in cells, and adsorbed on a mica surface [54]. Figure 14a shows an example of high-resolution images of a double stranded DNA chain deposited on mica, taken by shear-force topography imaging with a SNOM apparatus. In this figure, the DNA was clearly resolved with a height difference of 1.4 nm, which corresponds to the diameter of the DNA strand. On the other hand, the lateral resolution of this figure was evaluated to be 14 nm from the FWHM of the line profile across the DNA chain. Panel b in Fig. 14 shows a fluorescence image with near-field excitation of a rhodamine-6G (R6G) molecule, which
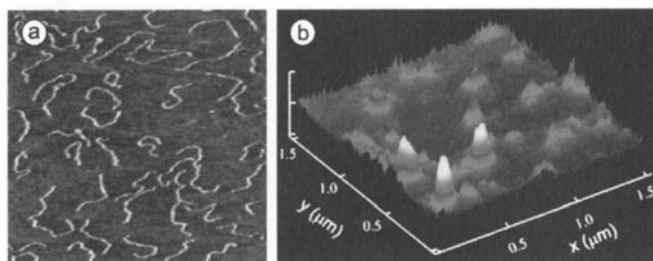
Fig. 14 Shear force image (**a**) and near-field fluorescence image (**b**) of 1kbp DNA fragments labeled with R6G. The DNA sample consists of one fluorophore per strand, and the emission was accumulated for 10 ms/pixel. The maximum signal is 240 counts/pixel and background is 40 counts/pixel. Reprinted with permission of [54], copyright (1998) IOP Publishing Ltd

was labeled at the end of a DNA. Here, the optical data obtained simultaneously with shear force information enables an easy comparison with the high-resolution topography, indicating that each bright spot presents a single R6G molecule at the chain end. Although the intensity varies one by one due to the different circumstances around R6G, some molecules emit fluorescence with intensities 6 times larger than the background level of the photon counting detector, and the diameter of the individual intensity peaks was ca. 70 nm This result suggests that SNOM can provide a clear image of a single DNA chain with a sufficient signal-to-noise ratio and a spatial resolution of 70 nm.

Apart from DNA, the high resolution of SNOM makes it possible to show up the conformational features of a synthetic polymer. Many studies by STM and AFM, both scanning probe microscopes, have already revealed the morphology of isolated chains adsorbed on a flat surface like a mica sheet [55, 56]. In contrast to these scanning probe microscopes, SNOM can detect in situ features of polymer chains located inside the polymer film below the sample surface. As reviewed by Richards et al., the decay length of the evanescent near-field inside the sample depends on the wavelength of light, the aperture diameter, and refractive index of the sample [57, 58]. They estimated the length by the Bethe-Bouwkamp formula for a conjugated polymer blend sample [59]. The calculation for 488 nm laser light through an aperture of 100 nm in diameter showed that the near field light from the tip penetrates to about 100 nm below the surface. Using this advantage, one can get a image of a fluorescently labeled single chain dispersed among large number of identical non-labeled chain matrix [60].

Ultrathin films of poly(isobutyl methacrylate) (PiBMA) have been investigated to demonstrate the ability of single polymer imaging, because they form a stable monolayer on the water surface with a thickness of only 1 nm, and sequential deposition of the monolayer provides very flat thin films with a tailor made inner structure [61]. Scheme 2 depicts the chemical structures of sample polymers. Besides the non-labeled PiBMA homopolymer, a labeled PiBMA (PiBMA-Pe) was synthesized by means of copolymerization of isobutyl methacrylate and 3-perylenylmethyl methacrylate. The copolymer

$M_w = 3.3 \times 10^6$

$M_w/M_n = 1.23$

$m/n = 0.01$
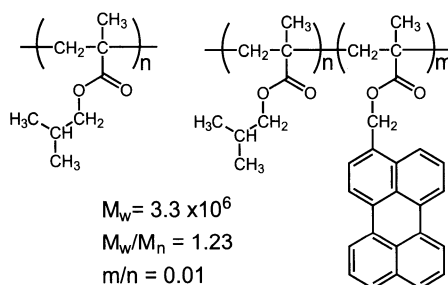
Scheme 2 Chemical structures of PiBMA and perylene labeled PiBMA copolymer

bears perylene (Pe) chromophores at the side chain, whose fraction was suppressed to ca. 1% in order to avoid the influence of labels on the morphology of the polymer chain. In Scheme 2, the molecular weight and its dispersion are also given for labeled PiBMA. The molecular weights of these polymers were very large in the order of 10^6 so that they had large sizes of a few hundred nanometers, hence, their individual features were observable by SNOM with a resolution of 100 nm.

The sample films for SNOM measurements were prepared by the LB technique. Figure 15 shows the layer structure. The PiBMA layer in the middle, in which a very small quantity of PiBMA-Pe was embedded, was sandwiched between the non-labeled layers of poly(vinyl octanal acetal). The near field light from the probe tip excites the Pe dyes attached to the labeled PiBMA-Pe chains that constitute a part of the monolayer film. Thus, the very thin and transparent LB film with a flat surface is regarded as an ideal SNOM sample without any artifacts caused by tip-sample interaction.

Figure 16 shows a SNOM image for PiBMA thin films, containing the labeled PiBMA-Pe polymers with a fraction $F = 0.14\%$, taken with perylene fluorescence intensity under the excitation at 442 nm by a He-Cd laser [26, 60]. Several small spots are observed in the picture, although the surface was very flat over the whole area of the topographic images taken at the same time.
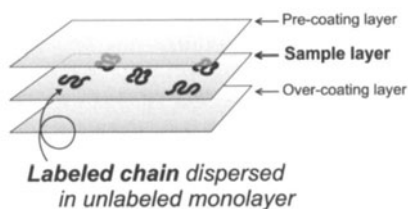
Fig. 15 Layer structure of a sample film containing labeled PiBMA chains in the middle layer of PiBMA. Two monolayers of poly(vinyl octanal acetal) were deposited as the precoat and overcoat layers to protect the specimen from the air and the substrate
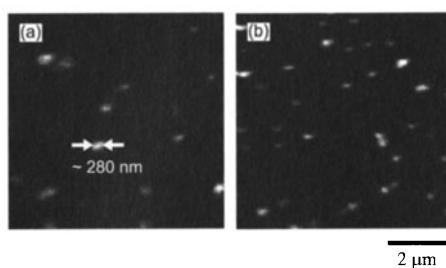
Fig. 16 SNOM images of single polymer chains of PiBMA labeled with perylene, observed by the fluorescence intensity profile. (**a**) $F = 0.14\%$, (**b**) $F = 0.2\%$ The excitation wavelength was 442 nm. Reprinted with permission of [26], copyright (2003) The Chemical Society of Japan

As fraction F was gradually increased, the number of spots also increased. This suggests that each spot corresponds to a single chain incorporated into the monolayer. Another merit of the LB film lies in the well-defined surface area and plane density of molecules. Since the surface area A occupied by a monomer unit of PiBMA is measured by the surface-pressure isotherm, the plane density ϱ of PiBMA-Pe chain is simply given as follows, $\varrho = F/(AD_p)$ where D_p is the degree of polymerization, and then AD_p represents the area occupied by a single PiBMA-Pe chain. The plane density of bright spots in Fig. 16 was in good agreement with the calculated value, indicating that each spot in these pictures represents a single chain embedded in the monolayer. Thus, the quantitative evidence supported the statistically random dispersion of polymer chains in the monolayer.

It is obvious in Fig. 16 that some spots are large and some are small; the spots vary both in size and brightness, probably resulted from molecular weight dispersion of the sample. Although PiBMA has a narrow molecular weight dispersion of $Mw/Mn = 1.23$, there is still a large difference in size from $Mw = 10^6$ to 10^7. However, a large portion of the spots have diameters around 200–300 nm in FWHM of the line profile. Considering the instrumental spatial resolution of ca. 100 nm, the real diameter of a fluorescent polymer is estimated to be ca. 200 nm. This is quite small considering the large molecular weight of the sample polymer. For example, the chain length at a fully extended form is estimated as ca. 8000 nm, on the other hand, the diameter of a circle occupied with a perfectly contracted chain is calculated as ca. 110 nm. Therefore, taking into account these values for a single chain, the SNOM image indicates that the polymers in 2-dimensional monolayers tend to take a contracted conformation as shown in Fig. 17, because they cannot be entangled with other chains and have to exclude each other in order to avoid making free areas in the plane. Although this behavior has been predicted by de Gennes' scaling theory [62], and also by surface viscosity measure-

Fig. 17 Schematic illustration of a single polymer chain contracted in a two-dimensional monolayer. Reprinted with permission of [26], copyright (2003) The Chemical Society of Japan

ments [63, 64], the real image of fluorescence SNOM provided unambiguous evidence of the chain contraction in the two-dimensional polymer systems.

3.3
Phase Separation Structure of Conjugated Polymers

Many of the SNOM studies have been focused on nano-imaging of conjugated polymers. There is great interest in conjugated polymers because of their potential use in a wide variety of electro-optic applications such as thin film transistors, displays, and solar cells. Since the net performance of devices is largely affected by the nano-structure of conjugated polymers, extensive studies have been conducted at a molecular level using TEM and AFM. In contrast to these microscopes, SNOM can provide simultaneously many kinds of images based on a topographic shear force response, optical absorption/fluorescence intensities, and electric response induced by near-field illumination. Hence one can get direct information on the relationships between the nano-structures and the photoinduced electric properties. A typical example of SNOM work is found in the application to light-emitting polymers composed of poly(9,9-dialkylfluorene) (PDF) and its copolymers [57, 58, 65–67]. Figure 18 shows SNOM images of a polymer blend containing 10% poly(9,9-dioctylfluorene-alt-benzothiadiazole) (PDF-B) and 90% another type PDF-based polymer (PDF-P). Panel a in Fig. 18 is a topographic image, where the appearance of protruded domain suggests the phase-separated structure of this blend film. By measuring both the shear force height image (panel a) and fluorescence image (panel b), it becomes possible to distinguish the distribution of PDF-B polymers. Figure 18b was taken with an excitation wavelength at 488 nm, in which only PDF-B was selectively excited, and imaged by collecting the fluorescence through an appropriate filter for PDF-B emission bands. Therefore, the intensity mapping in panel b displays selectively the presence of PDF-B. From these images, the PDF-B domain was unambiguously identified to the protruded
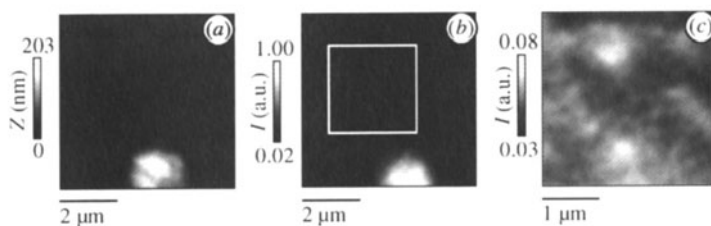
Fig. 18 (**a**) Shear force topographic image of a conjugated PDF blend film with PDF-B/PDF-P= 10/90 (**b**) Corresponding fluorescence SNOM image for (**a**). (**c**) An enlarged fluorescence image taken from the white box shown in (**b**). Reprinted with permission of [58], copyright (2003) The Royal Society

area in the previous topographic image. Figure 18c is an enlarged fluorescence image taken from the dark area of panel b, which is indicated with a white box shown in b and assigned to the PDF-B-poor domain. The magnification in both the *xy*-scales and the intensity signals clearly showed that the PDF-B polymers distributed even in the dark region in panel b, suggesting the presence of further phase separation in a smaller scale far below the spatial resolution of SNOM.

Since PDF is a conjugated and stiff-chain polymer, it tends to afford highly oriented domain structures like liquid crystalline polymers. The alignment of polymer chains results in anisotropic fluorescence, which is polarized parallel to the direction of the stiff backbone. A SNOM image is usually formed by collecting the total intensity of fluorescence in a given wavelength range, while scanning the probe tip over the sample surface. If we can use dual detectors equipped with orthogonal polarizers separately, each component of the polarized fluorescence is detected by two detectors, allowing one to calculate the anisotropy of fluorescence, i.e. the degree of ordering at each point of the sample film with a resolution of 100 nm. Teetsov et al. modified a commercial aperture-type SNOM apparatus to achieve the dual polarization collection; the diagram of their SNOM instrument is shown in Fig. 19 [68–70]. The
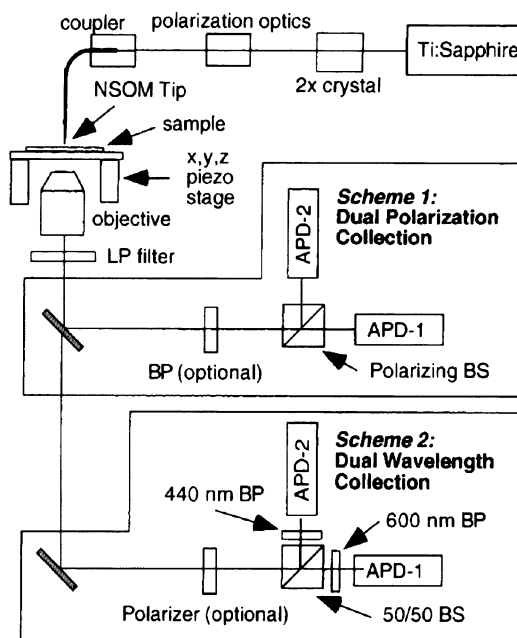
Fig. 19 Diagram of the SNOM instrument equipped with dual detectors for both polarization and wavelength measurements. *Scheme 1*: two images are collected simultaneously at orthogonal polarizations. *Scheme 2*: two images are collected at two wavelengths. Reprinted with permission of [68], copyright (2000) American Chemical Society

fluorescence from a point excited by near-field light from a SNOM tip was collected with a high NA objective, split by a polarizing beam splitter (BS), and then fed onto the dual photon-counting detectors. Consequently, two fluorescence images based on orthogonal polarizations were taken simultaneously. Figure 20 shows SNOM images thus obtained for a pristine PDF film prepared by the spin-coating method. There is almost no contrast in the image of total fluorescence as shown in panel b, which is given by the sum of the signals from the dual detectors. However, both polarization components, indicated by the horizontal and vertical arrows in panels c and d, respectively, provided well-resolved nano-structures of the PDF film. Figure 20e represents the fluorescence anisotropy image calculated by taking subtraction of intensities from the dual detectors (the signals in c and d), and then by dividing it with the total intensity at each pixel. These figures show that the PDF film is composed of the preferentially oriented domain of polymer chains with a size
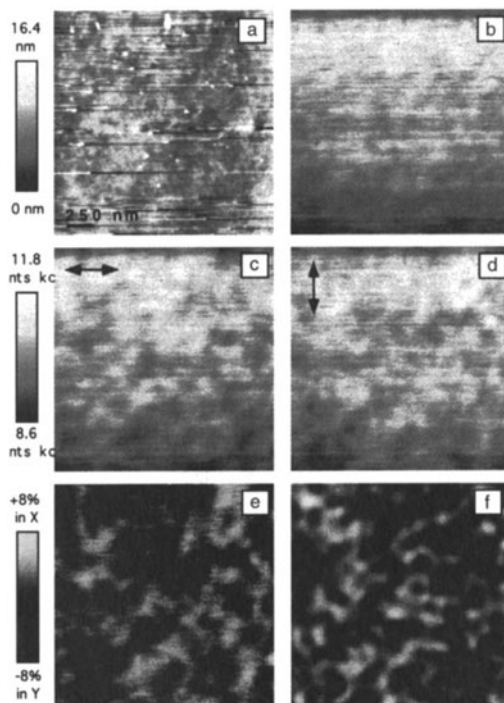
Fig. 20 SNOM images of a 250 nm thick film of poly(9,9-didodecylfluorene) prepared by spin coating from toluene solution: (**a**) topography, (**b**) total fluorescence intensity calculated from sum of the two polarized images (**c**) and (**d**) fluorescence collected simultaneously at orthogonal polarization, (**e**) anisotropy image calculated from panels c and d, and (**f**) simulated anisotropy image assuming the polymers are perfectly oriented in 15 nm cubic domains. Reprinted with permission of [68], copyright (2000) American Chemical Society

of a few tens nanometers. These figures clearly exemplify the feasibility of nano-imaging based on molecular orientation.

Besides PDF derivatives, many SNOM works have been reported using another type of conjugated polymers, poly(phenylene vinylene) (PPV) which is conductive and often used as a hole transporting material in organic devices. The photoinduced electric performances such as excitation energy transfer, charge separation, and charge carrier mobility depend critically on the nano-structures of the polymer assemblies either in pristine bulk films or in blended films with dyes and electron acceptors. Therefore high-resolution SNOM images taken by photo-excitation may provide invaluable information on not only the structures but also the photo-electric performance related to the structure. In addition to the SNOM studies on PDF films, nanometer scale domain structures and phase separated structures of PPV films have been reported by high-resolution imaging of various contrast mechanisms, e.g. transmission [71], fluorescence [72], spectral shifts [73], time-resolving [74], polarization [75], photoconductivity [76], etc. The images were obtained mostly by either the polymer chain alignment or a wavelength shift in the absorption and fluorescence spectra between the order and disorder domains.

3.4
Two-Dimensional Polymer Blends

The morphology of polymer blends in bulk systems has been extensively studied because of the wide range of applications of polymeric materials owing to the improved mechanical and thermal characteristics compared with single component polymers. However, there are few reports on 2-dimensional morphology for polymer blend and its phase-separated structures.

PiBMA is again employed in this section as one component of the monolayer, and poly(octadecyl methacrylate) (PODMA) as another component [77–79]. The former provides a liquid-like monolayer on the water surface, but the latter behaves as a solid-like monolayer due to the strong cohesive force between the long alkyl side chains [80]. Scheme 3 illustrates the chemical structures of the polymers and fluorescent probes. PiBMA and PODMA were labeled separately with pyrene (Py), perylene (Pe), and eosin (Eo) dyes, which were appropriate pairs for energy transfer experiments as a donor and an acceptor. The mixed solution of PiBMA and PODMA was spread on water at 20 °C and then annealed at 40 °C. Figure 21 shows some photos of the phase separation morphology on water during the annealing period, taken by the Brewster Angle Microscope (BAM), indicating the progress of phase-separation on the water surface. The crystalline side chain of PODMA starts melting on water at 40 °C, and the monolayer becomes

R:

Py   Pe

Eo
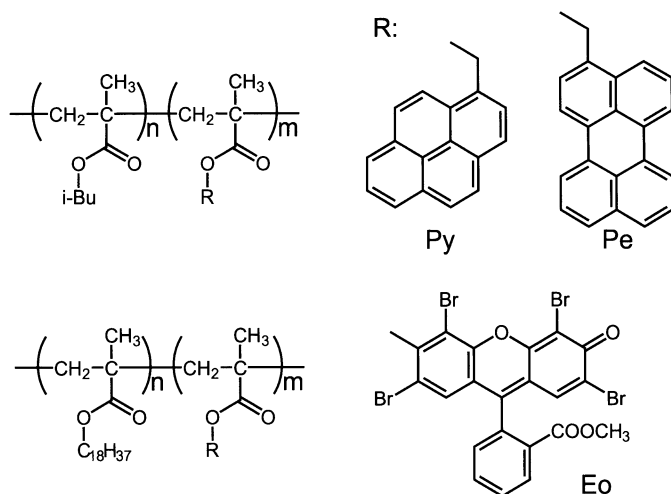
Scheme 3 Chemical structures of PiBMA and PODMA used for two-dimensional phase separation experiments, and the fluorescent labels

(a)   (b)   (c)
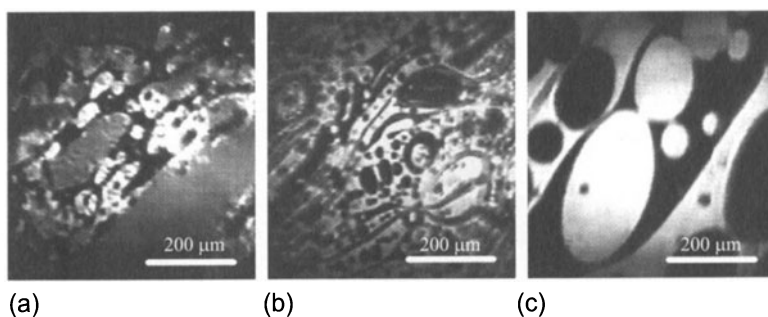
Fig. 21 BAM images of a PiBMA/PODMA mixed monolayer on the water surface at 40 °C. The annealing time was (**a**) 0 min (**b**) 10 min and (**c**) 60 min. Reprinted with permission of [80], copyright (1999) The Society of Polymer Science, Japan

a liquid-like one [80]. Therefore, the phase separation proceeds very quickly, yielding a completely separated monolayer of the polymer blend.

Figure 22 shows three pictures of the PiBMA-Py/PODMA-Pe blend monolayer annealed for 60 min, then deposited on a substrate. These were taken by SNOM with three different filter sets for the excitation and fluorescence wavelengths: panel a is the fluorescence image of Py, which was selectively excited at 325 nm and observed at 370–410 nm; the middle panel b is of Pe fluorescence excited at 442 nm and detected at wavelengths longer than 470 nm [77, 78]. This means that the bright part of panel a indicates the presence of a PiBMA monolayer, and the bright area of panel b corresponds to the PODMA monolayer. These two pictures show perfectly complementary features of two components, indicating that the phase separation was com-
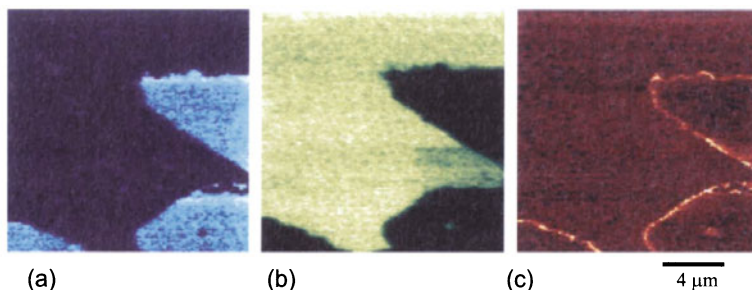
Fig. 22 Fluorescence SNOM images of a phase-separated polymer monolayer after annealing for 60 min. The scanning area was $15 \times 15 \ \mu m^2$ and the scale bar indicates 4 μm. (**a**) Py fluorescence image. The excitation wavelength was 325 nm and the optical filters used collected only the fluorescence of Py (**b**) Pe fluorescence image, taken by 442 nm excitation and by emission at wavelengths longer than 470 nm (**c**) Energy transfer image. The excitation wavelength was 325 nm and the Pe fluorescence was collected with the same optical filters as in (**b**). Reprinted with permission of [77], copyright (1999) American Chemical Society

plete, and that the surface was covered by one of them without any cracks or defects.

As shown in panel c in Fig. 22, it is very interesting to take a SNOM image with excitation of Py at 325 nm and by monitoring Pe fluorescence at wavelengths longer than 470 nm. Under these experimental conditions, Py was selectively excited, but Py fluorescence could not be detected. Therefore, the fluorescence from Pe observed was emitted only through the excitation energy transfer from Py to Pe. Hence, the bright area in panel c indicates the boundary region, in which PiBMA-Py/PODMA-Pe were molecularly mixed and two different labels approached each other within the Foerster radius (critical energy transfer radius) of 3.3 nm. Thus, the energy transfer mapping by SNOM provides a novel method to depict the area molecularly mixed at the phase boundary. This technique will be applicable to other molecular assemblies and polymer systems for indicating the degree of mixing at the molecular level.

SNOM is capable of obtaining simultaneous optical and topographic images with a high-resolution. Furthermore, it can be equipped with a time-correlated single photon counting system and a short-pulse laser system in order to obtain images of fluorescence, or to measure fluorescence decays at individual points with a spatial resolution of less than 100 nm. The further utility of energy transfer mapping can be recognized by point-by-point analysis of the fluorescence decay curves under the SNOM image. The samples used in this experiment were PODMA-Pe as the donor and PiBMA-Eo as the acceptor. The Eo dyes of the latter component quench the excited state of the former Pe through the energy transfer mechanism. The closer the mutual distance of these two dyes, the faster the rate constant of quenching is. Therefore,
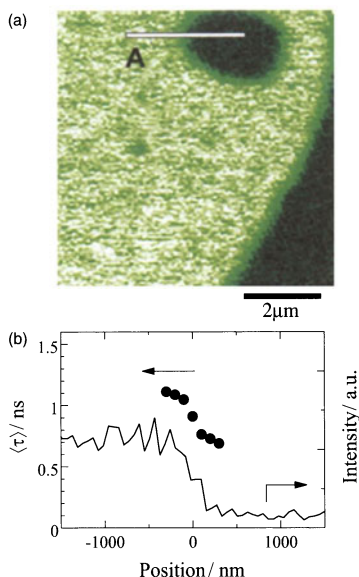
Fig. 23 (**a**) SNOM image for a PODMA-Pe/PiBMA-Eo monolayer after annealing for 60 min (**b**) Fluorescence lifetime and intensity profiles. The excitation wavelength was 415 nm. The *closed circles* and the *solid line* indicate the lifetime and the intensity, respectively, measured along the line A in panel a. Reprinted with permission of [78], copyright (2001) American Chemical Society

the decay rate of Pe fluorescence reflects the local concentration of Eo dyes around Pe molecules at the observed point.

Figure 23b shows the line profiles across the boundary of PODMA-Pe/PiBMA-Eo along the solid line indicated in panel a [78]. In panel b, the fluorescence intensity and lifetime of Pe emission are plotted at every 100 nm displacement over the whole length of the boundary region. As shifting the position observed from the PODMA phase to PiBMA phase, both the fluorescence intensity and the lifetime of Pe decrease steeply, showing a rapid increase of the concentration of Eo dyes attached to PiBMA segments. The intensity of fluorescence is simply proportional to the number of Pe under the aperture of SNOM, which may be changed with morphological distribution of Pe polymers, irrespective of the local concentrations of Pe and Eo. On the other hand, the lifetime measurement directly manifests the alteration of local concentration of Eo chromophores around Pe at the specific point. Therefore, the lifetime profile in Fig. 23 provides unambiguous indication for the gradient of the composition of both polymers across the boundary of two domains. These experiments show the high potential of the energy transfer method for the structural analysis, when it is combined with nanometric time-resolving microscopy.

3.5
Polymer Networks

The three-dimensional network of polymer chains has also attracted much attention in polymer science and technology. Although a great number of researchers have devoted their efforts toward clarifying the network structure using X-ray diffraction, light scattering, and optical microscope measurements, the origin of the unique and particular properties is not yet understood in relation to the structure of networks. The microscopic images of polymer gels in real space have been reported only at low magnifications in a micrometer scale using optical LSCM and LSCFM [18, 81], whereas polymer gels are known to form fractal structures over a wide range of dimensions from nanometer to micrometer regions. A large-scale structure observed is made of microscopic structures in a nanometric scale, that are again composed of molecular scale assemblies with a huge number of polymer chains. Therefore, nano-imaging of polymer gel may provide novel insight into the networks yet invisible so far. Here, we introduce an application of SNOM for a PMMA chemical gel labeled with fluorescence probes such as Pe and Eo chromophores [82].

The sample was prepared by radical copolymerization of MMA monomer in toluene solutions containing a small amount of 3-perylenylmethyl methacrylate as a fluorescent monomer and ethylene glycol dimethacrylate as a cross-linker. The sample for SNOM measurements was prepared from the solid gel thus obtained, which was sliced using a microtome, yielding a very thin film with a thickness of ca. 100 nm, and then the inner structure was observed by SNOM.

Figure 24 shows three pictures taken in different SNOM modes. Panel a is the shear force topographic picture, in which the oblique lines display scratch of the surface made with the knife edge of the microtome. Panel b shows an
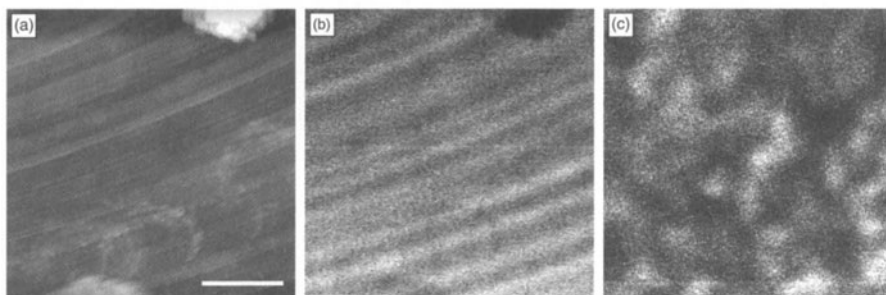
Fig. 24 SNOM images of a polymer network of PMMA with cross link density of 0.1%. (**a**) Shear force topographic image, (**b**) transmission image and (**c**) fluorescence image. The scale bar indicates 1 μm and the wavelength of the light source was 442 nm. Reprinted with permission of [82], copyright (2000) American Chemical Society

optical transmission image obtained by scattered light at the surface. As like as panel a, the surface topography appeared, showing only oblique lines made by the knife edge. However, panel c in Fig. 24, image of fluorescence of Pe in the same area as panels a and b, shows inhomogeneous distribution of fluorescence intensity, instead of the surface topography. The structure with a size of 500–600 nm was observed, suggesting the inhomogeneous and domain-like network structure of the PMMA gel. These pictures indicate that SNOM can be used to reveal the nano-structures inside the sample film, whereas AFM gives simply topographic images of the surface. The size of inhomogeneity became markedly small with the increase in crosslink density. These results indicate that the SNOM picture taken in the fluorescence mode actually represents the fluctuation of segment density in the polymer networks, although the fluorescent probes were introduced into the polymer chains at a statistically random distribution.

The inhomogeneous structure was monitored by the energy transfer method. The rate of energy transfer between a donor molecule and an acceptor molecule is determined by the distance of separation in a nanometer dimension. Therefore, the inhomogeneity of segment density results in faster decay of donor fluorescence compared with homogeneous distribution. To observe this phenomenon, Pe and Eo dyes were introduced into the PMMA
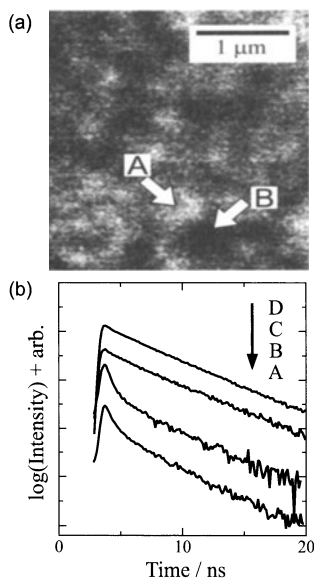
Fig. 25 (a) Fluorescence SNOM image of a PMMA gel labeled with Pe and Eo dyes (b) Fluorescence decay curves of Pe observed for: (curves A and B) PMMA gel at points A and B indicated in panel a, (curve C) PMMA bulk sample without crosslinker, (curve D) spin-cast PMMA film containing Pe dyes. Reprinted with permission of [26], copyright (2003) The Chemical Society of Japan

chains in the gel; the latter dye Eo acts as an energy acceptor for the Pe donor. Figure 25a shows again a SNOM picture of PMMA gel, in which the marked positions A and B were examined by the time-resolving measurement for Pe fluorescence and the decay data are shown in Fig. 25b. The decay functions at these points obviously consist of multi-component functions, but the average lifetimes are far shorter than the intrinsic decay function of the isolated Pe in a spin-cast film, which is plotted with the line D. For comparison, a control PMMA sample labeled with both Pe and Eo dyes was prepared at the same concentrations as the gel. This spin cast film provides a homogeneous distribution of these dyes in the bulk, hence the decay curve C is very similar to curve D for the isolated Pe with a random distribution. These results indicate that the PMMA gel has large local densities at least 10 times higher than the homogeneous distribution.

It is also very interesting that the fast decay rate due to the high density of polymer segment was almost constant irrespective of the positions observed. As seen in Fig. 25a, point A is much brighter than point B, suggesting that the segment density at A is higher than that at B. However, the energy transfer experiment obviously indicates that the density is independent of the observed position. This discrepancy can be explained by assuming a structural hierarchy of PMMA gel. Since the energy transfer takes place between molecules closer than ca. 10 nm, the fluorescence decay function indicates the local environment of a micro-cluster in the molecular scale of 1–10 nm. In a larger scale of 10–1000 nm, the clusters are connected and form aggregates with an inhomogeneous structure, which was observed by the fluorescence SNOM. Therefore, the dark and bright parts of SNOM image represent simply the small and large numbers of clusters, respectively, in which the local concentration of polymer segment in the molecular level is always very high, regardless of the brightness of the SNOM image in a large scale of a few hundred nanometers.

3.6
Development of SNOM

Previous SNOM measurements have been performed by detecting the fluorescence signal from the specimen in many cases. Fluorescence SNOM is so sensitive that it can detect the signal from a single molecule and provides valuable information such as the orientation and spatial distribution of the fluorescent molecules not only from the intensity but also from the spectra and time-resolved profiles. Needless to say, however, the fluorescence SNOM measurement can be applied only to the chemical species which is fluorescent in a visible range. For a non-fluorescent specimen, the fluorescence labeling must be carried out, but the introduction of dye molecules often involves complicated chemical synthetic processes. The fluorescence SNOM limits its versatility in variation of observable species, while it is

highly sensitive and gives one various kinds of molecular information. Therefore, another spectroscopic method is desired to directly observe a variety of chemicals. Vibrational spectroscopy could be a promising technique for the SNOM measurement with chemical information [83–89]. The infrared absorption and Raman scattering spectra can be obtained for all chemical species in principle, and they provide much information on the chemicals as the "fingerprint" of a molecule. Therefore, the vibrational spectroscopy SNOM has attracted the attention of many researchers because it would allow the direct spectral characterization of various chemicals with a nanometric spatial resolution. However, Raman scattering spectroscopy has been considerably difficult because the Raman scattering cross section is very low (a factor of 10^{14}) compared to that for fluorescence emission. It is well known that the Raman scattering intensity is greatly enhanced on a rough metal surface: surface enhanced Raman spectroscopy (SERS). The SERS mechanism was introduced to excite the specimen in a local area in order to increase the Raman intensity. In Raman SNOM, a sharp metal stylus without an aperture is used; this type of SNOM is often called the apertureless SNOM in contrast to the SNOM using an optical fiber probe. The sample is illuminated by a focused laser beam in a diffraction-limited size. A sharp metal tip (a gold or silver-coated AFM cantilever is typically used) is on the focal spot. At the tip end, the electric field intensity is enhanced by the surface
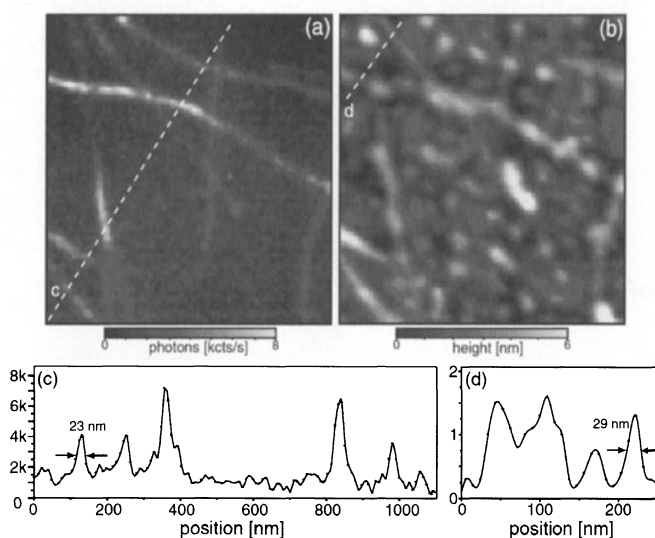
Fig. 26 (**a**) Near-field Raman image and (**b**) simultaneously obtained surface topography of single wall carbon nanotubes. Scan area is $1 \times 1\,\mu m^2$ Numerous circular features in the topography are attributed to contaminant water droplets. The cross-section profiles for Raman and topographic images are shown in panels c and d, respectively. Reprinted with permission of [87], copyright (2003) American Institute of Physics

plasmon excitation of the metal tip. This localized and enhanced field excites the specimen and induces the detectable Raman scattering from a nanometric area [84–87]. Figure 26 indicates the Raman SNOM image of single wall carbon nanotubes (SWNTs), which was obtained by collecting the G' band of SWNT at a wavenumber of 2615 cm^{-1} attributed to the overtone of the defect mode. In the Raman scattering image of Fig. 26a, the individual SWNTs are clearly imaged, whereas a lot of circular dots are seen besides the SWNTs in the simultaneously observed topographic image of panel b. This indicates the ability of the Raman SNOM to distinguish chemical species. Each SWNT was observed as a strand with a width of 23 nm, indicating the high spatial resolution better than $\lambda/25$. With regard to the infrared spectroscopy, the absorption contrast for the minute sample volume in the order of attoliter. Keilmann and his co-workers have reported that the scattering intensity in the apertureless SNOM configuration is dependent on the infrared absorption at the illumination wavelength [88, 89]. A phase-separated blend of PS and PMMA was observed at wavelengths of 9.68 and 10.17 μm, which were attributed to the absorption bands for PS and PMMA, respectively, and each component was distinguished by selecting the appropriate wavelength

The near-field vibrational spectroscopy has been greatly developed in recent years. However, the number of chemical species practically imaged is
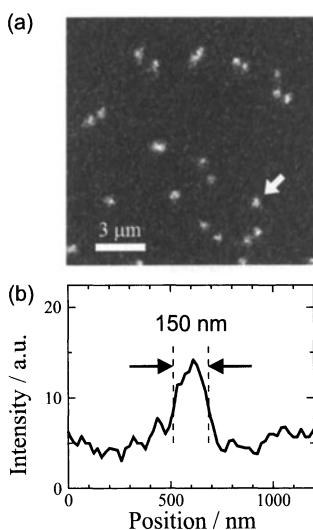
Fig. 27 (**a**) DUV-SNOM image of polystyrene nano-particles with a diameter of 100 nm (**b**) As shown in the cross-section profile for the arrowed particle, the bead has a circular shape with a diameter of 150 nm This indicates the high spatial resolution beyond the diffraction limit. Reprinted with permission of [90], copyright (2004) American Institute of Physics

still limited. In contrast to the vibrational characterization, another approach has been reported for the direct imaging of a variety of chemicals, that is, near-field fluorescence spectroscopy in the deep ultra-violet (DUV) region [90]. The DUV light at a wavelength below 300 nm can induce the $\pi-\pi^*$ transition of a carbon-carbon double bond. For example, benzene has an absorption band around 250 nm and emits the fluorescence at 270–300 nm. Therefore, all aromatic chemical species can be excited in the DUV range. Previously, we could not use the UV light shorter than 400 nm in SNOM because it is strongly absorbed by the dopant included in the core of the fiber probe. In the DUV-SNOM, the probe is fabricated from an optical fiber with a pure quartz core, which is transparent at $\lambda > 220$ nm. Figure 27 indicates the DUV-SNOM image of nano-spheres of PS with a diameter of 100 nm. The side-chain phenyl group in PS was excited by the near-field at a wavelength of 266 nm, and the benzene excimer emission at 300–340 nm was collected. The PS beads were clearly observed in the DUV-SNOM image. The observed diameter for the 100 nm beads was ca. 150 nm, indicating the high spatial resolution better than 100 nm beyond the diffraction limit. Thus, DUV-SNOM allows direct imaging of the aromatic polymer without any chemical modification such as fluorescence labeling. Figure 28 shows a DUV-SNOM image for a phase-separated polymer blend composed of PS and PMMA, in which the former PS domains were selectively observed without any fluorescent labels. As mentioned above, also the Raman SNOM would enable the direct

(a)

(b)

5 μm
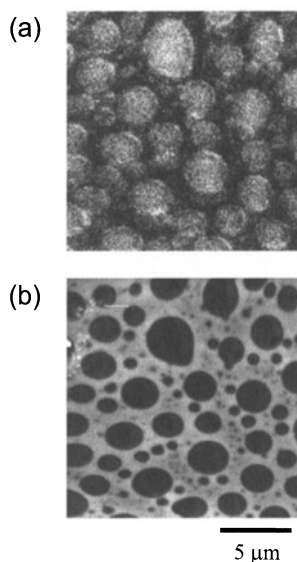
Fig. 28 (**a**) DUV-SNOM and (**b**) topographic images of a phase separation structure of a polystyrene/poly(methyl methaacrylate) blend thin film. The polystyrene is directly observed without any labeling procedure

imaging of chemicals. Due to the difficulty of signal enhancement, however, Raman imaging has been reported for only a few kinds of chemicals at the present stage. On the other hand, since DUV-SNOM is operated by collecting the inherently strong fluorescence emission, a variety of chemicals can be observed with the high sensitivity and the sub-wavelength spatial resolution. The direct imaging by the DUV-SNOM has been performed not only for PS but also other aromatic polymers and biological materials: polycarbonate, poly(ehtyleneterephthalate), proteins, and DNA. Thus, DUV-SNOM expands the range of wavelength and chemicals examined, and provides versatile spectroscopic techniques useful in the analysis of polymer systems.

4
Summary

Optical microscopy, a conventional tool for investigating materials, is still making great progress with the introduction of novel optical techniques. In recent years LSCM has been introduced to a variety of scientific fields, exhibiting the particular advantage of 3-dimensional imaging with a sub-micron scale resolution, while keeping the merits of an optical method such as high sensitivity of detection, time-resolution for molecular and excitation dynamics and spectroscopic analysis of materials. SNOM has brought further improvement particularly in the spatial resolution beyond the diffraction limit of light, and has extended the ability of optical analysis to nanometer dimensions. With the aid of novel ideas and techniques, SNOM has been continuously improved both in resolution and in sensitivity. It has already realized single molecule detection with a lateral resolution of ca. 30 nm, which is one order higher than the resolution of LSCM and two orders higher than the resolution of conventional optical microscopes. The importance of nano-scale science is now widely recognized, and much attention has been paid to organic materials and their assemblies. Therefore, optical microscopy is expected to make more contributions to the soft materials science as a tool for seeing in nanometer dimensions.

References

1. Wilson T (1990) Confocal Microscopy. Academic Press, London
2. Webb RH (1996) Rep Prog Phys 59:427
3. Brakenhoff GJ, Blom P, Barends P (1979) J Microsc 117:219
4. Gensch T, Hofkens J, van Stam J, Faes H, Creutz S, Tsuda K, Jerome R, Masuhara H, De Schryver FC (1998) J Phys Chem B 102:8440

5. Verhoogt H, van Dam J, Posthuma de Boer A, Draaijer A, Houpt PM (1993) Polymer 34:1325
6. Li L, Sosnowski S, Chaffey CE, Balke ST, Winnik MA (1994) Langmuir 10:2495
7. Kumacheva E, Li L, Winnik MA, Shinozaki DM, Cheng PC (1997) Langmuir 13:2483
8. Harmon ME, Schrof W, Frank CW (2003) Polymer 44:6927
9. Vorobyova O, Winnik MA (2001) J Polym Sci B 39:2317
10. Vorobyova O, Winnik MA (2001) Macromolecules 34:2298
11. Wu J, Li H, Winnik MA, Farwaha R, Rademacher J (2004) J Polym Sci A 42:5005
12. Ribbe AE, Hashimoto T (1997) Macromolecules 30:3999
13. Jinnai H, Nishikawa Y, Morimoto H, Koga T, Hashimoto T (2000) Langmuir 16:4380
14. Jinnai H, Kitagishi H, Hamano K, Nishikawa Y, Takahashi M (2003) Phys Rev E 67:021801
15. Newby BZ, Composto RJ (2000) Macromolecules 33:3274
16. Moffitt M, Rharbi Y, Tong JD, Farhina JPS, Li H, Winnik MA, Zahalka H (2003) J Polym Sci B 41:637
17. Ma Y, Farinha JPS, Winnik MA, Yaneff PV, Ryntz RA (2004) Macromolecules 37:6544
18. Jinnai H, Yoshida H, Kimishima K, Funaki Y, Hirokawa Y, Ribbe AE, Hashimoto H (2001) Macromolecules 34:5186
19. Vanden Bout DA, Yip W-T, Hu D, Fu D-K, Swager TM, Barbara PF (1997) Science 277:1074
20. Huser T, Yan M (2001) J Photochem Photobio A 144:43
21. Huser T, Yan M, Rothberg LJ (2000) Proc Natl Acad Sci USA 97:11187
22. Sartori SS, De Feyter S, Hofkens J, Van der Auweraer M, De Schryver F, Brunner K, Hofstraat JW (2003) Macromolecules 36:500
23. Schindler F, Lupton JM, Feldmann J, Scherf U (2004) Proc Natl Acad Sci USA 101:14695
24. Hu D, Yu J, Barbara PF (1999) J Am Chem Soc 121:6936
25. Lee J, Lee J, Lee M, Lee K-J-B, Ko D-S (2004) Chem Phys Lett 394:49
26. Ito S, Aoki H (2003) Bull Chem Soc Jpn 76:1693
27. Vallee RAL, Cotlet M, Hofkens J, De Schryver F, Muellen K (2003) Macromolecules 36:7752
28. Vallee RAL, Tomczak N, Kuipers L, Vancso GJ, van Hulst NF (2003) Phys Rev Lett 91:038301
29. Vallee RAL, Vancso GJ, van Hulst NF, Calbert JP, Cornil J, Bredas JL (2003) Chem Phys Lett 372:282
30. Tomczak N, Vallee RAL, van Dijk EMH, Kuipers L, van Hulst NF, Vancso GJ (2004) J Am Chem Soc 126:4748
31. Tomczak N, Vallee RAL, van Dijk EMH, Garcia-Parajo M, Kuipers L, van Hulst NF, Vancso GJ (2004) Euro Polym J 40:1001
32. Hofkens J, Vosch T, Maus M, Koehn F, Cotlet M, Weil M, Herrmann A, Muellen K, De Schryver FC (2001) Chem Phys Lett 333:255
33. Born M, Wolf E (1980) Principles of Optics. Pergamon Press, Oxford
34. Denk W, Strickler JH, Webb WW (1990) Science 248:73
35. Diaspro A, Robello M (2000) J Photochem Photobiol B:Biol 55:1
36. Nakamura O (1999) Microsc Res Tech 47:165
37. Hell SW, Wichmann J (1994) Opt Lett, 19:780
38. Klar T, Hell SW (1999) Opt Lett 24:954
39. Klar T, Jakobs S, Dyba M, Egner A, Hell SW (2000) Proc Nat Acad Sci USA 97:8260

40. Westphal V, Blanca CM, Dyba M, Kastrup L, Hell SW (2003) Appl Phys Lett 82:3125
41. Osborne MA, Barnes CL, Balasubramanian S, Klenerman D (2001) J Phys Chem B 105:3120
42. Kang SH, Shortreed MR, Yeung ES (2001) Anal Chem 73:1091
43. Paesler MA, Moyer PJ (1996) Near-Field Optics: Theory, Instrumentation, and Applications. John Wiley & Sons, New York
44. Ohtsu M (1998) Near-Field Nano/Atom Optics and Technology. Springer, Tokyo
45. Kawata S, Ohtsu M, Irie M (2002) Nano-Optics. Springer, Berlin
46. Betzig E, Trautman JK, Harris TD, Weiner JS, Kostelak RL (1991) Science 251:1468
47. Betzig E, Trautman JK (1992) Science 257:189
48. Vanden Bout DA, Kerimo J, Higgins DA, Barbara PF (1997) Acc Chem Res 30:204.
49. Dunn RC (1999) Chem Rev 99:2891
50. Synge EH (1928) Phil Mag 6:356
51. Binnig G, Rohrer H, Gerber Ch, Weibel E (1982) Phys Rev Lett 49:57
52. Binnig E, Quate CF, Gerber Ch (1986) Phys Rev Lett 56:930
53. Pangaribuan T, Yamada K, Jiang S, Ohsawa H, Ohtsu M (2002) Jpn J Appl Phys 31:L1302
54. Garcia-Parajo MF, Veerman JA, van Noort SJT, de Grooth BG, Greve J, van Hulst NF (1998) Bioimaging 6:43
55. Kumaki J, Nishikawa Y, Hashimoto T (1996) J Am Chem Soc 118:3321
56. Kumaki J, Hashimoto T (1998) J Am Chem Soc 120:423
57. Richards D, Cacialli F (2004) Phil. Trans R Soc Lond. A 362:771
58. Richards D (2003) Phil. Trans R Soc Lond. A 361:2843
59. Bethe HA (1944) Phys Rev 66:163
60. Ito S, Aoki H, Anryu M (2001) Trans Mater Res Soc Japan 26:929
61. Naito K (1989) J Colloid Interface Sci 131:218
62. de Gennes PG (1979) Scaling Concepts in Polymer Physics. Cornell University, Ithaca, N.Y.
63. Sato N, Ito S, Yamamoto M (1996) Polym J 28:784
64. Sato N, Ito S, Yamamoto M (1998) Macromolecules 31:2673
65. Stevenson R, Milner, RG, Richards D, Arias AC, Mackenzie JD, Halls JJM, Friend RH, Kang DJ, Blamire M (2001) J Microscopy 202:433. (S22 PF)
66. Chappell J, Lidzey DG (2003) J Microscopy 209:188. (N19 blend PF)
67. Kwak ES, Kang TJ, Vanden Bout DA (2001) Anal Chem 73:3257. (N31 decay)
68. Teetsov J, Vanden Bout DA (2000) J Phys Chem B 104:9378
69. Teetsov J, Vanden Bout DA (2001) Macromol Symp 167:153
70. Teetsov J, Vanden Bout DA (2002) Langmuir 18:897
71. Hsu JH, Wei PK, Fann WS, Chuang KR, Chen SA (1998) Ultramicroscopy 71:263
72. DeAro JA, Lemmer U, Moses D, Buratto SK (1999) Synthetic Metals 101:300
73. Schaller RD, Lee LF, Johnson JC, Haber LH, Saykally RJ, Vieceli J, Benjamin H, Nguyen TQ, Schwartz BJ (2002) J Phys Chem B 106:9496
74. Nabetani Y, Yamasaki M, Miura A, Tamai N (2001) Thin Solid Films 393:329
75. Tan CH, Inigo AR, Hsu JH, Fann W, Wei PK (2001) J Phys Chem Solids 62:1643
76. DeAro JA, Moses D, Buratto SK (1999) Appl Phys Lett 75:3814
77. Aoki H, Sakurai Y, Ito S, Nakagawa T (1999) J Phys Chem B, 103:10553
78. Aoki H, Ito S (2001) J Phys Chem B 105:4558
79. Aoki H, Kunai Y, Ito S, Yamada H, Matsushige K (2002) Appl Surf Sci 188:534
80. Sakurai Y, Sato N, Ito S, Yamamoto M (1999) Kobunshi-Ronbunshu 56:850
81. Hirokawa Y, Jinnai H, Nishikawa Y, Okamoto T, Hashimoto T (1999) Macromolecules 32:7093

82. Aoki H, Tanaka Ito SS, Yamamoto M (2000) Macromolecules 33:9650
83. Jahncke CL, Paesler PA, Hallen HD (1995) Appl Phys Lett 67:2483
84. Deckert V, Zeisel D, Zenobi R, Vo-Dinh T (1998) Anal Chem 70:2646
85. Hayazawa N, Inouye Y, Sekkat Z, Kawata S (2001) Chem Phys Lett 335:369
86. Hayazawa N, Yano T, Watanabe H, Inouyea Y, Kawata S (2003) Chem Phys Lett 376:174
87. Hartschuh A, Sanchez EJ, Xie SX, Novotny L (2003) Phys Rev Lett 90:095503
88. Knoll B, Keilmann F (1999) Nature 399:134
89. Taubner T, Hillenbrand R, Keilmann F (2004) Appl Phys Lett 85:5064
90. Aoki H, Hamamatsu T, Ito S (2004) Appl Phys Lett 84:356

Editor: S. Kobayashi

Generalized Gaussian Structures:
Models for Polymer Systems with Complex Topologies

Andrey A. Gurtovenko[1,2] (✉) · Alexander Blumen[3]

[1]Biophysics and Soft Matter Group,
 Laboratory of Physics and Helsinki Institute of Physics,
 Helsinki University of Technology, P.O.Box 1100, 02015 Helsinki, Finland
 agu@fyslab.hut.fi

[2]Institute of Macromolecular Compounds, Russian Academy of Sciences,
 Bolshoi Prospect 31, V.O., 199004 St. Petersburg, Russia
 agu@fyslab.hut.fi

[3]Theoretische Polymerphysik, Universität Freiburg, Hermann-Herder-Str. 3,
 79104 Freiburg, Germany
 blumen@physik.uni-freiburg.de

Abstract A fundamental and long-standing problem in polymer physics is to deduce the relationship between the topology of a polymer and its dynamics. Generalized Gaussian structures (GGS), originating from the familiar Rouse model, represent a valuable tool for this purpose. This review summarizes theoretical efforts that have been undertaken in studying the dynamics of polymer systems with complex internal topologies by employing the GGS approach. The dynamic properties of a wide range of polymeric structures (ranging from polymer networks to dendritic and hybrid polymers) are discussed, while emphasizing systems that can be treated analytically (or semi-analytically). These studies provide considerable insight into the problem of relating the structure of a polymer to its dynamics. In many cases the GGS-treatment represents a first step in understanding the dynamics of polymers, and it may serve as a reference point for the development of more realistic models.

Keywords Polymers · Dynamics · Theory · Gaussian Structures · Networks · Dendrimers

1
Introduction

One of the basic challenges in polymer physics is to understand how the underlying geometries – and especially the topologies – of polymeric materials affect their dynamic behavior. This problem has a long-standing history and is becoming of increased importance as new polymeric materials with more and more complex architectures are synthesized. Polymers, being intricate systems, demonstrate a wide range of dynamic features that cannot be fully understood without elucidating the connections between structure and dynamics. Therefore, theoretical models that allow analytical insights into this problem are extremely valuable.

The pioneering ideas of Rouse, starting with the bead-and-spring model for linear flexible chains [1, 2] resulted in a basic approach that could be used to treat the dynamics of polymers. This (essentially coarse-grained) model was designed to study dynamic features of flexible macromolecules on scales larger than the distances covered by a few monomers: in the Rouse model a polymer chain is envisaged as being a sequence of beads connected by harmonic entropic springs. As such, the approach is very general (universal). Furthermore, the solvent (or, the surrounding medium consisting, say, of other polymer chains in the case of concentrated polymer systems) is substituted by a continuum, which is felt by the chain's beads through the viscous friction and the thermal noise. In a certain sense Rouse's approach leads to a "minimal" model which is very simplified, but which captures the most fundamental feature that distinguishes macromolecules from simple liquids, namely the polymer's *connectivity*. In spite of the fact that it disregards several important features, the Rouse model captures the dynamic properties of many systems, including concentrated polymer solutions and melts of rather short chains [2, 3].

The extension of Rouse's approach from linear chains to other polymer systems is quite straightforward and leads eventually to the concept of generalized Gaussian structures (GGS), which are the subject of this review. In the framework of the GGS approach, a polymer system is modeled as a collection of beads (subject to viscous friction), connected to each other by means of elastic springs in a system-specific way. Initially, the GGS concept was inspired by the study of cross-linked polymer networks; however, its applications have turned out to cover large classes of substances, such as dendritic polymers, hybrid polymers, and hierarchically-built structures.

A GGS, being a generalization of the Rouse model, has all the limitations of its predecessor: it does not account for excluded volume interactions and for entanglement effects. However, one may note that excluded volume effects are often screened. This occurs especially in rather dense media, such as dry polymer networks and polymer melts [2, 4]. The entanglement effects, in

turn, are not dominant as long as one stays below the entanglement limit. In the case of polymer networks this means high densities of cross-links, which then implies that the network strands between the cross-link points are rather short. The hydrodynamic, solvent-mediated interactions are also generally screened in dense systems [2]. We will not discuss their role in this review and we wish only to point out that they can be incorporated in the GGS as in the Zimm model, in a pre-averaged manner [5].

Bearing in mind all of the above restrictions (which may influence the global picture, depending on the situation at hand), the GGS approach represents an important step in the theoretical understanding and treatment of the dynamics of complex polymer systems. The basic simplicity of the GGS-approach often allows theoretical (analytical or semi-analytical) solutions to dynamical problems, even for very intricate polymer architectures. This great advantage is lost when the models become more and more involved, when they include interactions which the GGS disregards; such additions certainly make the models more realistic, but they also make them less tractable analytically. This eventually leads to a situation in which only computer simulations may help; these, on the other hand, are in general restricted to much shorter time domains than the temporal ranges accessible through GGS approaches.

In this article we review theoretical works which have employed the GGS model. We start – evidently – with the classical Rouse chain [1], but we will emphasize the developments that have occurred over the last decade. We want to stress from the beginning that our paper is essentially devoted to the *dynamics* of polymeric systems; a detailed analysis of the statistical equilibrium properties of Gaussian structures is beyond the scope of this paper. Also, we do not aim to provide an exhaustive exposition of the GGS literature. Our choice of topics reflects in large part our research interests and is, in this sense, biased. We would also like to point out that our choice covers only limited classes of complex polymeric systems, and that we focus on such particular systems in which one can attain, to a large degree, an (almost) analytical solution of the dynamical problem.

Our review starts with the general formulation of the GGS model in Sect. 2. In the framework of the GGS approach many dynamical quantities of experimental relevance can be expressed through analytical equations. Because of this, in Sect. 3 we outline the derivation of such expressions for the dynamical shear modulus and the viscosity, for the relaxation modulus, for the dielectric susceptibility, and for the displacement of monomers under external forces. Section 4 provides a historical retrospective of the classical Rouse model, while emphasizing its successes and limitations. The next three sections are devoted to the dynamical properties of several classes of polymer networks, ranging from regular and fractal networks to network models which take into account structural heterogeneities encountered in real systems. Sections 8 and 9 discuss dendrimers, dendritic polymers, and hyperbranched polymers.

Finally, we end the review with the so-called hybrid polymers, which display several levels of organization; examples for two-level organization are networks bearing dendritic wedges, dendrimer-based polymer networks, and regular lattices built from highly disordered subunits.

2
Generalized Gaussian Structures: The Model

In this section we formulate the theoretical framework of the so-called generalized Gaussian structures [6–9]. A generalized Gaussian structure (GGS) represents the extension of the classical Rouse model [1, 2], developed for linear polymer chains, to systems of arbitrary topology: it is modeled as a structure consisting of N_{tot} beads connected by harmonic springs, see Fig. 1. For simplicity, all of the beads of the GGS are subject to the same friction constant ζ with respect to the surrounding viscous medium (the solvent). The GGS-approach is essentially a coarse-grained one: The friction constant of the GGS beads mirrors the overall friction of polymer fragments directly attached to a given point (bead). In turn, the chain fragments between the beads are assumed to be long enough, so that they obey Gaussian statistics. Normally, a chain fragment of about ten monomers fulfills this requirement. This allows each chain fragment to be satisfactorily modeled by an elastic (entropic) spring.

The potential energy of the GGS in the absence of external forces, U_{elast}, contains the elastic contributions of the harmonic springs (bonds) connected to each other:

$$U_{elast}(\{R\}) = \frac{K}{2} \sum_{bonds} [R_n - R_m]^2 = \frac{K}{2} \sum_{n=1}^{N_{tot}} \sum_{m=1}^{N_{tot}} A_{nm} R_n R_m , \tag{1}$$
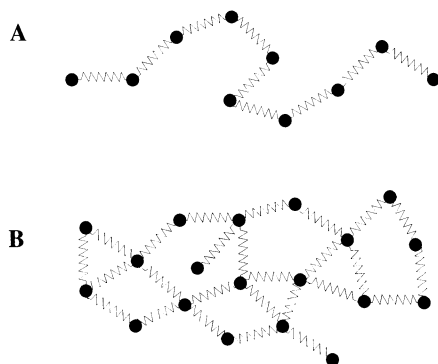
Fig. 1 (A) Schematic representation of the bead-and-spring Rouse chain and (B) a particular example of a GGS

where $R_n(t) = (X_n(t), Y_n(t), Z_n(t))$ and $R_m(t) = (X_m(t), Y_m(t), Z_m(t))$ are the position vectors of the nth and mth GGS beads, respectively. The summation in the first sum of Eq. 1 goes over all pairs of beads n, m directly connected by elastic springs (bonds). The quantity $K = 3k_B T/b^2$ is the elastic constant of a harmonic spring, where k_B is the Boltzmann constant, T is the temperature, and b^2 is the mean square end-to-end distance for the unstretched spring. On the right-hand-side (rhs) of Eq. 1 we remark that the potential energy U_{elast} can be represented through the connectivity matrix $A = (A_{nm})$ of the given GGS, which is also called the Kirchhoff matrix or the generalized Rouse matrix [6, 7, 10–12]. The connectivity matrix A contains all of the information about the topology of the GGS in question and is constructed as follows. Starting with all matrix elements equal to zero, we set the non-diagonal element A_{nm} equal to (– 1) if the nth and mth beads are directly connected by a spring (otherwise, A_{nm} stays equal to zero). The diagonal element A_{nn} is set to equal the number of springs (bonds) emanating from the nth bead. Obviously, $\det A = 0$ by construction and, therefore, at least one of its eigenvalues vanishes. If the structure does not separate into disjointed, unconnected substructures then the vanishing eigenvalue is non-degenerate. Note that for a linear polymer chain this procedure leads to the well-known Rouse matrix [1, 2].

The dynamics of the GGS are described by a set of linearized Langevin equations of motion. In addition to the friction and elastic forces, one has also stochastic forces due to the random collisions of the solvent with the solute (the GGS beads) and, in general, a superimposed field due to forces external to the polymer system. We note that at the time-scales usually treated in the study of polymers, the inertial term is rather unimportant; thus we neglect it. Taking all this into account, the Langevin equation of motion for the lth bead of the GGS reads:

$$\zeta \frac{dR_l(t)}{dt} + K \sum_{m=1}^{N_{tot}} A_{lm} R_m(t) = f_l(t) + F_l^{(ext)}(t) . \tag{2}$$

Here $f_l(t)$ are the stochastic forces and $F_l^{(ext)}(t)$ is the external force acting on the lth GGS bead. Because of the fluctuation-dissipation theorem, the stochastic forces (thermal noise) $f_l(t)$ are connected with the dissipative force (friction). In Eq. 2 the thermal noise $f_l(t)$ is assumed to be Gaussian with zero mean value, so that one has $\langle f_l(t) \rangle = 0$ and $\langle f_{l\alpha}(t) f_{m\beta}(t') \rangle = 2k_B T \zeta \delta_{lm} \delta_{\alpha\beta} \delta(t - t')$ (here α and β denote the x, y, and z directions).

It is important to keep in mind (see the "Introduction") that the GGS approach provides a rather simple description of polymer systems; it does not take into account interactions such as the excluded volume effects or entanglements. In some special cases (such as for polymer melts or dry polymer networks) the excluded volume interactions may be screened [2, 4]. The entanglement effects, in turn, are quite small for sufficiently short polymer chains [3]. Also, our GGS treatment here does not account for hydrodynamic

interactions which may be important in dilute polymer solutions. Note in this regard that the latter interactions may be included in the theory in a simplified, pre-averaged fashion [5, 13]. However, as will be demonstrated below, in spite of all these restrictions (crucial in some special cases), the GGS approach often leads to a reasonable description of polymer dynamics, allowing (due to its simplicity) analytical insights into the problem. Note that, despite the fact that we concentrate here mostly on homopolymers, the GGS approach allows extensions to heteropolymers, by allowing us to include several classes of beads and bonds into the picture (these beads and bonds may differ in their friction and elasticity constants, respectively) [14–21]. Thus, the GGS model can serve in many cases as a primary basis for understanding the fundamental problem of polymer physics, namely: how does the topology of a polymer affect its dynamical properties?

3
Target Dynamical Quantities

3.1
Mechanical Viscoelastic Relaxation

3.1.1
Dynamical Shear Modulus (Storage and Loss Moduli) and Viscosity

We start our exposition with basic dynamical features of polymers (often probed experimentally) and focus on mechanical relaxation. Here we encounter one of the most familiar properties of polymers, namely viscoelasticity. In general, polymers do not behave like solids or liquids; instead, they take an intermediate position, by which elastic or plastic behavior depends on the time-scale of the process under observation.

It is the aim of this subsection to present the derivation of analytic viscoelastic expressions in the GGS framework. As before, we take the GGS structure to be embedded in the viscous medium; for example, starting with a dilute polymer solution, the medium is given by the solvent. To measure the mechanical properties, one creates a macroscopic perturbation (strain) in the embedding medium. This external perturbation produces, in turn, a mesoscopic strain at the level of the polymer (GGS). A subsequent change of the polymer's configuration leads to the relaxation of the stress in the sample, which can be measured, allowing us to determine, for instance, the dynamic modulus.

Let us consider the influence of a flow (or velocity) field in the solvent. In terms of the Langevin equations of motion, Eq. 2, we then have [2, 22]:

$$F_l^{(\text{ext})}(t) = \zeta V_l(t),$$

(3)

where $V_l(t)$ is the velocity of the solvent at the location of the lth GGS bead, given by the position vector $R_l(t)$. Focusing now on *shear* flow, the velocity field may be written as $V_l(t) = (gY_l(t), 0, 0)$ where g is the velocity gradient. Such a two-dimensional flow can be generated in a polymer solution between two parallel plates, by letting one of them move. To obtain the frequency-dependent dynamic modulus and viscosity we consider the case of an oscillatory flow, where the velocity gradient g obeys $g = g_0 \exp(i\omega t)$ [2, 3, 22]. Then the perturbation of the solvent becomes:

$$V_{xl}(t) = g_0 \left[\exp(i\omega t) \right] Y_l(t), \quad V_{yl}(t) = 0 \quad \text{and} \quad V_{zl}(t) = 0 . \tag{4}$$

Furthermore, we assume that the applied velocity gradient g is small enough, so that the shear stress depends linearly on it; this is the domain of linear viscoelasticity.

Now the viscoelastic response of the polymer can be computed in two ways. The first consists of the direct evaluation of the stress arising in the polymer due to the strain induced by the perturbed viscous medium (solvent). The second way (which is in many ways equivalent to the first) is to calculate the additional virtual work which arises in the total system due to the presence of the polymer. Detailed descriptions of both methods can be found elsewhere [1, 2, 5, 9, 22–25]. Here we apply the second method, based on virtual work, in order to calculate the dynamic modulus and the viscosity.

The additional work W (the increase in energy loss) per unit volume and per unit time due to the presence of GGS in the solvent is given by [22]:

$$W = -\frac{1}{V} \sum_{l=1}^{N_{\text{tot}}} \langle F_l \cdot V_l^* \rangle = -\frac{1}{V} g_0 \exp(-i\omega t) \sum_{l=1}^{N_{\text{tot}}} \langle F_{xl} \cdot Y_l \rangle . \tag{5}$$

Here F_l is the force by which the perturbed viscous medium acts on the lth bead of the GGS and V_l is the velocity of the medium at the position of the lth GGS bead. Now V_l is given by Eq. 4 and the asterisk means complex conjugate; furthermore, V is the total volume of the system and $\langle \cdots \rangle$ denotes the average over the GGS configurations. Inserting the external forces imposed by the shear flow (see Eqs. 3 and 4) into Eq. 2 leads to the following set of equations of motion for the Cartesian coordinates of the position vectors of the GGS beads $R_l(t) = (X_l(t), Y_l(t), Z_l(t))$:

$$\zeta \left[\frac{dX_l(t)}{dt} - g_0 \exp(i\omega t)Y_l(t) \right] + K \sum_{m=1}^{N_{\text{tot}}} A_{lm}X_m(t) = f_{xl}(t) , \tag{6}$$

$$\zeta \frac{dY_l(t)}{dt} + K \sum_{m=1}^{N_{\text{tot}}} A_{lm}Y_m(t) = f_{yl}(t) , \tag{7}$$

and a similar equation for $Z_l(t)$. Note that due to the shear character of the external forces (the X component of the perturbation velocity of the solvent depends on the Y component of the position vector of the bead on

which the perturbation acts), Eq. 6 and Eq. 7 for the X and Y coordinates get coupled. The force F_{xl} in Eq. 5 is due to the action of the perturbed viscous medium on the X coordinate of the lth GGS-bead. Thus, one has $F_{xl} = \zeta[\dot{X}_l - g_0 \exp(i\omega t)Y_l]$. Therefore, we can simplify Eq. 5 using Eq. 6. This leads to

$$W = \frac{1}{V}g_0 \exp(-i\omega t)K \sum_{m=1}^{N_{\text{tot}}} A_{lm}\langle X_m(t) \cdot Y_l(t)\rangle. \tag{8}$$

To proceed further it is necessary to to transform the Cartesian coordinates R to the normal coordinates Q:

$$R_l(t) = \sum_{k=1}^{N_{\text{tot}}} C_{lk}Q_k(t). \tag{9}$$

Since the perturbation of the viscous medium is assumed to be small ($|g| \ll 1$), we can use the normal coordinates of the *unperturbed* GGS (in the absence of any external force $F_l^{(\text{ext})}(t)$, see Eq. 2) for our purposes. Then the transformation given by Eq. 9 simultaneously diagonalizes the potential energy U_{elast} of the unperturbed GGS, see Eq. 1, and preserves the diagonal form of the dissipative function R_{diss}:

$$U_{\text{elast}} = \frac{K}{2}\sum_{l=1}^{N_{\text{tot}}}\sum_{m=1}^{N_{\text{tot}}} A_{lm}R_lR_m = \frac{K}{2}\sum_{k=1}^{N_{\text{tot}}} \lambda_k Q_k^2 \tag{10}$$

and

$$R_{\text{diss}} = \frac{\zeta}{2}\sum_{l=1}^{N_{\text{tot}}} \dot{R}_l^2(t) = \frac{\zeta}{2}\sum_{k=1}^{N_{\text{tot}}} \dot{Q}_k^2. \tag{11}$$

Here λ_k are eigenvalues of the connectivity matrix A of the GGS. Each normal coordinate $Q_k = (Q_{1k}, Q_{2k}, Q_{3k})$ has a simple time behavior: it decays exponentially with time, $Q_k(t) \simeq Q_k(0)\exp(-t/\tau_k)$, where τ_k is introduced through

$$\tau_k = \frac{\tau_0}{\lambda_k}, \tag{12}$$

and $\tau_0 = \zeta/K$ is the characteristic relaxation time of the GGS. The normal mode transformation given by Eq. 9 reduces Eq. 8 to the following form:

$$W = \frac{1}{V}g_0 \exp(-i\omega t)K \sum_{k=2}^{N_{\text{tot}}} \lambda_k\langle Q_{1k}(t) \cdot Q_{2k}(t)\rangle. \tag{13}$$

Now the work W is fully determined by the correlation functions $\langle Q_{1k}(t) \cdot Q_{2k}(t)\rangle$. Note that in Eq. 13 the summation starts with $k = 2$, since we denote the vanishing eigenvalue (which is always present in a free-floating GGS) by λ_1, hence $\lambda_1 = 0$. The quantity $\langle Q_{1k}(t) \cdot Q_{2k}(t)\rangle$ can be easily computed from the equations of motion, Eqs. 6 and 7. Here we just outline the way

to do it. After the normal mode transformation of Eqs. 6 and 7, both equations are multiplied by $Q_{2k}(t)$ and averaged over the configurations. In this way one has from Eqs. 6 and 7:

$$\zeta \frac{d}{dt}\langle Q_{1k} \cdot Q_{2k}\rangle + 2K\lambda_k \langle Q_{1k} \cdot Q_{2k}\rangle - \zeta g_0 \exp(i\omega t)\langle Q_{2k}^2\rangle = 0 \tag{14}$$

and

$$\frac{1}{2}\zeta \frac{d}{dt}\langle Q_{2k}^2\rangle + K\lambda_k \langle Q_{2k}^2\rangle = k_B T. \tag{15}$$

Equation 15 has the equilibrium solution $\langle Q_{2k}^2\rangle = k_B T/K\lambda_k$. Inserting this solution into Eq. 14, one finally obtains for $\langle Q_{1k}(t) \cdot Q_{2k}(t)\rangle$ (by taking it proportional to $g_0 \exp[i\omega t]$):

$$\langle Q_{1k}(t) \cdot Q_{2k}(t)\rangle = k_B T g_0 \exp(i\omega t) \frac{\tau_k/2}{K\lambda_k[1 + i\omega\tau_k/2]}, \tag{16}$$

where we used Eq. 12. This leads immediately to the following closed form for W:

$$W = g_0^2 \frac{1}{V} k_B T \sum_{k=2}^{N_{tot}} \frac{\tau_k/2}{1 + i\omega\tau_k/2}. \tag{17}$$

The quantity W is directly related to the complex dynamic viscosity η^* through $W(\omega) = g_0^2 \eta^*(\omega)$ [2, 22]. Therefore, one has for η^*:

$$\eta^*(\omega) = \nu k_B T \frac{1}{N_{tot}} \sum_{k=2}^{N_{tot}} \frac{\tau_k/2}{1 + i\omega\tau_k/2}, \tag{18}$$

where we introduced $\nu = N_{tot}/V$, the number of GGS beads per unit volume of polymer solution. Now, because of the relation $G^* = i\omega\eta^*$ [1–3, 5, 22], the dynamic modulus $G^*(\omega)$ is given by:

$$G^*(\omega) = \nu k_B T \frac{1}{N_{tot}} \sum_{k=2}^{N_{tot}} \frac{i\omega\tau_k/2}{1 + i\omega\tau_k/2}. \tag{19}$$

We recall that so far we considered dilute polymer solutions. It is noteworthy that even for concentrated solutions, as long as the entanglement effects are still negligible (this holds for polymers of low molecular weight), both the complex dynamic modulus and the viscosity continue to follow the structure of Eqs. 19 and 18, the only difference [3] being a change in the prefactor $\nu k_B T$. Given that we are mostly interested in the frequency dependences of the shear dynamic modulus and of the viscosity, we will present in the following the viscoelastic properties of the GGS mostly in terms of reduced quantities. As an example, in the case of the shear modulus $G^*(\omega) = G'(\omega) + iG''(\omega)$, the

reduced storage, $[G'(\omega)]$ and loss, $[G''(\omega)]$, moduli read:

$$[G'(\omega)] = G'(\omega)/\nu k_B T = \frac{1}{N_{tot}} \sum_{k=2}^{N_{tot}} \frac{(\omega \tau_k/2)^2}{1 + (\omega \tau_k/2)^2} \tag{20}$$

and

$$[G''(\omega)] = G''(\omega)/\nu k_B T = \frac{1}{N_{tot}} \sum_{k=2}^{N_{tot}} \frac{\omega \tau_k/2}{1 + (\omega \tau_k/2)^2} . \tag{21}$$

In turn, for the reduced shear viscosity $[\eta'(\omega)]$ (we recall that $\eta^*(\omega) = \eta'(\omega) - i\eta''(\omega)$) we have:

$$[\eta'(\omega)] = \eta'(\omega)/\nu k_B T = \frac{1}{N_{tot}} \sum_{k=2}^{N_{tot}} \frac{\tau_k/2}{1 + (\omega \tau_k/2)^2} . \tag{22}$$

Here $[\eta'(\omega)]$ is meant to be the viscosity due to the polymer (GGS) only, the contribution of the viscosity of the solvent being assumed to be already subtracted from Eq. 22. Note that the relaxation times involved in the mechanical relaxation, $\tau_k/2$ in Eqs. 20, 21, and 22, are half those of the normal modes, Eq. 12. This is a direct consequence of the fact that only the second moments of the displacements (or, alternatively, only the $\langle Q^2 \rangle$) contribute to the mechanical viscoelastic properties, as may be verified by reconsidering the derivation given above. As we will demonstrate in the following, this is not the case for the dielectric relaxation. It is instructive to emphasize that the derivation presented here does not use any assumptions about the topology of the GGS system. Therefore, the expressions for the shear dynamic modulus and the viscosity, Eqs. 20, 21, and 22, hold for arbitrary GGS topologies. Note also the fundamental fact that the eigenfunctions of the connectivity matrix A of the GGS do not appear: in the GGS-scheme the shear modulus and the viscosity depend only on the eigenvalues of A. Thus, in order to be able to evaluate $G'(\omega)$ and $G''(\omega)$ (as well as $\eta'(\omega)$), it suffices to determine the eigenvalues λ_k (or the relaxation times τ_k) only. This simplifies our consideration of the dynamics of the particular GGS systems we are interested in.

3.1.2
Time-Dependent Relaxation Modulus and Relaxation Spectrum

We turn from the *frequency-dependent* shear modulus and viscosity considered above to the *time-dependent* relaxation modulus. As mentioned in the previous section, we focus on the *linear* viscoelastic domain, in which the shear stress $\sigma(t)$ depends linearly on the velocity gradient $g(t)$ [2]. The relaxation modulus $G(t)$ is now implicitly introduced through a relation between

$g(t)$ and the ensuing stress $\sigma(t)$:

$$\sigma(t) = \int_{-\infty}^{t} G(t - t')g(t')\,\mathrm{d}t' \tag{23}$$

and, using $g(t) = g_0 \exp(i\omega t)$,

$$\sigma(t) = g_0 \exp(i\omega t) \int_{0}^{\infty} G(\tau) \exp(-i\omega\tau)\,\mathrm{d}\tau . \tag{24}$$

On the other hand, the stress $\sigma(t)$ imposed on the GGS by the perturbation of the viscous surrounding medium can be computed based on the additional work W due to the presence of the GGS; one finds that $\sigma(t) = g_0 \exp(i\omega t)(1/i\omega)G^*(\omega)$ where $G^*(\omega)$ is given by Eq. 19, see for example [2, 22, 24, 25]. Equating this expression to Eq. 24 leads to the connection between the complex shear modulus and the relaxation modulus:

$$G^*(\omega) = i\omega \int_{0}^{\infty} G(\tau) \exp(-i\omega\tau)\,\mathrm{d}\tau . \tag{25}$$

Combining it with Eqs. 20 and 21 for the real and the imaginary components of $G^*(\omega)$ results in a simple expression for $G(t)$. We write it in the reduced form

$$[G(t)] = G(t)/\nu k_B T = \frac{1}{N_{\mathrm{tot}}} \sum_{k=2}^{N_{\mathrm{tot}}} \exp\left(-\frac{2t}{\tau_k}\right) , \tag{26}$$

where we divided the relaxation modulus $G(t)$ by the factor $\nu k_B T$, with ν being the number of GGS beads per unit volume. One should note that the equilibrium modulus G_e (which is zero for GGS in dilute solutions but may take a non-zero value in the case of, say, dry polymer networks) is not included in Eq. 26. Thus, $[G(t)]$ describes only the transient time-dependent evolution of the system and vanishes at very long times.

A physically straightforward interpretation of the relaxation modulus $[G(t)]$ is that it represents the response of the stress to a shear jump [2, 9]. Furthermore, the relaxation modulus $[G(t)]$ (as well as the dynamic shear modulus $[G^*(\omega)]$) can be rewritten in terms of the logarithmic density of relaxation times, the so-called relaxation spectrum $H(\tau)$ [3, 26]:

$$[G(t)] = \int_{0}^{\infty} H(\tau) \exp(-t/\tau)\,\mathrm{d}\ln\tau . \tag{27}$$

If one has a discrete set of relaxation times, the relaxation spectrum can be represented as a sum of delta functions (see Eqs. 27 and 26):

$$H(\tau) = \frac{2}{N_{\text{tot}}} \tau \sum_{k=2}^{N_{\text{tot}}} \delta\left(\tau - \frac{\tau_k}{2}\right) . \tag{28}$$

In the case of a continuous spectrum of eigenvalues, in other words when the eigenvalues $\lambda(\xi)$ are defined by some continuous variable ξ, the relaxation spectrum $H(\tau)$ can rewritten as (see [12] and also Sect. 7.5.1):

$$H(\tau) = -\frac{1}{N_{\text{tot}}} \frac{d\xi}{d\ln\tau} . \tag{29}$$

It is now important to note that the relaxation spectrum (the eigenvalue spectrum of the GGS) itself determines many important dynamical features. In particular, it fixes $G(t)$ and $G^*(\omega)$ through Eqs. 27 and 25. Also, global aspects such as scaling carry over. Thus, if the relaxation spectrum of the particular GGS decays as $\tau^{-\alpha}$ where $\alpha > 0$, the viscoelastic dynamical properties of the GGS also scale, so that both the storage modulus $G'(\omega)$ and the relaxation modulus $G(t)$ exhibit power-law behavior; one finds, using Eqs. 27 and 25, that $G'(\omega) \sim \omega^\alpha$ and $G(t) \sim t^{-\alpha}$.

3.2
Dielectric Relaxation

Besides mechanical viscoelastic experiments, one can also perform dielectric relaxation measurements, which constitute another well-established technique in polymer physics. Dielectric relaxation is related to the frequency-dependent complex dielectric susceptibility, $\varepsilon^*(\omega)$. One usually focuses on $\Delta\varepsilon^*(\omega)$, which is introduced as follows:

$$\Delta\varepsilon^*(\omega) = \frac{\varepsilon^*(\omega) - \varepsilon_\infty}{\varepsilon_0 - \varepsilon_\infty} . \tag{30}$$

In Eq. 30, ε_0 and ε_∞ denote the limiting low- and high-frequency dielectric constants, respectively. In general, for the $\Delta\varepsilon^*(\omega)$ of polar molecules embedded in non-polar solvents under an oscillatory electric field $E = E_0 \exp(i\omega t)$ we have [27]:

$$\Delta\varepsilon^*(\omega) \simeq \int_0^\infty \left(-\frac{d}{dt} C_0(M; t)\right) \exp(-i\omega t) \, dt , \tag{31}$$

when the local fields are not important. In Eq. 31 $C_0(M; t)$ is the normalized autocorrelation function of the total dipole moment $M(t)$ of the polymer

system:

$$C_0(M; t) = \frac{\langle M(0)M(t) \rangle}{\langle M^2(0) \rangle} . \tag{32}$$

In general, the expression for $\Delta\varepsilon^*(\omega)$, Eq. 31, can not be reduced to a simple, compact form. However, we proceed to show that this becomes possible under certain conditions.

Here we focus on the dielectric response of a polar GGS whose bonds (springs) possess dipole moments directed along them (the material is then of type A following Stockmayer's classification) [22, 28, 29]. In other words, in the model one assigns a longitudinal dipole moment m_j to each bond j of the GGS; the magnitude of every m_j is directly proportional to the length of the jth bond, but its orientation is arbitrary. The total dipole moment $M(t)$ of the GGS is given then by:

$$M(t) = \sum_{j=1}^{N_{\text{bond}}} \mu_j P_j(t), \tag{33}$$

where N_{bond} is the total number of bonds of the GGS, $\mu_j = d_j\mu$ is the dipole moment per unit length, $d_j \in \{+1, -1\}$ gives the orientation, and $P_j = R_l - R_m$ is the end-to-end vector of the jth bond between the lth and the mth GGS beads.

To proceed, we assume that the orientations of the dipole moments $\{m_j\}$ along the GGS bonds (defined by d_j) are random and uncorrelated [30–32]. This key feature simplifies the situation considerably. Then, for the autocorrelation function of $M(t)$, after averaging over all possible distributions of bonds' orientations, with the average denoted below by $\langle \cdots \rangle_{\text{orient}}$ (here we follow [31] closely), we have:

$$\langle\langle M(0)M(t) \rangle\rangle_{\text{orient}} = \sum_{j=1}^{N_{\text{bond}}} \sum_{i=1}^{N_{\text{bond}}} \mu^2 \langle d_j d_i \rangle_{\text{orient}} \langle P_j(0)P_i(t) \rangle \tag{34}$$

$$= \mu^2 \sum_{j=1}^{N_{\text{bond}}} \langle P_j(0)P_j(t) \rangle .$$

In deriving Eq. 34 we made use of the condition of random orientation, $\langle d_j d_i \rangle_{\text{orient}} = \delta_{ji}$. Equation 34 can be simplified further with the help of the normal mode transformation, see Eq. 9:

$$\langle\langle M(0)M(t) \rangle\rangle_{\text{orient}} = \mu^2 \sum_{k=1}^{N_{\text{tot}}} \langle Q_k^2 \rangle \exp(-t/\tau_k) \sum_{j=1}^{N_{\text{bond}}} \left(C_{lk}^{(j)} - C_{mk}^{(j)} \right)^2, \tag{35}$$

where we used the orthogonality of the normal modes Q and also their simple exponential decay with time: $\langle Q_k(0)Q_{k'}(t) \rangle = \delta_{kk'} \langle Q_k^2 \rangle \exp(-t/\tau_k)$. Here, as

before, $\tau_k = \tau_0/\lambda_k$. In Eq. 35 the superscript j of $C_{lk}^{(j)}$ and of $C_{mk}^{(j)}$ recalls that bond j is determined by R_l and R_m; in other words $P_j = R_l - R_m$. The quantity $\langle Q_k^2 \rangle$ can be easily determined from the Langevin equation of motion (see Eq. 2 with $F_l^{(ext)}(t) = 0$). Performing the transformation of this equation to normal coordinates one finds, for each component $\langle Q_{1k}^2 \rangle$, $\langle Q_{2k}^2 \rangle$, and $\langle Q_{3k}^2 \rangle$, an equation of the form of Eq. 15, from which the equilibrium solution for $\langle Q_k^2 \rangle = \langle Q_{1k}^2 \rangle + \langle Q_{2k}^2 \rangle + \langle Q_{3k}^2 \rangle$, namely

$$\langle Q_k^2 \rangle = \frac{3k_B T}{K\lambda_k} \tag{36}$$

follows [30, 31].

A further simplification of Eq. 35 for GGS follows by noting that the combination of Cartesian coordinates of the GGS beads involved in $\langle\langle M(0)M(t)\rangle\rangle_{orient}$, see Eq. 34, is directly related to the potential energy $U_{elast}(\{R\})$ of the GGS, see Eq. 1. Indeed, with the use of Eq. 10 one has [31]:

$$U_{elast}(\{R\}) = \frac{K}{2} \sum_{j=1}^{N_{bond}} P_j^2 = \frac{K}{2} \sum_{k=1}^{N_{tot}} \langle Q_k^2 \rangle \sum_{j=1}^{N_{bond}} \left(C_{lk}^{(j)} - C_{mk}^{(j)} \right)^2 \tag{37}$$

$$= \frac{K}{2} \sum_{k=1}^{N_{tot}} \lambda_k \langle Q_k^2 \rangle ,$$

and therefore [31]

$$\sum_{j=1}^{N_{bond}} (C_{lk}^{(j)} - C_{mk}^{(j)})^2 = \lambda_k . \tag{38}$$

Inserting Eq. 38 into Eq. 35 finally leads to the following compact form for $\langle\langle M(0)M(t)\rangle\rangle_{orient}$ [30–32]:

$$\langle\langle M(0)M(t)\rangle\rangle_{orient} = \mu^2 \frac{3k_B T}{K} \sum_{i=1}^{N_{tot}} \exp(-t/\tau_k) . \tag{39}$$

It is now a straightforward matter to compute the dielectric susceptibility $\Delta\varepsilon^*(\omega)$. From Eq. 39 the normalized autocorrelation function of the total dipole moment $C_0(M; t)$ reads:

$$C_0(M; t) = \frac{1}{N_{tot}} \sum_{k=1}^{N_{tot}} \exp\left(-t/\tau_k \right) , \tag{40}$$

where again $\tau_k = \tau_0/\lambda_k$. Inserting Eq. 40 in Eq. 31 now leads to the dielectric susceptibility $\Delta\varepsilon^*$; expressing it in terms of its real and imaginary parts,

$\Delta\varepsilon^* = \Delta\varepsilon' - i\Delta\varepsilon''$, we find [31, 32]:

$$\Delta\varepsilon'(\omega) = \frac{1}{N_{\text{tot}}} \sum_{k=2}^{N_{\text{tot}}} \frac{1}{1 + (\omega\tau_k)^2} \tag{41}$$

and

$$\Delta\varepsilon''(\omega) = \frac{1}{N_{\text{tot}}} \sum_{k=2}^{N_{\text{tot}}} \frac{\omega\tau_k}{1 + (\omega\tau_k)^2} . \tag{42}$$

Here again the sums are taken over all finite relaxation times; the infinite time τ_1 related to $\lambda_1 = 0$ is not included, because the term corresponding to λ_1 contributes a constant to $C_0(M; t)$ in Eq. 40 and, therefore, vanishes in Eq. 31 after differentiation with respect to time.

The approach presented here was first developed for the dielectric relaxation of regular mesh-like polymer networks built from macromolecules with longitudinal dipole moments [30], and was later applied to disordered polymer networks [31, 32]. Its key assumption, namely the absence of any correlations in the orientations of the dipole moments of the different GGS bonds is obviously rather simplified. However, it leads, as shown above, to simple analytical expressions for the dielectric susceptibility, a very important dynamical quantity in experimental studies of polymers; we can now analyze it in great detail for particular GGS systems of interest. Another advantage of this model arises from the fact that one has a straightforward correspondence between the mechanical and the dielectric relaxation forms. From the expressions for the storage and loss modulus, Eqs. 20 and 21, and from those for the dielectric susceptibility $\Delta\varepsilon^*$, Eqs. 41 and Eq. 42, one sees readily that [31]

$$\Delta\varepsilon'(\omega) = 1 - [G'(2\omega)] \tag{43}$$

and that

$$\Delta\varepsilon''(\omega) = [G''(2\omega)] . \tag{44}$$

One may furthermore note that the dielectric susceptibility is determined by relaxation times which are twice larger than those appearing in the expressions for the mechanical relaxation. Again, we would like to emphasize that to calculate $\Delta\varepsilon^*(\omega)$ (as well as $G^*(\omega)$) we need only the eigenvalues λ_k (or the relaxation times τ_k) of the GGS, but not the corresponding eigenfunctions.

3.3
Displacement of Monomers under External Forces

One more dynamical characteristic to be considered here in detail is the displacement of GGS beads under external forces [7, 9, 33]. This dynamic quantity is also of special interest because of recent experimental developments that have demonstrated how to perform micromanipulations on polymers. In

particular, individual DNA molecules were dragged by optical or magnetic tweezers [34–36]; similar experiments were performed with magnetic beads in actin networks [37].

Let us consider a situation in which a time-dependent external force $F_l^{(\text{ext})}(t)$ is applied to the GGS beads; see the Langevin equation of motion, Eq. 2. Now, averaging this equation over the thermal noise components $f_l(t)$, we have for $\langle R_l(t) \rangle$:

$$\frac{\mathrm{d}\langle R_l(t) \rangle}{\mathrm{d}t} + \frac{1}{\tau_0} \sum_{m=1}^{N_{\text{tot}}} A_{lm} \langle R_m(t) \rangle = \frac{1}{\zeta} F_l^{(\text{ext})}(t) \,. \tag{45}$$

Equation 45 has the following formal solution [7, 9, 33]:

$$\langle R_l(t) \rangle = \frac{1}{\zeta} \int_{-\infty}^{t} \mathrm{d}\tau \sum_{m=1}^{N_{\text{tot}}} \left(\exp\left[-\frac{(t - \tau)}{\tau_0} A \right] \right)_{lm} F_m^{(\text{ext})}(\tau) \,, \tag{46}$$

where $A = (A_{lm})$ is the connectivity matrix of the GGS. As an example, we consider here the special case of a constant external force that is switched on at $t = 0$ and acts only on one particular bead, say n, along the y-direction, so that

$$F_m^{(\text{ext})}(t) = \delta_{mn} F_0^{(\text{ext})} \theta(t) \cdot e_y \,. \tag{47}$$

For this kind of external force, Eq. 46 simplifies to

$$\langle Y_n(t) \rangle = \frac{1}{\zeta} F_0^{(\text{ext})} \int_0^t \mathrm{d}\tau \left(\exp\left[-\frac{(t - \tau)}{\tau_0} A \right] \right)_{nn} \,. \tag{48}$$

Note that $\langle Y_n(t) \rangle$ still depends on the bead positions in the GGS; in other words on the index n. As a consequence, even for an external force of such a simple form we need both the eigenvalues and the eigenfunctions of the connectivity matrix A of the GGS in order to obtain the average displacement of the nth GGS bead. The need to determine the eigenfunctions may be overcome by further averaging over all beads in the GGS [7, 9, 33]:

$$\langle\langle Y(t) \rangle\rangle = \frac{1}{N_{\text{tot}}} \sum_{n=1}^{N_{\text{tot}}} \langle Y_n(t) \rangle \tag{49}$$

$$= \frac{F_0^{(\text{ext})}}{N_{\text{tot}} \zeta} \int_0^t \mathrm{d}\tau \, Tr \left(\exp\left[-\frac{(t - \tau)}{\tau_0} A \right] \right)$$

$$= \frac{F_0^{(\text{ext})}}{N_{\text{tot}} \zeta} \int_0^t \mathrm{d}\tau \sum_{k=1}^{N_{\text{tot}}} \exp\left[-\frac{(t - \tau)}{\tau_0} \lambda_k \right] \,,$$

where $Tr(X)$ denotes the trace of the matrix X. In Eq. 49 we used the fact that the trace is invariant under normal mode transformations, such as Eq. 9, which represents an orthogonal transformation which rotates the Cartesian axes.

To present Eq. 49 in a more meaningful form, we recall that for a GGS, which is a connected object, only one eigenvalue vanishes, $\lambda_1 = 0$. Separating this eigenvalue from the non-vanishing ones and performing the integration in Eq. 49, we finally obtain the following for $\langle\langle Y(t)\rangle\rangle$ [7, 9, 33]:

$$
\begin{aligned}
\langle\langle Y(t)\rangle\rangle &= \frac{F_0^{(\mathrm{ext})}}{N_{\mathrm{tot}}\zeta}t + \frac{F_0^{(\mathrm{ext})}}{N_{\mathrm{tot}}\zeta}\tau_0 \sum_{k=2}^{N_{\mathrm{tot}}} \frac{1 - \exp(-t\lambda_k/\tau_0)}{\lambda_k} \\
&= \frac{F_0^{(\mathrm{ext})}}{N_{\mathrm{tot}}\,\zeta}\,t + \frac{F_0^{(\mathrm{ext})}}{N_{\mathrm{tot}}\,\zeta} \sum_{k=2}^{N_{\mathrm{tot}}} \tau_k\left[1 - \exp(-t/\tau_k)\right].
\end{aligned}
\tag{50}
$$

The first term in Eq. 50 mirrors the displacement (drift) of the GGS as a whole under the constant external force; it involves the friction which acts on the whole GGS, $\zeta_{\mathrm{GGS}} = N_{\mathrm{tot}}\zeta$. The second term displays the intra-GGS relaxation and is governed by the set of relaxation times (eigenvalues) of the GGS. As we will see in the following, the bead displacements given by Eq. 50 are a very useful tool in probing the dynamical features of polymer systems with complex topologies.

4
Historical Retrospective: The Linear Rouse Chain

4.1
50 Years of the Rouse Model

In 1948, two Soviet physicists, Kargin and Slonimskii, published a paper in which they introduced a "bead and spring" model for linear polymers [38]. Their model did not include Brownian fluctuating forces and, in a certain sense, was a precursor to Bueche's publication [39], which appeared six years later. Since the Kargin-Slonimskii model was only published in Russian, it did not make a strong impact internationally. In 1953 Rouse published his paper "*A theory of linear viscoelastic properties of dilute solutions of coiling polymers*" [1], in which he explicitly introduced stochastic Brownian forces into the bead and spring linear chain model. This fundamental model of polymer chain dynamics became known in the literature as the *Rouse model*; the paper by Rouse is one of the most cited publications in polymer physics (the search engine of the "Web of Science" finds over 2200 citations for the period from 1986 to 2003). In this section we succinctly recall its main features.

Let us consider a GGS that has a linear topology and that consists of $N_{tot} \equiv N$ beads connected by elastic springs, see Fig. 1A. The Langevin equation of motion, Eq. 2, can be rewritten for the inner chain beads, $1 < j < N$, in the form [1, 2, 40, 41]:

$$\zeta \frac{d}{dt} R_j(t) + K[2R_j(t) - R_{j+1}(t) - R_{j-1}(t)] = f_j(t), \tag{51}$$

where $R_j(t)$ is the position vector of the jth bead. The equations of motion for the end beads ($j = 1$ and $j = N$) are:

$$\zeta \frac{d}{dt} R_1(t) + K[R_1(t) - R_2(t)] = f_1(t) \tag{52}$$

and

$$\zeta \frac{d}{dt} R_N(t) + K[R_N(t) - R_{N-1}] = f_N(t). \tag{53}$$

The determination of the eigenvalues of the A matrix corresponding to Eqs. 51, 52, and 53 is best performed by a transformation from Cartesian coordinates to normal coordinates, Eq. 9. Here the transformation can be formulated as:

$$R_j(t) = \sum_{k=1}^{N} \left[A \sin(j\psi_k) + B \cos(j\psi_k) \right] Q_k(t), \tag{54}$$

where ψ_k denotes the phase shift along the Rouse chain. Inserting Eq. 54 into Eq. 51 leads to the following expression for the non-vanishing eigenvalues in terms of the ψ_k [1, 2]:

$$\lambda_k = 2(1 - \cos \psi_k) = 4 \sin^2 \left(\frac{\psi_k}{2} \right). \tag{55}$$

The ψ_k are now fixed by Eqs. 52 and 53, which play the role of boundary conditions. It turns out that one finds, as before, a single vanishing eigenvalue, $\lambda_1 = 0$. The remaining $(N - 1)$ non-vanishing eigenvalues $\{\lambda_2, ..., \lambda_N\}$ are fixed by having

$$\psi_k = \frac{\pi}{N}(k - 1), \quad k = 2, ..., N \tag{56}$$

as solutions, to be inserted in Eq. 55. The corresponding relaxation times τ_k are given by Eq. 12, while $\tau_0 = \zeta/K$ is the characteristic relaxation time of the Rouse chain. It is a simple matter now to determine the maximal relaxation time τ_{chain} of the Rouse chain of N beads (τ_{chain} is often referred to as the Rouse time):

$$\tau_{chain} \equiv \frac{\tau_0}{\lambda_2} \simeq \frac{1}{\pi^2} N^2 \tau_0. \tag{57}$$

Hence τ_{chain} grows as the square mass of the polymer chain, $\tau_{chain} \sim M^2$.

Remarkably, the boundary conditions, Eqs. 52 and 53, allow to establish the exact form of the normal mode transformation, Eq. 54, for the Rouse chain [40]:

$$R_j(t) = \frac{1}{\sqrt{N}} Q_1(t) + \sqrt{\frac{2}{N}} \sum_{k=2}^{N} \left[\cos\left(j - \frac{1}{2}\right) \psi_k \right] Q_k(t). \tag{58}$$

Here the numerical constants $1/\sqrt{N}$ and $\sqrt{2/N}$ were determined from the transformation of the potential energy and the dissipative function of the Rouse chain, see Eqs. 10 and 11. The normal coordinate $Q_1(t)$ corresponds to the vanishing eigenvalue $\lambda_1 = 0$ and is related to the position vector of the center of mass R_{COM}:

$$R_{COM}(t) \equiv \frac{1}{N} \sum_{j=1}^{N} R_j(t) = \frac{1}{\sqrt{N}} Q_1(t). \tag{59}$$

Using Eq. 59 and the equation of motion for $Q_1(t)$, it is a simple matter to compute the mean-square displacement of the center of mass of the Rouse chain at time t, averaged over the fluctuating forces:

$$\langle (R_{COM}(t) - R_{COM}(0))^2 \rangle = \frac{6k_B T}{N\zeta} t. \tag{60}$$

Therefore, the diffusion coefficient D_{chain} of the Rouse chain as a whole equals:

$$D_{chain} = \lim_{t \to \infty} \frac{1}{6t} \langle (R_{COM}(t) - R_{COM}(0))^2 \rangle = \frac{k_B T}{N\zeta}, \tag{61}$$

in other words, in the framework of the Rouse model, D_{chain} is inversely proportional to the mass of the chain ($D_{chain} \sim M^{-1}$), a result which simply states that the chain feels all friction forces on its monomers additively. It is also instructive to study the relaxation of the end-to-end vector $r(t) = R_N - R_1$ of the Rouse chain. Its autocorrelation function can be reduced to the following compact form [2, 40, 41]:

$$\langle r(t)r(0) \rangle = \frac{6}{N} \frac{k_B T}{K} \sum_{k=2,4,6,\ldots}^{N} \cot^2\left(\frac{\psi_k}{2}\right) \exp(-t/\tau_k). \tag{62}$$

Based on this expression, one can estimate the decay of $\langle r(t)r(0) \rangle$ in the intermediate time domain ($\tau_0 \ll t \ll \tau_{chain}$):

$$\langle r(t)r(0) \rangle \simeq \frac{12}{\pi^2} \frac{k_B T}{K} N \exp\left(-\sqrt{\frac{t}{\tau_{chain}}}\right), \tag{63}$$

which obeys a square-root time dependence. For $t > \tau_{chain}$ the autocorrelation function ends up with an exponential decay which is characterized by the Rouse time τ_{chain}.

Now we turn to the dynamic viscoelastic properties of Rouse chains in dilute solutions. The storage and loss moduli of the Rouse chain are given by Eqs. 20 and 21, where the finite relaxation times are defined through Eqs. 55 and 56. Similar to all free-floating GGS, at very low frequencies, $\omega \ll 1/\tau_{\text{chain}}$, one has $G'(\omega) \sim \omega^2$ and $G''(\omega) \sim \omega$. It is more interesting, however, to consider the behavior of the Rouse chain in the intermediate frequency domain, $1/\tau_{\text{chain}} \ll \omega \ll \tau_0$, where one has [1–3]:

$$[G'(\omega)] = [G''(\omega)] \simeq \frac{1}{2\sqrt{2}} \sqrt{\omega\tau_0}. \tag{64}$$

This square-root dependence on ω is a fundamental feature of linear chains in the Rouse model. The shear modulus at intermediate frequencies is a signature of the internal, "intra-chain" dynamics, which is determined by the topology of the GGS. As stressed before, the viscoelastic relaxation forms can be expressed through the relaxation spectrum $H(\tau)$, see Eq. 27. Here one finds [3]:

$$H(\tau) \simeq \frac{1}{2\sqrt{2}} \frac{1}{\pi} \sqrt{\frac{\tau_0}{\tau}}, \quad \text{where} \quad \tau_0 < \tau < \tau_{\text{chain}}. \tag{65}$$

One should note the appearance of a square-root behavior (now as a function of τ) in the $H(\tau)$ of Rouse chains. Given the close relation between $H(\tau)$ and $G(t)$, see Eq. 27, it can be shown that in the intermediate time domain, $\tau_0 < t < \tau_{\text{chain}}$, the relaxation modulus $G(t)$ depends on time as:

$$[G(t)] \simeq \frac{1}{\pi\sqrt{2}} \sqrt{\frac{\tau_0}{t}}. \tag{66}$$

In other words, it also obeys a square-root dependence on time.

It has to be emphasized that the knowledge of the full form of the normal mode transformation, see Eq. 58, allows one to compute dynamic characteristics which are not averaged over the beads and which depend, therefore, on the position of the particular bead along the Rouse chain. To conclude this section, we will discuss two such examples.

First, let us focus on the mean-square displacement $\langle \Delta R_j^2(t) \rangle = \langle (R_j(t) - R_j(0))^2 \rangle$ of the jth bead. Using Eq. 58, one obtains [41]:

$$\langle \Delta R_j^2(t) \rangle = \frac{6k_B T}{N\zeta} t + \frac{12k_B T}{NK} \sum_{k=2}^{N} \cos^2 \left[\left(j - \frac{1}{2} \right) \psi_k \right] \frac{1 - \exp(-t/\tau_k)}{\lambda_k}. \tag{67}$$

At $t \gg \tau_{\text{chain}}$, the behavior of the $\langle \Delta R_j^2(t) \rangle$ is governed by the first term in Eq. 67, which is simply the mean square displacement of the center of mass of the Rouse chain, see Eq. 60. Thus, we have the usual diffusive behavior of a free Brownian particle, whose root mean square behavior follows the ordinary law $\sim t^{1/2}$. At intermediate times, $\tau_0 \ll t \ll \tau_{\text{chain}}$, one has the following

behavior for $\langle \Delta R_j^2(t) \rangle$:

$$\langle \Delta R_j^2(t) \rangle \simeq \frac{12 k_B T}{\pi K} \sqrt{\frac{t}{\tau_0}} . \tag{68}$$

Thus, in the intermediate time domain the root mean square displacement of a bead increases more slowly with time ($\sim t^{1/4}$) than ordinary diffusion. The physical reason for this is clear: The fact that a given bead is connected to other beads in the chain effectively slows down its diffusive motion [41]. To complete the picture, we also consider the displacement of a bead under the influence of an external force, see Eq. 50; in the same domain of intermediate times ($\tau_0 \ll t \ll \tau_{\text{chain}}$) one finds:

$$\langle \langle Y(t) \rangle \rangle \simeq \frac{2 F_0^{(\text{ext})}}{\pi K} \sqrt{\frac{t}{\tau_0}} . \tag{69}$$

Not surprisingly, the temporal behavior in Eqs. 68 and 69 is the same (see also Eqs. 67 and 50), a consequence of the fluctuation-dissipation theorem, which relates the diffusion in the absence of an external field to the drift in such a field.

Finally, we consider the relaxation of the end-to-end subchain vector between neighboring beads, $u_j = (R_{j+1} - R_j)$, where $j = 1, ..., (N-1)$. The autocorrelation function of the u_j can also be computed using the normal mode transformation, Eq. 58. One finds [40]:

$$\langle u_j(t) u_j(0) \rangle = \frac{6 k_B T}{NK} \sum_{k=2}^{N} \sin^2 \left(j \psi_k \right) \exp(- t/\tau_k) . \tag{70}$$

Interestingly, the expression for the autocorrelation function $\langle u_j(t) u_j(0) \rangle$ is reminiscent of that of the relaxation modulus $G(t)$, Eq. 26. Their behaviors at $\tau_0 \ll t \ll \tau_{\text{chain}}$ do indeed coincide (compare with Eq. 66):

$$\langle u_j(t) u_j(0) \rangle \simeq \frac{3 k_B T}{\pi K} \sqrt{\frac{\tau_0}{t}} . \tag{71}$$

4.2
Successes and Limitations of the Rouse Approach: Comparison with the Zimm and the Reptation Pictures

The Rouse model was initially designed to treat the dynamics of polymers in very dilute solutions [1]. Ironically, however, it turned out that dilute solutions are not appropriate systems for it. Indeed, in the Rouse model the maximal relaxation time, τ_{chain}, and the diffusion coefficient, D_{chain}, scale with the molecular weight, M, as M^2 and M^{-1}, respectively (see Eqs. 57 and 61). Furthermore, it is a straightforward matter to demonstrate that for the Rouse model at $\omega = 0$ the zero shear viscosity [$\eta'(0)$] is proportional to M, see Eq. 22. All these theoretical findings disagree with the experimental data

on dilute polymer solutions, where in θ-solvents one finds that $\tau_{chain} \sim M^{3/2}$, $D_{chain} \sim M^{-1/2}$, and $[\eta'(0)] \sim M^{1/2}$ [3]. The reason for this disagreement is that in dilute solutions the hydrodynamic interactions play a crucial role. These interactions are fully ignored in the Rouse model: the solvent is modeled as a continuous *immobile* medium, which is felt by the beads only through their viscous friction. However, in dilute polymer solutions the motion of a particular bead affects all the other beads through the perturbation of the solvent; in other words, the solvent mediates effective interactions between the beads. As was first demonstrated by Zimm [5], taking into account the hydrodynamic interactions significantly improves the agreement between experiment and model.

In the Zimm model (see Fig. 2A) the hydrodynamic interactions are included by employing the Oseen tensor H_{lm}; the tensor describes how the mth bead affects the motion of the lth bead. This leads to equations of motion that are not linear anymore and that require numerical methods for their solution. In order to simplify the picture, the Oseen tensor is often used in its preaveraged form, in which one replaces the operator by its equilibrium average value [5]. For chains in θ-solvents, this leads for the normal modes to equations similar to the Rouse ones, the only difference residing in the values of the relaxation times. An important change in behavior concerns the maximum relaxation time τ_{chain}, which in the Zimm model depends on N as $N^{3/2}$ and implies a speed-up in relaxation compared to the Rouse model. Accordingly, the zero shear viscosity decreases in the Zimm model and scales as $N^{1/2}$. Also, in the Zimm model the diffusion coefficient
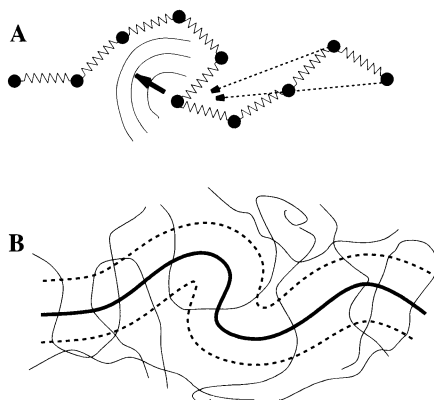
Fig. 2 (**A**) Schematic representation of the Zimm model, which takes into account hydrodynamic interactions. The beads affect (through the solvent) the motion of a bead which is distant from them along the chain (not connected directly to them by means of springs). (**B**) Schematic representation of the reptation model. A given, long polymer chain moves in the tube formed by other chains

of chains, $D_{\text{chain}} \sim N^{-1/2}$, is larger than in the Rouse model. Moreover, the Zimm molecular mass dependencies of the maximal relaxation time, of the diffusion coefficient, and of the zero shear viscosity are all consistent with the experimental findings [3]. The Zimm model also agrees with the experiment with respect to the frequency dependence of the storage and loss moduli of dilute polymer solutions under θ-conditions: both $G'(\omega)$ and $G''(\omega)$ show a $\omega^{2/3}$-behavior, in contrast to the Rouse situation, where the behavior turns out to be proportional to $\omega^{1/2}$, see Eq. 64 [2, 3].

As the concentration of the polymer solution increases, the experiments show a systematic change from Zimm-like to Rouse-like behavior (see for example the monograph of Ferry [3] and references therein). The reason for this finding is the screening of the hydrodynamic interactions: in the semidilute regime different polymer chains start to overlap and the hydrodynamic interactions between fragments of the same chain are screened from each other by the presence of other chains. The dynamic crossover from the Zimm to the Rouse behavior was the subject of a number of theoretical studies [42–44]. The dynamics of semidilute solutions is well-represented in terms of the so-called "blob" model. A blob is a group of monomers of a given chain, whose size is of the order of the hydrodynamic screening length ξ_H. At scales smaller than ξ_H, monomers of a particular chain do not feel the presence of the other chains and, therefore, the hydrodynamic interactions are not screened, leading to a Zimm-like behavior. At larger scales, the intra-blob (Zimm) relaxation ends, the blobs can be envisaged as being Stokes spheres, and the mutual interactions between them draw their mobility down, which gives rise to a Rouse-like behavior [44]. Furthermore, the results of recent computer simulations [45] show that the time scales matter as well as the length scales: at times shorter than the blob relaxation time there is no screening of the hydrodynamic interactions and the polymer motion is essentially Zimm-like on *all* length scales [45]. This also explains the experimental observation of an incomplete screening on length scales above the hydrodynamic screening length ξ_H [46].

With a further increase in concentration one reaches the regime of concentrated solutions and melts. Here it is crucial to distinguish two different situations, which involve either short (unentangled) or long (entangled) chains. The border line between these situations is given by the so-called entanglement length N_e [2, 3], which is different for different polymers (for instance, the molecular weight of a polystyrene macromolecule at entanglement length is about 20 000). For polymer melts of short chains ($N < N_e$) the Rouse model provides an excellent description of the long-time dynamical behavior, a fact well-documented both experimentally [3, 47] and by computer simulations [48–53]; some deviations, however, have also been reported [54]. In melts of short chains the hydrodynamic interactions are absent (there is no solvent in the melt) and entanglement effects do not play a noticeable role. The dynamics of a particular chain in the melt can be viewed as being that

of a Rouse chain embedded in an effective viscous medium, created by the other chains of the melt [2, 3]. It should be noted that it is still an open question as to why such a complicated system as a short-chain polymer melt can be described well by means of the simple Rouse model.

In melts of long chains (longer than the entanglement length N_e) the topological constraints lead to a considerable slowing down of the motion of the monomers. The individual chains do not follow the Rouse behavior anymore. The dynamics of such entangled melts can be described in terms of the reptation (tube) model, first proposed by de Gennes [4]. Here each chain moves in an effective tube formed by the other chains, see Fig. 2B. At short times the chain does not feel the tube and one finds an unconstrained Rouse-like behavior. This holds up to a time τ_e, which is just the maximal relaxation time of a Rouse chain of length N_e ($\tau_e \sim N_e^2$). At longer times the polymer chain can only move along the tube; evidently, in the course of time, the original tube is slowly destroyed by the forward and backward motions of the chain [2, 4, 55]. The longest relaxation time is the time of disengagement of the chain from the original tube (or, equivalently, the average lifetime of the tube); it is found to scale as N^3 [2, 4, 41]. The diffusion of the chain in the entangled melt is also slowed down when compared to the Rouse behavior; in the tube model the diffusion coefficient turns out to be proportional to N^{-2} [2, 4]. An extension of the tube model to concentrated solutions and melts of *polydisperse* entangled polymers was also carried out [56]. We note that the crossover from the Rouse behavior to reptation has been confirmed through numerous computer simulations [48, 57–59]. Furthermore, reptation successfully explains the appearance of a plateau region in the relaxation modulus, as observed in uncrosslinked polymer melts of high molecular weight [3].

All in all, the Rouse model provides a reasonable description of polymer dynamics when the hydrodynamic interactions, excluded volume effects and entanglement effects can be neglected; a classical example of its applicability is short-chain polymer melts. Since the Rouse model is exactly solvable for polymer chains, it represents a basic reference frame for comparison with more involved models of polymer dynamics. In particular, the decoupling of the dynamics of the Rouse chain into a set of independently relaxing normal modes is fundamental and plays an important role in other cases, such as more complex objects of study, or in other models, such as the Zimm model.

5
Regular Mesh-Like Polymer Networks

After the above historical retrospective devoted to linear Rouse chains, we follow the extension of this approach to polymer systems that have more complex topologies. We focus first on the dynamics of networks cross-linked from

Rouse chains. The fundamental feature here is the appearance of coopera-
tive interchain motions due to cross-linking. First approaches to evaluating
the dynamical properties of such networks started from the intrachain relax-
ation, and accounted for the connectivity between chains only in simplified,
effective ways. For instance, the dynamics of Rouse chains that have fixed
(constant) end-to-end distances were studied [60]. Alternatively, Mooney
considered Rouse chains with fixed (immobile) ends as a model for a poly-
mer network [3, 61]. In particular, he found that the relaxation modulus of
such a chain coincides with that of a Rouse chain with free ends, except for
a constant contribution, which can be considered as being the nonvanishing,
equilibrium modulus of the network. However, the idea of the GGS formalism
is to take the connectivity exactly into account, see Eqs. 1 and 2. In order to
gradually increase the complexity of the networks, one can start by first con-
sidering chains cross-linked into regular spatial structures. This is the subject
of the present section.

5.1
Regular Network Models for Cooperative Interchain Relaxation

5.1.1
3-D Model Networks

The classical Rouse treatment was originally developed for linear chains. If
one views the linear polymer chain as a one-dimensional regular string of
beads connected by springs, then a straightforward and obvious extension is
to build from beads and springs regular lattices of higher dimensions. Such
an approach was suggested by Gotlib [62] for studying the low-frequency
modes of polymer networks. Since real cross-linked polymers are normally
3-D structures, cubic networks were first to attract the attentions of re-
searchers [24, 30, 62, 63]. Cubic networks were employed to study interchain
friction effects [62, 63], dielectric relaxation [30], and various aspects of me-
chanical viscoelastic relaxation [24, 64, 65]. One should, of course, note at all
stages of our discussion that only the *topological* structure of the networks
is regular. In their *spatial appearance* in solution, the networks are quite dis-
ordered (stretched, folded, and twisted), as befits their very mobile beads.
All of the GGS displayed in this review are drawn such as to render their
topologies clear; hence the drawings are, in fact, very atypical of the general
locations of the beads in *space*.

In the following we sketch some simple ways for determining the dynam-
ics of simple cubic networks: here we prefer not to use the general approach,
exemplified by Eqs. 2 and 9, which involves matrix diagonalizations [64, 65],
because for cubic networks the analysis can be done in a simple way by means
of normal mode (Fourier) transformations. We remark that simple cubic net-
works are also a coarse-grained model for more complex systems, like those

built from Rouse chains connected regularly into a cubic framework. We will study such systems in detail in Sect. 5.2.1. Coarse-graining implies replacing each Rouse chain by a spring; the price to be paid for this is that the intrachain eigenfrequencies are lost.

We hence start with a cubic network formed by beads which have an identical friction constant, ζ, and which are connected to each other by means of elastic Hookean springs with elasticity constant K, see Fig. 3. The network is embedded into an effective viscous medium and is a regular structure in the sense of connectivity only. Every site of the cubic network is denoted by a three-dimensional index $\mathbf{\Omega} = (\alpha, \beta, \gamma)$. The Langevin equation of motion, Eq. 2, can be rewritten here as:

$$\zeta \frac{\mathrm{d}}{\mathrm{d}t} R(\alpha, \beta, \gamma; t) + K[6R(\alpha, \beta, \gamma; t) - R(\alpha + 1, \beta, \gamma; t) \tag{72}$$
$$- R(\alpha - 1, \beta, \gamma; t) - R(\alpha, \beta + 1, \gamma; t) - R(\alpha, \beta - 1, \gamma; t)$$
$$- R(\alpha, \beta, \gamma + 1; t) - R(\alpha, \beta, \gamma - 1; t)]$$
$$= f(\alpha, \beta, \gamma; t).$$

Here $R(\alpha, \beta, \gamma; t)$ denotes the position vector of the network junction $\mathbf{\Omega} = (\alpha, \beta, \gamma)$ and $f(\alpha, \beta, \gamma; t)$ is the corresponding stochastic force (thermal noise), again assumed to be Gaussian with zero mean value.

In spite of the fact that it is easy to get a solution for the cubic polymer network with free boundaries (in a quite analogous way as for the linear Rouse chain with free ends), we will consider here a network with periodic boundary conditions (PBC). In doing so, we use the same formalism as later, when we consider more complex systems, for which analytical solutions are known only under PBC. In our case such PBC mean that $R(1, \beta, \gamma; t) = R(N + 1, \beta, \gamma; t)$, $R(\alpha, 1, \gamma; t) = R(\alpha, N + 1, \gamma; t)$, and $R(\alpha, \beta, 1; t) = R(\alpha, \beta, N + 1; t)$, where N is a number of beads along a given di-
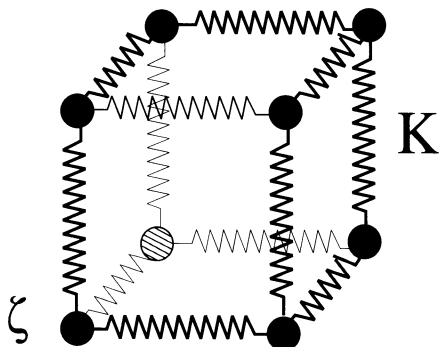
Fig. 3 One elementary cell of a cubic network built from beads (each having friction constant ζ) which are connected by elastic springs each with elasticity constant K

rection of the network (the total number of junctions in our cubic networks
being equal to N^3).

The Langevin equation of motion, Eq. 72, can be easily solved by means
of a transformation from the Cartesian coordinates R to the normal coordi-
nates Q, Eq. 9. The transformation reads:

$$R(\alpha, \beta, \gamma; t) = \frac{1}{N^{3/2}} \sum_k \exp[i(\alpha k_1 + \beta k_2 + \gamma k_3)] \, Q(k_1, k_2, k_3; t). \qquad (73)$$

Here the triple $k = (k_1, k_2, k_3)$ is not a reciprocal vector as in solid state
physics, because the network does not possess translational symmetry. We
will view k rather as describing a phase shift between the different Ω.

Inserting Eq. 73 into the Langevin equations of motions, Eq. 72, immedi-
ately leads to the eigenvalues of the simple cubic network [24, 30, 62, 63]:

$$\lambda(k) = 2(3 - \cos k_1 - \cos k_2 - \cos k_3). \qquad (74)$$

The periodic boundary conditions allow us, in turn, to restrict k to the values:

$$k_1 = \frac{2\pi m_1}{N}, \quad k_2 = \frac{2\pi m_2}{N}, \quad \text{and} \quad k_3 = \frac{2\pi m_3}{N}, \qquad (75)$$

where the integers m_1, m_2, and m_3 range from 0 to $(N - 1)$. Equations 74
and 75 fully determine the eigenvalues of the cubic network. Each normal
mode $Q(k; t)$ then decays exponentially with the relaxation time (see also
Eq. 12):

$$\tau(k) = \frac{\tau_0}{\lambda(k)}, \qquad (76)$$

where $\lambda(k)$ are as in Eq. 74 and τ_0 is its characteristic relaxation time,
$\tau_0 = \zeta/K$. Remarkably, since the normal modes (the eigenfunctions), Eq. 73,
are also known, it is possible to obtain analytical expressions not only for
the macroscopic dynamic characteristics (dynamic modulus and viscosity),
but also for the local quantities (not averaged over the Ω), such as the au-
tocorrelation function of the end-to-end chain vector between neighboring
cross-links [66]. Note that Eq. 74 was also obtained in [64, 65], by means of
rather complicated operations involving connectivity matrices.

Now we compare the viscoelastic mechanical properties of a topological
cubic structure to those of a linear chain. Since for the former the relaxation
times are known, see Eqs. 76, 74 and 75, it is now a straightforward matter
to calculate the dynamic modulus and to estimate its behavior in different
frequency domains analytically. It turns out that the storage modulus $G'(\omega)$
of cubic networks obeys a $\omega^{3/2}$ form in the region of intermediate frequen-
cies; this is very different from the behavior of a Rouse chain, where in the
intermediate range $G'(\omega)$ has a $\omega^{1/2}$ form, see Fig. 4.

The underlying reason for these findings is the fact that for a cubic net-
work the relaxation spectrum $H(\tau)$ decays as $\tau^{-3/2}$, and thus more quickly
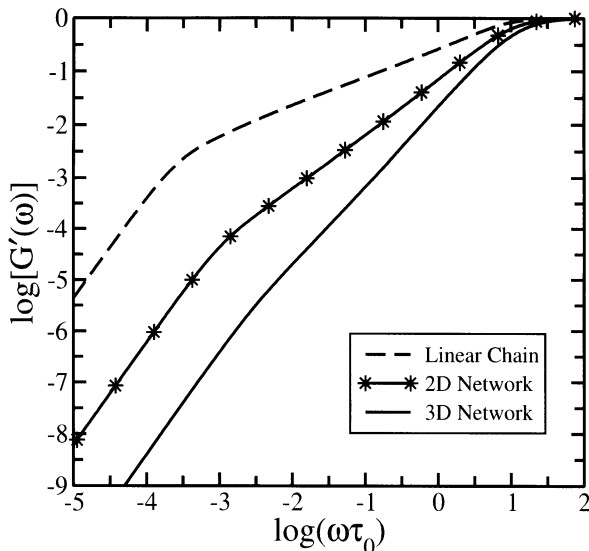
Fig. 4 Reduced storage modulus [$G'(\omega)$] plotted on double logarithmic scales versus the reduced frequency $\omega\tau_0$. Shown are results for a linear Rouse chain of 250 beads (*dashed line*), for a topologically-square network (250×250), *solid line* with stars, and for a topologically cubic network ($150 \times 150 \times 150$), *solid line*. For simplicity, the characteristic time $\tau_0 = \zeta/K$ was chosen to be the same for all three systems

than for the Rouse chain, where $H(\tau)$ obeys a $\tau^{-1/2}$ form. This $H(\tau)$-behavior also leads to a faster decay of the relaxation modulus, which now follows $G(t) \sim t^{-3/2}$ instead of $G(t) \sim t^{-1/2}$ for the Rouse chain. Physically, the behavior of the cubic network can be understood based on the increased growth of the number of nearest neighbors, next-nearest neighbors, next-next-nearest neighbors, and so on. This picture is very akin to the definition of the fractal dimension; in fact, in Sect. 6 we will see that similar power-law forms for $G'(\omega)$, $G''(\omega)$, and $G(t)$ also hold for fractal networks, but that the exponents are related to the *spectral* dimension of the fractal.

It is perhaps also worth noting that the $\tau^{-3/2}$ behavior of the relaxation spectrum $H(\tau)$ of a cubic network is due to its three-dimensional connectivity character but *not* to the details of the particular network structure. In the fractal framework the spectral dimension of all these networks is 3, and the relaxation behavior is universal. In this regard the work of Denneman et al [64] is very instructive. The authors considered Hookean springs cross-linked into the three Bravais cubic lattices, namely simple cubic (sc) (this corresponds to the network considered above), body-centered cubic (bcc), and face-centered cubic (fcc). They succeeded in finding analytical expressions for the eigenvalues of the sc lattice (they coincide with Eq. 74) but not for the bcc and fcc lattices, which were treated numerically. It turns out (in agreement with the statement above), that the dynamic modulus for all

three cubic lattices has the same frequency behavior, the only difference being a slightly different value of the characteristic (minimal) relaxation time. In [64] it is found that $\tau_{sc} > \tau_{bcc} > \tau_{fcc}$ and that this difference results in a shift of the corresponding modulus curves along the frequency axis.

5.1.2
2-D Model Networks

In order to illustrate the fundamental role of the dimensionality in the dynamical behavior of networks, it is instructive to consider topologically two-dimensional networks, see Fig. 5 for an example. While as a rule many cross-linked polymers display a three-dimensional character, say, based on their $H(\tau)$-behavior, two-dimensional structures may be realized in polymer films, by deposition on surfaces, and so on. Furthermore, two-dimensional networks are intermediate between the two cases (1-D and 3-D) already discussed; two-dimensional systems have dynamical features which interpolate between the previous findings.

A comparative study of the equilibrium properties of coarse-grained topological cubic and square networks was performed by Ronca and Allegra, who employed electrical analogs for this purpose [67]. In particular, they found that the mean-square radius of gyration of a two-dimensional network increases logarithmically with the total number of network junctions, while it is of the same order of magnitude as that of a single bond in the case of a three-dimensional network. A more general result, based on fractal systems and ideas, and which also includes this finding, is provided in [6].
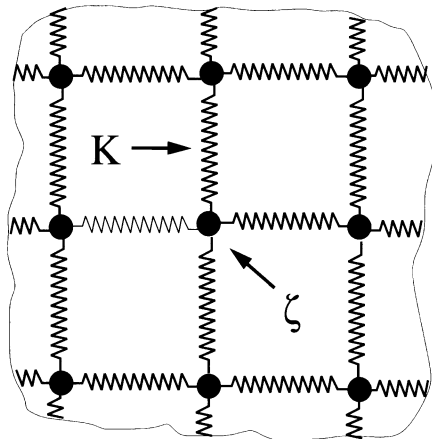
Fig. 5 Sketch of a square network built from beads each with friction constant ζ, which are connected by elastic springs each with elasticity constant K

The dynamics of a topologically square network can be treated along the lines used for the cubic network above. The Langevin equations of motion for a square network are similar to those of the cubic network:

$$\zeta \frac{\mathrm{d}}{\mathrm{d}t} R(\alpha, \beta; t) + K[4R(\alpha, \beta; t) - R(\alpha + 1, \beta; t) \tag{77}$$
$$- R(\alpha - 1, \beta; t) - R(\alpha, \beta + 1; t)$$
$$- R(\alpha, \beta - 1; t)]$$
$$= f(\alpha, \beta; t),$$

where $R(\alpha, \beta; t)$ denotes the position vector of a bead and where we set $\Omega = (\alpha, \beta)$. Applying the two-dimensional analog ($k_3 = 0$) of the normal mode transformation, Eq. 73, one obtains the following set of eigenvalues for the square network [68, 69]:

$$\lambda(k) = 2(2 - \cos k_1 - \cos k_2), \tag{78}$$

where the phase shift $k = (k_1, k_2)$ between the Ω is given by Eq. 75 with $k_3 = 0$. The same analytical expression for the eigenvalues (relaxation times) was previously found by Denneman et al [65].

Analysis of the dynamical viscoelastic quantities shows that the relaxation spectrum $H(\tau)$ of the two-dimensional network goes as $H(\tau) \sim 1/\tau$ [65, 68–70]. Hence 2-D networks do indeed show dynamical behavior intermediate between that of linear chains and that of 3-D networks. Moreover, in a fractal picture, square networks may be viewed as being fractals and as having a spectral dimension of 2. Now $H(\tau) \sim 1/\tau$ leads to an ω^1-behavior for the storage modulus $G'(\omega)$, see Fig. 4, and to $G(t) \sim 1/t$.

At this stage one can already note the general scaling behavior of $H(\tau)$ and its dependence on the dimensionality d of the networks. One can summarize our discussion by noting that for all d considered $H(\tau) \sim \tau^{-d/2}$ and thus also $G'(\omega) \sim \omega^{d/2}$ and $G(t) \sim t^{-d/2}$. In Sect. 6 we will see that these expressions stay unchanged when replacing d by $\tilde{d}$, the *spectral* dimension. Furthermore, the above-mentioned differences in the equilibrium properties of two- and three-dimensional networks are also manifest in the local dynamic properties, stressing the universal role of d. We mention that the mean-square displacement of a bead of a 2-D network under stochastic forces grows with the time t as $\log(t/\tau)$, while the same dynamical quantity in a 3-D network reaches a finite, limiting value at long times [68, 69]. This concurs with the findings of Ronca and Allegra [67], is in line with the previously mentioned findings on the mean-square radius of gyration (fluctuation-dissipation theorem), and is a special case of the fractal picture [6].

5.2
Topologically-Regular Networks Built from Rouse Chains:
Exactly Solvable Models

5.2.1
Topologically-Cubic Networks

After the simple topological structures (cubic and square) just discussed, we turn now to the analysis of regular networks built from Rouse chains. This allows us to study an important problem in polymer network dynamics, namely the way in which the cross-linking of Rouse chains (or, as we will discuss in later sections, of more complex units) into larger structures is reflected in the dynamics of the resulting networks.

For simplicity we consider end-linked polymer networks and we disregard, as is usual with GGS, entanglement effects. A simple model of a three-dimensional structure, which explicitly takes into account the connectivity between polymer chains, is a regular cubic network cross-linked from Rouse chains. Remarkably, it turns out that under certain conditions the dynamical problem for such a network can be fully solved analytically [25, 66, 71]. This solution provides insight into the network's dynamics and is, therefore, worth detailed consideration.

We start with a regular cubic network which has cross-link points (network junctions) as vertices; these are connected by means of identical Rouse chains, see Fig. 6. All Rouse chains in the network consist of the same number n of beads (having a friction constant ζ); they are connected among
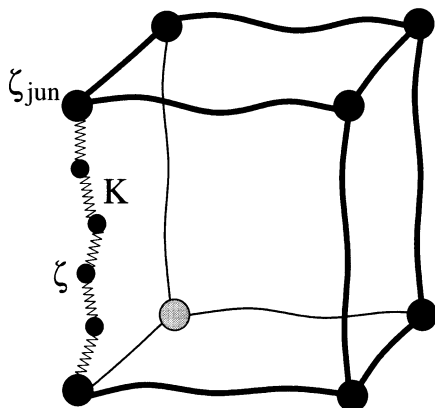
Fig. 6 An elementary cell of a topologically-regular cubic network cross-linked from Rouse chains. One of the network chains between two cross-links (junctions) is shown in detail. Note that the dynamic problem of such a network can be exactly solved only under the condition that the friction constant of each network junction, ζ_{jun}, is three times larger than that of a chain bead, see text for details

themselves and via the corresponding cross-links by $(n + 1)$ identical elastic springs each with elasticity constant K. Each cell of the cubic network under study contains one junction (cross-link) and three Rouse chains attached to it; it is denoted by the three-dimensional index $\mathbf{\Omega} = (\alpha, \beta, \gamma)$. The network is assumed to consist of N^3 junctions (cross-links), so there are N junctions along each of the three network directions and the α, β, and γ indices range from 1 to N. The whole network is embedded into a continuous viscous medium. Then one has the following Langevin equations of motion for the beads of the chains:

$$\zeta \frac{d}{dt} R_p(\mathbf{\Omega};j;t) + K[2R_p(\mathbf{\Omega};j;t) - R_p(\mathbf{\Omega};j+1;t) - R_p(\mathbf{\Omega};j-1;t)] \tag{79}$$
$$= f_p(\mathbf{\Omega};j;t)$$

and for the network junctions (cross-linking points of the chains):

$$\zeta_{jun} \frac{d}{dt} R_0(\alpha, \beta, \gamma;t) + K[6R_0(\alpha, \beta, \gamma;t) - R_1(\alpha, \beta, \gamma;1;t) \tag{80}$$
$$- R_1(\alpha - 1, \beta, \gamma;n;t) - R_2(\alpha, \beta, \gamma;1;t)$$
$$- R_2(\alpha, \beta - 1, \gamma;n;t) - R_3(\alpha, \beta, \gamma;1;t)$$
$$- R_3(\alpha, \beta, \gamma - 1;n;t)]$$
$$= f_0(\alpha, \beta, \gamma;t).$$

Here $R_p(\mathbf{\Omega};j;t)$ denotes the position vector of the jth bead of the pth Rouse chain in the network cell $\mathbf{\Omega} = (\alpha, \beta, \gamma)$ (we recall that $j = 1, ..., n$ and $p = 1, ..., 3$), $R_0(\mathbf{\Omega};t)$ is the corresponding position vector of the network junction $\mathbf{\Omega}$, and $f_p(\mathbf{\Omega};j;t)$ and $f_0(\mathbf{\Omega};t)$ are stochastic forces acting on the chain beads and on the network junctions. Note that the chain beads and the network junctions (cross-links) may have different friction constants, ζ and ζ_{jun}, respectively. For simplicity, we apply periodic boundary conditions and choose, because of later convenience, to express them through the coordinates of the chain beads:

$$R_1(0, \beta, \gamma;n;t) = R_1(N, \beta, \gamma;n;t), \tag{81}$$
$$R_2(\alpha, 0, \gamma;n;t) = R_2(\alpha, N, \gamma;n;t), \tag{82}$$

and

$$R_3(\alpha, \beta, 0;n;t) = R_3(\alpha, \beta, N;n;t). \tag{83}$$

To solve the Langevin equations of motion, one can use the following transformations from Cartesian coordinates R to normal coordinates Q:

$$R_p(\mathbf{\Omega};j;t) = \sum_{k,\psi} \exp(i\mathbf{\Omega} \cdot k)(A_p \sin j\psi + B_p \cos j\psi)Q(k;\psi;t) \tag{84}$$

and

$$R_0(\boldsymbol{\Omega}; t) = \sum_{\boldsymbol{k}, \psi} \exp(\mathrm{i}\boldsymbol{\Omega} \cdot \boldsymbol{k}) B_0 Q(\boldsymbol{k}; \psi; t). \tag{85}$$

Here the triple $\boldsymbol{k} = (k_1, k_2, k_3)$ is related to the "global" phase shift between different network cells and $\boldsymbol{\Omega} \cdot \boldsymbol{k}$ is the scalar product. In contrast, the intra-chain quantity ψ corresponds to "local" phase shifts between neighboring beads along the chains. As usual, an exponential decay of every normal mode is characterized by the relaxation time $\tau(\psi)$ connected with the eigenvalues $\lambda(\psi)$ of the corresponding connectivity matrix of the network through Eq. 12, with $\tau_0 = \zeta/K$. Inserting the normal mode transformation, Eq. 84, into the Langevin equations of motion for the beads of the chains, Eq. 79, leads to the following set of eigenvalues $\lambda(\psi)$:

$$\lambda(\psi) = 2(1 - \cos\psi). \tag{86}$$

Formally, the expression for the eigenvalues has the same form as that for the linear Rouse chain. Now, however, the intrachain phase shift ψ has to be coupled to the triple $\boldsymbol{k} = (k_1, k_2, k_3)$. The latter can be easily determined by inserting the equations of motion for non-junction chain beads, Eq. 79, into the periodic boundary conditions, Eqs. 81 to 83. It brings us again to Eq. 75 for k_1, k_2, and k_3.

In order to obtain the intrachain phase shift ψ as well as the transformation from the Cartesian coordinates to the normal coordinates, seven constants, A_1, A_2, A_3, B_0, B_1, B_2, and B_3, have to be determined, see Eqs. 84 and 85. For these purposes one can use the Langevin equations of motion for the network junctions (cross-links), Eq. 80. Formally we also add the following six conditions at the junction points:

$$R_0(\alpha, \beta, \gamma; t) = R_1(\alpha - 1, \beta, \gamma; n + 1; t), \tag{87}$$

$$R_0(\alpha, \beta, \gamma; t) = R_2(\alpha, \beta - 1, \gamma; n + 1; t), \tag{88}$$

$$R_0(\alpha, \beta, \gamma; t) = R_3(\alpha, \beta, \gamma - 1; n + 1; t), \tag{89}$$

$$R_0(\alpha, \beta, \gamma; t) = R_1(\alpha, \beta, \gamma; 0; t), \tag{90}$$

$$R_0(\alpha, \beta, \gamma; t) = R_2(\alpha, \beta, \gamma; 0; t), \tag{91}$$

$$R_0(\alpha, \beta, \gamma; t) = R_3(\alpha, \beta, \gamma; 0; t). \tag{92}$$

The physical meaning of Eqs. 87 to 92 is that we envisage the chains to be connected in such a way that three chain beads create a junction point. Equations 87 to 92 express the conditions that the coordinates of the beads 0 (or, equivalently, $(n + 1)$) lie exactly at the positions of the junctions. Logically then, the friction constant of a network junction is three times larger than that of a network chain bead:

$$\zeta_{\mathrm{jun}} = 3\,\zeta. \tag{93}$$

It turns out that under these conditions the modes of the network system can be determined analytically. In this case the Langevin equations for the network junctions, Eq. 80, may be represented as a superposition of three equations of motion for chain beads, Eq. 79. Considering Eq. 80 and the boundary conditions for the cross-links points, Eqs. 87 to 92, jointly, leads to the following sets of allowed values for the intrachain phase shift ψ (which, in turn, fixes the eigenvalues through Eq. 86) [25, 66, 71]:

$$\cos\left[(n+1)\psi_1\right] = \frac{1}{3}(\cos k_1 + \cos k_2 + \cos k_3),\tag{94}$$

$$\sin\left[(n+1)\psi_2\right] = 0,\tag{95}$$

and

$$\sin\left[(n+1)\psi_3\right] = 0.\tag{96}$$

Or, alternatively, one has:

$$\psi_1 = \frac{2\pi}{n+1}l_1 \pm \frac{1}{n+1}\arccos\left[\frac{1}{3}(\cos k_1 + \cos k_2 + \cos k_3)\right],\tag{97}$$

$$\psi_2 = \frac{\pi}{n+1}l_2,\tag{98}$$

and

$$\psi_3 = \frac{\pi}{n+1}l_3.\tag{99}$$

Here $l_1 = 0, ..., (n/2)$, $l_2 = 1, ..., n$, and $l_3 = 1, ..., n$, provided that n is an even integer. Note that in Eq. 97 the sign $+$ should be taken for $l_1 = 0$ and both signs $\pm$ for $l_1 \neq 0$.

Equations 97 to 99 indicate that there are three branches in the relaxation spectrum of the polymer network under study. First, the main branch ψ_1, defined by Eq. 97, includes the phase shift along the Rouse chain (see the first term in Eq. 97) and also $k = (k_1, k_2, k_3)$. Therefore, this branch involves both intra- and interchain relaxation processes, which are coupled in a rather complicated way, see Eq. 97. Remarkably, when the intrachain phase shift does not contribute to ψ_1 ($l_1 = 0$ in Eq. 97) one has a purely interchain sub-branch, $\psi_{\text{net}} \equiv \psi_1(l_1 = 0)$ [25, 66]:

$$\psi_{\text{net}} = \frac{1}{n+1}\arccos\left[\frac{1}{3}(\cos k_1 + \cos k_2 + \cos k_3)\right],\tag{100}$$

which corresponds to the cooperative network relaxation only. In contrast, when $l_1 \neq 0$, intrachain relaxation also shows up. The corresponding subbranch depends now on the phase shift k between the network sites. More specifically, each intrachain mode $2\pi l_1/(n+1)$ in Eq. 97 is split into bands consisting of a large number of sublines. These sublines are related to the different values of k. Second, the sets ψ_2 and ψ_3, defined by Eqs. 98 and 99, give the purely intrachain branches of the relaxation spectrum. In fact, this

is a single double-degenerated branch, which does not depend on the phase shift between the network cells and which coincides with the spectrum of the Rouse chain with fixed ends [25, 66].

At this point, it is worth pointing out the relation between the present network model built from Rouse chains and the coarse-grained interpretation of the cubic network considered in Sect. 5.1.1. The underlying idea is that, on sufficiently large scales ($k \ll 1$), which correspond to the relaxation of the large network, both models must lead to the same set of relaxation times (eigenvalues). The comparison of Eq. 74 in the coarse-grained case with Eqs. 86 and 100 for a network cross-linked from Rouse chains leads to the following relationship between the characteristic relaxation times of both models [25, 66]:

$$\tau_{CG} = 3(n + 1)^2 \tau_0 , \tag{101}$$

where CG indicates coarse-graining. Equation 101 has a nice physical interpretation in terms of the elasticity and friction constants, namely $K_{CG} = K/(n + 1)$ and $\zeta_{CG} = 3(n + 1)\zeta$. In other words, the elastic constant of a spring in a coarse-grained network is equal to the overall elasticity of the Rouse chain between the cross-links (one has $(n + 1)$ springs of elasticity K connected in series) and the friction of a junction in a coarse-grained network corresponds to the friction of a junction ($\zeta_{jun} = 3\zeta$) in a network of Rouse chains plus half of the contributions of the six Rouse chains ($6(n/2)\zeta$) directly attached to this junction. These relations provide a straightforward mapping of the cooperative interchain relaxation of a network built from Rouse chains to a less-detailed, coarse-grained model.

To summarize, the relaxation times (or eigenvalues) of a rather complex system such as a 3-D topologically-regular network end-linked from Rouse chains were determined analytically. In fact, one can do even better: it is possible to construct all of the *eigenfunctions* of the network analytically (which amounts to the transformation from Cartesian coordinates to normal coordinates). Briefly, to construct the normal mode transformation, see Eqs. 84 and 85, one has to combine the Langevin equations of motion of a network junction, Eq. 80, and the boundary conditions in the network junctions, Eqs. 87 to 92. After some algebra one finds [25, 66]:

$$R_p(\boldsymbol{\Omega}; j; t) \simeq \sum_{k, \psi_1} \frac{\exp(ik_p)\sin(j\psi_1) + \sin[(n + 1 - j)\psi_1]}{\sin[(n + 1)\psi_1]} \tag{102}$$

$$\times \exp(i\boldsymbol{\Omega} \cdot \boldsymbol{k}) \, Q_1(\boldsymbol{k}; \psi_1; t)$$

$$+ \sum_{k, \psi_2} \exp(i\boldsymbol{\Omega} \cdot \boldsymbol{k}) f_p(\boldsymbol{k}, \psi_2) \sin(j\psi_2) \, Q_2(\boldsymbol{k}; \psi_2; t)$$

$$+ \sum_{k, \psi_3} \exp(i \, \boldsymbol{\Omega} \cdot \boldsymbol{k}) f_p(\boldsymbol{k}, \psi_3) \sin(j\psi_3) Q_3(\boldsymbol{k}; \psi_3; t) .$$

Here $Q_1(\boldsymbol{k}; \psi_1; t)$, $Q_2(\boldsymbol{k}; \psi_2; t)$, and $Q_3(\boldsymbol{k}; \psi_3; t)$ are three sets of normal coordinates (eigenfunctions), which are related to the corresponding branches of the relaxation spectrum (ψ_1, ψ_2, and ψ_3), the $f_p(\boldsymbol{k}, \psi)$ are functions of $\boldsymbol{k}$, ψ_2, and ψ_3; furthermore, the index p represents a particular chain in a given network cell and can take the values 1, 2, or 3 for one of the three chains in the network cell, respectively, or the value 0 for a network junction.

Knowledge of the eigenfunctions, Eq. 102, allows us to get analytical expressions not only for the macroscopic dynamic characteristics (averaged over all monomers), but also for local quantities of interest, related to individual cross-links or individual chain monomers [25, 66]. In view of space restrictions we will not provide these details here, instead we turn to the discussion of the macroscopic viscoelastic properties of the system. The reader interested in the details is referred to the original papers [25, 66].

An analysis of the viscoelastic mechanical relaxation of polymer networks built from Rouse chains shows the appearance of a new characteristic time (in addition to τ_0), namely the (maximal) relaxation time of a chain between neighboring network junctions, τ_{chain}. This time is of the order of magnitude of τ_{CG}, see Eq. 101, in other words $\tau_{\text{chain}} \simeq (n + 1)^2 \tau_0$; in general, it separates the intrachain from the interchain relaxation processes of the network. In particular, the storage modulus $G'(\omega)$ at rather high frequencies, $\omega > 1/\tau_{\text{chain}}$, (in the domain of the intrachain relaxation) behaves as $\omega^{1/2}$, in other words
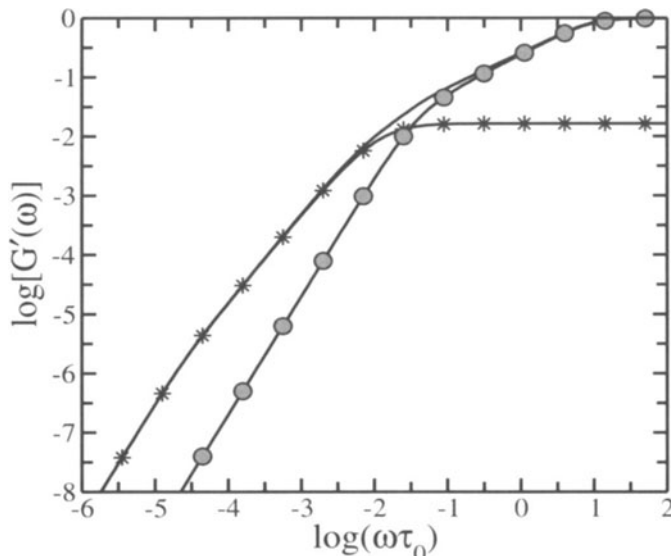
Fig. 7 Reduced storage modulus $[G'(\omega)]$ plotted on double logarithmic scales versus the reduced frequency $\omega\tau_0$ for a 3-D topologically-regular cubic ($40 \times 40 \times 40$) network cross-linked from Rouse chains of 20 beads each (*solid line*). Also shown are the contributions to the $[G'(\omega)]$ that come from intrachain relaxation (*solid line with circles*) and interchain relaxation (*solid line with stars*)

in the same fashion as the linear Rouse chain, see Fig. 7. In contrast, in the domain of large-scale cooperative relaxation, $\omega < 1/\tau_{\text{chain}}$, one observes the $\omega^{3/2}$-behavior typical of topologically-regular cubic networks [25, 66, 71]. Furthermore, given that we have an analytical solution, one can directly compare the contributions of the intra- and of the interchain relaxation to the network's dynamics. For instance, under reasonable choices for the number of beads in the network's chains, the storage modulus $G'(\omega)$ is determined mainly by interchain processes at low frequencies and by intrachain processes at high frequencies, see Fig. 7. The same holds with respect to the frequency behavior of the dynamic viscosity $\eta'(\omega)$ of the system, plotted in Fig. 8. What is of particular interest here is that the intra- and interchain relaxation processes contribute in comparable ways to the viscosity at zero frequency [25], see Fig. 8. We recall that the analytical treatment of a topologically cubic network built from Rouse chains assumed that Eq. 93 holds, which relates the friction constants of the junctions to those of the chain beads. However, it turns out that this condition does not influence our general conclusions much. A special numerical analysis [21] found almost no changes in the dynamic modulus of the network when the ratio ζ_{jun}/ζ was varied between 0.1 to 10.

We close by noting that for rather long Rouse chains one can use a continuum description. The derivation of the relaxation times (eigenvalues) of the network then closely follows the procedure used above [71, 72]. The main results stay unchanged. For a three-dimensional polymer network one ob-
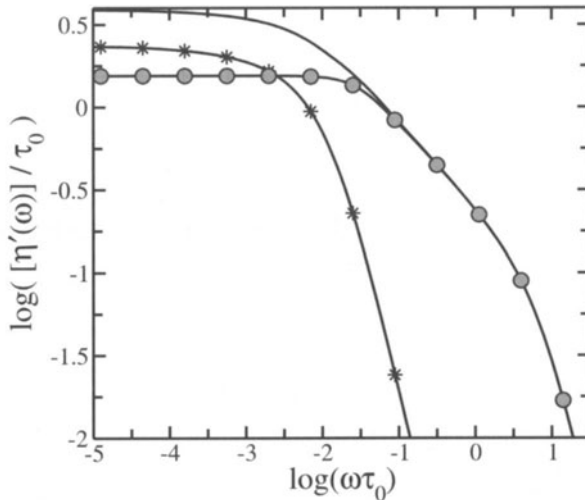
Fig. 8 Reduced shear viscosity $[\eta'(\omega)]$ plotted on double logarithmic scales versus the reduced frequency $\omega\tau_0$ for the same network built from Rouse chains as in Fig. 7. Again, we show the contributions of intrachain relaxation (*solid line with circles*) and interchain relaxation (*solid line with stars*)

serves two major relaxation domains: a Rouse-like, rather small-scale intra-chain relaxation region, where $H(\tau) \sim \tau^{-1/2}$, and a cooperative, large-scale network relaxation region, where $H(\tau) \sim \tau^{-3/2}$ [71, 72]. Historically, networks built from continuous elastic chains were considered earlier than their discrete analogs. However, in the spirit of this review, we chose to focus our exposition on discrete networks, true GGS, built from Rouse chains.

5.2.2
Topologically-Square Networks

The considerations of the previous section carry over to topologically-regular networks of lower dimensionality; for example to a two-dimensional square network built from Rouse chains. We stress again that such a network is two-dimensional only in the sense of connectivity, and that we consider its motion in the three-dimensional Cartesian space (schematically the network behaves as a fishing net in water or, more accurately, honey). In the case of a square network built from Rouse chains an analytical solution is again possible if the friction constant of the network junctions is twice as large as that of the chain beads (see Eq. 93 for the three-dimensional case) [68, 69]. The derivation of the eigenvalues proceeds as in Sect. 5.2.1, again leading to Eq. 86, where the intrachain phase shift ψ is now given by (see Eqs. 97 to 99) [68, 69]:

$$\psi_1 = \frac{2\pi}{n+1} l_1 \pm \frac{1}{n+1} \arccos\left[\frac{1}{2}(\cos k_1 + \cos k_2)\right] \qquad (103)$$

and

$$\psi_2 = \frac{\pi}{n+1} l_2, \qquad (104)$$

where $l_1 = 0, ..., (n/2)$ and $l_2 = 1, ..., n$ (here n is assumed to be even); furthermore, $k = (k_1, k_2)$ are restricted by Eq. 75. Of particular interest here is that the structure of the eigenmodes is simpler than in the three-dimensional case: the purely intrachain branch of the spectrum, which coincides with the spectrum of a single Rouse chain and which is doubly degenerate in a cubic network (see Eqs. 98 and 99 for ψ_2 and ψ_3) is not degenerate anymore (see Eq. 104 for ψ_2).

The relaxation spectrum (as well as the viscoelastic quantities derived from it) obeys features typical of two dimensions: while one finds the standard Rouse chain behavior, $H(\tau) \sim 1/\sqrt{\tau}$, at rather short times (on small scales of motion), at longer times $H(\tau)$ goes as $1/\tau$, a behavior intermediate between that of uncrosslinked Rouse chains and that of three-dimensional networks. Once again we note in the exponents of τ the parallelism between regular and fractal networks, as discussed in Sect. 5.1.2.

It is noteworthy that the same results were found by Chompff and Duiser using a different approach [70]. They proposed a decoupling procedure which, upon being applied to polymer chains cross-linked into a network,

leads to an assembly of uncrosslinked chains of various lengths. The essence of the approach may be illustrated with a simple example: let us consider four chains of N monomers (beads), each of which is connected by one end to a certain cross-link point (single network junction), while the other end of each of these four chains is assumed to be fixed in space. It can be shown by means of simple operations involving the connectivity matrix that this system is equivalent to a single chain of $2N$ monomers and to two chains of N monomers (all of the chains have fixed ends). The appearance of a chain of double length ($2N$ monomers) reflects the interchain connections [70]. The relaxation spectrum, which is obtained by applying the above decoupling procedure to a square network consisting of Rouse chains, is found to follow a Rouse chain behavior at rather short times, $H(\tau) \sim 1/\sqrt{\tau}$, whereas at longer times $H(\tau)$ goes as $1/\tau$ [70], in other words it displays two-dimensional character.

5.3
Regular Networks Built from Complex Cells of Arbitrary Internal Topology

The analysis of the previous section centered on systems of Rouse chains end-linked into regular networks and demonstrated the influence of the GGS-structure on the dynamics; one observes Rouse chain behavior in determined (time or frequency) ranges, whereas in other ranges the relaxation is dominated by the large-scale network structure. In this section we extend this study to more complex systems and replace the Rouse chains by rather arbitrary building blocks (subunits). For such subunits, even when they are connected into regular networks, the possibility of a general analytical treatment gets lost. However, under certain conditions, the network's symmetry still provides opportunities to simplify the problem considerably.

For this we turn to a formalism which allows us to study the dynamics of regular networks built from topologically complex cells (substructures). We let the cells (consisting of beads connected by elastic springs) have an arbitrary internal architecture, and require only that they be topologically identical to each other, see Fig. 9. Obviously, the regular networks built from Rouse chains which were considered in Sect. 5.2 also fall into this category; in this case a cell of the network contains a junction and d Rouse chains directly attached to the junction (here d is the dimensionality of the network).

Below we consider a (topologically) cubic network (following [31, 74] closely). An elementary cubic cell of the network is denoted by $\boldsymbol{\Omega} = (\alpha, \beta, \gamma)$ (here α, β, and γ range from 1 to N) and it contains s beads, which we number by the index $j \in \{1, ..., s\}$. The whole network consists then of $N_{tot} = sN^3$ beads, denoted by $(j, \boldsymbol{\Omega}) \equiv (j, \alpha, \beta, \gamma)$. All of the beads (which have identical friction constants ζ) are connected to their neighbors by means of elastic springs all of which have the same elasticity constant K. The Langevin equation of mo-
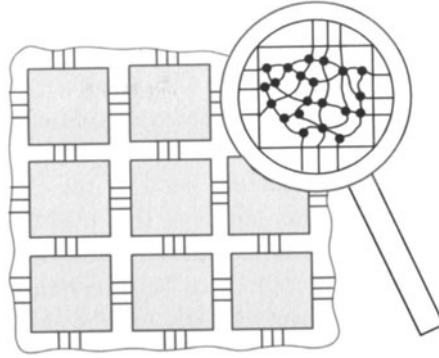
Fig. 9 Schematic representation of a regular network built from complex cells. For clarity's sake a two-dimensional square network is shown. Each cell has some arbitrary internal GGS structure (see magnifying glass), which is identical in all cells

tion for the lth bead of the network is given by Eq. 2 with $F_l^{(\text{ext})}(t) = 0$. Because of the symmetry of the regular network, the determination of the eigenvalues of the connectivity matrix A simplifies considerably. The elastic term in Eq. 2 reads [31, 73, 74]:

$$\sum_{m=1}^{N_{\text{tot}}} A_{lm} R_m(t) = \sum_{i=1}^{s} \sum_{\Omega'} A_{j\Omega i\Omega'} R_{i\Omega'}(t) \tag{105}$$

$$= \sum_{i=1}^{s} A_{j\Omega i\Omega} R_{i\Omega}(t) + \sum_{i=1}^{s} \sum_{\substack{\Omega' \\ \Omega' \neq \Omega}} A_{j\Omega i\Omega'} R_{i\Omega'}(t).$$

Here we let $l \to (j, \Omega)$ and $m \to (i, \Omega')$. Because of symmetries, we can now set $B_{ji}^{(\text{int})} \equiv A_{j\Omega i\Omega}$ and $B_{ji}^{(\text{ext})}(\Delta) \equiv B_{ji}^{(\text{ext})}(\Omega - \Omega') \equiv A_{j\Omega i\Omega'}$ in Eq. 105. This brings us to [31, 74]:

$$\sum_{m=1}^{N_{\text{tot}}} A_{lm} R_m(t) = \sum_{i=1}^{s} B_{ji}^{(\text{int})} R_{i\Omega}(t) + \sum_{i=1}^{s} \sum_{\Delta} B_{ji}^{(\text{ext})}(\Delta) R_{i\Omega-\Delta}(t), \tag{106}$$

where $\Delta = \Omega - \Omega'$ denotes the difference between the network cells Ω and Ω', given in the units of number of intervening cells in each direction. In Eq. 106 the matrix $B^{(\text{int})} = (B_{ji}^{(\text{int})})$ specifies the connections inside a given cell consisting of s beads. In contrast, the matrices $B^{(\text{ext})}(\Delta) = (B_{ji}^{(\text{ext})}(\Delta))$ define the intercell connections: their non-zero elements $B_{ji}^{(\text{ext})}(\Delta)$ are equal to -1, indicating that bead j of cell Ω and bead i of cell $\Omega' = \Omega - \Delta$ are connected by a spring (bond). In a regular network built from cells, each elementary cell is directly connected to its nearest-neighbor cells only;

for a topologically-cubic network the Δ are therefore given by the set $\{(1,0,0),(-1,0,0),(0,1,0),(0,-1,0),(0,0,1),(0,0,-1)\}$.

Due to the symmetry inherent in Eq. 106, the diagonalization of the connectivity matrix A of the network can be now simplified. From a formal point of view the situation is very close to that met in solid state physics (Bravais lattice with a basis) [75–77], where the basis of the lattice plays the role of our elementary network cell. Note, however, that in the arguments leading to Eq. 106 only the connectivity (a topological feature) enters. Hence, the networks considered here are not required to be translationally invariant. As an example, the positions of the beads (j, Ω), $(j, \Omega + \Delta)$, and $(j, \Omega + 2\Delta)$ are not necessarily related by a single translation operator, as would be (in first-order) the case in a crystal. Here we have a network consisting of flexible substructures (cells), whose conformations change widely under the underlying random stochastic forces, and hence differ much from cell to cell. Nevertheless, using Eq. 106, we can proceed quite formally: we apply periodic boundary conditions to the whole network and look for solutions to our Langevin equations of the form:

$$R_{j\Omega}(t) = \sum_{k_1,k_2,k_3} C_{jk} \exp(i[k_1\alpha + k_2\beta + k_3\gamma]) \exp(-\lambda(k)t/\tau_0). \tag{107}$$

Here $\Omega = (\alpha, \beta, \gamma)$, the C_{jk} are constants, $\tau_0 = \zeta/K$ is the characteristic relaxation time, and $k = (k_1, k_2, k_3)$ is given by $k_i = 2\pi m_i/N$, where the m_i are integers with $0 \le m_i \le (N-1)$ for $i = 1, 2,$ and 3 (see also Eq. 75). We recall that the triple k is not a reciprocal vector, as in solid state physics; it is simply a means to count the eigenmodes. We now define the new matrices:

$$B_{ji}(k) = B_{ji}^{(int)} + \sum_{\Delta} B_{ji}^{(ext)}(\Delta) \exp(-ik\cdot\Delta). \tag{108}$$

The matrices $B(k) = \{B_{ji}(k)\}$ include all relevant information concerning the intra-cell topology and the way in which the cells of the network are connected to each other. All in all there are N^3 k-values and therefore N^3 different $B(k)$ matrices. Using the $B(k)$ matrices, the Langevin equations, Eq. 2, are reduced to [31, 73, 74]:

$$\lambda(k)C_{jk} = \sum_{i=1}^{s} B_{ji}(k)C_{ik}. \tag{109}$$

The symmetry, therefore, helped to simplify the problem: instead of having to diagonalize A, which is a $(sN^3 \times sN^3)$-matrix, we only need now to diagonalize N^3 different $(s \times s)$-matrices [31, 74].

It is important to stress at this point that the derivation of Eq. 109 is general and that it holds for an arbitrary topological structure of the cells involved. Moreover, the cubic network considered here is only a particular example; the approach can be easily extended to other network types. For instance, all

of the results of this section are also valid for a square network built from complex substructures; to describe it one simply has to set $k_3 = 0$ in all the k-dependent equations established so far. Also, the method discussed here can be extended to copolymer networks, whose building blocks (cells) may consist of different beads (say, with different mobilities) [21]. In the following sections we will use the general formalism developed in this section for various systems of complex topology, such as polymer networks bearing dendritic wedges [78], dendrimer-based polymer networks [74], and networks made up from disordered subunits [31, 73].

6
Fractal Polymer Networks

After discussing the situation in topologically-regular, mesh-like polymer networks in the previous section, we turn now to the general situation. Here we will display the possibilities of describing complex networks using ideas of scale freedom. Typical of such approaches are models based on fractal structures and notions akin to them. In a first step we will consider a phenomenological, general approach that leads to classic viscoelastic models; this allows us to make connections both to the microscopic models discussed in the previous paragraphs and also to global descriptions, rooted in fractional differential equations. In the next steps we then turn our attention to simple fractal networks, such as ladder models, and to Sierpinski gasket structures.

6.1
General Approach: Generalized Viscoelastic Models

Historically, the viscoelastic properties of polymers were initially modeled by combining springs and dashpots. A sequential combination of a spring and a dashpot is called the Maxwell model. Denoting the stress by σ and the strain by ε, we have for the spring

$$\sigma_1(t) = E\,\varepsilon_1(t) \tag{110}$$

and for the dashpot

$$\sigma_2(t) = \eta\frac{\mathrm{d}\varepsilon_2(t)}{\mathrm{d}t}\,, \tag{111}$$

where E is related to Young's modulus and ε to the viscosity. The equation for σ and ε then reads (constitutive equation):

$$\sigma(t) + \tau\frac{\mathrm{d}\sigma(t)}{\mathrm{d}t} = \tau E\frac{\mathrm{d}\varepsilon(t)}{\mathrm{d}t}\,, \tag{112}$$

with $\tau = \eta/E$. As already noted in Sect. 3.1.2, the response of $\sigma(t)$ to a stepwise change in ε (to $\varepsilon(t) = \varepsilon_0\theta(t)$) is the relaxation modulus $G(t)$. For the Maxwell model it follows:

$$G(t) = E\,\varepsilon_0 \exp(-\,t/\tau)\,, \tag{113}$$

which is clearly the special case of Eq. 26 for one mode with $\tau_k = 2\tau$. Now, Eq. 25 can be rewritten in terms of the storage modulus

$$G'(\omega) \equiv \omega \int_0^\infty G(t)\sin(\omega t)\,dt \tag{114}$$

and of the loss modulus

$$G''(\omega) \equiv \omega \int_0^\infty G(t)\cos(\omega t)\,dt\,. \tag{115}$$

In the case of the Maxwell model these are simply

$$G'(\omega) = E\,\varepsilon_0 \frac{(\omega\tau)^2}{1 + (\omega\tau)^2} \tag{116}$$

and

$$G''(\omega) = E\,\varepsilon_0 \frac{\omega\tau}{1 + (\omega\tau)^2} \tag{117}$$

which are, again, special cases of Eqs. 20 and 21. Evidently, realistic polymer models are not well-represented by these simplistic forms, Eqs. 116 and 117; in general, Eqs. 20 and 21 have to be used. A notable exception occurs when $G(t)$ is (at least, over a certain range of t) self-similar; in other words when it is an algebraic function of time,

$$G(t) \sim t^{-\alpha}\,, \tag{118}$$

see Eq. 66 as an example. Then such a behavior can be captured by changing the derivatives in the constitutive equation, Eq. 112, to fractional derivatives [8, 9]. Furthermore, the scaling displayed by $G(t)$ in Eq. 118 is typical of anomalous diffusion.

Regular diffusion, better known as Brownian motion, is characterized (in the absence of directed, external fields) by a linear increase of the mean-square displacement with time, see Eq. 60 for the motion of the center of mass. For anomalous diffusion this simple relation does not hold anymore. Then the temporal evolution of the mean-square displacement is non-linear, and at long times often obeys

$$\langle R^2(t)\rangle \sim t^\gamma\,, \tag{119}$$

with $\gamma \neq 1$. In the case that $\gamma < 1$, one denotes the behavior as subdiffusive. We remark that, in many instances, such as in the presence of a constant,

non-zero electric field (say, oriented along the y-axis), Eq. 119 turns out to be equivalent to the relation [2, 9, 13]

$$\langle Y(t) \rangle \sim t^{\gamma} , \tag{120}$$

where we have $R = (X, Y, Z)$. For simply-structured particles (the ideal case being point-like objects) the pattern of motion of Eqs. 119 and 120 often results from disorder [79–84]; for polymer chains – as studied here, see Eq. 68 – the motion of the monomers also obeys Eq. 119 in the absence of disorder; the reason for this is the relaxation of the internal modes of the structure [85]. Furthermore, Eq. 119 is also obeyed during several motional stages in melts of polymer chains; then one has reptation [4] and the processes giving rise to disentanglement are characterized by different exponents γ in Eq. 119 [2, 4, 41].

   Recently, besides the classical way of describing anomalous diffusion via continuous time random walks (CTRW) and Lévy-walk models [79–83, 86–92], descriptions based on fractional derivatives have also attracted much interest [8, 9, 93–95]. As a reminder, one has as the defining relation for fractional derivation the Riemann-Liouville expression:

$$\frac{d^{\alpha}f}{dt^{\alpha}} \equiv \frac{1}{\Gamma(-\alpha)} \int_{0}^{t} \frac{f(\tilde{t})}{(t-\tilde{t})^{\alpha+1}} \, d\tilde{t} . \tag{121}$$

In Eq. 121 $\Gamma(z)$ is the Gamma-function and the expression extends the (integer) recursive integration to the domain of real α; differentiation is obeyed for $\alpha > 0$, integration for $\alpha < 0$. In general, all differentiation rules such as

$$\frac{d^{\alpha}f}{dt^{\alpha}} = \frac{d^{\beta}}{dt^{\beta}} \left(\frac{d^{\alpha-\beta}f}{dt^{\alpha-\beta}} \right) \tag{122}$$

hold. Now it turns out that replacing the usual derivatives by fractional derivatives in the constitutive equation of the Maxwell-model, Eq. 112, leads to:

$$\sigma(t) + \tau^{\alpha-\beta} \frac{d^{\alpha-\beta}\sigma(t)}{dt^{\alpha-\beta}} = \tau^{\alpha} E \frac{d^{\alpha}\varepsilon(t)}{dt^{\alpha}} \quad (\text{with} \quad 1 > \alpha > \beta) , \tag{123}$$

an expression which offers an excellent description of many polymeric substances, see [8, 9] for details.

   Following the developments outlined in [8, 9], we now stress the fact that anomalous diffusion in the scaling form of Eqs. 119 and 120 is closely connected to descriptions based on fractional derivatives, given that they allow us to invert, in a simple way, the integral expressions which follow from the theory of linear response, when the anomalous behavior has a power-law character going as Eq. 119, with $\gamma < 1$. For technical reasons and because of an intimate relation to linear response we prefer, as in [8, 9], to extend the lower integration limit in Eq. 121 to $-\infty$; in this way we obtain the Weyl-form.

It is now a simple matter to show that the Weyl-form of fractional calculus is an exceedingly powerful mathematical method when treating materials whose internal processes obey algebraic decays. We follow here the description given in [9]. Denoting the response of the system to an external perturbation $\Psi(t)$ by $\Phi(t)$, one can express the relation between these two functions in terms of $\Phi_s(t)$, the response of the system to a step perturbation $\theta(t)$. Namely, because of the superposition principle and of causality, in the framework of linear response one obtains:

$$\Phi(t) = \int_{-\infty}^{t} d\tilde{t}\, \Phi_s(t - \tilde{t}) \frac{d\Psi(\tilde{t})}{d\tilde{t}} . \tag{124}$$

In general, Eq. 124 is difficult to invert, being an integral relation. However, for algebraic Φ_s, in other words $\Phi_s \equiv \frac{C}{\Gamma(1-\gamma)} \left(\tau_0/t\right)^{\gamma}$, where $0 < \gamma < 1$, it follows that

$$\Phi(t) = C\tau_0^{\gamma} \frac{1}{\Gamma(1 - \gamma)} \int_{-\infty}^{t} \frac{d\tilde{t}}{(t - \tilde{t})^{\gamma}} \frac{d\Psi(\tilde{t})}{d\tilde{t}} = C\tau_0^{\gamma} \frac{d^{\gamma}\Psi(t)}{dt^{\gamma}} , \tag{125}$$

where we used the repeated differentiation given in Eq. 122. Clearly, now Eq. 125 can be readily inverted, since it is a simple fractional derivative. The inversion reads

$$\Psi(t) = \frac{1}{C\tau_0^{\gamma}} \frac{d^{-\gamma}\Phi(t)}{dt^{-\gamma}} . \tag{126}$$

Evidently, one can simply read-off from Eq. 126, by inverting the argument leading from Eq. 124 to Eq. 125, that the response $\Psi_s(t)$ to a step perturbation $\theta(t)$ of Φ is:

$$\Psi_s(t) = \frac{C^{-1}}{\Gamma(1 + \gamma)} \left(\frac{t}{\tau_0}\right)^{\gamma} . \tag{127}$$

This last relation makes it clear that the strain (extension) of the object under an external stress (force) now simply obeys, due to $0 < \gamma < 1$, the subdiffusive law expressed by Eq. 120. Given that many macromolecular systems display such a subdiffusive behavior, it now becomes evident why they can be described very well through expressions involving fractional derivatives; as long as the response is linear, scaling behavior and fractional derivatives reflect the same underlying physics. In the following subsections we will see that fractal GGS also show scaling, where γ is related to the spectral dimension $\tilde{d}$ of the fractal.

6.2
A Simple Fractal Network: The Ladder Model

Here we start with the ladder model, which is a simple example of a hier-archical (scaling) network [26, 96–100]. The model has its electrical analog and turns out to be a basic element in the fractional differential picture [8, 9]. From a mathematical point of view, in a simple ladder model version the equations are identical to those of the Rouse model for a single chain. Ladder models are very useful for providing a microscopic (if somewhat idealized) picture of gels, as well as in modeling different gelation stages. If one focuses on end-linking reactions in a prepolymer which is far below the entanglement limit, one finds a power-law behavior, $G^*(\omega) \sim (i\omega)^\alpha$, near the gel point for the complex dynamic modulus [101–103]. This behavior appears in quite ex-tended frequency ranges and is followed by a liquidlike behavior in the case of a pregel and by a solidlike behavior for a postgel structure. Moreover, for stoichiometrically-balanced gels, one often finds $\alpha \cong 1/2$. This value appears to be rather insensitive to the choice of the prepolymer, to the cross-linker functionality, and to the chain length [101, 102].

In order to describe pregel, postgel and gel situations, ladder models were used [100]. A ladder model is depicted schematically in Fig. 10; it consists of springs (with spring constants $E_0, E_1, E_2, ...$) along one of the struts of the lad-der and dashpots (with viscosities $\eta_0, \eta_1, \eta_2, ...$) along the ladder rungs. Three different types of boundary conditions can now be envisaged: finite ladder ar-rangements are appropriate to model pregels and postgels; for a pregel the ladder finishes with a spring (E_n) and a dashpot (η_n) in series (a Maxwell element) and for a postgel with a spring (E_n). On the other hand, an infinite ladder arrangement (Fig. 10) is necessary to model the gel point. The complex
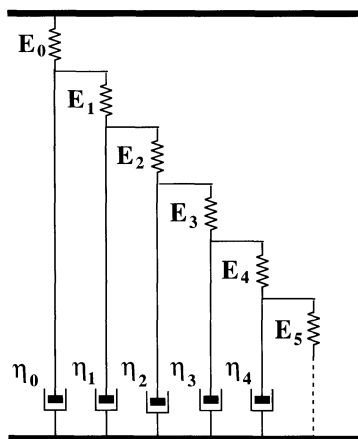
Fig. 10 Infinite ladder model

dynamic modulus $G^*(\omega)$ in the case of a pregel reads [100]:

$$G^*(\omega) = \cfrac{E_0}{1+} \cfrac{(i\omega)^{-1}(E_0/\eta_0)}{1+} \cfrac{(i\omega)^{-1}(E_1/\eta_0)}{1+} \cdots \\ \cfrac{(i\omega)^{-1}(E_n/\eta_{n-1})}{1+} \cfrac{(i\omega)^{-1}(E_n/\eta_n)}{1}, \tag{128}$$

and, correspondingly, one has for a postgel situation [100]:

$$G^*(\omega) = \cfrac{E_0}{1+} \cfrac{(i\omega)^{-1}(E_0/\eta_0)}{1+} \cfrac{(i\omega)^{-1}(E_1/\eta_0)}{1+} \cdots \\ \cfrac{(i\omega)^{-1}(E_{n-1}/\eta_{n-1})}{1+} \cfrac{(i\omega)^{-1}(E_n/\eta_{n-1})}{1}, \tag{129}$$

where the standard notation of continued fractions, $a/(b +)f = a/(b + f)$, is used.

For $G^*(\omega)$ at the gel point (an infinite ladder arrangement) the expression is akin to Eqs. 128 and 129, but it involves an infinite continued fraction. A simple special case may be obtained by making all of the springs and all of the dashpots equal ($E_0 = E_1 = \ldots = E$ and $\eta_0 = \eta_1 = \ldots = \eta$). Then at the gel point the complex dynamic modulus $G^*(\omega)$ reduces to [100]:

$$G^*(\omega) = E(i\omega\tau_{\text{lad}})^{1/2}\left[\left(1 + \frac{i\omega\tau_{\text{lad}}}{4}\right)^{1/2} - \left(\frac{i\omega\tau_{\text{lad}}}{4}\right)^{1/2}\right], \tag{130}$$

where $\tau_{\text{lad}} = \eta/E$ is the characteristic relaxation time of the ladder model under study. In the low-frequency domain, $\omega\tau_{\text{lad}} \ll 1$, Eq. 130 leads to a power-law behavior, $G^*(\omega) \simeq E(i\omega\tau_{\text{lad}})^{1/2}$. Thus, an infinite ladder arrangement built from identical springs and identical dashpots leads to a power-law behavior for the storage modulus, $G'(\omega) \sim \omega^\alpha$, with $\alpha = 1/2$ [100].

That we recover the intermediate $G'(\omega)$-behavior of the Rouse model in this way is only surprising at first sight. In fact, a second look at Fig. 10 clarifies the equivalence between the ladder model and the Rouse chain. In both there is a sequential connection between neighboring elements through harmonic springs; furthermore, each element has a local, dissipating, energy sink. The behavior of finite ladder arrangements built from identical springs and dashpots may appear even more familiar now. Their storage modulus also demonstrates a $\omega^{1/2}$-behavior, but only in an intermediate frequency domain, which here extends up to a crossover frequency which was numerically found to be $\omega\tau_{\text{lad}} \simeq 4/n^2$, where n is related to the ladder length, see Eqs. 128 and 129. This corresponds exactly to the behavior of Rouse chains.

Moreover, for the pregel finite ladder ending with a Maxwell element (a spring and a dashpot in series) one finds at low frequencies a liquidlike behavior, $G'(\omega) \sim \omega^2$. For the postgel ladder, which consists of $(n + 1)$ springs in series and whose ends are both springs, one finds a solidlike behavior, $G'(\omega) \simeq E/(n + 1)$; this is also the low-frequency behavior of a Rouse chain whose ends are fixed.

Furthermore, recall that one often finds α values which deviate from 1/2 [103]. It turns out that the above ladder model can be modified in several ways, so that α can take arbitrary values between 0 and 1. One of these possibilities is to choose the spring constants E_k and the viscosities η_k so that they fulfill [97, 100]:

$$E_k = C_1 k^{(1-2\alpha)} \quad \text{and} \quad \eta_k = C_2 k^{(1-2\alpha)}, \tag{131}$$

where C_1 and C_2 are constants. It can be shown that the complex dynamic modulus $G^*(\omega)$ of a ladder built from such springs and dashpots does indeed follow a ω^α-behavior [97]:

$$G^*(\omega) \sim \omega^\alpha . \tag{132}$$

Another possibility, which mimics the geometrical situation better, is to connect the dashpots through springs in a network structure, say a fractal one, while keeping the simple forms $E_k = E = \text{const}$ and $\eta_k = \eta = \text{const}$ [8, 9, 100]. Again, this model gives rise to a ω^α-behavior for $G^*(\omega)$. We close by noting that all these ladder models are mechanical realizations for fractal elements [8, 9], since they fulfill equations of the form

$$\sigma(t) = C \frac{d^\alpha \varepsilon(t)}{dt^\alpha}, \quad \text{with} \quad 0 \leq \alpha \leq 1. \tag{133}$$

6.3
Dual Sierpinski Gasket Structures

Let us turn now to GGS which show more complex structures. Foremost in our mind is to focus on GGS whose eigenvalue spectra can be readily determined. As previously discussed, the evaluation of the main relaxation forms, Eqs. 20, 21, and 50 is straightforward, under the condition that all eigenvalues are known. This also determines the way to proceed: what is needed is to diagonalize the A matrix in Eq. 10 in order to obtain the corresponding eigenvalues needed to compute the relaxation functions.

Given that the interesting intermediate temporal range is limited by the two (terminal) regions previously discussed, say, for $G'(\omega)$ by the domains at quite small and at quite large frequencies, regions in which all finite GGS systems behave in the same way, one has to consider very large GGS. This is the case because one has to work out the behavior typical for the GGS-class under investigation, behavior which shows up only in the intermediate range; hence it is very important that the GGS considered be very large in order for the intermediate range to be sufficiently large.

Now, the problem that one faces when using numerical procedures is the limited options available when the size of the GGS gets large. In this case, the numerical procedures may fail, given that currently only matrices of up to 5000×5000 elements can be readily diagonalized; one has to bear in mind

that we need *all* the eigenvalues of A in the subsequent calculations of the dynamical properties.

In the following we will focus on several regular fractal structures, for which, due to their particular features, it is possible to determine *all* of the eigenvalues semi-analytically. We stop first to note that in general the spectra of such objects are not smooth at all [104–106]. Nonetheless, as will become evident in the following, the fact that such spectra are discrete and highly discontinuous will (if at all) hardly show up in the relevant experimental quantities. Now, apart from very fine details, it turns out that the major factor that determines the scaling behavior of the relaxation forms considered by us in the intermediate frequency range is the spectral dimension [6–9, 94, 104–113]. Evidently, in order to be able to clearly show by numerical means that only the spectral dimension is decisive, we have to use very large GGS again.

The first class of deterministic fractals on which we focus are the so-called dual Sierpinski gaskets. As we proceed to discuss, they are very closely related to the general Sierpinski gaskets; the advantage of working with dual Sierpinski gaskets is that their spectra can be determined exactly through iterative procedures, without the need to diagonalize A numerically [105, 106, 110]. In this way we are in a position to study extremely large fractals. An example of a dual Sierpinski gasket is given in Fig. 11, with $d = 2$ as embedding space.

As for all Sierpinski-type gaskets, the construction starts [106] from a simplex of δ-sites ($\delta = d + 1$ and in Fig. 11 $\delta = 3$); a triangle here. Such simplexes are then iteratively connected to each other. There are two commonly-used possibilities for continuing the construction. In the classical picture [114] all sites of the simplex also belong to other simplexes of the same kind; one hence superposes pairwise sites belonging to different simplexes, obtaining the usual Sierpinski gaskets [114]. A second possibility consists of connecting the given simplex via *additional bonds* to other simplexes; this is the situation displayed in Fig. 11. There, all basis sites of the smallest triangle are connected to the tips of further identical triangles. Hence the upper part of
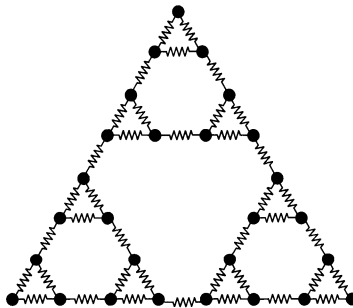
Fig. 11 Dual Sierpinski gasket, embedded in $d = 2$

Fig. 11 depicts one complete iteration, leading to the second generation of the fractal. The construction then gets iterated to higher generations, in Fig. 11 up to the third. In fact, the so-created object is identical to what would have been obtained by taking the usual Sierpinski gasket, inserting a vertex at the center of each of its triangles and connecting the vertices to each other [104]. We stop to note that both the Sierpinski gasket and also its dual are naturally embedded in the $d = \delta - 1$ dimensional space, here in $d = 2$. Note that going from the usual Sierpinski gasket to its dual reduces the coordination number of the sites of the fractal from $d + 2$ to $d + 1$. However, as can be easily seen (and as was also pointed out in [104–106, 110]), the usual gasket and its dual have exactly the same fractal $\bar{d}$ and spectral $\tilde{d}$ dimensions; these are, for a general d-dimensional embedding space, setting $\delta = d + 1$:

$$\bar{d} = \frac{\ln(d + 1)}{\ln 2} = \frac{\ln \delta}{\ln 2} \tag{134}$$

and

$$\tilde{d} = \frac{2\ln(d + 1)}{\ln(d + 3)} = \frac{2\ln \delta}{\ln(\delta + 2)} . \tag{135}$$

As a side-remark, we note that for special values of d, namely for $d = 3, 7, 15$, and so on, $\bar{d}$ is an integer. Then, as shown in [106, 115], other possibilities for embedding the dual Sierpinski gaskets into Euclidean space exist.

The major advantage of focusing on dual Sierpinski gaskets is that their eigenvalues can be obtained iteratively [105, 106, 110]. One proceeds as follows: from the eigenvalue spectrum at stage n, one obtains the eigenvalues at stage $n + 1$ by first assigning to each non-vanishing eigenvalue λ_{n-1} two new eigenvalues $\lambda_n^\pm$ through the relation:

$$\lambda_n^\pm = \frac{(\delta + 2) \pm \sqrt{(\delta + 2)^2 - 4\lambda_{n-1}}}{2} , \tag{136}$$

with

$$\delta = d + 1 . \tag{137}$$

In this way, we carry the degeneracies of λ_{n-1} over to λ_n^+ and λ_n^-. Furthermore, δ, with degeneracy $\left[(\delta - 2)\delta^{n-1} + \delta\right]/2$, and $\delta + 2$, with degeneracy $\left[(\delta - 2)\delta^{n-1} - (\delta - 2)\right]/2$, as well as the nondegenerate value $\lambda_1 = 0$, which corresponds to the translation of the whole GGS are added to this spectrum as eigenvalues. It is then a simple matter to verify that the number of eigenvalues at each stage is indeed equal to $N = \delta^n$. Moreover, in [106] these results were tested numerically by diagonalizing, for relatively small N values, the corresponding A matrices. These results support the correctness of the whole procedure in an additional, independent manner.

Using this procedure, it is now a simple matter to compute the eigenvalues iteratively by numerical means, even for very large values of N. Having
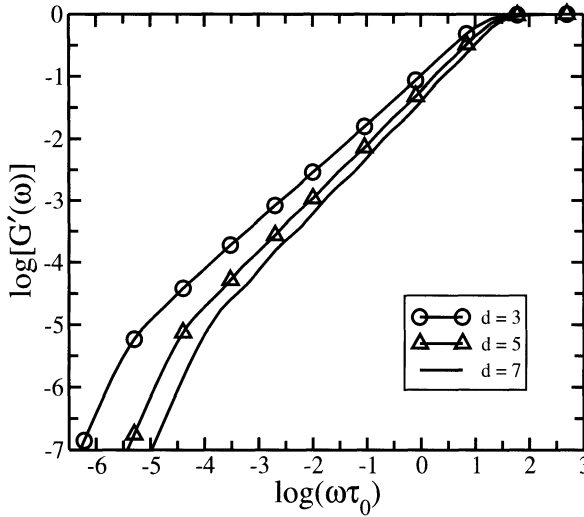
Fig. 12 Reduced storage modulus $[G'(\omega)]$ plotted on double logarithmic scales versus the reduced frequency $\omega\tau_0$ for different dual Sierpinski gaskets with $d = 3$, 5 and 7

found the eigenvalues, it is then straightforward to numerically determine the different relaxation quantities of interest.

Here we start by focusing on $[G'(\omega)]$, Eq. 20 together with Eq. 12, which is plotted in Fig. 12 in double logarithmic scales using the data of [106] for several dual Sierpinski gaskets, for $d = 3$ ($N = 4^9$), $d = 5$ ($N = 6^7$), and $d = 7$ ($N = 8^6$). Clearly evident is the limiting, connectivity-independent behavior at very small and very large ω, $[G'(\omega)] \sim \omega^2$ and $[G'(\omega)] \sim$ const, respectively. In the intermediate regime, in which $[G'(\omega)] \sim \omega^\alpha$ holds (where α is d-dependent), a careful analysis [106] demonstrates that to a very good approximation $\alpha = \tilde{d}/2$, where $\tilde{d}$ is the spectral dimension. For larger d one also sees some oscillations in the intermediate regions; these are due to the hierarchical structure of the underlying dual Sierpinski gasket [106]. Similar behavior is also found for $[G''(\omega)]$, where $[G''(\omega)] \sim \omega^\alpha$, with $\alpha = \tilde{d}/2$ in the intermediate domain. It remains to consider $\langle\langle Y(t)\rangle\rangle$, which for small and for large t is a linear function of t. In its intermediate domain one finds $\langle\langle Y(t)\rangle\rangle \sim t^\gamma$, but now $\gamma = 1 - \tilde{d}/2$ [106].

We close this section by noting that the relations between the scaling exponent and the spectral dimension are very general. We will meet them again in Sect. 9.3, in the study of regular hyperbranched fractals. It is also noticeable that the inclusion of hydrodynamic interactions into the dynamic picture leads to the loss of scaling for Sierpinski-type polymers in the intermediate regime [116, 117].

7
Heterogeneous Polymer Networks

Up to now we have focused on the dynamics of regular networks. However, most polymer networks and gels are random, so regular models do not reflect the experimental situation accurately [118–126]. The wealth of possible inhomogeneities in real cross-linked polymers is, in fact, huge and it precludes any possibility of achieving a complete, unified theoretical treatment for all types of heterogeneous networks. A plethora of factors affect the way in which polymers form, and they lead to networks with large structural and dynamical differences. Structural factors that may differ widely include the lengths of the strands, the appearance of dangling chains, different local cross-link densities, and cross-link agglomerations. In this section we will outline several theoretical approaches developed to treat inhomogeneous polymer networks, although we do not aim to present a complete coverage of the subject.

7.1
Monodisperse Random Nets

We start with the approach of Martin and Eichinger [10, 127, 128], who considered regular network structures and introduced randomness into them through cross-linking. They started from a regular network consisting of N vertices (cross-links), an example might be a simple ring. Now every vertex is assigned the same functionality f, where f is larger than the number, $2d$, of nearest neighbors in the regular network. We then add to the network $(f - 2d)N/2$ bonds. The procedure then consists of increasing the functionality of all of the vertices in steps of one. This was achieved in [10, 127, 128] by inserting additional bonds sequentially and stochastically into the network. In Fig. 13 we show a possible realization of a random network with trifunctional junctions, $f = 3$. By repeating this procedure, we can generate random
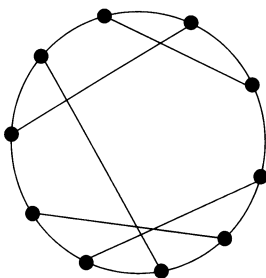
Fig. 13 Example of a random net (reduced net) consisting of $N = 10$ trifunctional beads. All beads have the same functionality, $f = 3$, and there are no double bonds

nets with junctions of higher functionality. Such random networks are called "reduced nets" [10, 127, 128]. Note that the above procedure automatically leads to connected networks.

Following the creation of reduced nets, one diagonalizes their connectivity matrices. This is done for different realizations, with f and N fixed $(10 \leq N \leq 100)$ [127]. In all cases, in the limit of large N, the eigenvalues λ_k of the reduced nets appear to be linear functions of k; in other words one finds that [127]:

$$\lambda_k \simeq \frac{a}{N}k + b, \tag{138}$$

where a and b are constants. In fact, in [127] the constants a and b in Eq. 138 were found to obey (for $f > 2$):

$$a \simeq 2\sqrt{3f}\left(1 - \frac{f-3}{2N}\right) \tag{139}$$

and

$$b \simeq f - \sqrt{3f} + \frac{f + (f-3)\sqrt{3f/4}}{N}. \tag{140}$$

Remarkably, the spectrum of eigenvalues of a trifunctional reduced net ($f = 3$) differs from that of reduced nets with higher cross-link functionality, $f \geq 4$: Eqs. 139 and 140 give $a = 6$ and $b = 3/N$ for $f = 3$, so that the minimal eigenvalues of a trifunctional net decrease as $1/N$ when the size N of the net goes up (see Eq. 138 with $k = 1$). In contrast, for $f \geq 4$ the minimal eigenvalue of reduced nets is of the order of unity, so it does not depend on the net size in the limit of large N [127].

The above reduced net model is then modified to account for local intrachain degrees of freedom in randomly cross-linked networks. For this purpose each Gaussian bond of the reduced net is replaced by a Rouse chain consisting of n beads, in other words $(n + 1)$ springs [128]. The whole network then contains $N(1 + nf/2)$ beads; this makes a direct numerical diagonalization of the corresponding connectivity $(N(1 + nf/2)) \times (N(1 + nf/2))$ matrix hardly feasible, even for only moderately large networks. It turns out that such large matrices can be handled by first reducing them algebraically to smaller ones; for details see [10, 128]. This procedure, when applied to a reduced net built from Rouse chains, yields [128]:

   (*i*) n eigenvalues of the form:

$$\lambda_k = 2\left(1 - \cos\frac{\pi k}{n+1}\right) = 4\sin^2\frac{\pi k}{2(n+1)}, \quad k = 1, 2, ..., n; \tag{141}$$

which are $N(f - 2)/2$ times degenerate and coincide with those of Rouse chains with fixed ends [61].

(ii) Nn non-degenerate eigenvalues, given by:

$$\lambda_k = 2(1 - \cos\theta_{\sigma,k}) = 4\sin^2\theta_{\sigma,k}/2. \tag{142}$$

Here $\theta_{\sigma,k}$ is one of the n real solutions of the following trigonometric polynomial of order $(n + 1)$ [128]:

$$\cos\left[(n + 3/2)\theta\right] + (f - 1)\cos\left[(n + 1/2)\theta\right] - (f - \Lambda_\sigma)\cos\left[\theta/2\right] = 0, \quad (143)$$

where Λ_σ is one of the N eigenvalues of the connectivity matrix of the underlying reduced net.

(iii) N eigenvalues obtained from the complex solutions to Eq. 143, namely one for each Λ_σ. These solutions may be estimated as being $\theta \simeq \pi - i\ln(f - 1)$, leading to eigenvalues approximately equal to $f^2/(f - 1)$ [10, 128].

The relaxation spectrum $H(\tau)$ for such systems was found to obey $\tau^{-0.54}$ and $\tau^{-0.53}$ for tetrafunctional and trifunctional networks, respectively [128]. Remarkably, the authors found that the ratio of the maximal relaxation time of the random network, τ_{net}, to that of the Rouse chain, τ_{chain} (see also Eq. 57), is approximately [128]:

$$\frac{\tau_{\text{net}}}{\tau_{\text{chain}}} \simeq \frac{\pi^2(f + (f + 2)/n)}{2(f - 2\sqrt{f - 1})}, \tag{144}$$

which is around 87 for $f = 3$ and around 37 for $f = 4$ in the case of long Rouse chains between the vertices, $n \gg 1$. Thus, the random network considered here has a substantial domain of cooperative interchain relaxation ($\tau_{\text{net}}/\tau_{\text{chain}} \gg 1$). On the other hand, the relaxation spectrum of the random network is still very narrow; it does not depend on the network size (on the number of vertices in the underlying reduced net, N).

We conclude by noting that [128] finds in the intermediate domain $1/\tau_{\text{net}} < \omega < 1/\tau_{\text{min}}$ that $G'(\omega) \sim \omega^{0.57}$ and $G''(\omega) \sim \omega^{0.50}$; this means that this result here should be considered with care, since in the domain $1/\tau_{\text{chain}} < \omega < 1/\tau_{\text{min}}$ the storage modulus $G'(\omega)$ is expected to mirror the behavior of a Rouse chain. Some deviations are possible only in the domain of cooperative relaxation, $1/\tau_{\text{net}} < \omega < 1/\tau_{\text{chain}}$. However, the width of this domain is finite and rather small, see Eq. 144; for $f = 3$ it amounts to about two orders of magnitude. Therefore, it does not seem possible to extract reliable information about scaling from the $G'(\omega)$-plot. Finally, we remark that the above model of random networks is, in a certain sense, too regular, since all vertices have the same functionality f. As we will see in the next section, removing this requirement renders a cross-linked system much more disordered and, consequently, less tractable.

7.2
Small-World Rouse Networks

In very dilute solutions, long flexible macromolecules hardly see each other. It is then reasonable, at least as a first step, to consider each chain separately. Now, given the flexibility of the chain and the stochastic features involved, monomers that are distant from one another along the chain's backbone may get to be close to each other in space. Such monomer pairs can be then chemically cross-linked by means of, say, irradiation. The polymer structure obtained by cross-linking in this fashion represents a realization of a so-called "small-world network" (SWN) [129–135].

In general, SWN are built starting from an underlying, fully-ordered lattice (say one-dimensional), in which one inserts (with probability q) additional bonds between randomly-chosen points. In this way the SWN are intermediate between regular lattices and random graphs: on the one hand, a SWN has well-defined local connections, provided by the underlying regular lattice. On the other hand, the small amount of additional bonds strongly reduces the minimal distances between lattice points [129, 130]. One intriguing property of SWN built from a linear chain (ring) consists of the appearance of a so-called "pseudo-gap" in the density of states, $\varrho(\lambda)$, which goes for small λ as [133]:

$$\varrho(\lambda) \sim \sqrt{\frac{1}{\lambda}} \, \exp\left(-\frac{C}{\sqrt{\lambda}}\right), \tag{145}$$

where C is a constant. Equation 145 implies that the probability of finding SWN eigenvalues very close to $\lambda = 0$ is extremely small.

Now, the cross-linked chain discussed above may be viewed as being a SWN. Here the original chain plays the role of the underlying regular lattice, while the random cross-linking of the monomers by irradiation creates the extra bonds. Or, one starts from a SWN and views its sites as being beads and its bonds as being elastic springs, see Fig. 14 as an example. Such GGS are called small-world Rouse networks (SWRN), as introduced by Jespersen et al [136].
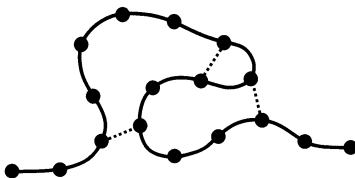
Fig. 14 Example of a SWRN constructed from a Rouse chain by inserting into it additional bonds (shown here as *dashed lines*) between randomly chosen beads

To study how the disorder (additional bonds) introduced into a regular lattice affects its dynamics, several features were investigated [32]. For this a specific realization of a SWRN is constructed starting from a Rouse chain consisting of $N = 1000$ beads connected by elastic springs. Then additional links (AL) – springs with the same elastic constant – are inserted; these connect each bead of the initial Rouse chain to another bead, picked randomly, with probability q/N, see Fig. 14. The eigenvalues of the corresponding connectivity matrix are then computed using direct numerical diagonalization techniques; after accumulating the eigenvalues from a sufficient number of realizations (in [32], 100 are used), one uses them to calculate, among others, the dynamic functions $[G'(\omega)]$ and $[G''(\omega)]$.

In Fig. 15 we display the storage modulus $[G'(\omega)]$ of such a SWRN for different values of q. The case $q = 0$ is the standard Rouse chain, whose $[G'(\omega)]$ (and $[G''(\omega)]$) were amply discussed in Sect. 4. In particular, for $q = 0$ one can distinguish in Fig. 15 three characteristic scaling domains; in them $[G'(\omega)]$ scales (from the low frequency side) as ω^2, $\omega^{1/2}$, and ω^0, respectively. The non-trivial behavior is the intermediate one; for the Rouse chain one finds a $\omega^{1/2}$-law [1–3]. This behavior changes drastically when $q \neq 0$: even a small number of additional bonds inserted into the Rouse chain destroys the scaling in the intermediate range. In Fig. 15 this already takes place for $q = 0.02$. Moreover, with increasing q the intermediate range itself gets smaller; this is due to the fact that the additional bonds increase the stiffness of the system
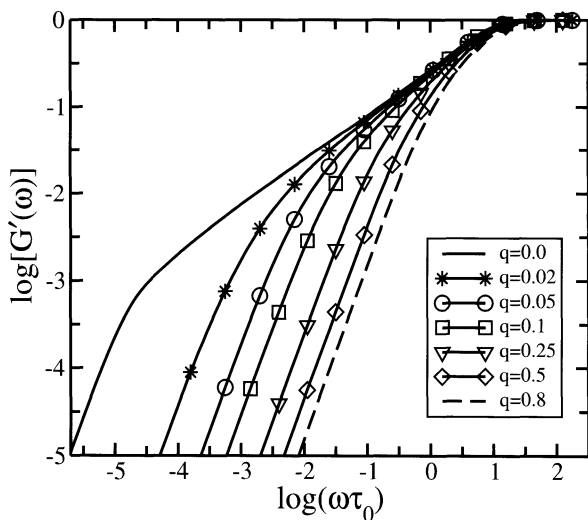
Fig. 15 Reduced storage modulus $[G'(\omega)]$ plotted on double logarithmic scales versus the reduced frequency $\omega\tau_0$ for a SWRN consisting of $N = 1000$ beads. The probability q of having additional links present varies from $q = 0$ (Rouse chain) to $q = 0.8$. All $[G'(\omega)]$-curves were averaged over 100 SWRN realizations

and lead to the disappearance of low-lying modes, the so-called "pseudo-gap" SWRN situation [32]. Hence, by starting from $q = 0$ and increasing q, the $[G'(\omega)]$-curves in the domain of the terminal, ω^2-relaxation shift strongly to the right. This fact can be used, in particular, to experimentally determine changes in the spectrum due to disorder.

As for the loss modulus $[G''(\omega)]$, the effects of disorder on it are similar to those on $[G'(\omega)]$. $[G''(\omega)]$ displays a maximum, whose position is mainly determined by rather high frequency modes, which correspond to the motion of just a few SWRN beads; hence the position of the maximum depends only weakly on q. At intermediate frequencies, as discussed in Sect. 4, the loss modulus of the Rouse chain ($q = 0$) also obeys the scaling behavior $[G''(\omega)] \sim \omega^{1/2}$ on the left side of the maximum, see Eq. 64 [1–3]. Even a slight increase of q quickly destroys the intermediate scaling behavior: scaling is extremely sensitive to the presence of even a few additional bonds, which transform the Rouse chain into a SWRN [32]. Also, the largest deviations of $[G''(\omega)]$ from the Rouse chain case happen on the low-energy side, again reflecting the fact that it is here that most changes of the spectrum occur. Another interesting feature of $[G''(\omega)]$ is the fact that for fixed N its maximum increases with increasing q. The explanation is straightforward: the increase in disorder (number of additional bonds) in SWRN does not lead to an increase in the energy loss, which is related to the area under the $[G''(\omega)]$-curves in linear scales. However, since with increasing q the shape of the $[G''(\omega)]$-curves is strongly squeezed in the low-frequency domain, the maximal value of the loss modulus $[G''(\omega)]$ has to increase with q in order to keep the aforementioned area constant [32]. In summary, the dynamical properties of SWRN show a strong sensitivity to disorder.

Similar conclusions can be drawn from considering the motion of SWRN beads under external forces [136], as given by $\langle\langle Y(t)\rangle\rangle$, see Eq. 50, when the parameter q is varied. For $q = 0$ one finds the usual Rouse behavior at intermediate times $\langle\langle Y(t)\rangle\rangle \sim \sqrt{t/\tau_0}$, see Eq. 69. Again, introducing additional bonds into the Rouse chain changes the situation drastically: increasing q increases the stiffness of the polymer system, and therefore decreases the maximum relaxation time of the SWRN. This shortens the domain of intermediate times and for large q even leads to the appearance of a plateau-type behavior [136].

7.3
Polymer Networks with Random (Nonfractal) Heterogeneities: Localization Effects

Vilgis and Heinrich [137, 138] studied the segmental dynamics of polymer networks with random (nonfractal) heterogeneities based on an earlier treatment by Deam and Edwards [139]. The starting point was a long flexible chain of N segments which is randomly cross-linked instantaneously at M sites,

which creates inhomogeneities (clustering) in the local cross-link density. In this approach the cross-links act as constraints on the motion of the chain; the constraints are taken into account by applying additional (localization) harmonic potentials to the chain [137–139].

Essentially, the model under study is a GGS with additional harmonic potentials; the corresponding Langevin equations of motion are given by Eq. 2, with an external "localizing" force $F_l^{(ext)}$ [137, 138, 140]:

$$F_l^{(ext)}(t) = \frac{b^2 k_B T}{3} \, q_0^2(R) \, R_l(t) , \tag{146}$$

where b is the length of the Kuhn segment and $q_0(R)$ is the so-called localization parameter given by [137, 138, 140]:

$$q_0(R) \equiv q_0 + \delta q_0(R) = \frac{6M(R)}{Nb^2} . \tag{147}$$

The quantity $M(R) = M_0 + \delta M(R)$ is a cross-link distribution. In heterogeneous networks the cross-links are distributed nonuniformly; in other words the cross-link distribution $M(R)$ (as well as the localization parameter $q_0(R)$) is spatially dependent. It is assumed that its spatially dependent term $\delta M(R)$ obeys a simple Gaussian distribution [137, 138]:

$$P\left(\{\delta M(R)\}\right) = N \, \exp\left[-\frac{1}{2\Delta} \int d^3R \, \delta M^2(R) \right] , \tag{148}$$

so that

$$\langle \delta M(R) \rangle = 0 \quad \text{and} \quad \langle \delta M(R)\delta M(R') \rangle = \Delta \, \delta(R - R') , \tag{149}$$

where Δ is a measure of the heterogeneity of the network.

It should be emphasized that the Langevin equations in the form given by Eqs. 2 and 146 are not simple to solve because one needs to average over both the stochastic Brownian forces $f_l(t)$ and the random part of the localization parameter $\delta q_0(R)$ (the crosslink density $\delta M(R)$). Such calculations were performed in [137, 138] with the use of perturbation theory, taking $\delta q_0(R)$ as being a small parameter. As an illustration, here we present the final expression for the mean square displacement of a network bead [137, 138]:

$$\langle (R_l(t) - R_l(0))^2 \rangle \simeq \left[\frac{t/\tau_0}{1 + \sqrt{1 + 4\Delta \, t^2/\zeta} + q_0^2(t/\tau_0)} \right]^{1/2} \tag{150}$$

where, as before, $\tau_0 = \zeta/K$. Using Eq. 150, one obtains different limiting behaviors. First of all, the usual Rouse $\sqrt{t/\tau_0}$-behavior of the mean-square displacement of the chain segment in the absence of cross-links follows readily from Eq. 150 for $\Delta = 0$ and $q_0 = 0$ (compare with Eq. 68). Next, if there is no disorder in the cross-link distribution (if $\Delta = 0$), a network segment still follows the Rouse behavior at relatively short times $t \ll \tau_0 q_0^{-2}$ and becomes localized at longer times, $\langle (R_l(t) - R_l(0))^2 \rangle \sim q_0^{-1}$. This is a known result [141],

also confirmed experimentally [47]. Finally, in a random network the het-erogeneities enhance (on average) the localization. The disorder introduces a new characteristic time scale $\tau_\Delta \sim \sqrt{\zeta/\Delta}$; for $t > \tau_\Delta$ a new (larger) localiza-tion parameter is effective, namely $q_{\text{eff}}^2 = q_0^2 + (\Delta/K)$. Again, localization takes place for $t \to \infty$ [137, 138].

7.4
Polydisperse Polymer Networks: Length Distribution of Network Strands

In this section we focus on an approach originated by Sommer [142] for treat-ing polydisperse polymer networks. Sommer considered moderately cross-linked networks, in which the chains between cross-links are long enough to obey Gaussian statistics but are still shorter than the average entanglement distance. In this case the standard Rouse model can be used for treating the dynamics of the chains. The key assumption is now the separation of time-scales between the motions of the network chains and the motions of the cross-link points [142]. The chains' subsystem turns then into a set of inde-pendently moving chains of various lengths.

Taking the cross-linking process to be stochastic and uncorrelated, one ex-pects the distribution of cross-links to obey a Poisson form. This, in turn, implies an exponential distribution in the length N of the chains [142]. Ex-plicitly, the distribution is

$$P(N) \simeq \frac{1}{N_c} \exp\left[-\frac{N}{N_c}\right], \tag{151}$$

where N_c is the average number of chain beads. Such a length distribution was also obtained in [143] and verified through computer simulations [144].

The relaxation modulus $G(N; t)$ of a single Rouse chain consisting of N beads is given by Eq. 26, and its relaxation times $\tau_k(N) = \tau_0/\lambda_k(N)$ obey Eqs. 55 and 56. In the domain of long times, $G(N; t)$ depends mainly on the longest relaxation time, $\tau_{\text{chain}}(N)$, see Eq. 57, and may be approximated by $G(N; t) \sim (t/\tau_0)^{-1/2} \exp(-t/\tau_{\text{chain}})$ [142]. The total relaxation modulus $G(t)$ of a polydisperse polymer network is the sum over the relaxation moduli $G(t; N)$ of different network chains, taken with their corresponding weights $P(N)$ ac-cording to Eq. 151:

$$G(t) \simeq \int P(N)G(N; t)\, dt. \tag{152}$$

In the domain of long times this integral can be evaluated with the use of the saddle-point method. Finally, one has [142]:

$$G(t) \sim \left(\frac{\tau_{\text{chain}}(N_c)}{t}\right)^{1/3} \exp\left[-C\left(\frac{t}{\tau_{\text{chain}}(N_c)}\right)^{1/3}\right], \tag{153}$$

where C is a constant and $\tau_{chain}(N_c)$ is the longest relaxation time of a Rouse chain of length N_c. As a result, one expects from Eq. 153 the relaxation modulus to display a stretched exponential pattern with a Kohlrausch exponent of 1/3. A rather good agreement between this theoretical expression and the experimental data for natural rubber [145, 146] seems to hold [142]. Evidently, at very long times the modes of the network will also make themselves felt, which may change the overall picture.

7.5
Inhomogeneous Polymer Networks Consisting of Domains of Different Sizes

In this section we consider polymer networks in which the heterogeneities may be visualized as cross-link agglomerations; such agglomerations may appear because of the random arrangements of cross-links. This kind of heterogeneity is well-documented experimentally [125, 126, 147–150]. For instance, dynamic and static light scattering experiments on polyacrylamide hydrogels [150] reveal densely cross-linked regions embedded in surroundings with smaller cross-link densities. Below we discuss a GGS framework for treating polymer networks that have such heterogeneities.

7.5.1
General Approach for Describing Cross-Linked Polymers Consisting of Cross-Link Agglomerations

To address the existence of cross-link agglomerations in polymer networks and gels, the following simple model was proposed [151]. An inhomogeneous cross-linked polymer is treated as an ensemble of regions (domains) with finite sizes, see Fig. 16. Two assumptions here are that (i) the domains are independent (they do not interact with each other), and (ii) the internal topological structures of all the domains are identical. Each domain is taken now to be a GGS, consisting of beads connected by elastic springs in an arbitrary
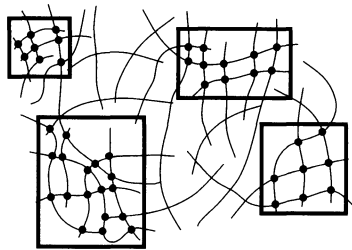
Fig. 16 Sketch of a heterogeneous polymer network consisting of domains (cross-link agglomerations) of different sizes

way (but the same for all of the domains). The detailed structure inside the domains may be a mesh-like network, a fractal network, a dendritic structure, and so on. The only difference between the domains is the numbers N_u of relaxing units inside each domain, the number density of the relaxing units ν_u being the same for all of the domains. Note that N_u is not necessarily the number of beads in the GGS; relaxing units, in general, can contain several GGS-beads like, say, elementary cells of mesh-like networks. Thus, in the present model the disorder associated with the randomness of cross-linking is reduced to a broad size distribution of the domains in the network.

First, we focus on the relaxation inside a single domain of finite size; to get the dynamical behavior of the whole heterogeneous network one needs then to average over all of the domains in the system. The shear dynamic modulus $G^*(\omega)$ (and, correspondingly, the relaxation modulus $G(t)$) of polymer networks and gels often shows a power law behavior (especially at the sol-gel transition), see [101, 102, 152–154] and also Sect. 6. Therefore, we consider here a class of GGS-domains for which the relaxation modulus $G(N_u; t)$ obeys this power law behavior in the region of internal, "intra-domain" relaxation:

$$[G(N_u; t)] \simeq \left(\frac{t}{\tau_u}\right)^{-\gamma}. \tag{154}$$

Here $[G(N_u; t)]$ is the reduced relaxation modulus of a domain (divided by $\nu_u k_B T$, where ν_u is the number density of relaxing units), γ is a positive constant, $\gamma > 0$, and τ_u is the characteristic relaxation time of a relaxing unit, which is assumed to be the same for all of the domains.

As was pointed out in Sect. 3.1, the mechanical relaxation is characterized by the relaxation spectrum $H(\tau)$ which is connected to $[G(N_u; t)]$ through Eq. 27. If $[G(N_u; t)]$ scales as given by Eq. 154, the corresponding relaxation spectrum $H(N_u; \tau)$ also follows a scaling behavior [3, 151, 155]:

$$H(N_u; \tau) \simeq \gamma \left(\frac{\tau}{\tau_{char}}\right)^{-\gamma}. \tag{155}$$

Since the domains are finite, they can be characterized by their maximal relaxation times $\tau_{max}(N_u)$, which depend on the number of relaxing units N_u inside them. It is a straightforward matter to demonstrate, using Eqs. 155 and 29, that as long as the power law behavior of $[G(N_u; t)]$ holds inside the domain ($t < \tau_{max}(N_u)$), the relaxation times can be represented as $\tau(\xi) \simeq \tau_u(N_u/\xi)^{1/\gamma}$, where ξ is a continuous variable ξ, see Sect. 3.1.2 and [151]. Therefore, for $\tau_{max}(N_u)$ one immediately has ($\xi = 1$):

$$\tau_{max}(N_u) \simeq \tau_u N_u^{\alpha} \tag{156}$$

with $\alpha = 1/\gamma$. Note that $\alpha > 0$, since $\tau_{max}(N_u)$ increases as the size of the domains increases. At times exceeding $\tau_{max}(N_u)$ one has an exponential decay of

the relaxation modulus $[G(N_u; t)]$ of a domain of finite size [151]:

$$[G(N_u; t)] \simeq \frac{1}{N_u} \left(\frac{\tau_{max}(N_u)}{t} \right) \exp \left(- \frac{t}{\tau_{max}(N_u)} \right) . \qquad (157)$$

In other words, at $t > \tau_{max}(N_u)$ the relaxation modulus of the domain is mainly governed by the maximal relaxation time $\tau_{max}(N_u)$ which, in turn, is defined by the number of relaxing units inside the domain, see Eq. 156.

Now, to obtain the relaxation modulus of the whole heterogeneous network one has to average over all of the domains, in a similar way to the previous section, see Eq. 152. To proceed, one has to assume a distribution for the domain sizes; we let this distribution $P(N_u)$ have the rather general form [151]:

$$P(N_u) \simeq N_u^{\sigma} \exp \left[- C \left(\frac{N_u}{N_d} \right)^{\delta} \right], \qquad (158)$$

where δ and σ are parameters ($\delta > 0$), N_d is the number of relaxing units in a domain of *average* size, and C is a constant. Performing now the averaging with respect to the distribution function $P(N_u)$ and focusing on long times (therefore, assuming that the main contribution comes from the terminal relaxation of each domain, see Eq. 157), we finally end up with the following asymptotic expression for the relaxation modulus $[G(t)]$ of the heterogeneous network [151]:

$$[G(t)] \simeq \frac{1}{N_d} \left(\frac{t}{\tau_d} \right)^{(\sigma - 3\delta/2)/(\alpha + \delta)} \exp \left[- C' \left(\frac{t}{\tau_d} \right)^{\delta/(\alpha + \delta)} \right], \qquad (159)$$

where C' is a constant and

$$\tau_d \simeq \tau_{max}(N_d) = \tau_u N_d^{\alpha}, \qquad (160)$$

see Eq. 156 for $N_u = N_d$. Thus, Eq. 159 indicates that the $[G(t)]$ of inhomogeneous polymer networks formed by non-interacting domains of different sizes decays at long times, $t \gg \tau_d$, following a stretched exponential pattern whose exponent is $\delta/(\alpha + \delta)$. This exponent ranges between 0 and 1 for all positive values of δ and α. Note that mathematically this nonexponential behavior arises from the averaging with respect to the distribution, Eq. 158; it has the same mathematical origin as Eq. 153 discussed in the previous section for polydisperse polymer networks [142]. Stretched exponential forms were also reported in several studies which dealt with the free-volume theory of glassy relaxation [156], with the electric birefringence in dilute solutions of polyelectrolytes [157], with trapping processes [158, 159], and so on.

A concrete form of the distribution $P(N_u)$, Eq. 158 – in other words values for the parameters δ and σ – may be determined based on physical arguments. For instance, the distribution of chain lengths in polydisperse polymer networks was shown to have a Poisson form [142], see Eq. 151 of the previous section. Therefore, one has in this case $\delta = 1$ in Eq. 158 and also $\alpha = 2$,

since now each domain is just a single Rouse chain, see Eq. 156. This leads immediately to a stretched exponential behavior with index $\delta/(\alpha + \delta) = 1/3$, so that we reproduce Sommer's result [142], Eq. 153. We note that a power-law prefactor N_u^σ in the distribution function $P(N_u)$, Eq. 158, influences only the power-law preexponential term in Eq. 159. Given that the asymptotic behavior of $[G(t)]$ is governed mainly by the stretched exponential term, we skip the power-law terms of Eqs. 158 and 159 in the examples that we provide below.

7.5.2
Mesh-Like Inhomogeneous Polymer Networks

We start by choosing for the domains of Fig. 16 topologically-cubic networks built from Gaussian springs [151, 160], see Sect. 5.1.1. The relaxation spectrum $H(\tau)$ of such domains obeys a $\tau^{3/2}$ behavior, see [24, 30, 62–65] and also Sect. 5.1.1. According to Eq. 156, each such domain containing N_u cross-links has a maximal relaxation time $\tau_{\max} \simeq \tau_0 N_u^{2/3}$; in other words, here we have $\alpha = 2/3$. For $P(N_u)$, see Eq. 158, an analog of the Poisson distribution of Eq. 151, namely $P(N_u) \sim \exp[-(N_u/N_d)]$ is used [151, 160]. We recall that this distribution corresponds to random and uncorrelated cross-linking. Thus, in this case $\delta = 1$, and from Eq. 159 one has for the relaxation modulus $G(t)$ of the 3-D heterogeneous mesh-like network as a whole [151, 160]:

$$[G(t)] \sim \exp\left[-C'\left(\frac{t}{\tau_d}\right)^{3/5}\right]. \tag{161}$$

Besides 3-D heterogeneous networks, it is also interesting to consider their two-dimensional analogs. For this we take as domains the topologically-square networks studied in Sect. 5.1.2. It is then straightforward to demonstrate that the parameter α in Eq. 156 is equal to 1, since $H(\tau)$ follows a $1/\tau$ behavior [65, 68–70, 151]. Furthermore, in order to average over the domains one can use here the same form for $P(N_u)$ as that employed above for the 3-D networks, with $\delta = 1$. As a result, the relaxation modulus $[G(t)]$ of the heterogeneous 2-D network has the following long-time behavior [151]:

$$[G(t)] \sim \exp\left[-C'\left(\frac{t}{\tau_d}\right)^{1/2}\right]. \tag{162}$$

This is another example of a stretched exponential behavior at long times. In principle, one can apply the same calculations to any network built from domains of arbitrary internal architecture, as long as the relaxation spectrum inside the domains obeys a power-law form, see Eq. 155. For instance, the networks may belong to any type of regular lattice topology (bcc, fcc, tetrahedral, triangular, hexagonal) or even be fractal structures.

7.5.3
Inhomogeneously Cross-Linked Polymeric Gels

In this section we apply the above approach to inhomogeneous polymeric gels which display random cross-link agglomerations. In Sect. 6.2 we pointed out that the shear modulus of gels often displays a power law decay and that this behavior can be well reproduced by the ladder model [100]. Therefore, here we employ the ladder model, see Fig. 10, for the internal structure of the domains. We are interested in units of finite size, so that the ladder ends either with a spring or with a Maxwell element (a spring and a dashpot in series) [100]. We use here ladders with Maxwell elements as final elements (pre-gel regime), since in this case the condition that different domains relax independently is easier to justify: this corresponds to cross-link agglomerations (domains) inserted into a more dilute environment.

As was discussed in Sect. 6.2, the complex shear modulus $G^*(\omega)$ of the simplest ladder model follows a $\omega^{1/2}$ behavior [100], so Eq. 156 gives us $\tau_{max} \simeq \tau_{lad} N_u^2$ (so $\alpha = 2$). Note that the same dependence of τ_{max} on the size of a ladder network was also proved numerically [100]. Therefore, using a Poisson-type distribution, $P(N_u) \sim \exp[-(N_u/N_d)]$ and setting $\delta = 1$, one has from Eq. 159 [151]:

$$[G(t)] \sim \exp\left[-C'\left(\frac{t}{\tau_d}\right)^{1/3}\right]. \tag{163}$$

Thus, we again find for inhomogeneously cross-linked gels a stretched exponential decay of the relaxation modulus $G(t)$ on scales larger than the average size of the structural inhomogeneities (cross-link agglomerations). Remarkably, the stretched exponential index here, $1/3$, coincides with that found by Sommer for polydisperse polymer networks [142], see Sect. 7.4. This is an expected result, since a ladder model is equivalent to a linear Rouse chain, see Sect. 6.2.

Furthermore, the above treatment can be easily extended to a more general situation when the internal structure of the domains is given by ladder models for which the shear modulus $G^*(\omega)$ follows a ω^β-behavior with $0 < \beta < 1$ inside the domains, see Eq. 132 of Sect. 6.2. In this case $\tau_{max} \simeq \tau_{lad} N_u^{1/\beta}$ (so $\alpha = 1/\beta$), and using a Poisson distribution with $\delta = 1$ leads to (see Eq. 159):

$$[G(t)] \sim \exp\left[-C'\left(\frac{t}{\tau_d}\right)^{\beta/(1+\beta)}\right]. \tag{164}$$

Thus, the microscopic (intra-domain) power-law behavior of the relaxation modulus of inhomogeneous gels, $[G(t)] \sim t^{-\beta}$ with $0 < \beta < 1$, is replaced on much larger scales by a stretched exponential decay, Eq. 164. Note that Eq. 163 follows from Eq. 164 for $\beta = 1/2$.

As regards applications, a recent study [161, 162] of the stress relaxation in near-critical gels (where the same long-time relaxation behavior of gels was derived on the basis of quite different considerations) is of particular interest. As a model for polymeric gels, the authors considered a system consisting of N vertices (monomers in the context of gelation) which were randomly connected by means of cN edges (cross-links), where c is the concentration of cross-links. A pre-gel situation was considered ($c < c_{crit}$ where c_{crit} is the critical concentration at the percolation transition). Then a given realization of the system can be decomposed into finite connected components (clusters). The density of eigenvalues for such a system was calculated analytically in the mean-field approximation. It was found [161, 162] that the eigenvalue density shows a Lifshits tail for small eigenvalues, giving rise to a stretched exponential decay for the relaxation modulus at very long times, $\exp[-(t/\tau^*)^{1/3}]$.

8
Dendritic Polymers

8.1
Tree-Like Networks

8.1.1
Tree-Like Gaussian Structures

In this section we focus on the dynamics of tree-like polymer networks [11, 163, 164]; these have no closed loops, which makes them simpler than usual networks with mesh-like topologies, see Sect. 5. There were several early studies of the dynamics of tree-like structures built from elastic Gaussian springs. For instance, Chompff treated small tree-like structures [163] ("branched stars" according to his terminology) using the decoupling procedure, see also [165] and Sect. 5.2.2. Ronca determined the dynamical structure factor for tree-like networks [166]. A comprehensive treatment of tree-like Gaussian networks was performed by Graessley [11], whose work we outline below.

Graessley analyzed the equilibrium and the dynamical properties of polymers based on small, tree-like micronetworks [11, 167, 168]. These Gaussian micronetworks represent perfectly branched, symmetrical GGS, which grow from a central bead, see a particular example in Fig. 17; the micronetworks are finite Cayley trees (dendrimers). The peripheral beads of these micronetworks are assumed to be fixed in space. When calculating the quasi-equilibrium elastic properties, the peripheral beads are taken to move affinely with the macroscopic deformations [167, 168]. The evaluation of the relaxation spectrum $H(\tau)$ and of the relaxation modulus $G(t)$ is done in two steps. First, the spectrum of an ensemble of isolated tree-like micronetworks with
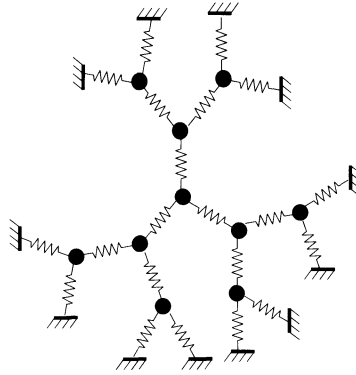
Fig. 17 A tree-like Gaussian micronetwork of third order, $J = 3$, which is built from trifunctional beads, $f = 3$

fixed peripheral beads is computed; then the contribution associated with the relaxation of the beads which are remote from the periphery is determined [11].

A single tree-like Gaussian micronetwork is built, following the GGS procedure, from beads with friction constant ζ which are connected by springs with elasticity constant K, see Fig. 17. All beads have the same functionality f and J denotes the order of the tree; the peripheral beads are attached to immobile points, fixed in space. Graessley determines the relaxation spectrum of these micronetworks by analytical steps, aiming at diagonalizing the corresponding connectivity matrices A, see Eq. 2. The diagonalization is based on the successive partitioning of the determinant of $(A - \lambda I)$ and leads to the following characteristic equation [11]:

$$C_1^{[(f-1)^{J-2}]} \cdot C_2^{[(f-1)^{J-3}]} \cdots C_{J-1}^f \cdot \left[C_J - \frac{1}{(f-1)C_{J-2}} \right] = 0 .\tag{165}$$

Here the $C_m(f, \lambda)$ are defined iteratively as follows:

$$C_1(f, \lambda) = f - \lambda$$

and

$$C_m(f, \lambda) = f - \lambda - \frac{f-1}{C_{m-1}(f, \lambda)} .\tag{166}$$

Hence the $C_m(f, \lambda)$ have the structure of continued fractions. Then, in the limit of large J, the relaxation modulus $G(t)$ of the micronetwork ensemble is given by (we omit here the constant equilibrium modulus G_e) [11]:

$$G(t) = Mk_B T \frac{f(f-2)}{f-1} \sum_{m=1}^{J-2} (f-1)^{J-1-m} \sum_{r=1}^{m} \exp\left[-\frac{2t}{\tau_m(r)} \right],\tag{167}$$

where M is the number of micronetworks per unit volume. In Eq. 167 the relaxation times $\tau_m(r)$ are, as before, related to the eigenvalues through $\tau_m(r) = \tau_0/\lambda_m(r)$, see also Eq. 76, and, as usual, $\tau_0 = \zeta/K$. The eigenvalues $\lambda_m(r)$ of the connectivity matrix A of the tree-like micronetwork are the roots of Eq. 165 and are found to fulfill [11]:

$$\lambda_m(r) = f - 2\sqrt{f-1} \, \cos\frac{\pi r}{m+1}, \quad \text{with} \quad r = 1, \dots, m. \tag{168}$$

Following Graessley, the relaxation modulus of a macroscopic network is associated with contributions to the modulus from beads which are remote from the periphery [11]. Now, the sum over m in $G(t)$, Eq. 167, is related to the beads which are at a distance of m strands from the fixed peripheral beads [11]. Therefore, the contributions from beads remote from the periphery are related to terms in Eq. 168 with m large. Thus, to determine the relaxation times of the macroscopic network, it is enough to consider the limiting contribution, $m \to \infty$; this implies a continuous set of relaxation times [11]:

$$\tau(\xi) \simeq \frac{\tau_0}{f - 2\sqrt{f-1} \, \cos\pi\xi}, \tag{169}$$

where $0 < \xi < 1$, see also Sect. 3.1.2. Now, the relaxation spectrum $H(\tau)$ of the macroscopic network can be calculated with the use of Eq. 29; finally, one finds [11]:

$$H(\tau) \simeq \nu k_B T \frac{1}{2\pi\sqrt{f-1}} \frac{\tau_0/\tau}{\sqrt{1 - \frac{1}{4(f-1)}(f - \tau_0/\tau)^2}}, \tag{170}$$

where ν is the number of beads per unit volume. In turn, the relaxation modulus $G(t)$ reads [11]:

$$G(t) \simeq \nu k_B T \exp[-2ft/\tau_0] \, I_0\big[4\sqrt{f-1} \, t/\tau_0\big], \tag{171}$$

where $I_0[x]$ stands for the modified Bessel function of order zero [11].

Equation 169 implies that the relaxation spectrum ranges from $\tau_{\min} = \tau_0/(f + 2\sqrt{f-1})$ to the maximal relaxation time

$$\tau_{\max} = \frac{\tau_0}{f - 2\sqrt{f-1}}. \tag{172}$$

Note that Eq. 168 correctly reproduces the limiting case $f = 2$ corresponding to the standard Rouse chain, see Eq. 55. On the other hand, Eq. 172 has to be viewed with care for $f = 2$. Furthermore, due to the limit $m \to \infty$, $\tau_{\max}$ does not depend on the network's size (on J). Moreover, the width of the relaxation spectrum is characterized by the ratio $\langle\tau^2\rangle/\langle\tau\rangle^2$, which is found to be equal to $f/(f-2)$ [11]. This means that the spectrum gets narrower with increasing f. Thus, the relaxation spectrum of the tree-like network built from Gaussian

springs is rather narrow and is limited by the longest relaxation time $\tau_{\max}$, Eq. 172, which does not depend on the network's size.

8.1.2
Tree-Like Networks Built from Rouse Chains

A decade later, Graessley's model of tree-like networks was extended by Kloczkowski et al [12, 169], mainly by replacing the bonds between the beads by Rouse chains. In [12, 169] the tree grows from a central chain, see Fig. 18 (not from a central bead, as in Graessley's case). Here, the branching points (junctions) are connected by means of Rouse chains; each chain consists of $(n - 1)$ beads each with friction constant ζ and n elastic springs each with elasticity constant K. Again, the two-step approach of Graessley [11] is used to compute the relaxation spectrum of the network. First, one calculates the spectrum of a tree-like micronetwork with fixed periphery, which is characterized by the functionality f of junctions (branching points) and by the number of tiers J. Then, one determines the part of the spectrum related to the motion of beads far away from the fixed points.

In solving the eigenvalue problem, use is made of the symmetry of the tree-like structure [12, 169, 170]. The system's symmetry reduces the characteristic equation for the eigenvalues of the connectivity matrix A, $\det(A - \lambda I) = 0$, to the product of determinants of submatrices corresponding to subsequent generations (tiers). The characteristic equation which defines the eigenvalues λ is then [12]:

$$A_1^{m_J} \cdot A_2^{m_{J-1}} \cdots A_{J-1}^{m_2} (A_J^2 - 1) = 0 \,. \tag{173}$$

Here $m_l = 2(f - 1)^{l-1}$ with $2 \leq l \leq J$ and

$$A_k = a_k U_{n-1}(1 - \lambda/2) - U_{n-2}(1 - \lambda/2), \quad 1 \leq k \leq J, \tag{174}$$
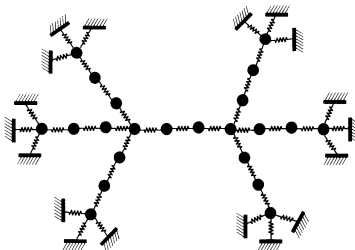
Fig. 18 Sketch of a tetrafunctional ($f = 4$) tree-like micronetwork built from Rouse chains. The network consists of two tiers of chains; each Rouse chain between tetrafunctional branching points has three springs ($n = 3$)

where $U_n(x) = \sin[(n+1)x]/\sin(\arccos x)$ are the Chebyshev polynomials of the second kind [171] and the coefficients a_k satisfy the recurrence relation

$$a_k = f - \lambda - \frac{(f-1)[a_{k-1}U_{n-2}(1-\lambda/2) - U_{n-3}(1-\lambda/2)]}{a_{k-1}U_{n-1}(1-\lambda/2) - U_{n-2}(1-\lambda/2)}, \tag{175}$$

for $2 \le k \le J$, with $a_1 = (f - \lambda)$.

From the characteristic equation, Eq. 173, one obtains the following (rather involved) equations for the eigenvalues λ [12]:

$$U_k\big(F(1-\lambda/2)\big) + \sqrt{f-1}\, U_{n-2}(1-\lambda/2)U_{k-1}\big(F(1-\lambda/2)\big) = 0 \tag{176}$$

for $1 \le k \le (J-1)$ and

$$\left[\frac{U_k\big(F(1-\lambda/2)\big) + \sqrt{f-1}\, U_{n-1}\big(1-\lambda/2\big)U_{k-1}\big(F(1-\lambda/2)\big)}{U_{k-1}\big(F(1-\lambda/2)\big) + \sqrt{f-1}\, U_{n-1}\big(1-\lambda/2\big)U_{k-2}\big(F(1-\lambda/2)\big)}\right]^2 = \frac{1}{f-1} \tag{177}$$

for $k = J$, where the function $F(x)$ is given by:

$$F(x) = \frac{U_n(x) + (f-2)U_{n-1}(x) - (f-1)U_{n-2}(x)}{2\sqrt{f-1}}. \tag{178}$$

By then applying Graessley's procedure, the authors [12] extract the contribution to the spectrum from beads far away from the periphery in the limit when the number of tiers J goes to infinity. They show that a solution of the eigenvalue problem, see Eqs. 176 and 177, can be obtained in the limit $k \to \infty$ from [12]

$$F\left(1 - \frac{\lambda}{2}\right) = \cos\frac{\pi r}{k+1}, \quad \text{with} \quad r = 1, ..., k, \tag{179}$$

where $F(x)$ is given by Eq. 178. This simplified equation is then solved analytically in the cases that $n = 1$ or that $n = 2$. When $n = 1$ (a single spring between the branching points, see the previous section) one recovers Graessley's solution [11], see Eq. 168. For $n > 2$ the eigenvalues λ can be found numerically from Eqs. 179 and Eq. 178. It turns out, however, that the relaxation spectrum $H(\tau)$ (the distribution function of relaxation times τ) can be obtained without the numerical solution of Eq. 179. As discussed above, one can introduce a continuous variable $\xi = r/(k+1)$ ($0 < \xi < 1$), see Eq. 179; $H(\tau)$ is calculated then using Eq. 29 [12], obtaining:

$$H(\tau) = \frac{\nu k_B T \tau_0}{2\pi\tau} \frac{F'(x)}{\sqrt{1 - F^2(x)}}, \tag{180}$$

where $\tau_0 = \zeta/K$, ν is the number of beads per unit volume, $F(x)$ is given by Eq. 178, $F'(x)$ denotes the derivative $(d/dx)F(x)$, and

$$x = 1 - \frac{\lambda}{2} = 1 - \frac{\tau_0}{2\tau}. \tag{181}$$

Now, making use of Eqs. 27 and 180, one has for the relaxation modulus $G(t)$ [12]:

$$G(t) = \nu k_{\mathrm{B}} T \ \exp[-4t/\tau_0] \ \frac{1}{\pi} \int\limits_{-\infty}^{1} dx \ \frac{F'(x)}{\sqrt{1 - F^2(x)}} \ \exp[4tx/\tau_0] \,. \tag{182}$$

Analysis of Eq. 180 shows that $H(\tau)$ consists of continuous bands of relaxation times; the number of bands increases with n, in other words with the length of the Rouse chains between the branching points [12]. To be noted is that in logarithmic scales in an intermediate regime the bands of $H(\tau)$ show an almost linear behavior with slope $1/2$ as a function of τ; the Rouse chains between branching points seem to be responsible for this behavior. Also, it is shown in [12] that the maximal relaxation time $\tau_{\max}$ of the whole relaxation spectrum is approximately given by

$$\tau_{\max} \simeq \tau_0 \frac{n(nf - f + 2)}{2(f - 2\sqrt{f - 1})} \,. \tag{183}$$

For the special case $n = 1$, Eq. 183 recovers Graessley's result, Eq. 172. For quite long chains, $n \gg 1$, the maximal relaxation time $\tau_{\max}$ goes as $n^2\tau_0$, which leads to a considerable broadening of the relaxation spectrum in the domain of short times, a fact due to the inclusion of the chains between the branching points. Thus, for tree-like networks the relaxation spectrum turns out to be broader than in Graessley's model of the previous section.

However, this change does not affect the long-time regime, determined by the relaxation of the whole network. Indeed, one can easily connect $\tau_{\max}$ with the maximal relaxation time $\tau_{\max}^{\mathrm{CG}}$, Eq. 172, of Graessley's structure, viewed as being a coarse-grained model. Here "CG" stands for "coarse-grained", by which we imply, as in Sect. 5, that the Rouse chains between branching points are replaced by single elastic springs each with elasticity constant $K_{\mathrm{CG}} \simeq K/n$, and that a coarse-grained bead (junction) accumulates the overall friction of half of each chain directly attached to it; in other words that $\zeta_{\mathrm{CG}} \simeq f(n/2)\zeta$; then the characteristic times of both models, τ_0 and τ_{CG}, are related as follows:

$$\tau_{\mathrm{CG}} \simeq \frac{fn^2}{2} \tau_0 \,. \tag{184}$$

Taking Eq. 183 for large n, inserting Eq. 184 into it and recalling Eq. 172 leads to:

$$\tau_{\max} \simeq \tau_0 \frac{n^2 f}{2(f - 2\sqrt{f - 1})} \simeq \tau_{\mathrm{CG}} \frac{1}{f - 2\sqrt{f - 1}} = \tau_{\max}^{\mathrm{CG}} \,. \tag{185}$$

In other words, the maximal relaxation times of both models coincide. As already observed, these times do not depend on the size of the network (on J).

Moreover, in both models the relaxation spectrum is quite narrow. The reason for this behavior is that in both models the peripheral beads are kept fixed; this prevents big network portions from moving with respect to each other and, therefore, eliminates the very low-frequency modes. Furthermore, letting the number of tiers J go to the limit $J \to \infty$ is also questionable; a perfect tree with $f > 2$ cannot grow indefinitely in 3-D because the number of monomers increases exponentially with J.

8.2
Trifunctional Dendrimers

Recently, interest in polymers with perfect tree-like topologies was enhanced by developments in the synthesis of regular branched structures (dendrimers). Dendrimers are macromolecules that have regularly branched architectures [172–175]. They display a series of unique properties, which are well characterized by their generation number g; their applications are broad and range from serving as building blocks for constructing complex polymer materials with new architectures to their use as novel non-viral vectors for drug and gene delivery.

Several works have been devoted to the theoretical studies of the equilibrium and dynamic properties of dendrimers [13, 33, 176–184]. These studies were complemented by computer simulations [185–191]. In most studies trifunctional dendrimers were considered (the functionality of the branching points was taken to be three, $f = 3$). The reason for this is two-fold. First, $f = 3$ holds for polyamidoamine [172] and polyether [173] dendrimers, which were extensively studied experimentally. Second, the number of monomers in a dendrimer increases exponentially with the generation number g, and, for a given g the increase depends on f. Therefore, larger f mean much larger dendritic systems at the same g. This leads to larger connectivity matrices within the GGS (Rouse-Zimm) formalism and to more densely packed structures when Monte Carlo or molecular dynamics simulations are used.

Now, in a GGS approach one has to determine the eigenvalues of the connectivity matrix A of the dendrimer. Most work centered then on the direct diagonalization of A with the use of analytical [179] or numerical methods [13, 33, 180]. In this respect, the theoretical study of Cai and Chen [179] is of particular interest. They considered the GGS dynamics of trifunctional dendrimers built from beads (each having a friction constant ζ) and springs (each having an elasticity constant K). The model is certainly appropriate when viewing it as arising from a dendrimer structure consisting of flexible, long spacers. We note that many dendrimers with several spacers between the branching points were synthesized. On the other hand, the GGS approach is an approximation when the inter-bead bonds are stiff or when, due to density, other interactions may enter the picture.

In general, it has to be emphasized that many interactions may become important for the dynamics of dendrimers, depending on their geometrical features and on the dendrimers' concentration in solution. For instance, excluded volume interactions play a fundamental role when the dendritic structure is densely packed, as is the case for covalently-bound dendritic (Cayley) trees without spacers. For such molecules one cannot even define a θ-temperature at which the dendrimer would behave in a quasi-ideal (Gaussian) fashion. The reason is that to compensate the three-body repulsions which increase with increasing density (with increasing g), one has to decrease the supposed θ-temperature in order to render the two-body attractions stronger [182, 191–193]. This compensation, however, cannot be achieved fully. On the other hand, the hydrodynamic interactions turn out to be important for dilute solutions of dendrimers; in contrast to linear chains, however, the pre-averaging techniques have to be used with care [194]. For instance, important features of dendrimer solutions such as the non-monotonic dependence of the zero-shear rate viscosity of dendrimers on the generation number can be only observed when the hydrodynamic interactions are explicitly taken into account [190]. With increasing concentration the hydrodynamic interactions are getting screened and the GGS approximation seems to be acceptable as long as the dendrimer density (the number of generations) does not get quite high. We note that since the strands between the branching points of dendrimers are as a rule rather short, entanglement effects in dendrimers can in general be neglected [195].

Cai and Chen attacked the problem through a direct analytical diagonalization of the connectivity matrix of trifunctional dendrimers and gave a very clear physical interpretation for the normal modes and relaxation times encountered [179]. In particular, they found that the normal modes can be categorized into two general groups: (i) normal modes involving bead motions with a mobile central monomer (which is also called core) and (ii) normal modes involving motions with an immobile core [179]. In the linear viscoelasticity framework of our review, any displacement of the dendrimer beads can be formulated as a linear combination of these normal modes. A trifunctional dendrimer of generation g consists of

$$N_{\text{tot}} = 3(2^g - 1) + 1 \tag{186}$$

beads. Note that g differs here from J, the order of a tree in Graessley's model, see Sect. 8.1.1; one has $g = (J - 1)$. As before, the displacement of the dendrimer as a whole is determined by the vanishing eigenvalue $\lambda = 0$. For the other $(N_{\text{tot}} - 1)$ non-vanishing eigenvalues Cai and Chen find implicit analytical expressions, based on the underlying dendrimer symmetry [179]. Compared to the work reported in the last two sections, these equations are more transparent, since they involve trigonometric and hyperbolic functions only.

It turns out that exactly g nonvanishing eigenvalues of the first group (modes involving a mobile core) exist, which can be found by solving the following equation [179]:

$$2\left[\sin(g+2)\chi - \sqrt{2}\,\sin(g+1)\chi\right] = \sin g\chi - \sqrt{2}\sin(g-1)\chi\,, \tag{187}$$

where χ is given by

$$\chi = \arccos\left[(3-\lambda)/2\sqrt{2}\right]\,, \tag{188}$$

with $0 < \chi < \pi$. All g eigenvalues of this group lie in the range $(3 - 2\sqrt{2},\ 3 + 2\sqrt{2})$. Since significant contributions to several various dynamical quantities come from the smallest eigenvalues, these eigenvalues are of particular interest and importance. For large dendrimers, $g \gg 1$, the smallest eigenvalue $\lambda_{\min}^{(1)}$ involving the motion of the core is approximately [179]:

$$\lambda_{\min}^{(1)} \simeq 3 - 2\sqrt{2}\cos(\pi/g)\,, \tag{189}$$

very close to $(3 - 2\sqrt{2})$ for large g.

The second group of normal modes (for an immobile core) involves beads belonging to two subbranches which stem from a common root (branching point). The motions may involve displacements of rather large parts of the molecule with respect to each other; such parts may be either the main branches themselves or smaller subbranches. All in all, there are g subgroups within this group, in which the central bead (core) stays immobile. A specific feature of this group of normal modes is their degeneracy. In the case when the main branches move as a whole with respect to each other, the degeneracy equals 2; it increases when larger and larger parts of the dendrimer stay immobile. The smallest eigenvalue $\lambda_{\min}^{(2)}$ of this group of normal modes fulfills the relation [179]:

$$\sinh(g+1)\chi = \sqrt{2}\,\sinh g\chi\,, \tag{190}$$

with

$$\chi = \ln\left[\frac{1}{2\sqrt{2}}\left(3 - \lambda + \sqrt{1 - 6\lambda + \lambda^2}\right)\right]\,, \quad \chi > 0\,. \tag{191}$$

For large g one has approximately [179]:

$$\lambda_{\min}^{(2)} \simeq 2^{-(g+1)}\,. \tag{192}$$

One may note this important result; for a freely floating dendrimer the smallest eigenvalue depends exponentially on the generation number (on the dendrimer's size).

Using Eqs. 189 and 192, one can now compare the corresponding maximal relaxation times $\tau_{\max} = \tau_0/\lambda_{\min}$, where $\tau_0 = \zeta/K$, stemming from the two

different groups of eigenmodes. One has:

$$\tau_{max}^{(1)} \simeq \frac{\tau_0}{3 - 2\sqrt{2}} \tag{193}$$

and

$$\tau_{max}^{(2)} \simeq \tau_0 \, 2^{(g+1)} \,. \tag{194}$$

Note that the maximal relaxation time $\tau_{max}^{(1)}$ of the first group, Eq. 193, does not depend on the dendrimer's size and coincides with the maximal relaxation time of Graessley's coarse-grained tree-like network with a fixed periphery, see Eq. 172. In contrast, the maximal relaxation time of the second group, $\tau_{max}^{(2)}$, increases exponentially with the number of generations. It often represents the longest relaxation time of the dendrimer as a whole, because, for large g, it significantly exceeds $\tau_{max}^{(1)}$. As a side remark, we note that the underlying physical reason for the extremely narrow relaxation spectrum of a tree-like network with fixed peripheral beads is due to the fact that its immobile periphery prevents the motion of whole (sub)branches relative to each other and the related appearance of the corresponding size-dependent eigenmodes. From Eq. 186 it is evident that the longest relaxation time is proportional to the total number of beads, N_{tot}, of the dendrimer, so $\tau_{max}^{(2)} \simeq \tau_0 N_{tot}$. Therefore, the longest relaxation time of a dendrimer is smaller than that of a linear chain (τ_{chain}) of the same molecular weight (see Eq. 57), but much larger than that of a chain consisting of g beads [179].

The dynamic properties of trifunctional dendrimers were studied in [13, 33] by numerically diagonalizing the connectivity matrices of dendrimers with g ranging from $g = 3$ to $g = 9$. Excellent agreement was found between the eigenvalues determined in this way and those obtained using the analytical procedure of Cai and Chen [179]. The eigenvalues were then used to calculate the displacements of monomers under external forces and also the dynamic shear modulus, see Sect. 3. Remarkably, no power-law behavior (no scaling) was found in the domain of intermediate frequencies (times) [13, 33]. This is in contrast to the behavior of linear polymer chains, of topologically-regular and of mesh-like and fractal networks. Instead, for dendrimers one sees a nearly logarithmic behavior in the double logarithmic plots of $G'(\omega)$, $G''(\omega)$, and $\langle\langle Y(t)\rangle\rangle$. This fact appears as the signature of the exponential growth of the dendrimer [13, 33]. In particular, the storage modulus $[G'(\omega)]$ at intermediate frequencies can be well described through $[G'(\omega)] \sim (1 + \ln(\omega\tau_0))$, which is clearly different from the $(\omega\tau_0)^{1/2}$-behavior typical of Rouse chains.

8.3
Generalized Dendrimers

Apart from the trifunctional dendrimers considered above, more general structures are possible. The functionality of the inner branching points, the functionality of the core (central monomer), and the number of spacers may vary [74, 180, 184, 196]. We consider first the basic dendrimer topology (a single spring between branching points), and introduce a generalized dendrimer (GD), characterized by the functionality of the core, f_c, by the functionality of the other inner branching points, f, and by the number of generations, g, see an example in Fig. 19 [74]. Such a GD represents a wide class of dendritic structures, which include among others the "classical" dendrimers ($f_c = f$) and the dendritic wedges [78] ($f_c = (f - 1)$). Furthermore, star polymers are GD with $f = 2$ and f_c arbitrary, the latter being just the number of arms of the star.

We recall that for large GGS (and for dendrimers in particular) the numerical diagonalization methods are extremely time-consuming; today's reasonable limit (in terms of computer time and accuracy) is $N_{tot} \simeq 10^4$, given that all of the eigenvalues are needed. Also, the direct analytical diagonalization of the connectivity matrix of the GD (in line with the methods discussed in the previous section) is rather cumbersome. Fortunately, it turns out that it is possible to get all of the GD eigenvalues and eigenfunctions in a more analytically-minded way, without going into a detailed analytical matrix diagonalization [74]. The idea, as in the case of topologically-regular mesh-like networks, see Sect. 5, is to use a judicious analytical form for the eigenmodes, which then serves as an ansatz to simplify the equations. The method which we display below was first developed for classical dendrimers [196] (for them $f = f_c$, so all the beads have the same functionality), and then applied to
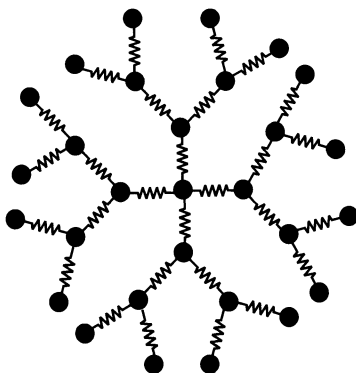
Fig. 19 Example of a generalized dendrimer of third generation, $g = 3$. The functionality of the core, f_c and the functionality of the inner beads, f, differ and equal 4 and 3, respectively

dendritic wedges [78] (a wedge has one main branch less than the classical dendrimer).

In order to solve (as far as possible analytically) the eigenvalue problem, it is important to focus on the underlying topological symmetry of the GD. Taking this symmetry into account at a very early stage significantly simplifies the procedure. The classification of the normal modes, originally proposed by Cai and Chen for trifunctional dendrimers [179], can be naturally extended to GD. The eigenmodes of the GD belong, as before, to two general classes: class (i) involves normal modes in which the core is mobile, class (ii) consists of normal modes with an immobile core. That this assumption is correct is verified *a posteriori*, by counting all of the independent modes determined in this way. We continue by displaying the analytical approach and the main results.

A generalized dendrimer characterized by f_c, f, and g consists of

$$N_d = f_c \frac{(f-1)^g - 1}{f-2} + 1 \tag{195}$$

beads for $f \geq 3$ and of

$$N_d = (f_c g + 1) \tag{196}$$

beads for $f = 2$. When the core is mobile, the motion of the GD may involve all of its beads. The Langevin equations for the inner GD beads, Eq. 2, can be rewritten as [74]:

$$\zeta \frac{dR_{j,m}(t)}{dt} + K\left[fR_{j,m}(t) - R_{j-1,n}(t) - \sum_{l=1}^{f-1} R_{j+1,l}(t) \right] = 0, \tag{197}$$

using the fact that each inner bead is connected to one bead from the previous and to $(f-1)$ beads from the next generation. Here, for simplicity's sake, the stochastic force $f(t)$ was excluded (say, by thermally averaging over the external fluctuations), since at this stage we are interested only in linear relations involving the normal modes, and thus the averaging can be performed at every stage in the calculations. In Eq. 197 $R_{j,m}(t)$ is the position vector of the mth bead of the inner generation j, where $0 < j < g$ and $j = 0$ corresponds to the core.

In order to simplify the picture we assume the following structure for the solutions [74, 78]:

$$R_{j,m}(t) = \sum_k C_k \Pi_k(j, m) \exp[-\lambda_k t / \tau_0], \tag{198}$$

where $\tau_0 = \zeta/K$, the C_k are j-independent constants, and λ_k and $\Pi_k(j, m)$ are the eigenvalues and eigenfunctions, respectively. Equation 198 may be viewed as being a normal mode transformation, such as Eq. 9. To proceed, we use the following observation: the normal modes can be characterized by motions involving one root bead (branching point) and all its descendants of higher

generations. For such a subwedge that has the root as its ancestor, beads that belong to the same generation move in the same manner [74, 78, 196]. Thus, if the GD core moves, (in other words the core is the root), one has

$$\Pi_k(j, m) = \Pi_k(j) \tag{199}$$

for all of the beads of generation j, see also Fig. 3 in [179]. Now, using Eqs. 198 and 199, the Langevin equation, Eq. 197, gets simplified to

$$(-\lambda_k)\Pi_k(j) + \left[f\Pi_k(j) - \Pi_k(j-1) - (f-1)\Pi_k(j+1) \right] = 0 . \tag{200}$$

One immediately obtains $\Pi_k(j) = \text{const}$ as a solution of Eq. 200; its eigenvalue $\lambda_1 = 0$ is related to the displacement of the dendrimer as a whole, under the influence of fluctuating forces. In the same fashion one can also simplify the boundary conditions – the equations of motion for the core, $j = 0$, and for the peripheral beads, $j = g$. In so doing, the eigenvalue problem for the normal modes of class (i) is readily solved. We outline the final results and refer to [74, 78] for the details.

The eigenvalues λ_k and the eigenfunctions $\Pi_k(j)$ corresponding to normal modes with a mobile core (class (i)) read [74]:

$$\lambda_k = f - 2\sqrt{f-1} \, \cos\psi_k \tag{201}$$

and

$$\Pi_k(j) = \left\{ (f-1)\sin\left[(j+1)\psi_k\right] + (f_c - f)\sqrt{f-1} \, \sin\left(j\psi_k\right) \right. \tag{202}$$
$$\left. + (f - f_c - 1)\sin\left[(j-1)\psi_k\right] \right\} (f-1)^{-j/2} ,$$

where the ψ_k are fixed by

$$\sin\left[(g+1)\psi_k\right] = \frac{f - f_c - 1}{\sqrt{f-1}} \, \sin\left(g\psi_k\right) . \tag{203}$$

Interestingly, as long as the inequality $(g+1)/g > |f - f_c - 1|/\sqrt{f-1}$ holds, Eq. 201 gives g distinct solutions.

In contrast, when $(g+1)/g \leq |f - f_c - 1|/\sqrt{f-1}$, only $(g-1)$ modes (spatially periodic) follow from Eqs. 201, 202, and 203. In this case one additional normal mode (essentially spatially exponential) appears. For the new mode two cases must be distinguished: when $(f - f_c - 1) > 0$ the new eigenvalue Λ and its eigenfunction $\Pi(j)$ are given by [74]

$$\Lambda = f - 2\sqrt{f-1} \, \cosh\psi \tag{204}$$

and

$$\Pi(j) = \left\{ (f-1)\sinh\left[(j+1)\psi\right] + (f_c - f)\sqrt{f-1} \, \sinh\left(j\psi\right) \right. \tag{205}$$
$$\left. + (f - f_c - 1)\sinh\left[(j-1)\psi\right] \right\} (f-1)^{-j/2} ,$$

where ψ is the solution of

$$\sinh\left[(g+1)\psi\right] = \frac{f - f_c - 1}{\sqrt{f-1}} \; \sinh\left(g\psi\right). \tag{206}$$

On the other hand, when $(f - f_c - 1) < 0$ the eigenvalue and eigenfunction of the exponential normal mode obey [74]

$$\Lambda = f + 2\sqrt{f-1} \; \cosh\psi \tag{207}$$

and

$$\Pi(j) = (-1)^j \left\{ (f-1)\sinh\left[(j+1)\psi\right] - (f_c - f)\sqrt{f-1}\sinh\left(j\psi\right) \right. \tag{208}$$
$$\left. + (f - f_c - 1)\sinh\left[(j-1)\psi\right] \right\} (f-1)^{-j/2},$$

where ψ is determined from (refer to Eq. 206):

$$\sinh\left[(g+1)\psi\right] = -\frac{f - f_c - 1}{\sqrt{f-1}} \; \sinh\left(g\psi\right). \tag{209}$$

We note that the case $(f - f_c - 1) = 0$ does not lead to the appearance of exponential normal modes, because one always has $(g + 1)/g > 0$ in this case.

Thus, in class (i) (normal modes involving the core) one finds $(g + 1)$ distinct, *nondegenerate* eigenvalues. In general, GD may have *both* spatially periodical and exponential normal modes of class (i). Note that classical dendrimers $(f_c = f)$ [196] and dendritic wedges $(f_c = (f - 1))$ [78] have only periodic normal modes in class (i), because for these two systems the inequality $(g + 1)/g > |f - f_c - 1|/\sqrt{f-1}$ is automatically fulfilled.

It is important to emphasize that the minimal nonvanishing eigenvalue of class (i) is finite and does not depend on the generation number g, so it it is insensitive to the GD size. Indeed, one can demonstrate that for spatially periodical normal modes the eigenvalues are bound from below by $f - 2\sqrt{f-1}$, which is always positive, see Eq. 201. In turn, the eigenvalue Λ of the spatially exponential mode (when it exists) is bound from below by $(f_c + 1) - (f - 1)/(f - f_c - 1)$ for large g, so it is independent of g (note that for $f_c = (f - 1)$ no eigenvalue of exponential type exists). Thus, the values of the eigenvalues in class (i) are not very sensitive to g; this is, however, not the case for the eigenvalues of class (ii).

The normal modes of class (ii) have an immobile core. In the case when only the core is immobile, the degeneracy of the corresponding eigenvalues is $(f_c - 1)$-fold: one can consider those in which the main GD branches move to be eigenmodes. In order to keep the core immobile, only two neighboring main branches have to move against each other. Now focusing on one such branch, one can pick for it exactly $(f_c - 1)$ different partner branches [74, 78, 179, 196].

When the core is immobile, the problem turns (due to the symmetry of the system) into that of separate, mobile subwedges. The Langevin equations of

motion simplify in the same way as before. When only the core is immobile, the eigenvalues λ_k are again defined by Eq. 201, but the eigenfunctions $\Pi_k(j)$ and ψ_k are given [74, 78] by

$$\Pi_k(j) = (f - 1)^{-j/2} \sin \left(j\psi_k \right) \tag{210}$$

and

$$\sin \left[(g + 1)\psi_k \right] = \sqrt{f - 1} \sin \left(g\psi_k \right), \tag{211}$$

where $j = 1, ..., g$. The number of distinct solutions ψ_k again depends on an expression involving the parameters of the GD; Eq. 211 gives g distinct solutions if $(g + 1) > \sqrt{f - 1} \, g$. We note that this inequality can be fulfilled only for $(f = 3; g = 1)$, $(f = 3; g = 2)$, and $(f = 4; g = 1)$. In all other cases, Eq. 211 gives only $(g - 1)$ solutions. Then an exponential normal mode also appears, whose eigenvalue is of the form of Eq. 204, with $\Pi(j)$ and ψ given by [74, 78]:

$$\Pi_k(j) = (f - 1)^{-j/2} \sinh \left(j\psi_k \right) \tag{212}$$

and

$$\sinh \left[(g + 1)\psi \right] = \sqrt{f - 1} \sinh \left(g\psi \right) . \tag{213}$$

In this way one has g different eigenvalues in all cases. Now, taking into account the $(f_c - 1)$-fold degeneracy discussed before, one has a total of $(f_c - 1)g$ class (ii) normal modes, in which next-neighbors to the core move.

In general, larger groups of non-core GD beads can stay immobile. One can use n (with $0 < n < (g - 1)$) to denote the last generation in which all $f_c(f - 1)^{n-1}$ beads are immobile. Evidently, $(f - 1)$ mobile beads are attached to each of the immobile beads. A set of $(f - 1)$ subwedges implies a $(f - 2)$-fold degeneracy, so that the total degeneracy is now $f_c(f - 1)^{n-1}(f - 2)$-fold, with $n \in \{1, ..., g - 2\}$. In the general case the eigenvalues λ_k are still given by Eq. 201, with $\Pi_k(j; n)$ and ψ_k obeying [74, 78]:

$$\Pi_k(j; n) = (f - 1)^{-j/2} \sin \left[(j - n)\psi_k \right] \tag{214}$$

and

$$\sin \left[(g + 1 - n)\psi_k \right] = \sqrt{f - 1} \sin \left[(g - n)\psi_k \right]. \tag{215}$$

Similar to the situation when only the core is immobile, Eq. 215 has $(g - n)$ distinct solutions if $(g - n + 1) > \sqrt{f - 1} \, (g - n)$. If this condition is not fulfilled, one obtains only $(g - n - 1)$ solutions in this way. Then one additional solution exists; it obeys Eq. 204, where now the corresponding eigenfunction $\Pi(j; n)$ and the ψ are given by [74, 78]:

$$\Pi(j; n) = (f - 1)^{-j/2} \sin \left[(j - n)\psi \right] \tag{216}$$

and

$$\sinh \left[(g - n + 1)\psi \right] = \sqrt{f - 1} \sinh \left[(g - n)\psi \right]. \tag{217}$$

Furthermore, in the special situation in which only the peripheral beads move $(n = (g - 1))$ one has the $f_c(f - 1)^{(g-2)}(f - 2)$-fold degenerate eigenvalue $\lambda = 1$.

Thus, in class (ii) one has $(g - n)$ distinct eigenvalues for each $n \in \{1, ..., g - 1\}$; these are $f_c(f - 2)(f - 1)^{n-1}$-fold degenerate. The case $n = 0$ provides g distinct eigenvalues, each $(f_c - 1)$ times degenerate. Taking into account the $(g + 1)$ eigenvalues of class (i) too, one has a total of N_d eigenvalues, N_d being given by Eqs. 195 and 196. In this way, one obtains *all* of the eigenvalues (relaxation times) of the GD, with their correct degeneracy.

The normal modes of two kinds found for GD correspond to two different physical pictures. Spatially periodic normal modes are internal modes inside the GD sub-branches; their eigenvalues are bound from below by a g-independent value, $f - 2\sqrt{f - 1}$, see Eq. 201. In turn, spatially exponential normal modes can be visualized through the motion of whole sub-branches against each other. The corresponding eigenvalues may be very small in value, providing a dominant contribution to the GD dynamics at long times. It was shown [74, 78, 196] that the minimal, non-vanishing eigenvalue of the whole GD, λ_{min}^{GD}, does indeed belong to class (ii), and that for large g it is approximately:

$$\lambda_{min}^{GD} \simeq \frac{(f - 2)^2}{(f - 1)^{(g+1)}} . \tag{218}$$

In other words it decreases exponentially with g. As expected, the minimal GD eigenvalue, λ_{min}^{GD}, corresponds to a mode in which the largest (main) branches of the GD move.

Thus, the approach described above avoids having to perform direct operations on the connectivity matrix and makes it possible to get all of the GD eigenvalues and eigenfunctions. All of these analytical findings were also checked by extensive numerical matrix diagonalizations [74], which establish perfect agreement. Moreover, the general results obtained in this section reproduce the special results obtained previously for the classical dendrimers $(f_c = f)$ [179, 196] and for the dendritic wedges $(f_c = f - 1)$ [78] nicely. For instance, Eq. 218 for $f = 3$ agrees with the approximate expression for the minimal eigenvalue of trifunctional dendrimers, Eq. 192. Also, the approach can be extended to copolymeric dendrimers built from beads with different mobilities [197].

In Fig. 20 we present the storage modulus $[G'(\omega)]$ of GD of fourth generation with trifunctional inner branching beads, while the functionality of the core, f_c, varies from 1 to 10. Noteworthy is the fact that in the intermediate frequency domain the $[G'(\omega)]$-curves do not scale (they do not show a power-law behavior). In this region the $G'(\omega)$-curves reveal the underlying dendritic structure. Increasing the functionality of the core from $f_c = 1$ to $f_c = 10$ influences mainly the low-frequency domain, given that the contribution of the maximal relaxation time of the GD increases with f_c because of increasing
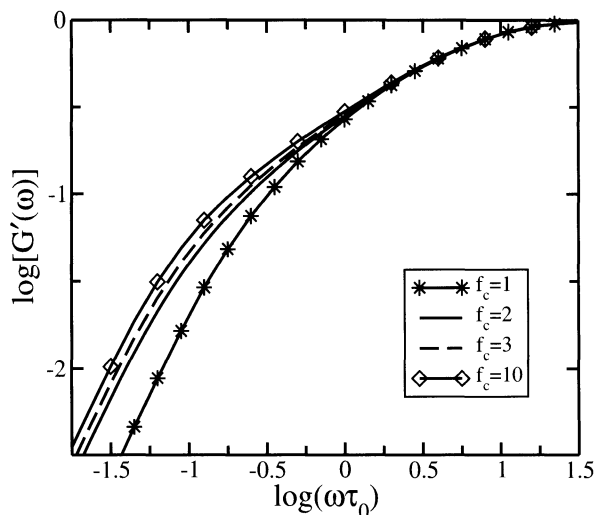
Fig. 20 Reduced storage modulus $[G'(\omega)]$ plotted on double logarithmic scales versus the reduced frequency $\omega\tau_0$ for GD of fourth generation, $g = 4$, with trifunctional inner beads, $f = 3$. The functionality of the core, f_c, is varied from 1 to 10

mode degeneracy. As a result, the $[G'(\omega)]$-curves in Fig. 20 shift to the left when f_c increases [74].

As a final remark, we note that only the basic GD were discussed here. The approach presented here can be further generalized by replacing each interbead bond by Rouse chains with P bonds (spacers). The classification of the normal modes for such dendrimers with $P > 1$ is similar to that for $P = 1$ and was performed by Ganazolli et al [184]. It was demonstrated that in this case the eigenvalues can be grouped as follows. There are $(1 + gP)$ nondegenerate eigenvalues corresponding to the class (*i*) normal modes in the terms of this section. The rest belong to class (*ii*); there are namely gP subgroups of $(f_c - 1)$-degenerate eigenvalues and $(g - 1 - k)P$ subgroups of eigenvalues with degeneracy $f_c(f - 1)^k(f - 2)$, where $k = 0, 1, 2, ..., (g - 2)$ [184]. Note that the eigenvalues of such GD with $P > 1$ were only obtained numerically [184]; the analytical treatment of these dendritic systems may be a subject for further study.

8.4
Side-Chain Dendritic Polymers

As discussed in Sect. 8, the relaxation spectrum of a dendrimer differs considerably from that of a polymer chain. Due to the symmetry of the dendrimer many of its eigenvalues (relaxation times) are degenerate. This contrasts with the relaxation times of the Rouse chain which are all distinct (nondegenerate), see Sect. 4. Therefore, considering hybrid structures formed

Fig. 21 Polymer chain bearing a dendritic wedge in its middle

both by dendrimers and by chains is of particular interest. In this class one finds structures which consist of chains with pendant dendritic groups. These structures, called *side-chain dendritic polymers*, were recently synthesized [198–201].

A GGS model was used to treat side-chain dendritic polymers [78]. The model is given in Fig. 21; it consists of chains bearing dendritic wedges (CBDW) in their middles. A dendritic wedge (DW) differs from a conventional classical dendrimer in that its core has one main branch less: $f_c = (f - 1)$. For such DW the results of the previous section hold [74, 78]. In particular, the maximal relaxation time of a DW is the same as that of a classical dendrimer, because this time corresponds to the motion of two main branches against each other.

We do not expect the problem of determining the eigenvalues of CBDW to have a simple, analytical solution. In [78] the problem was solved numerically. The chains contain N_{chain} beads each; for symmetry's sake N_{chain} is taken to be an odd number, so that the DW divides the chain into two identical halves. Provided that the parameters of the wedge, f (functionality), g (generation number), and $f_c = (f - 1)$, are given, such a wedge consists of N_w beads, as given by Eq. 195.

An interesting question concerns the relationship between the chain length and the DW size. The longest relaxation times of a chain and of a wedge are given by $\tau_{max}^{(ch)} \simeq \tau_0 N_{chain}^2$ and $\tau_{max}^{(w)} \simeq \tau_0 (f - 1)^{g+1}$, respectively, see Eqs. 57 and 218, where $\tau_0 = \zeta/K$ is assumed to be the same both for the chain and for the wedge. In the case of short chains, when $\tau_{max}^{(w)} > \tau_{max}^{(ch)}$, the relaxation of the chain is strongly masked (screened) by the relaxation of the wedge, because of the high density (degeneracy) of the DW modes as compared to the modes of the chain. Thus, in the case of short chains one can expect an almost pure dendrimer-type relaxation.

Much more interesting is the situation when the chains is very long, so that $\tau_{max}^{(ch)} \gg \tau_{max}^{(w)}$; this happens for $N_{ch} \gg (f - 1)^{(g+1)/2}$. In this case, for a fixed chain length, the CBDW storage and loss moduli decrease with increasing g in the intermediate frequency domain, see Fig. 22 for $[G'(\omega)]$. This happens as long as the inequality $\tau_{max}^{(ch)} \gg \tau_{max}^{(w)}$ holds [78].

This theoretical result is in qualitative agreement with rheological data obtained for side-chain dendritic polymers that consist of a polyurethane main chain and of polyether wedges of second, third, and fourth generations [201].
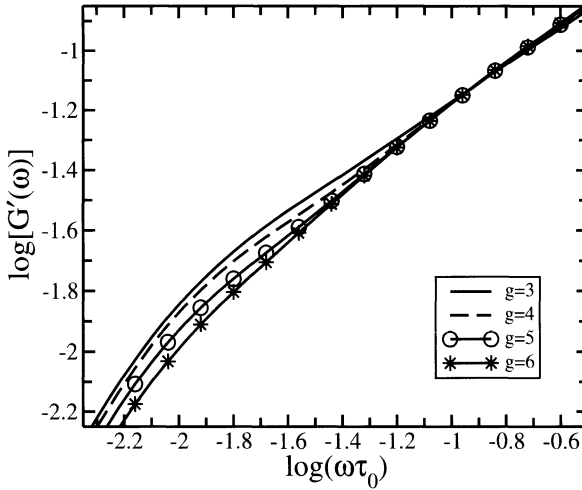
Fig. 22 Reduced storage modulus $[G'(\omega)]$ plotted on double logarithmic scales versus the reduced frequency $\omega\tau_0$ for chains bearing trifunctional dendritic wedges of third, fourth, fifth, and sixth generation. All chains have the same length and consist of 51 beads ($N_{\mathrm{chain}} = 51$) [78]

It has a nice physical interpretation; as pointed out above, at high frequencies (at small length scales) the CBDW dynamics is determined by the DW and the influence of the chain is hidden. On the other hand, in the low-frequency domain the CBDW dynamics is governed mainly by the long chain, since the internal modes of the DW are not activated there. In fact, on such large length scales the wedge behaves as a single "massive" particle having an overall friction constant of $N_w\zeta$. With increasing g the particle gets more damped and hinders the mobility of the central bead of the chain to which it is attached more and more. This, in turn, inhibits the excitation of large-scale, *asymmetric* modes of the chain, leading to a speed-up of the terminal relaxation. Interestingly, this has no effect on the longest relaxation time of the chain, because the corresponding eigenmode is symmetric with respect to the central bead; in fact, this mode is related to the stretching of the Rouse chain at its ends, a motion in which the central bead stays fixed [40].

Furthermore, the fact that a dangling DW suppresses some low lying frequencies of the chain can be detected at $\omega = 0$ by monitoring the zero shear viscosity $[\eta'(0)]$, see Eq. 22 . In general, $[\eta'(0)]$ is proportional to the sum of all finite relaxation times of the system in question. In the GGS framework, the $[\eta'(0)]$ of an isolated DW is found to increase with g. We note that for dendrimers in dilute solutions, plotting the experimentally measured $[\eta'(0)]$ versus g shows a maximum at some critical generation g_c. This feature is not found here; in [190] it was related to the role played by the hydrodynamic interactions. It turns out, however, that CBDW show the opposite trend, namely that $[\eta'(0)]$ decreases with increasing g for CBDW, see Fig. 23. This stems
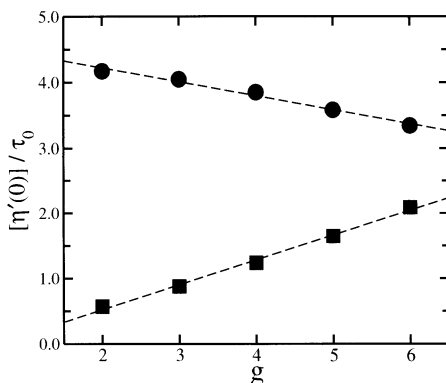
Fig. 23 Reduced zero shear viscosity $[\eta'(0)]/\tau_0$ plotted versus the number of generations, g, for trifunctional dendritic wedges. Shown are results for chains of 51 beads bearing dendritic wedges (*solid circles*) and for the corresponding individual dendritic wedges (*solid squares*)

from the fact that the main contribution to $[\eta'(0)]$ is from the long relaxation times, some of which get suppressed when the size of the pendant DW gets larger. This effect was indeed confirmed by rheological experiments on side-chain dendritic polymers [201], in which g increased from 2 to 4. To conclude, we note that the GGS approach, although being rather simplified, reproduces qualitatively many important dynamical features.

9
Hyperbranched Polymers

As discussed in the previous section, the theoretical study of the dynamics of branched polymers and especially of dendrimers is extremely interesting. Viewed chemically, however, dendrimers are not simple to prepare, since their geometrical perfection requires a whole series of reaction steps, with necessary purification from unwanted by-products [172, 202–204]. For this reason one rather prefers to perform batch reactions, which lead to randomly structured (hyperbranched) macromolecules. Depending on the procedure, good preparation methods may result in products whose polydispersity is limited. The theoretical question which one is then confronted with is to know which of the macromolecular properties are most influenced by disorder and which change less when the reaction products are not as symmetric as perfect dendrimers. With this aim in mind, we will consider randomly-branched polymers, a class of substances that is also important from a theoretical point of view, given that hyperbranched structures are, topologically speaking, trees; in other words they do not have loops. The following sec-

tion is devoted to randomly-branched polymers, whereas after it we will discuss more regularly-shaped hyperbranched structures, namely comblike and regularly-hyperbranched polymers.

It is important to realize that the validity domain of the GGS description is better known for linear chains than for general branched polymers. The reason is similar to that discussed in Sect. 8.2 for the dendrimers: there is no clear (unique) way to define a θ-temperature here, due to the higher local density of monomers around branching points [205]. For instance, for star polymers the θ-temperature depends on the number and the molecular weights of the arms [193, 206, 207]. In dilute solutions the standard (pre-averaged) Zimm approximation fails for stars [208] and hyperbranched polymers [209] and, therefore, the hydrodynamic interactions have to be taken into account explicitly. Also of interest is the fact that, distinct from general fractals (see Sect. 6.3), the introduction of hydrodynamic interactions for fractal hyperbranched structures does not destroy the dynamic scaling properties [210]. For concentrated solutions and for melts of branched polymers entanglement effects seem to come into play at smaller molecular weights than for linear chains; such effects depend on the particular macromolecular architecture and on the size of the dangling chains. To account for entanglements, the tube theory was successfully applied to several branched structures, including stars [211, 212], tree-like (Cayley tree) polymers [213], pom-pom polymers [214, 215], combs and H-polymers [55, 195]. The limitations discussed in this paragraph have to be kept in mind when considering the GGS dynamics of hyperbranched polymers.

9.1
Randomly-Branched Polymers

As stated above, topologically-hyperbranched macromolecules are trees; such structures are devoid of loops. One can then envisage the whole structure as starting from one central monomer, whose effective functionality in the network is f. In the simplest case the monomers attached to it may either have the same functionality (and thus be bound to other monomers) or be at the ends of dangling bonds. In this case (the functionality of each bead is either 1 or f) the (percolating) network is a subset of the (infinite) Cayley tree; clearly the same holds for the dendrimers. More disorder can also be envisaged: this is the case when some monomers in the network have functionalities different from 1 or f. We will consider both cases of disorder in the following.

We start with the simpler case [216], in which the random branched structures are constructed analogously to the dendrimers; we take $f = 3$ as an example. Then one begins with a three-functional starting unit but, distinct from the dendrimers, the branches are added not generation-wise but step-wise. We also keep track of orientation, taking it to point outwards from the origin. At each step a terminal vertex (TV) is chosen randomly and a pair of
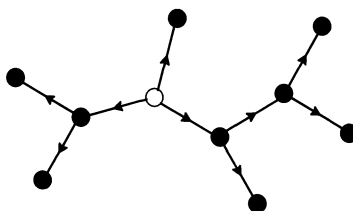
Fig. 24 A randomly branched structure with $N = 10$. The open circle represents the point from which the GGS starts to grow

branches are attached to it (with outward orientation), by which two new TV are created, see Fig. 24. This procedure defines a particular class of branched polymers, for which the functionality of all internal vertices equals $f = 3$, and where N_t, the number of TV, is related to N by $N_t = 1 + N/2$. Evidently, the dendrimers belong to this class. When contrasting ordered with disordered structures, it is reasonable to take their N values to be very close, in order to highlight the effects of topological randomness on the dynamics. The above construction automatically attaches a direction to each bond, a feature which is useful when also taking angular constraints into account.

In [216] the dynamics of such randomly-branched objects were evaluated in the GGS framework, which was extended by also including angular and hydrodynamic interactions. In the calculations 10^5 realizations were used for objects as large as $N = 190$ and for generations up to $g = 6$. We present $[G''(\omega)]$ for such a random hyperbranched structure in Fig. 25. The data are from [216] and we consider two situations, namely one in which the angles between bonds are unrestrained (classical GGS-case) and one in which the angles have a preferential orientation, see [216] for details. Note that in Fig. 25 a shallow minimum for $1 < \omega\tau_0 < 10$ appears, a fact also observed in [180]. Interestingly, in $G'(\omega)$ and $G''(\omega)$ the effect of the disorder is not very strong [216]. This, of course, may be due to the fact that the sixth generation ($g = 6$) is still too small to show large structural variations. Much more pronounced in $G'(\omega)$ and $G''(\omega)$ are the influences of the hydrodynamic interactions and of the angular restrictions. The two effects go in different directions; while the hydrodynamic interactions act to reduce the dynamical range (and thus the width of the intermediate domain), the inclusion of angular restrictions increases the dynamical range (and hence the width of the intermediate domain). Interestingly, the effect goes in the same way for both regular structures and disordered hyperbranched molecules [216].

Moreover, the quantity that turns out to be most affected by disorder is $G(t)$. It shows large deviations from exponentiality and a clear-cut dependence on the geometrical and hydrodynamical aspects [216]. Evidently, it would be worthwhile to go to much larger values of N. Here, however, we reach a dilemma: while the eigenvalues of some regular structures can be obtained iteratively up to very high values of N [104–106], see also Sect. 6,
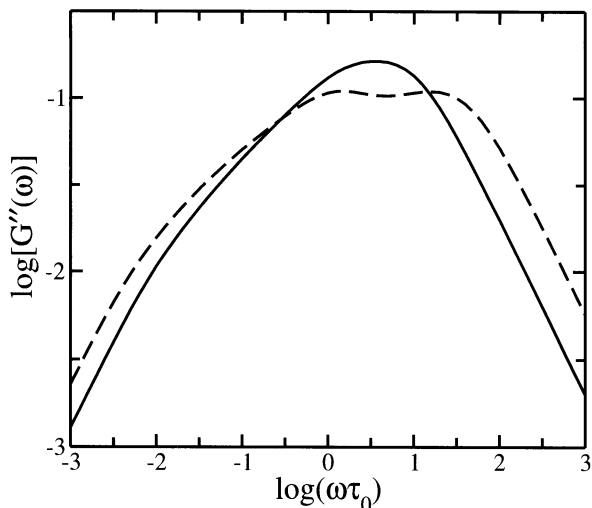
Fig. 25 Reduced loss modulus $[G''(\omega)]$ plotted on double logarithmic scales versus the reduced frequency $\omega\tau_0$ for random branched polymers with $g = 6$ and $N = 190$. Shown are the cases in which the angles between branching points are free (*solid line*) and in which a tetrahedral arrangement of angles is preferred (*dashed line*)

disordered structures do not offer such possibilities in general. In fact, with disordered structures the main problem does not stem from the technical difficulties associated with diagonalizing matrices for structures larger than, say $N = 100$, but from the need to average over many different realizations.

In this way one has consider other analytical methods apt to treating disorder. Here the advantage is that one deals with trees. Now, one may envisage the trees to have been created sequentially, according to a given probabilistic pattern. As we proceed to show, this feature allows us, based on the replica formalism, to develop a systematic way to compute the ensemble-averaged eigenvalue spectrum [217, 218]. In this way one automatically takes into account the averaging over distinct structural realizations. Here we follow the procedure of [219], which, by extending the theoretical study of gel dynamics given in [162], results in an integral equation formalism. Interestingly, as also found before [162], for specific probability distributions of the springs' strengths, the integral expressions take a particularly simple form.

In the model considered in [219], each realization of a randomly branched structure starts from a single monomer, to which one tries to attach a bond that ends in a new monomer with probability p. The attempt to add a bond is repeated f times, so that the number of bonds added to a starting monomer obeys a binomial distribution, and is, at most, f. The next step repeats the procedure of adding a bond $(f - 1)$ times at each of the monomers created in the previous step. Proceeding iteratively one obtains a randomly branched loopless structure [219]. The process of adding bonds ends if no bonds are

added in a given step. This event occurs with probability 1 below the perco-lation threshold $p_c = 1/(f-1)$ [220–222]; however, for $p > p_c$, there is a finite probability that the process never stops, and thus an infinite branched struc-ture is formed.

For each of the structures obtained in this way, one has a Langevin equa-tion, see Eq. 2, from whose eigenvalues the usual dynamic quantities follow. These involve for a certain structure S only the eigenvalues' density $\varrho_S(\lambda)$ of the corresponding Laplace matrix A^S. Now, the ensemble-averaged density of eigenvalues is given by

$$\varrho(\lambda) = \langle \varrho_S(\lambda) \rangle \equiv \sum_S \omega_S \varrho_S(\lambda), \qquad (219)$$

where the sum extends over all structures, each of the $\varrho_S(\lambda)$ is normalized, and ω_S denotes the probability that S is created in the iterative growth pro-cedure. Each S created in this way is connected, so that A^S has only one zero eigenvalue, whose corresponding eigenvector is homogeneous. Therefore, it is convenient to split off the resulting delta peak of $\varrho(\lambda)$ at $\lambda = 0$ with weight ϱ_0 by writing

$$\varrho(\lambda) = \varrho_0 \delta(\lambda) + \varrho_+(\lambda). \qquad (220)$$

From the density of states $\varrho(\lambda)$ one can obtain in a simple way the basic quan-tities, namely the mean bead displacement at time t, the relaxation modulus $G(t)$ and the loss and storage moduli $G'(\omega)$ and $G''(\omega)$. We dispense from dis-playing these expressions which depend on $\varrho(\lambda)$ here, and point to [219] for the details.

The procedure used in [219] to determine $\varrho(\lambda)$ is as follows. The construc-tion of the class of randomly-branched macromolecules considered above is not changed if one places the monomers from which the structures are built on the nodes of an f-functional Cayley tree and fills in the bonds, with probability p, in the order of increasing chemical distance from the starting monomer 0 at the origin. On the other hand, one may draw the bonds in ar-bitrary order, given that their probabilities of showing up are independent. Therefore, the w_S defined in Eq. 219 is the same as the probability of finding that the origin belongs to an S-cluster in the bond-diluted Cayley tree. Due to the symmetry of the Cayley tree, this probability is also independent of the choice of any particular monomer as being the origin.

One then considers, in the diluted Cayley tree picture for a particu-lar monomer j, the diagonal element $R_{jj}(\lambda) = R(\lambda)$ of the resolvent $R(\lambda) = \langle (A^C - \lambda 1)^{-1} \rangle$, averaged over all bond distributions [219]:

$$R(\lambda) = \left\langle (A^C - \lambda 1)^{-1}_{jj} \right\rangle. \qquad (221)$$

A particular realization C of the Cayley tree for a certain placement of bonds is formed by disjoint clusters of beads, a cluster being a set of beads connected

to each other by bonds. Because of this, the A^C corresponding to C can be written in block diagonal form, with block matrices given by the A^S of the corresponding clusters. One has therefore

$$(A^C - \lambda 1)^{-1}_{jj} = (A^S - \lambda 1)^{-1}_{jj}, \tag{222}$$

where S consists only of the monomers belonging to the cluster of j. Furthermore, the probabilities $\omega_{k,S}$ that a certain monomer is at a certain position k of S do not depend on k; one has thus $\omega_{k,S} = \omega_S / |S|$, where $|S|$ denotes the number of monomers inside S. This leads to

$$R(\lambda) = \sum_S \sum_{k=1}^{|S|} \omega_{k,S}(A^S - \lambda 1)^{-1}_{kk} = \sum_S \omega_S \frac{1}{|S|} \sum_{k=1}^{|S|} (A^S - \lambda 1)^{-1}_{kk}. \tag{223}$$

Using the relation

$$\varrho(\lambda) = \lim_{\varepsilon \to 0} \frac{1}{\pi} \operatorname{Im} R(\lambda + i\varepsilon), \tag{224}$$

one has for the normalized density of states of the S cluster,

$$\varrho_S(\lambda) = \lim_{\varepsilon \to 0} \frac{1}{\pi} \frac{1}{|S|} \operatorname{Im} \sum_{k=1}^{|S|} (A^S - (\lambda + i\varepsilon)1)^{-1}_{kk}. \tag{225}$$

In fact, due to the symmetries mentioned, one can even choose for j in Eq. 221 the origin

$$R(\lambda) = \left\langle (A^C - \lambda 1)^{-1}_{00} \right\rangle. \tag{226}$$

Now, the average over the disorder can be performed [219] with the help of the replica method, see [223]. Allowing the strength of each bond to be weighted [162] according to a normalized coupling strength distribution $D(\mu)$

$$F(r_j, r_k) \equiv q + p \int_0^\infty d\mu \, D(\mu) \exp\left[-i\frac{\mu}{2}(r_j - r_k)^2\right], \tag{227}$$

and performing the necessary recursive integrations, one is led [219] to the equations for a tree of generation g, namely to

$$R^{(g)}(\lambda) = -\frac{1}{\lambda} \int_0^\infty dx \, e^{-x} \left\{ \phi^{(g)}(x) \right\}^f \tag{228}$$

and to

$$\phi^{(g)}(x) = q + p \, \widehat{O} \, e^{-x} \left\{ \phi^{(g-1)}(x) \right\}^{f-1}. \tag{229}$$

Here $\widehat{O}$ is the linear operator

$$\widehat{O} = \int_0^\infty d\mu \, D(\mu) \exp\left[-\frac{\lambda}{\mu} x \partial_x^2\right] = \sum_{k=0}^\infty \frac{\langle \mu^{-k}\rangle_\mu}{k!} \left(-\lambda\right)^k \left(x\partial_x^2\right)^k , \tag{230}$$

where $\langle \ldots \rangle_\mu$ denotes the average over the distribution $D(\mu)$. For an infinite Cayley tree the recursion relations take the form of a single integral equation of the function $\phi(x) \equiv \lim_{g\to\infty} \phi^{(g)}(x)$:

$$\phi(x) = q + p\,\widehat{O}\, e^{-x} \{\phi(x)\}^{f-1} , \tag{231}$$

and furthermore

$$R(\lambda) = -\frac{1}{\lambda} \int_0^\infty dx \, e^{-x} \{\phi(x)\}^f . \tag{232}$$

As shown in [219] and paralleling [162], the analytical work simplifies considerably for the following distribution of bond strengths:

$$D(\mu) = \frac{1}{\mu^2} \exp(-1/\mu) , \tag{233}$$

since for it the operator $\widehat{O}$, Eq. 230, takes the form

$$\widehat{O} = \int_0^\infty d\mu \, \frac{1}{\mu^2} \exp(-1/\mu) \exp\left[-\frac{\lambda}{\mu} x \partial_x^2\right] = \left[1 + \lambda x \partial_x^2\right]^{-1} . \tag{234}$$

For instance, applying $1 + \lambda x \partial_x^2 = \widehat{O}^{-1}$ to both sides of Eq. 229, one obtains the ordinary second-order differential equation

$$\phi(x) + \lambda x \partial_x^2 \phi(x) = q + p\, e^{-x} \{\phi(x)\}^{f-1} . \tag{235}$$

For large λ one obtains analytically [219] that $\varrho(\lambda)$ obeys

$$\varrho(\lambda) \simeq f p \lambda^{-2} . \tag{236}$$

Equation 235 has to be solved subject to the boundary conditions

$$\phi(0) = 1 \quad \text{and} \quad \phi(\infty) = q . \tag{237}$$

These equations allow us to determine $\varrho(\lambda)$, as shown in [219]. The correspondence between the theoretically-determined $\varrho(\lambda)$ and the results of numerical diagonalizations turns out to be very good for small and medium-sized GGS. This leads us to expect that the analytic results may be also trusted for even larger GGS, constructed in the manner described above.

We turn now to quantities of special experimental importance, such as $G'(\omega)$ and $G''(\omega)$, which were evaluated using the method already discussed [219], and which turned out to be rather smooth curves. This fact is caused by the vast number of different hyperbranched structures with bonds

of different strengths, which all contribute to $G'(\omega)$ and $G''(\omega)$, and differs from the cases of single dendrimers or of hyperbranched structures with a fixed number of monomers [216]. In these cases one recognizes the signature of the underlying structures in the behavior of $G'(\omega)$ and $G''(\omega)$ at intermediate ω; thus doubly logarithmic plots of $G'(\omega)$ and $G''(\omega)$ in [33] and [13] showed logarithmic-type behavior for the dendrimers, which is related to their exponential growth with g.

9.2
Comblike Polymers

Comblike structures [205] form a special class of regularly-branched polymers. A comblike network is constructed starting from a Rouse chain of N beads called the root chain (or zeroth generation). Other N chains of the same or of different lengths are connected at one of their ends to the root chain. In general, this is the usual form of a regular comb (of first generation). On the other hand, one can also let each chain of this first generation act as a root chain, which leads to the next (second) generation, see a particular example in Fig. 26. The continuation of this procedure was proposed in [224], which leads to a comblike network of generation g, which, letting each chain have N beads, consists of $N_{ch} = 1 + N + N^2 + N^3 + ... + N^g$ chains. Using the underlying symmetry of the system in question, the eigenvalue problem can be recursively reduced to that of a related problem for smaller matrices. The resulting characteristic equation $|A - \lambda I| = 0$ was then analyzed in the limit of short and long relaxation times [224].

The authors [224] found that, in the short time limit, the relaxation times of the comblike structure are very close to the relaxation times of the corresponding number, $N_{ch} = (N^{g+1} - 1)/(N - 1)$, of free linear chains [224]. In the limit of long relaxation times, the complex dynamic modulus of the comblike
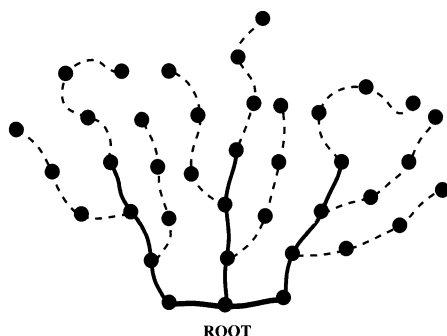
Fig. 26 Comblike structure of second generation growing from a root Rouse chain (generation zero). All chains of the comb consist of three beads, $N = 3$. The chains belonging to the last (second) generation, are represented by dashed lines

network turns out to be well approximated by [224]

$$[G^*(\omega)] \simeq \sum_{k=1}^{g} N^k \frac{i\omega\tau_k}{1 + i\omega\tau_k} , \tag{238}$$

where the sum only goes over the long relaxation times τ_k of each generation, which are given by [224]

$$\tau_k = \tau_0 \frac{(N^{g-k+1} - 1)N}{N - 1} , \tag{239}$$

with $\tau_0 = \zeta/K$ being, as usual, the characteristic time. From Eq. 239 it follows that the longest relaxation time of the comb of generation g is of the order of $\tau_0 N^g$, see Eq. 239 for $k = 1$. Using Eqs. 238 and 239 the storage modulus $[G'(\omega)]$ of the comblike network at low frequencies reduces to [224]:

$$[G'(\omega)] \simeq \frac{N^2}{(N - 1)\ln N} (\omega\tau_0) \tag{240}$$

$$\times \left[\arctan\left(\frac{N - 1}{N} \frac{1}{\omega\tau_0} \right) - \arctan\left(\frac{N - 1}{N^{g+1}} \frac{1}{\omega\tau_0} \right) \right] .$$

Thus, in the low-frequency region, $1/\tau_1 \ll \omega \ll 1/\tau_0$ (where $\tau_1 \sim \tau_0 N^g$, see Eq. 239 for $k = 1$), one has $[G'(\omega)] \sim (\omega\tau_0)$. This differs from the intermediate region, where one finds a Rouse chain behavior, $[G'(\omega)] \sim (\omega\tau_0)^{1/2}$, given that at higher frequencies the network behaves as an ensemble of free Rouse chains [224]. The above comblike structure, which can be thought of as being an example of a polymer network with dangling chains, has a dynamic behavior which qualitatively resembles that of a regular 2-D network built from Rouse chains, see Sect. 5.2.2.

The stretching of comblike networks of the first generation under external forces was studied in [225]. The authors considered a comb-ring (a comblike structure with the root being a closed Rouse chain (ring) of N beads). Based on the direct numerical diagonalization of the connectivity matrix A of the comb-ring, $\langle \delta Y_m(t) \rangle = \langle Y_m(t) \rangle - F_0^{(ext)} t/N_{tot}\zeta$ was calculated; this expression gives the displacement under an external force of the mth bead with respect to the center of mass of the system, see also Sect. 3.3. Here the index m numbers the beads in the chains attached to the backbone ring and ranges from $m = 1$ (the bead belongs the backbone) to $m = N$ (the bead is situated at the free end of one of the chains which form the comb-ring). It was found that the response of comb-rings to external forces depends much on the distance from the backbone to the particular bead on which the external force acts [225].

In the domain of very short times, $\langle \delta Y_m(t) \rangle$ is mainly governed by the functionality f of a particular bead. The stretching $\langle \delta Y_m(t) \rangle$ is minimal for beads which belong to the backbone ring ($f = 3$) and is maximal for beads at the tips of the chains ($f = 1$). The case of inner beads of chains ($f = 2$) is intermediate. In the region of very long times, the stretching $\langle \delta Y_m(t) \rangle$ reflects

the distance between the mth bead and the backbone. The limiting value of $\langle \delta Y_m(t) \rangle$ at $t \to \infty$ is found to be proportional to m (to the the distance from the root ring). At intermediate times the quantity $\langle \delta Y_m(t) \rangle$ displays scaling, in other words $\langle \delta Y_m(t) \rangle \sim t^\alpha$ [225]. Remarkably, the exponent α depends on m (on the position of the bead in the chain). For instance, in the case $N = 50$ one has $\alpha = 0.24$ for $m = 1$ and $\alpha = 0.53$ for $m = 50$, demonstrating again the strong sensitivity of $\langle \delta Y_m(t) \rangle$ on the bead–backbone distance. After averaging $\langle \delta Y_m(t) \rangle$ over all beads, α turns out to be $\alpha = 0.5$, an exponent typical of the standard Rouse chain, see Eq. 69.

9.3
Regular Hyperbranched Polymers

In this subsection we will consider (distinct from the dendrimers of Sect. 8) another class of regular hyperbranched polymers. We recall that the quest for simplicity in the study of complex systems has led to fruitful ideas. In polymers such an idea is scaling, as forcefully pointed out by de Gennes [4]. Now, the price to be paid in going from linear chains to star polymers [33, 194], dendrimers [13, 33, 194, 205] and general hyperbranched structures [216] is that scaling (at least in its classical form) is not expected to hold anymore (at least not in a simple form, which implies power-law dependences on the frequency ω or on the time t). One of the reasons for this is that while several material classes (such as the Rouse chains) are fractal, more general structures do not necessarily behave as fractals.

Interestingly, there exists a family of hyperbranched structures which obey dilation symmetry. These regular hyperbranched polymers (RHP) can be constructed iteratively, by going from generation g to generation $g + 1$ in a deterministic way (very reminiscent of the construction of the dendrimers, Sect. 8, and of the dual Sierpinski gaskets, Sect. 6). The original RHP with coordination number $f = 4$ were introduced by Vicsek [226], and their dynamical properties were later investigated in [227–230]. From this work it became clear that the eigenfunctions of RHP, and especially their eigenvalues, obey rather simple rules; the authors of [227–230] computed the eigenvalues of RHP with $f = 4$, the Vicsek fractals, by determining the roots of iteratively-constructed polynomials numerically.

Theoretically, when searching for scaling [9, 95], it is important to study other RHP in which f varies, as done in [231, 232]. The topology of RHP is displayed in Fig. 27, which shows the $f = 3$ structure schematically in 2-D. One starts from the object of generation $g = 1$, consisting here of $f + 1 = 4$ beads arranged in a star pattern, the central bead having three neighbors. To this object one attaches f identical copies of itself at the next generation, through f bonds, in a star-wise fashion. Hence the next stage object ($g = 2$) consists of 16 beads. The iteration is now obvious; Fig. 27 presents the finite $f = 3$ RHP for $g = 3$. Note that the structure is quite ramified in this way; the regular pattern
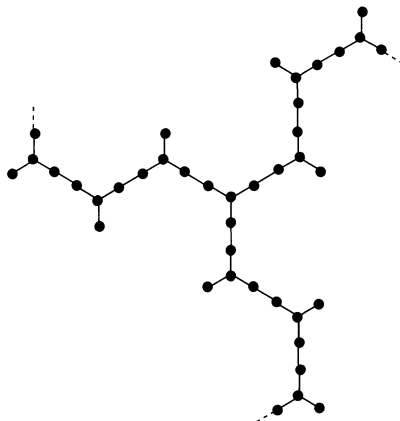
Fig. 27 An example of a regular hyperbranched polymer, RHP

of Fig. 27 has a fractal dimension $\bar{d}_r$ of

$$\bar{d}_r = \frac{\ln(f+1)}{\ln 3}, \tag{241}$$

since increasing the distance from the center (the radius) by a factor of 3 increases the number of beads inside it by $(f+1)$. Note that through Eq. 241, the extreme overcrowding found for dendrimers (where $\bar{d}_r = \infty$) does not appear in RHP.

We first recall some aspects related to the chemical realization of RHP [232, 233]. These include the geometry in terms of composition, structure and steric requirements and also their synthesis. Now, RHP consist of structural entities in which the valence equals 1, 2 and f, entities denoted by M_1, M_2 and M_f, respectively, which may be chosen from a set of different chemical species. One has then a large variety of M_f entities at one's disposal, such as the building blocks of polycarbosilanes [234, 235] or copolyesters [236–238]. For $f = 3$, condensed triarylamines are interesting candidates; they have been synthesized as bridged molecules [239, 240]. Moreover, even the case $f = 6$ can be realized [232, 233] by using triarylamines bound to rather small benzene rings [241].

As shown in [231, 232], the eigenvalues of RHP can be obtained very easily, for arbitrary f and g, through an algebraic iterative procedure, which involves the Cardano-solution for cubic equations [242]. These findings open the way to studying the dynamics of arbitrarily large, finite RHP theoretically.

To describe the determination of the RHP eigenvalues we follow the procedure of [231, 232]. In order to solve $(A - \lambda I)\, \boldsymbol{\Phi} = 0$ one notes [231] that the architecture of a RHP displays f-coordinated centers (fCC), connecting bonds, and also dangling bonds; hence each of its beads has either f, 2 or 1 neighbors. Setting ϕ_0 for the component of the fCC in $(A - \lambda I)\boldsymbol{\Phi} = 0$, typical

equations for its neighboring sites are [231]

$$(f - \lambda) \phi_0 = \sum_{j=1}^{f} \phi_j \,, \tag{242}$$

$$(2 - \lambda) \phi_f = \phi_0 + \phi_m \,, \tag{243}$$

and

$$(1 - \lambda) \phi_1 = \phi_0 \,. \tag{244}$$

One can then transform [231], by simple algebraic means, Eqs. 242 to 244 to a set involving the coordinates of nearest-neighboring fCC, obtaining:

$$(f - P(\lambda)) \tilde{\phi}_0 = \sum_{j=1}^{f} \tilde{\phi}_j \,, \tag{245}$$

$$(2 - P(\lambda)) \tilde{\phi}_f = \tilde{\phi}_0 + \tilde{\phi}_m \,, \tag{246}$$

$$(1 - P(\lambda)) \tilde{\phi}_1 = \tilde{\phi}_0 \,, \tag{247}$$

with

$$P(\lambda) = \lambda(\lambda - 3)(\lambda - f - 1) \,. \tag{248}$$

The procedure is then iterated k times, during which $P(\lambda)$ gets replaced by $p_k(\lambda) = P(p_{k-1}(\lambda))$.

For finite RHP Eq. 248 allows us to determine the eigenvalues at generation $g + 1$ from those at generation g through the relation [231]

$$P\left(\lambda_i^{(g+1)}\right) = \lambda_i^{(g)} \,. \tag{249}$$

Evidently, in this way each previous eigenvalue gives rise to three new ones, a fact already noted [227–230, 243] for the case $f = 4$. Moreover, at every generation one has the non-degenerate mode $\lambda_1 = 0$; furthermore there is one nondegenerate mode corresponding to the eigenvalue $(f + 1)$ and Δ_g new degenerate modes corresponding to the eigenvalue 1, where [231]

$$\Delta_g = (f - 2)(f + 1)^{g+1} + 1 \,, \tag{250}$$

an expression which extends the findings of [227–230] to arbitrary f. One can then show [231] that one has obtained all the eigenvalues in this way.

Furthermore, Eqs. 245, 248 and 249 can be used to compute the $\lambda_i^{(g)}$ iteratively [231], based on the roots of the polynomial

$$x^3 - (f + 4)x^2 + 3(f + 1)x - a = 0 \,. \tag{251}$$

Introducing

$$p = \frac{1}{3}\left[f(f-1)+7\right],\qquad\qquad(252)$$

$$q = \frac{1}{27}(5-f)(f+4)(2f-1),\qquad\qquad(253)$$

and

$$\varrho = |p/3|^{3/2}\qquad\qquad(254)$$

the roots of this polynomial are given by the Cardano-solution, see [242]

$$x_\nu = (f+4)/3 + 2\varrho^{1/3}\cos((\phi+2\pi\nu)/3),\quad\text{with}\quad \nu \in \{1,2,3\},\qquad(255)$$

where

$$\phi = \arccos((a-q)/2\varrho).\qquad\qquad(256)$$

Using this procedure one can determine the eigenvalue spectrum of very large RHP to very high accuracy [231]. Moreover, the spectral dimension also follows from Eq. 251. One has

$$\tilde{d} = \frac{2\ln(f+1)}{\ln(3f+3)}.\qquad\qquad(257)$$

From the so-determined eigenvalue spectrum one can then calculate all of the dynamical quantities discussed in Sect. 3. We exemplify the situation using the storage modulus $G'(\omega)$, given by Eq. 20 and presented in
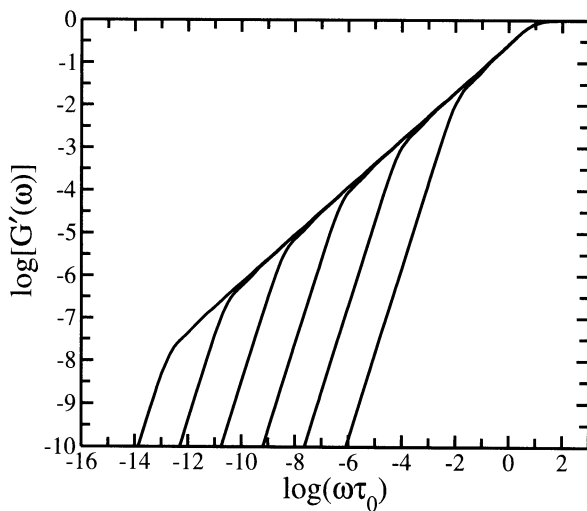
Fig. 28 Reduced storage modulus $[G'(\omega)]$ plotted on double logarithmic scales versus the reduced frequency $\omega\tau_0$ for RHP with $f = 3$. Shown are results for the fractals with $N = 4^3$, $N = 4^5$, $N = 4^7$, $N = 4^9$, $N = 4^{11}$, and $N = 4^{13}$ beads (from *right* to *left*)

Fig. 28. For this calculation finite fractals extending from $N = 4^3$ to $N = 4^{13}$ were used [231]. Clearly evident from Fig. 28 are the limiting, connectivity-independent behaviors at very small and very high ω; for $\omega \ll 1$ one has $G'(\omega) \sim \omega^2$ and for $\omega \gg 1$ one finds $G'(\omega) \sim \omega^0$. Again the fractal connectivity aspect is given by the in-between region; here by going from $N = 4^3$ to $N = 4^{13}$ one finds [231] a change in the minimal slope from 0.621 to 0.557. Comparing the last value to $\tilde{d}/2 \cong 0.55788$, Eq. 257, demonstrates, as for the fractals discussed in Sect. 6, that for the dynamic properties of fractals the fundamental quantity is the spectral dimension.

10
Hybrid Polymer Structures

10.1
Regular Structures Constructed From Small-World Rouse Networks

We end this review with a discussion of complex polymer systems which have two levels of organization. First, we further develop the domain approach formulated in Sect. 7.5 to describe heterogeneous polymer networks. There the cross-link agglomerations (clusters) formed due to random cross-linking were treated independently of each other. However, for sufficiently dense polymer systems the clusters are themselves interconnected; this is reflected, for example, in the non-zero values of the equilibrium moduli of polymer networks and gels [3]. In fact, the networks appear to be disordered on small length scales, but they are rather homogeneous on larger scales.

A simple way to take into account these structural features is to cross-link highly disordered pieces of a network in some regular fashion. To model such a situation, topologically-regular structures built from small-world Rouse networks (SWRN) were considered, see Fig. 29 [31, 73]. The SWRN themselves were discussed in Sect. 7.2 and the general treatment of topologically-regular networks built from arbitrary cells was the subject of Sect. 5.3. Bringing these developments together allows us to "decorate" a regular network (say square or cubic) by replacing its bonds with SWRN subunits. As an example, we consider here square networks composed of such SWRN. In the construction of a SWRN realization one starts from a Rouse chain consisting of n beads. Then one connects each bead in a random way to some other bead by means of additional bonds (springs), with a probability q/n. Finally, the SWRN realization is used as a pattern for the subunits of a 2-D $N \times N$ square network. In this way all of the SWRN subunits in the network are identical and one is fixed in each realization with respect to the pattern and size of the SWRN. This, on the other hand, allows us to use the procedures displayed in Sect. 5.3; one has a 2-D square network built from identical cells, each cell
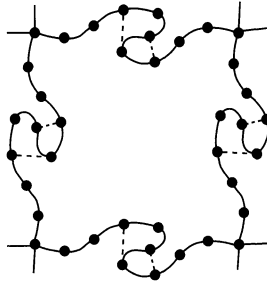
Fig. 29 Two-dimensional regular lattice built from SWRN subunits

consisting of one lattice junction and two SWRN attached to it ($s = (2n + 1)$) beads in total).

In Fig. 30 we show the storage modulus $[G'(\omega)]$ of a network built from SWRN. The case $q = 0$ corresponds to a regular network built from Rouse chains [25, 66, 68, 69], see also Sect. 5.2; for $q = 0$ $[G'(\omega)]$ displays several characteristic frequency ranges. Just next to the domain of very high frequencies one has a frequency region dominated by the internal relaxation of Rouse chains, $[G'(\omega)] \sim (\omega\tau_0)^{1/2}$; this domain is followed by the relaxation of the network, which for a square pattern is characterized by $[G'(\omega)] \sim \omega\tau_0$. Finally, at even lower frequencies, one has the domain of terminal relaxation, with the usual $[G'(\omega)] \sim (\omega\tau_0)^2$ dependence.
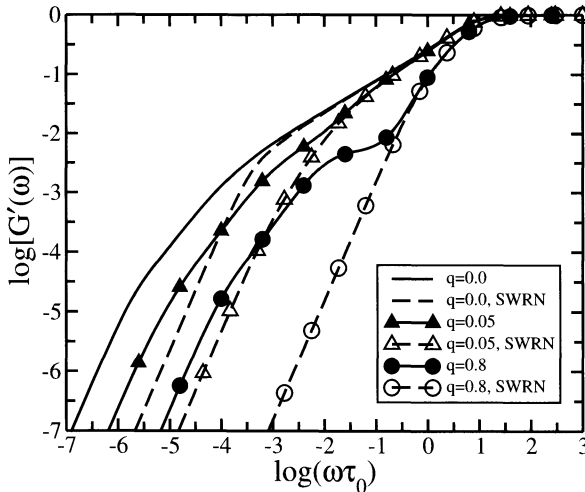
Fig. 30 Reduced storage modulus $[G'(\omega)]$ versus the reduced frequency $\omega\tau_0$ plotted on double logarithmic scales. Shown are results for 20×20 networks of SWRN-subunits ($n = 200$) with $q = 0$ (*solid line*), $q = 0.05$ (*solid line with triangles*), and $q = 0.8$ (*solid line with circles*). To point out the intra-subunit domains of relaxation, also displayed are the results for the corresponding, individual SWRN (*dashed lines*)

Remarkably, even a small number of additional bonds, $q \neq 0$, which transform the Rouse chains to SWRN, drastically change the relaxation behavior, see Fig. 30. With increasing q the domain of the intra-subunit (in other words, the intra-SWRN) relaxation gets smaller, revealing the increase with q of the rigidity of the SWRN subunits; parallel to this finding, for $q \neq 0$ the scaling (power-law) behavior disappears. Interestingly, for large q one observes a plateau-type behavior in $G'(\omega)$, in the region intermediate between intra-subunit and pure network relaxation. Such an unusual behavior is due to the gap in the relaxation spectrum of the network: this gap extends between the maximal relaxation time of a SWRN subunit and the minimal relaxation time of the network of cross-links [31, 73].

Similar dynamic features are displayed by the average displacement of the beads under external forces $\langle\langle Y(t)\rangle\rangle$, see Fig. 31. Again, with increasing q (number of additional bonds) the domain of internal relaxation of the SWRN-subunits becomes narrower. For large g one even observes a plateau-type behavior in the time region lying between the internal SWRN modes and the modes of the underlying network of cross-links. More specifically, after an initial domain of very short times one can see a regime corresponding to the internal relaxation of the SWRN. After this domain ends, the individual SWRN do not yet "feel" the large network structure and they behave like SWRN with immobile ends. The existence of a region leading to a plateau-like behavior is related to the previously-discussed pseudogap in the eigenvalue spectrum of individual SWN [133], see also Sect. 7.2. Now, this pseudogap lies between the minimal non-vanishing SWRN eigenvalue
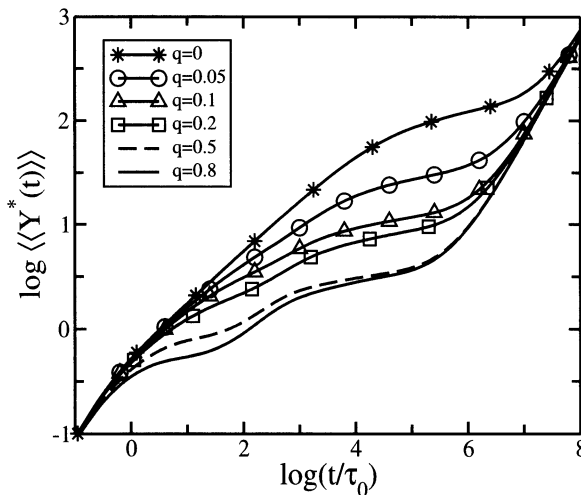
Fig. 31 Reduced average displacement $\langle\langle Y^*(t)\rangle\rangle = \langle\langle Y(t)\rangle\rangle \, \zeta/\tau_0 F_0^{(ext)}$ versus the reduced time (t/τ_0) plotted on double logarithmic scales for 2-D networks built from SWRN-subunits. Here q varies from 0 to 0.8. All curves are averaged over 100 SWN realizations

and the maximal eigenvalue of the underlying network of cross-links: in this regime the dynamics of the network are intermediate between those of SWRN with a free and with a frozen center of mass (given that through embedding the displacement of the center of mass gets hindered), so it tends to a flatter form [73]. Then one has an intermediate regime corresponding to the combined dynamics of the SWRN subunits and of the 2-D network. At longer times a cross-over domain appears, corresponding to the dynamics of the 2-D network, a domain which extends up to the region of the drift of the center of mass, see Fig. 31. In this way specific features of hybrid heterogeneous networks (which combine high local disorder and mesoscopic order) are mirrored by their relaxation forms, such as the shear dynamic modulus and the displacement of monomers under external forces [31, 73].

10.2
Polymer Networks Bearing Dendritic Wedges

In Sect. 8.4 we discussed side-chain dendritic polymers. Recently, even more complex polymer structures have been synthesized, namely polyurethane networks which bear dendritic wedges (DW) of different generations [244]. In these networks the DW are grafted to the middle of each chain of the network; see the sketch in Fig. 32. The existence of branched dangling DW in polymer networks renders these systems very interesting for dynamic studies, since we can achieve direct control over the mobility of the chains in the network by varying the generation number (the size) of the dangling DW [244]. Evidently, increasing the size of the DW leads to a corresponding decrease in the mobility of the elastic network strands to which the DW are attached.

The simplest GGS model for such polymer networks is the so-called "fixed-chain-ends" model: a single chain bearing dendritic wedges (CBDW), whose ends are fixed in space (immobile) [78]. From a physical point of view, it cor-
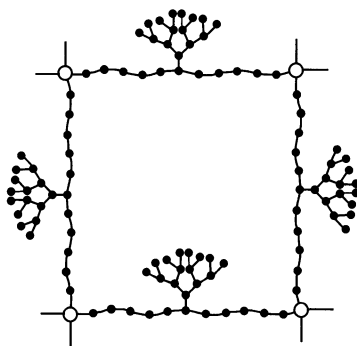
Fig. 32 2-D polymer network built from chains bearing dendritic wedges. Note that in the simplified "fixed-chain-ends" model the cross-linking points (depicted here as open beads) are assumed to be fixed in space, see text for details

responds to a situation in which the cross-links have extremely low mobility. In such a case the scales of motion of the network strands and of the cross-links are well separated [61, 142]. As we will see, even such a simple model captures some of the features of the dynamics of polymer networks bearing DW. As before in Sect. 8.4, we are mostly interested in the situation when the linear chain is long with respect to the length scale of the wedge (when its longest relaxation time exceeds that of the DW).

In Fig. 33 we display $[G'(\omega)]$ for chains with 51 beads, while varying g (the size) of the DW. Comparing the storage modulus $[G'(\omega)]$ for CBDW with free and with fixed ends reveals that at the beginning of the low-frequency domain (at moderately low frequencies) both systems behave in very similar fashions, which indicates that fixing the chain's ends in this ω-range does not affect the dynamics. At lower frequencies, however, the $[G'(\omega)]$ decay becomes slower for cross-linked CBDW than for free CBDW; this even leads for large g to a tendency to form a plateau close to the region where the terminal ω^2-behavior starts, see Fig. 33. Interestingly, the width of the quasi-plateau domain increases with g, so that for larger g the terminal relaxation of the storage modulus shows up at lower frequencies [78]. This flattening of $[G'(\omega)]$ appears in the low-frequency domain where no internal relaxation of the DW takes place; the behavior, hence, can be well reproduced by a simplified model
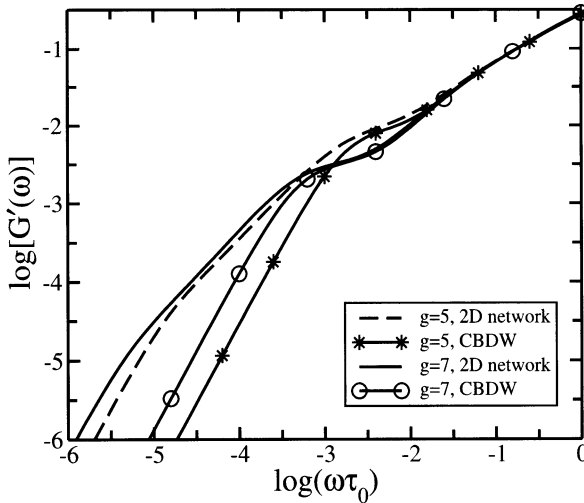
Fig. 33 Reduced storage modulus $[G'(\omega)]$ versus the reduced frequency $\omega\tau_0$ plotted on double logarithmic scales. Shown are results for 2-D networks bearing trifunctional dendritic wedges of fifth (*dashed line*) and seventh (*solid line*) generations. Also displayed are the results obtained from a simplified "fixed-chain-ends" model for the same dendritic wedges, namely $g = 5$ (*line with stars*) and $g = 7$ (*line with circles*). The chains between the cross-links consist of 51 beads each

in which a DW (grafted to a chain with fixed ends) is replaced by a single "big" bead accumulating the friction of the whole wedge, see also Sect. 8.4.

The tendency of the $[G'(\omega)]$-curves to form a plateau, see Fig. 33, implies, in fact, a very slow relaxation process. Given that the motion of the central monomer of the chain with fixed ends is hindered by the "massive" dangling DW, the behavior of the system in the low-frequency domain (where the intra-wedge relaxation is unimportant) is given by the relaxation of the two (almost independent) halves of the original chain. Such a behavior has a maximal relaxation time equal to $\tau_{chain}/4$, where τ_{chain} is given by Eq. 57. A slower relaxation process involves the center of mass of the whole CBDW with free ends (note that $\lambda_1 \neq 0$ because of the fixed ends). Therefore, a DW acting as a single big bead with friction constant $N_w\zeta$ also participates in this motion. This increases the overall friction involved and leads to a corresponding jump in the relaxation times [78]. Thus, one can attribute the flattening in $[G'(\omega)]$ to the difference between the longest relaxation time of the whole CBDW, $\tau_{max}^{(CBDW)}$, and of the corresponding time for a half chain, $\tau_{chain}/4$.

In real polymer networks the mobility of the cross-link points is intermediate between immobile and free, leading to cooperative modes which involve simultaneous, correlated motions of several CBDW. To model this situation one can use the approach based on regular networks built from complex cells, which was discussed in Sect. 5.3. More specifically, a topologically-square network formed from CBDW (see Fig. 32) can model a CBDW network [244]. In the framework of Sect. 5.3 the elementary cell consists of a cross-link point and two CBDW.

It turns out that the relaxation features observed for CBDW with immobile ends (or immobile cross-links) carry over to the regular networks built from CBDW, see Fig. 33. For large g one again sees the tendency of $[G'(\omega)]$ to form a plateau at intermediate frequencies; this behavior is followed at low frequencies by a power-law relaxation due to the underlying network of cross-links. As pointed out above, such a plateau stems from the gap in the spectrum of CBDW with fixed ends. This picture is very different from that encountered in the study of regular networks of Rouse chains, where the relaxation spectrum is continuous and no plateau appears [25, 66, 68, 69], see Sect. 5.2. Thus, the plateau-type behavior of $[G'(\omega)]$ found in polymer networks bearing DW is due to the large dangling DW, which slow down the relaxation at intermediate frequencies. As a final remark, we note that the choice of the regular network is not crucial here, since it affects only the low-frequency behavior. The most interesting and non-trivial domain is situated at higher frequencies and, therefore, is hardly influenced by the type of the network [78].

10.3
Dendrimer-Based Polymer Networks

We end our exposition of "hybrid" polymer systems with two levels of structural organization with dendrimer-based polymer networks. Due to the topological features of dendrimers (a tree-like structure growing from a central core), the number of peripheral monomers increases exponentially with the number of generations. Under certain conditions these monomers may be chemically active; this makes dendrimers very attractive for use as building blocks (dendrimer building blocks, DBB-blocks) in the construction of new types of hybrid polymer materials with well-structured, complex architectures. Recently DBB-based networks have attracted much attention [245–249]. Note that the connections between the DBB in a network can be permanent, leading to chemically cross-linked networks, as well as transient, giving rise to physical networks. We continue now in the GGS framework and discuss the case of permanently cross-linked DBB-based networks [74].

We follow now the description of [74]. The general approach of Sect. 5.3 of treating complex structures (cells) linked into topologically regular networks can be easily extended to the structures discussed here. A DBB based on a generalized dendrimer, characterized by f_c, f, and g, is used as the repeat unit, see Fig. 34. The main variable here is the number of connections, M_{cr}, between neighboring DBB, which can be simply computed as being the total number of connections stemming from each DBB divided by the number of its neighboring DBB.

The minimal value of M_{cr} in networks equals unity, meaning that the network is loosely cross-linked; tighter cross-linked situations, $M_{cr} > 1$, are also possible. Now, the DBB peripheral beads are most prone to serve as connec-
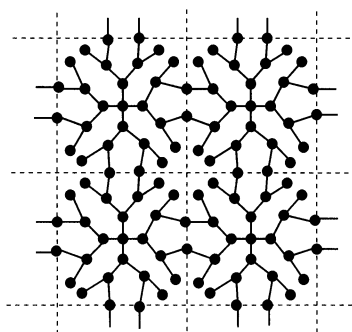
Fig. 34 Portion of a 2-D dendrimer-based polymer network, built from DBB of the third generation, $g = 3$, with trifunctional inner branching points, $f = 3$, and a tetrafunctional core, $f_c = 4$. The number of connections between the neighboring dendritic blocks, M_{cr}, is equal to 2

tions, given that their functionality inside the dendrimer is less than f. It is easy to show that a generalized dendrimer has $N_{per} = f_c(f-1)^{(g-1)}$ peripheral beads. In the case of a simple hypercubic topological structure, each building block has $2d_{lat}$ nearest neighbors, where d_{lat} is the dimensionality. Therefore, by cross-linking DBB in a symmetric way, one can use up to $N_{per}/2d_{lat}$ beads to connect neighboring DBB.

Now, in order to apply the general approach formulated in Sect. 5.3, one needs to specify the matrices $B^{(int)}$ and $B^{(ext)}$, see Eq. 106. Again following [74], we consider the case in which a link between two precursor dendrimers is established by the elimination of one bead, say, through a disproportionation reaction. As a side remark, we note that other cross-linking procedures are also possible, such as through the insertion of additional bonds. Due to the newly-created M_{cr} connections between each pair of neighboring dendritic cells, each cell now has $M_{cr}d_{lat}$ beads less than the precursor dendrimer with N_d beads, N_d being given by Eq. 195. Such a dendritic cell therefore contains $s = (N_d - M_{cr}d_{lat})$ beads, and the matrix $B^{(int)}$ can be built on the basis of the connectivity matrix of the original, precursor dendrimer by the removal of $M_{cr}d_{lat}$ beads. Furthermore, given that there are $2d_{lat}$ nearest neighbors to each dendritic cell, there are $2d_{lat}$ non-vanishing $B^{(ext)}$ matrices; each of them containing M_{cr} non-zero elements equal to (-1), see Sect. 5.3 for details.
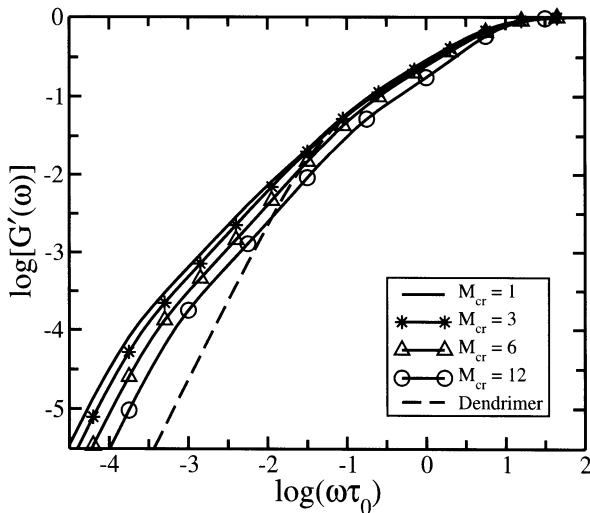
Fig. 35 Reduced storage modulus $[G'(\omega)]$ versus the reduced frequency $\omega\tau_0$ plotted on double logarithmic scales for 2-D (20 × 20) networks based on dendritic blocks with $f_c = 3, f = 3$, and $g = 5$. The number of connections, M_{cr}, (see text) ranges from 1 (loosely cross-linked) to 12 (fully cross-linked dendrimers without dangling bonds). The $[G'(\omega)]$-curve of the corresponding individual dendrimer is also displayed

Applying the method of Sect. 5.3, one can evaluate the viscoelastic behavior of dendrimer-based networks and focus on how far the number of connections between neighboring dendritic blocks, M_{cr}, affects the dynamics. It was found [74] that increasing M_{cr} leads to a systematic narrowing of the region of high frequencies, in which the pure dendrimer-like behavior dominates [74]. For larger M_{cr} the $[G'(\omega)]$-curves depart earlier from the corresponding $[G'(\omega)]$-curve of an individual dendrimer, see the $[G'(\omega)]$-plots for particular network systems presented in Fig. 35. The explanation is straightforward: the long relaxation times of the individual dendrimers are controlled by large amplitude motions, which involve whole dendrimer (sub)branches, see Sect. 8.3 for details. The connections between the dendritic blocks hinder these motions. This effect is found to be generic – it does not depend significantly on the parameters f_c, f, and g of the DBB, nor on the particular type (2-D or 3-D) of underlying regular topological structure into which the DBB are cross-linked [74]. Thus, the finding that connecting DBB into a network (by which the mobility of the peripheral DBB monomers is hindered) leads to a narrowing of their internal relaxation domain is a general fact, which can be used as a signature for cross-linking.

11
Conclusions

In this article we focused on the use of generalized Gaussian structures (GGS) to study the dynamics of complex polymer systems. Of particular interest to us were systems which (because of their underlying symmetry) could be treated to a large extent analytically. These systems included topologically-regular polymer networks, polymer networks built from subunits, fractal polymer networks and gels, dendrimers, hyperbranched polymers, and side-chain dendritic polymers. As systems of special recent interest we also considered hybrid systems, which are characterized by two levels of organization; as examples, we treated polymer networks bearing dendritic wedges and dendrimer-based polymer networks. The GGS-considerations show that iterative and hierarchical structuring procedures are well reflected both energetically (in the eigenvalue spectra) and in the dynamical features (relaxation). Many of the dynamical observables discussed here allow us to determine the structural aspects of polymer materials with complex topologies. Thus, in many cases the GGS-treatment of particular structures may help us to understand their basic dynamic features, and should be considered as a worthwhile first stage before moving on to more realistic (and, therefore, more involved) theoretical models.

References

1. Rouse PE (1953) J Chem Phys 21:1272
2. Doi M, Edwards SF (1986) The theory of polymer dynamics. Clarendon, Oxford
3. Ferry JD (1980) Viscoelastic properties of polymers, 3rd edn. Wiley, New York
4. de Gennes PG (1979) Scaling concepts in polymer physics. Cornell University Press, Ithaca, NY
5. Zimm BH (1956) J Chem Phys 24:269
6. Sommer J-U, Blumen A (1995) J Phys A–Math Gen 28:6669
7. Schiessel H (1998) Phys Rev E 57:5775
8. Friedrich Ch, Schiessel H, Blumen A (1999). In: Siginer DA, DeKee D, Chhabra RP (eds) Advances in the flow and rheology of non-Newtonian fluids. Elsevier, Amsterdam, p 429
9. Schiessel H, Friedrich Ch, Blumen A (2000). In: Hilfer R (ed) Applications of fractional calculus in physics. World Scientific, Singapore, p 331
10. Eichinger BE, Martin JE (1978) J Chem Phys 69:4595
11. Graessley WW (1980) Macromolecules 13:372
12. Kloczkowski A, Mark JE, Frisch HL (1990) Macromolecules 23:3481
13. Biswas P, Kant R, Blumen A (2001) J Chem Phys 114:2430
14. Hansen DR, Shen M (1975) Macromolecules 8:343
15. Hall WF, De Wames RE (1975) Macromolecules 8:349
16. Stockmayer WH, Kennedy JW (1975) Macromolecules 8:351
17. Wang FW, DiMarzio EA (1975) Macromolecules 8:356
18. Wang FW (1975) Macromolecules 8:364
19. Man VF, Schrag JL, Lodge TP (1991) Macromolecules 24:3666
20. Denneman AIM, Jongschaap RJJ (1996) J Rheol 40:589
21. Satmarel C, Gurtovenko AA, Blumen A (2003) Macromolecules 36:486
22. Yamakawa H (1971) Modern theory of polymer solutions. Harper and Row, New York
23. Peterlin A (1967) J Polym Sci Pol Phys 5:179
24. Gotlib YY, Gurtovenko AA (1997) Macromol Theor Simul 6:523
25. Gurtovenko AA, Gotlib YY (2000) Macromolecules 33:6578
26. Tschoegl NW (1989) The phenomenological theory of linear viscoelastic behavior. Springer, Berlin Heidelberg New York
27. Williams G (1972) Chem Rev 72:55
28. Stockmayer WH, Baur ME (1964) J Am Chem Soc 86:3485
29. Stockmayer WH (1967) Pure Appl Chem 15:539
30. Gotlib YY, Gurtovenko AA (1996) Macromol Theory Simul 5:969
31. Gurtovenko AA, Blumen A (2002) Macromolecules 35:3288

32. Blumen A, Gurtovenko AA, Jespersen S (2002) J Non-Cryst Solids 305:71
33. Biswas P, Kant R, Blumen A (2000) Macromol Theor Simul 9:56
34. Perkins TT, Smith DE, Larson RG, Chu S (1995) Science 268:83
35. Wirtz D (1995) Phys Rev Lett 75:2436
36. Quake SR, Babcock H, Chu S (1997) Nature 388:151
37. Amblard F, Maggs AC, Yurke B, Pergellis AN, Leibler S (1996) Phys Rev Lett 77:4470
38. Kargin VA, Slonimskii GL (1948) Dokl Akad Nauk SSSR 62:239
39. Bueche F (1954) J Chem Phys 22:603
40. Gotlib YY, Darinsky AA, Svetlov YE (1986) Physical kinetics of macromolecules. Khimiya, Leningrad
41. Grosberg AY, Khokhlov AR (1994) Statistical physics of macromolecules. AIP, New York
42. Edwards SF, Freed KF (1974) J Chem Phys 61:1189
43. Freed KF, Edwards SF (1974) J Chem Phys 61:3626
44. de Gennes PG (1976) Macromolecules 9:594
45. Ahlrichs P, Everaers R, Dünweg B (2001) Phys Rev E 64:040501(R)
46. Richter D, Binder K, Ewen B, Stühn (1984) J Phys Chem 88:6618
47. Ewen B, Richter D (1997) Adv Polym Sci 134:1
48. Kremer K, Grest GS (1990) J Chem Phys 92:5057
49. Paul W, Smith GD, Yoon DY (1997) Macromolecules 30:7772
50. Mondello M, Grest GS (1997) J Chem Phys 106:9327
51. Harmandaris V, Mavrantzas VG, Theodorou DN (1998) Macromolecules 31:7934
52. Padding JT, Briels WJ (2001) J Chem Phys 114:8685
53. Lyulin AV, Balabaev NK, Michels MAJ (2002) Macromolecules 35:9595
54. Paul W, Smith GD, Yoon DY, Farago B, Rathgeber S, Zirkel A, Willner L, Richter D (1998) Phys Rev Lett 80:2346
55. McLeish TCB (2002) Adv Phys 51:1379
56. Rubinstein M, Colby RH (1988) J Chem Phys 89:5291
57. Paul W, Binder K, Heermann DW, Kremer K (1991) J Chem Phys 95:7726
58. Pütz M, Kremer K, Grest GS (2000) Europhys Lett 49:735
59. Harmandaris VA, Mavrantzas VG, Theodorou DN, Köger M, Ramirez J, Öttinger HC, Vlassopoulos D (2003) Macromolecules 36:1376
60. Gotlib YY, Volkenshtein MV (1953) Dokl Akad Nauk SSSR 89:821
61. Mooney M (1959) J Polym Sci 34:599
62. Gotlib YY (1981) Pure Appl Chem 53:1531
63. Gotlib Y, Golovachev G (1994) J Non-Cryst Solids 172:850
64. Denneman AIM, Jongschaap RJJ, Mellema J (1998) J Eng Math 34:75
65. Denneman AIM, Jongschaap RJJ, Mellema J (1999) J Rheol 43:327
66. Gurtovenko AA, Gotlib YY (1998) Macromolecules 31:5756
67. Ronka G, Allegra G (1975) J Chem Phys 63:4104
68. Gotlib YY, Gurtovenko AA (2000) Macromol Theor Simul 9:407
69. Gurtovenko AA, Gotlib YY (2000) Macromol Theor Simul 9:416
70. Chompff AJ, Duiser JA (1966) J Chem Phys 45:1505
71. Gotlib YY, Salikhov KM (1963) Akust Zh (Acoustic J) 9:301
72. Ham JS (1957) J Chem Phys 26:625
73. Gurtovenko AA, Blumen A (2001) J Chem Phys 115:4924
74. Gurtovenko AA, Markelov DA, Gotlib YY, Blumen A (2003) J Chem Phys 119:7579
75. Kittel C (1986) Introduction to solid state physics, 6th edn. Wiley, New York
76. Ashcroft NW, Mermin ND (1981) Solid state physics. Sanders College, Philadelphia, PA

77. Ziman JM (1972) Principles of the theory of solids, 2nd edn. Cambridge University Press, Cambridge
78. Gurtovenko AA, Gotlib YY, Blumen A (2002) Macromolecules 35:7481
79. Scher H, Lax M (1973) Phys Rev B 7:4491
80. Scher H, Lax M (1973) Phys Rev B 7:4502
81. Scher H, Montroll EW (1975) Phys Rev B 12:2455
82. Shlesinger MF (1984) J Stat Phys 36:639
83. Zumofen G, Blumen A, Klafter J, Shlesinger MF (1989) J Stat Phys 54:1519
84. Schiessel H, Oshanin G, Blumen A (1995) J Chem Phys 103:5070
85. Blumen A (2001) Philos Mag B 81:1021
86. Klafter J, Blumen A, Shlesinger MF (1987) Phys Rev A 35:3081
87. Montroll EW, Weiss GH (1965) J Math Phys 6:167
88. Blumen A, Klafter J, White BS, Zumofen G (1984) Phys Rev Lett 53:1301
89. Schnörer H, Haarer D, Blumen A (1988) Phys Rev B 38:8097
90. Blumen A, Zumofen G, Klafter (1989) Phys Rev A 40:3964
91. Blumen A, Schnörer H (1990) Angew Chem 102:158
92. Blumen A, Schnörer H (1990) Angew Chem Int Edit 29:113
93. Hilfer R (ed) (2000) Applications of fractional calculus in physics. World Scientific, Singapore
94. Metzler R, Klafter J (2000) Phys Rep 339:1
95. Sokolov IM, Klafter J, Blumen A (2002) Physics Today 55:48
96. Blizard RB (1951) J Appl Phys 22:730
97. Schiessel H, Blumen A (1993) J Phys A–Math Gen 26:5057
98. Heymans N, Bauwens J-C (1994) Rheol Acta 33:210
99. Schiessel H, Metzler R, Blumen A, Nonnenmacher TF (1995) J Phys A–Math Gen 28:6567
100. Schiessel H, Blumen A (1995) Macromolecules 28:4013
101. Chambon F, Winter HH (1987) J Rheol 31:683
102. Winter HH, Morganelli P, Chambon F (1988) Macromolecules 21:532
103. Scanlan JC, Winter HH (1991) Macromolecules 24:47
104. Blumen A, Jurjiu A (2002) J Chem Phys 116:2636
105. Cosenza MG, Kapral R (1992) Phys Rev A 46:1850
106. Jurjiu A, Friedrich Ch, Blumen A (2002) Chem Phys 284:221
107. Cates ME (1984) Phys Rev Lett 53:926
108. Cates ME (1985) J Phys (Paris) 46:1059
109. Sommer J-U, Vilgis TA, Heinrich G (1994) J Chem Phys 100:9181
110. Marconi UMB, Petri A (1997) J Phys A–Math Gen 30:1069
111. Vilgis TA, Stapper M (1998) Eur Phys J B 2:69
112. Zilman AG, Granek R (1998) Phys Rev E 58:R2725
113. Licinio P (2001) Physica A 294:51
114. Mandelbrot BB (1982) The fractal geometry of nature. W.H. Freeman and Co., San Francisco, CA
115. Dhar D (1977) J Math Phys 18:577
116. Jurjiu A, Koslowski Th, Blumen A (2003) J Chem Phys 118:2398
117. Blumen A, Jurjiu A, Koslowski Th (2003) Macromol Symp 191:141
118. Brotzman RW, Eichinger BE (1981) Macromolecules 14:1445
119. Neuburger NA, Eichinger BE (1988) Macromolecules 21:3060
120. Zhao Y, Eichinger BE (1992) Macromolecules 25:6988
121. Gottlieb M, Gaylord RJ (1984) Macromolecules 17:2024
122. McKenna GB, Flynn KM, Chen YH (1989) Macromolecules 22:4507

123. Crissman JM, McKenna GB (1992) Polym Mater Sci Eng 67:487
124. McKenna GB, Crissman JM (1993) Polym Mater Sci Eng 68:280
125. Bastide J, Leibler L, Prost J (1990) Macromolecules 23:1821
126. Mendes E, Lindner P, Buzier M, Boué F, Bastide J (1991) Phys Rev Lett 66:1595
127. Martin JE, Eichinger BE (1978) J Chem Phys 69:4588
128. Martin JE, Eichinger BE (1980) Macromolecules 13:626
129. Watts DJ, Strogatz SH (1998) Nature (London) 393:440
130. Watts DJ (1999) Small worlds: The dynamics of networks between order and randomness. Princeton University Press, Princeton, NJ
131. Newman MEJ, Watts DJ (1999) Phys Rev E 60:7332
132. Barthélémy M, Amaral LAN (1999) Phys Rev Lett 82:3180
133. Monasson R (1999) Eur Phys J B 12:555
134. Newman MEJ, Moore C, Watts DJ (2000) Phys Rev Lett 84:3201
135. Jespersen S, Sokolov IM, Blumen A (2000) Phys Rev E 62:4405
136. Jespersen S, Sokolov IM, Blumen A (2000) J Chem Phys 113:7652
137. Vilgis TA, Heinrich G (1994) Phys Rev E 49:2167
138. Vilgis TA, Heinrich G (1994) Macromol Theor Simul 3:271
139. Deam RT, Edwards SF (1976) Philos T Roy Soc A 280:317
140. Vilgis TA (1992) Macromolecules 25:399
141. Vilgis TA, Boué F (1988) J Polym Sci Pol Phys 26:2291
142. Sommer J-U (1991) J Chem Phys 95:1316
143. Glatting G, Winkler RG, Reineker P (1995) Macromolecules 28:5906
144. Schultz M, Sommer J-U (1992) J Chem Phys 96:7102
145. Thirion P, Chasset R (1968) Rev Gen Caout Plast 45:859
146. McKenna GB, Gaylord RJ (1988) Polymer 29:2027
147. Weiss N, van Vliet T, Silberberg A (1981) J Polym Sci Pol Phys 19:1505
148. Wun KL, Prins W (1974) J Polym Sci Pol Phys 12:533
149. Hecht AM, Duplessix R, Geissler E (1985) Macromolecules 18:2167
150. Lindemann B, Schröder UP, Oppermann W (1997) Macromolecules 30:4073
151. Gurtovenko AA, Gotlib YY (2001) J Chem Phys 115:6785
152. Friedrich C, Heymann L (1988) J Rheol 32:235
153. te Nijenhuis K, Winter HH (1989) Macromolecules 22:411
154. Izuka A, Winter HH, Hashimoto T (1992) Macromolecules 25:2422
155. Alfrey T, Doty P (1945) J Appl Phys 16:700
156. Cohen MH, Grest GS (1981) Phys Rev B 24:4091
157. Degiorgio V, Bellini T, Piazza R, Mantegazza F, Goldstein RE (1990) Phys Rev Lett 64:1043
158. Blumen A, Klafter J, Zumofen G (1986) In: Zschokke I (ed) Optical spectroscopy of glasses. Reidel, Dordrecht, p 199
159. Bunde A, Havlin Y, Klafter J, Gräff G, Shehter A (1997) Phys Rev Lett 78:3338
160. Gurtovenko AA, Gotlib YY, Kilian H-G (2000) Macromol Theor Simul 9:388
161. Broderix K, Löwe H, Müller, Zippelius A (2001) Physica A 302:279
162. Broderix K, Aspelmeier T, Hartmann AK, Zippelius A (2001) Phys Rev E 64:021404
163. Chompff AJ (1970) J Chem Phys 53:1577
164. Doi M (1974) Polym J 6:108
165. Chompff AJ (1970) J Chem Phys 53:1566
166. Ronca G (1980) J Chem Phys 72:48
167. Graessley WW (1975) Macromolecules 8:186
168. Graessley WW (1975) Macromolecules 8:865
169. Kloczkowski A (2002) Polymer 43:1503

170. Kloczkowski A, Mark JE, Erman B (1989) Macromolecules 22:1423
171. Abramowitz M, Stegun IE (1964) Handbook of mathematical functions. National Bureau of Standards, Washington DC
172. Tomalia DA, Naylor AM, Goddard WA (1990) Angew Chem Int Edit 29:138
173. Hawker CJ, Fréchet JMJ (1990) J Am Chem Soc 112:7638
174. Fréchet JMJ (1994) Science 263:1710
175. NewKome GR (1996) Advances in dendritic macromolecules. JAI, London
176. de Gennes PG, Hervet H (1983) J Phys (Paris) 44:L351
177. Biswas P, Cherayil BJ (1994) J Chem Phys 100:3201
178. Boris D, Rubinstein M (1996) Macromolecules 29:7251
179. Cai C, Chen ZY (1997) Macromolecules 30:5104
180. La Ferla R (1997) J Chem Phys 106:688
181. Chen ZY, Cai C (1999) Macromolecules 32:5423
182. Ganazzoli F, La Ferla R (2000) J Chem Phys 113:9288
183. Ganazzoli F, La Ferla R, Terragni G (2000) Macromolecules 33:6611
184. Ganazzoli F, La Ferla R, Raffaini G (2001) Macromolecules 34:4222
185. Lescanec RL, Muthukumar M (1990) Macromolecules 23:2280
186. Mansfield ML, Klushin LI (1992) J Phys Chem 96:3994
187. Mansfield ML, Klushin LI (1993) Macromolecules 26:4262
188. Murat M, Grest GS (1996) Macromolecules 29:1278
189. Chen ZY, Cui SM (1996) Macromolecules 29:7943
190. Lyulin AV, Davies GR, Adolf DB (2000) Macromolecules 33:3294
191. Lyulin SV, Evers LJ, van der Schoot P, Darinskii AA, Lyulin AA, Michels MAJ (2004) Macromolecules 37:3049
192. Sheng YJ, Jiang S, Tsao HK (2002) Macromolecules 35:7865
193. Ganazzoli F (2002) Macromol Symp 190:55
194. Kant R, Biswas P, Blumen A (2000) Macromol Theor Simul 9:608
195. McLeish TCB, Milner ST (1999) Adv Polym Sci 143:195
196. Gotlib YY, Markelov DA (2002) Polymer Sci A (translated from Vysokomol Soedin, Russia) 44:1341
197. Satmarel C, Gurtovenko AA, Blumen A (2004) Macromol Theor Simul 13:487
198. Yin R, Zhu Y, Tomalia DA, Ibuki H (1998) J Am Chem Soc 120:2678
199. Percec V, Ahn CH, Ungar G, Yeardly DJP, Möller M, Sheiko SS (1998) Nature 391:161
200. Jahromi S, Coussens B, Meijerink N, Braam AWM (1998) J Am Chem Soc 120:9753
201. Jahromi S, Palmen JHM, Steeman PAM (2000) Macromolecules 33:577
202. Roovers J (ed)(1999) Branched Polymers I. Adv Polym Sci 142:1
203. Roovers J (ed)(1999) Branched Polymers II. Adv Polym Sci 143:1
204. Newkome GR, Morefield CN, Vögtle F (1996) Dendritic macromolecules: concepts, syntheses, perspectives. VCH, Weinheim
205. Freire JJ (1999) Adv Polym Sci 143:35
206. Ganazzoli F, Allegra G (1990) Macromolecules 23:262
207. Dondos A, Papanagopoulos D (1997) Polymer 38:6255
208. Shida K, Ohno K, Kawazoe Y, Nakamura Y (2004) Polymer 45:1729
209. Lyulin AV, Adolf DB, Davies GR (2001) Macromolecules 34:3783
210. Blumen A, Jurjiu A, Koslowski Th (2004) Macromol Symp 210:301
211. Milner ST, McLeish TCB (1997) Macromolecules 30:2159
212. Milner ST, McLeish TCB (1998) Macromolecules 31:7479
213. Blackwell RJ, Harlen OG, McLeish TCB (2001) Macromolecules 34:2579
214. Bishko G, McLeish TCB, Harlen OG, Larson RG (1997) Phys Rev Lett 79:2352
215. McLeish TCB, Larson RG (1998) J Rheol 42:81

216. von Ferber Ch, Blumen A (2002) J Chem Phys 116:8616
217. Kim Y, Harris AB (1985) Phys Rev B 31:7393
218. Rodgers GJ, Bray AJ (1988) Phys Rev B 37:3557
219. Jasch F, von Ferber Ch, Blumen A (2003) Phys Rev E 68:051106
220. Grimmet G (1989) Percolation. Springer, Berlin Heidelberg New York
221. Fisher ME, Essam JW (1961) J Math Phys 2:609
222. Ben-Avraham D, Havlin S (2000) Diffusion and reactions in fractals and disordered systems. Cambridge University Press, Cambridge, UK
223. Mezard M, Parisi G, Virasoro MA (1986) Spin glass theory and beyond. World Scientific, Singapore
224. Schulz M, Reineker P, Möller M (1995) J Chem Phys 103:10701
225. Burioni R, Cassi D, Blumen A (2002) Chem Phys 282:409
226. Vicsek T (1989) Fractal growth phenomena. World Scientific, Singapore
227. Jayanthi CS, Wu SY, Cocks J (1992) Phys Rev Lett 69:1955
228. Jayanthi CS, Wu SY (1993) Phys Rev B 48:10188
229. Jayanthi CS, Wu SY (1993) Phys Rev B 48:10199
230. Jayanthi CS, Wu SY (1994) Phys Rev B 50:897
231. Blumen A, Jurjiu A, Koslowski T, von Ferber Ch (2003) Phys Rev E 67:061103
232. Blumen A, von Ferber Ch, Jurjiu A, Koslowski T (2004) Macromolecules 37:638
233. Koslowski T, Jurjiu A, Blumen A (2004) J Phys Chem B 108:3283
234. Lach C, Müller P, Frey H, Mülhaupt R (1997) Macromol Rapid Commun 18:253
235. Frey H, Lach C, Schlenk C, Pusel T (2000) Polym Prepr 41:568
236. Möck A, Burgath A, Hanselmann R, Frey H (2001) Macromolecules 34:7692
237. Burgath A, Möck A, Hanselmann R, Frey H (1999) Polym Mater Sci Eng 80:126
238. Möck A, Burgath A, Hanselmann R, Frey H (1999) Polym Mater Sci Eng 80:173
239. Lambert C, Nöll G (1999) J Am Chem Soc 121:8434
240. Lambert C, Gaschler W, Schmälzlin E, Meerholz K, Bräuchle C (1999) J Chem Soc Perk T 2:577
241. Lambert C, Nöll G (2002) Chem Eur J 8:3467
242. Bronstein IN, Semendjajev KA (1985) Taschenbuch der Mathematik (Handbook of mathematics). Nauka and Teubner, Moscow and Leipzig, Ch 2.4.2
243. Schwalm WA, Schwalm MK, Giona M (1997) Phys Rev E 55:6741
244. Jahromi S, Litvinov V, Coussens B (2001) Macromolecules 34:1013
245. Kriesel JW, Tilley TD (1999) Chem Mater 11:1190
246. Jang WD, Jiang DL, Aida T (2000) J Am Chem Soc 122:3232
247. Gröhn F, Kim G, Bauer BJ, Amis EJ (2001) Macromolecules 34:2179
248. Gitsov I, Zhu C (2002) Macromolecules 35:8418
249. Dvornic PR, Li J, de Leuze-Jallouli AM, Reeves SD, Owen MJ (2002) Macromolecules 35:9323

Editor: L. Leibler

Author Index Volumes 101–182

Subject Index

Erratum to
Chemical Composition of Polymer Surfaces
Imaged by Atomic Force Microscopy
and Complementary Approaches

G. Julius Vancso (✉) · Henrik Hillborg · Holger Schönherr

MESA+ Institute for Nanotechnology and Faculty of Science and Technology,
Department of Materials Science and Technology of Polymers, University of Twente,
P.O. Box 217, 7500 AE Enschede, The Netherlands
g.j.vancso@tnw.utwente.nl

Unfortunately, the editor of this article Hans-Henning Kausch was published as author in the XML-version.

Erratum to
Generalized Gaussian Structures:
Models for Polymer Systems with Complex Topologies

Andrey A. Gurtovenko[1,2] (✉) · Alexander Blumen[3]

[1]Biophysics and Soft Matter Group,
 Laboratory of Physics and Helsinki Institute of Physics,
 Helsinki University of Technology, P.O.Box 1100, 02015 Helsinki, Finland
 agu@fyslab.hut.fi

[2]Institute of Macromolecular Compounds, Russian Academy of Sciences,
 Bolshoi Prospect 31, V.O., 199004 St. Petersburg, Russia
 agu@fyslab.hut.fi

[3]Theoretische Polymerphysik, Universität Freiburg, Hermann-Herder-Str. 3,
 79104 Freiburg, Germany
 blumen@physik.uni-freiburg.de

Unfortunately, the editor of this article L. Leibler was published as author in the XML-version.